

ELASTO-HYDRODYNAMIC AND THERMOFLUIDIC INSTABILITIES IN COMPLEX FLUID DROPLETS

A Thesis Submitted

in Partial Fulfilment of the Requirements

for the Degree of

DOCTOR OF PHILOSOPHY

by

Gudlavalleti V V S Vara Prasad

(2018MEZ0011)



DEPARTMENT OF MECHANICAL ENGINEERING
INDIAN INSTITUTE OF TECHNOLOGY ROPAR

July, 2023

Gudlavalleti V V S Vara Prasad: *ELASTO-HYDRODYNAMIC AND THERMOFLUIDIC
INSTABILITIES IN COMPLEX FLUID DROPLETS*

Copyright ©2023, Indian Institute of Technology Ropar

All Rights Reserved

DEDICATED
TO
MY PARENTS



నమఃశివాయ!

Declaration of Originality

I hereby declare that the work which is being presented in the thesis entitled **ELASTO-HYDRODYNAMIC AND THERMOFLUIDIC INSTABILITIES IN COMPLEX FLUID DROPLETS** has been solely authored by me. It presents the result of my own independent investigation/research conducted during the time period from July and 2018 of joining the Ph.D. program to July and 2023 of Ph.D. Thesis submission under the supervision of Dr. Devranjan Samanta, Assistant Professor, and Department of Mechanical Engineering, Indian Institute of Technology Ropar and Dr. Purbarun Dhar, Assistant Professor, and Department of Mechanical Engineering, Indian Institute of Technology Kharagpur. To the best of my knowledge, it is an original work, both in terms of research content and narrative, and has not been submitted or accepted elsewhere, in part or in full, for the award of any degree, diploma, fellowship, associateship, or similar title of any university or institution. Further, due credit has been attributed to the relevant state-of-the-art and collaborations (if any) with appropriate citations and acknowledgments, in line with established ethical norms and practices. I also declare that any idea/data/fact/source stated in my thesis has not been fabricated/ falsified/ misrepresented. All the principles of academic honesty and integrity have been followed. I fully understand that if the thesis is found to be unoriginal, fabricated, or plagiarized, the Institute reserves the right to withdraw the thesis from its archive and revoke the associated Degree conferred. Additionally, the Institute also reserves the right to appraise all concerned sections of society of the matter for their information and necessary action (if any). If accepted, I hereby consent for my thesis to be available online in the Institute's Open Access repository, inter-library loan, and the title & abstract to be made available to outside organizations.



Signature

Name:Gudlavalleti V V S Vara Prasad

Entry Number:2018MEZ0011

Program: Ph.D.

Department:Mechanical Engineering

Indian Institute of Technology Ropar

Rupnagar, Punjab 140001

Date:24-07-2023

Acknowledgement

I would like to express my deepest gratitude to my Ph.D. supervisors **Dr. Devranjan Samanta** and **Dr. Purbarun Dhar** for giving me an opportunity to work with them. Specially, I am very grateful to them for paving the way for me to do proper research by initiating my thought process in multiple ways. I would like to express my profound indebtedness to **Dr. Devranjan Samanta** for his invaluable guidance, endless encouragement, incredible patience, technical support, enlightenment, unconditional support, and timely intervention in difficult times. Especially, your phrase “*It is okay to be wrong, try yourself*” really had a great impact on my mind to realize that sometimes, it is *okay* to think *wrong* in truth-seeking. I would like to express my sincere gratitude and immeasurable appreciation to **Dr. Purbarun Dhar** for his inestimable guidance, continuous support, enlightenment and remarkable patience during my difficult times. Specially, your phrase “*Try to do little work every day*” really had great impact on my mind and lowers my bulk work pressure into *little* parts and it also *everyday* warns me about the importance of the time and the progress of work. I thank both for bestowing overwhelming trust, cultivating independent thinking, and having time for those long research-related discussions whenever needed, despite their busy schedule. Their work ethic, sincerity, and humbleness would always be a source of inspiration throughout my life. Both gave me enormous freedom to explore on my own, allowing me to become an independent researcher. Without their continuous monitoring of the progress of research work and efforts to arrange wide research facilities, it would have been impossible to complete this thesis in the present form.

I warmly thank my Doctoral Committee members, **Dr. Ekta Singla** (chairperson), **Dr. Himanshu Tyagi**, and **Dr. Chander Shekhar Sharma** of the Department of Mechanical Engineering, and **Dr. Vishwajeet Mehandia** of Department of Chemical engineering for continuously monitoring the progress of work and providing valuable suggestions and encouragement. I am very much thankful to the **Indian Institute of Technology Ropar** for providing the necessary infrastructure and financial support. I am also thankful to the **Ministry of Education**, Government of India, for providing scholarship to conduct this research work.

I can't thank enough all the lab mates, who helped and supported in all possible ways to get this work completed. **Dr. Nilamani Sahoo**, **Dr. Soumya Ranjan Mishra**, **Dr. Vivek Jaiswal**, **Dr. Ankur Chattopadhyay**, **Dr. Abhishek Kaushal**, **Mrs. Gargi Khurana**, **Mr. Khusro Kamaluddin**, **Mr. Pulak Gupta**, **Mr. Rahul Kumar**, **Mr. Somenath Gorai**, **Mr. Manglesh singh**, **Mr. Simranjeet Singh**, **Mr. Mohit Yadav**, **Mr. Ajay Gairola**, **Ms. Avni Tyagi**, **Mr. Saiyed Shahrukh Khan**, **Mr. Damodala Anand**, **Mr. Pawan Indolia**, **Mr. Harsh Vardan**, **Mr. Manjeet Meena** and **Mr. Veda Marrapu** are gratefully acknowledged. They were with me during all ups and downs throughout my thesis work and made my tenure enjoyable.

I would like to express my deep gratitude to **Dr. Parmod Kumar** for his helpful collaboration and kind support in the simulation studies during my doctoral research journey. I heartily thank **Mr. Debarshi Debnath**, **Mr. Manmohan Patel**, **Dr. Pushpendra Kumar Shukla**, **Mr. Saurabh Patel**, **Mr. Rahul Kumar**, **Mr. Shibli Khan**, **Mr. Shubankar**, **Ms. Tuba Fatima**, **Mr. Soham Das**, **Mr. Kuljeet**, **Mr. Ajit**, **Mr. Akshay**, **Mr. Akash**, **Mr. Armug Raj**, **Mr. Ayush**, **Mr. Nishad**, **Mr. Kapil** for their cordiality and invaluable support during my two-month stay at **Indian Institute of Technology Mandi**.

I would like to express my profound gratitude to **Dr. Neelkanth Nirmalkar** and his Ph.D. student **Mr. Harsh Sharma** for their kind collaboration in my doctoral research on nanobubble Leidenfrost phenomena. I want to express my heartfelt gratitude to **Dr. Manigandan Sabapathy** and his Ph.D. student **Mr. Chandra Shekhar** their valuable collaboration in my doctoral research on the microemulsion Leidenfrost study.

My deepest gratitude goes to my family for their unflagging love and support throughout my life. Thanks to my mother **Mrs. Gudlavalleti Vijayalakshmi**, my father **Mr. Gudlavalleti Srinivasa Rao** for their immeasurable sacrifices and blessings. They always soften the life difficulties for me, and I owe them all my achievements, including this. My sister's family **Mrs. Durgi Sandhya Rani**, **Mr. Durgi Manikanta** and **Mr. Durgi Neelavenkat** (Nephew) was always there with encouragement and care.

I heartily thank my friends **Mr. Chilukuri Sunil Kumar**, Assistant Engineer, Government of Telangana, (a B. Tech friend) and **Mr. Deepak** (2018MEZ0001) (a Ph.D. friend) for their unwavering support and kind help during various challenges in my personal life. Without their consistent backing and invaluable assistance, I wouldn't have been able to complete and submit my dissertation.


Mr. Rajat Dhiman and **Mr. Himanshu Shekhar** are also greatly acknowledged for providing the Ph.D. thesis Latex template to **IIT Ropar**. **Mr. SatyaJaswant**, **Mr. Devsingh**, **Mr. G. Venugopal**, **Mr. B. Rajesh**, **Mr. V. Satish**, **Mr. D. Yogeshwar**, **Mr. G. Vinay**, **Mr. S S Siddhartha**, **Mr. Gopal Chandra Pal**, **Mr. Anand S**, **Mr. Raushan Kumar**, **Mr. Mainak Pal**, **Mr. Jay Airao**, **Mr. Aleti Yesu**, **Mr. Joseph**, **Mr. Praveen**, **Mr. Rajib Dash**(Technical staff) and **Mr. Anuj Babbar**(Technical staff) to those who felt like family, offering invaluable support. Last but not least, I am thankful to **Mr. Pradeep Kumar Dubey** (Dubey canteen) for providing me food during midnight despite the COVID-19 pandemic situation. Thanks to these individuals who made this challenging task possible. Finally, I kneel in front of the almighty to give the wisdom and perseverance bestowed upon me during my doctoral research and throughout my life.

Vara Prasad

Certificate

This is to certify that the thesis entitled **ELASTO-HYDRODYNAMIC AND THERMOFLUIDIC INSTABILITIES IN COMPLEX FLUID DROPLETS**, submitted by **Gudlavalleti V V S Vara Prasad (2018MEZ0011)** for the award of the degree of **Doctor of Philosophy** of Indian Institute of Technology Ropar, is a record of bonafide research work carried out under my (our) guidance and supervision. To the best of my knowledge and belief, the work presented in this thesis is original and has not been submitted, either in part or full, for the award of any other degree, diploma, fellowship, associateship or similar title of any university or institution.

In our opinion, the thesis has reached the standard fulfilling the requirements of the regulations relating to the Degree.



Signature of the Supervisor(s)

Dr. Devranjan Samanta

Mechanical Engineering Department

Indian Institute of Technology Ropar

Rupnagar, Punjab 140001, India

Date:24-07-2023



Signature of the Supervisor(s)

Dr. Purbarun Dhar

Mechanical Engineering Department

Indian Institute of Technology Kharagpur

Kharagpur, West Bengal 721302, India

Date:24-07-2023

Lay Summary

This dissertation explores the impact dynamics of non-Newtonian fluids on superhydrophobic surfaces and investigates the use of external magnetic and electric fields to control droplet rebound and reduce ink wastage in alternative inkjet printing technologies. The study introduces novel parameters to understand the effect of external fields on non-Newtonian droplets and explores the role of elastohydrodynamic instabilities in determining magneto-elastic and electro-elastic effects that contribute to suppressing droplet rebound. Furthermore, the research examines thermofluidic instabilities arising from Leidenfrost dynamics by using complex fluid droplets and proposes new methods to enhance heat transfer and suppress the Leidenfrost effect. The study presents experimental findings, scaling analysis, and phase maps to identify various regimes of impact hydrodynamics of droplets, providing a detailed analysis of the role played by various parameters on droplet dynamics. Finally, the study proposes new methods for increasing the dynamic Leidenfrost temperature by using nanobubble-dispersed droplets and investigates the influence of various parameters on T_{DL} . The research findings have implications for inkjet printing and spray cooling processes.

Abstract

This dissertation presents research on the impact dynamics of non-Newtonian fluids on superhydrophobic surfaces, and the use of external magnetic and electric fields to control droplet rebound and reduce ink wastage in alternative inkjet printing technologies, including MHD and EHD inkjet printing. The findings of the study are presented in detail, and a new magnetic Bond number(Bo_m), magnetic Weissenberg number(Wi_m) and electric Eotvos number(Eo_e) and electrical Weissenberg number (Wi_e) are introduced to understand the effect of external fields on non-Newtonian droplets due to magnetoelastic and electro elastic instabilities respectively. The study also delves into the realm of thermofluidic instabilities arising from Leidenfrost dynamics by employing complex fluid droplets such as surfactants, nanocolloids, and nanobubbles dispersed fluids. The research aims to suppress or delay the Leidenfrost effect during spray cooling processes and introduces novel coolants or alters the substrate's microstructure to enhance heat transfer.

The first two objectives aim to address elastohydrodynamic instabilities and their role in determining the magneto-elastic and electro-elastic effects that contribute to suppressing droplet rebound.

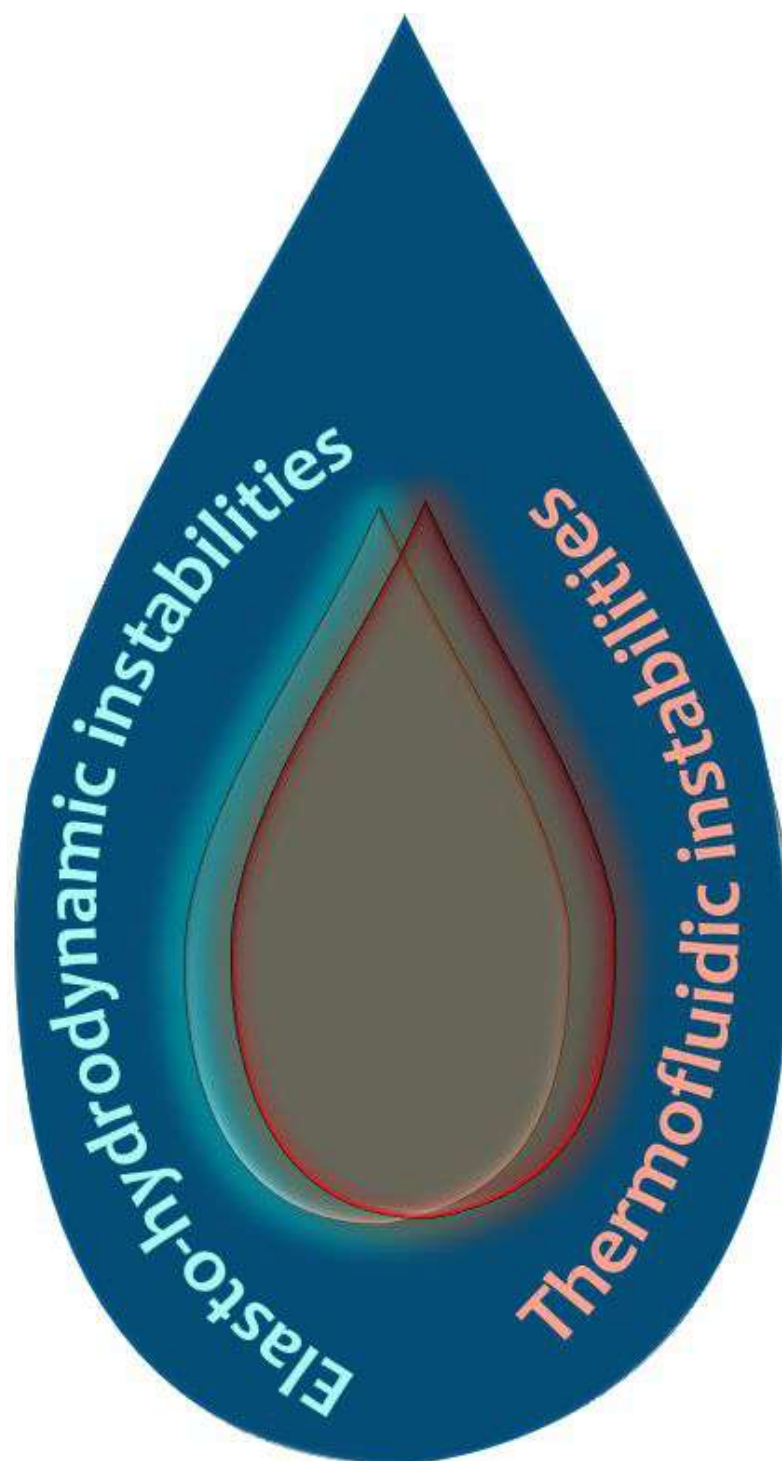
The first objective of the dissertation presents experimental and scaling analysis to propose the existence of magneto-elastic effects in the impact hydrodynamics of non-Newtonian ferrofluid droplets on superhydrophobic surfaces under a magnetic field. The study investigates the role of We , Bo_m , polymer concentration, and Fe_3O_4 concentration in ferrofluids. Adding polymers causes rebound suppression of droplets at lower Bo_m , compared to Newtonian ferrofluid droplets. Moreover, increasing magnetic nanoparticle concentration triggers earlier rebound suppression with increasing Bo_m for a fixed polymer concentration and We . The interplay between the elastic effects of polymer chains and magnetic nanoparticles is named the magneto-elastic effect, leading to rebound suppression. A scaling relationship shows that the rebound suppression is observed as the onset of magneto-elastic instability when the magnetic Weissenberg number (Wi_m) exceeds unity. The study also proposes a phase map to identify the various regimes of impact ferrohydrodynamics of droplets. The second objective of this dissertation involves the investigation of the electrohydrodynamics of non-Newtonian dielectric fluid droplets impacting superhydrophobic surfaces. The results of the experiments reveal the occurrence of an electro-elastic effect that can lead to anti-superhydrophobicity. The study examines the electrohydrodynamics of non-Newtonian dielectric fluid droplets on superhydrophobic surfaces and provide a detailed analysis of the role played by various parameters such as electric Eotvos number Eo_e , Weber number We , dielectric particle concentration TiO_2 , and polymer concentration (PEG-400) on droplet dynamics. The study proposes that the interplay of elastic relaxation dynamics of polymer chains and dielectric particles in the external electric field ambience leads to droplet rebound suppression on superhydrophobic surfaces.

The final three objectives of the dissertation present the potential role of thermofluidic instabilities of complex fluid droplets in suppressing the Leidenfrost effect by delaying the onset of dynamic Leidenfrost temperature during the impact of droplets on a hot surface.

The third objective of the dissertation proposes the addition of anionic and cationic surfactants to water droplets as a novel method to increase the dynamic Leidenfrost temperature T_{DL} , and the effect of surfactant concentration, Weber number(We), and Ohnesorge number(Oh) on the dynamic Leidenfrost temperature is experimentally investigated. The study also proposes a scaling relationship for T_{DL} in terms of We and Oh , and presents a regime map of different boiling regimes as a function of impact We and substrate temperature. The fourth objective of the dissertation reports that the addition of Al_2O_3 nanoparticles to water alters the behavior of droplets impacting on a superheated substrate, delaying the onset of dynamic Leidenfrost temperature and suppressing the overall Leidenfrost regime. The study find that increasing nanoparticle concentration delays the onset of T_{DL} at a specific Weber number (We), but for a constant concentration, the onset of T_{DL} decreases with increasing impact We . The authors observe that the colloid droplets exhibit vigorous spraying behavior due to the nanoparticulate residue deposition during the spreading and retraction stages. The residue on the heated substrate changes the departure diameter of the vapor bubbles during boiling, prevents bubble coalescence and vapor layer formation, and reduces the likelihood of attaining the dynamic Leidenfrost regime. The authors use scaling analysis of T_{DL} with impact We to explore the thermo-hydrodynamic behavior of impacting colloid droplets on a superheated substrate. Finally, the study segregate the different boiling regimes of colloid droplets over various impact We . The fifth objective of the dissertation proposes a new method for increasing the dynamic Leidenfrost temperature T_{DL} by using nanobubble-dispersed droplets and investigates the influence of impact Weber number (We), Ohnesorge number (Oh), and nanobubble concentration on T_{DL} . The findings suggest that using nanobubble-dispersed droplets can significantly delay T_{DL} and that the T_{DL} increases with increasing nanobubble concentration but decreases with increasing impact velocity for a particular concentration. The phase map presented in the study provides insights into the overall boiling behaviors of nanobubble-dispersed fluid droplets with substrate temperature against varied impact We . The overall investigation of the final three objectives of the dissertation has potential implications for thermal management systems operating at high temperatures.

Keywords: *droplets; non-Newtonian fluids; ferrofluids; ferrohydrodynamics; superhydrophobicity; rebound suppression; magnetic Bond number; magnetic Weissenberg number; magneto-elastic instability; dielectrics; electrohydrodynamics; electric Eotvos number; electric Weissenberg number; electro-elastic instability; heat transfer; boiling; phase change; Leidenfrost effect; surfactants; dynamic surface tension; Taylor-Marangoni instability; nanoparticles; colloids; residue; nanobubbles; self rewetting.*

Graphical Abstract



Contents

| | |
|-------------------------------------------------------------|---------------|
| Declaration | ix |
| Acknowledgement | xi |
| Certificate | xiii |
| Lay Summary | xv |
| Abstract | xvii |
| List of Figures | xxv |
| List of Tables | xxxv |
| List of Symbols | xxxvii |
| List of Abbreviations | xxxix |
| List of non-dimensional numbers | xli |
| 1 Introduction | 1 |
| 1.1 Droplet | 1 |
| 1.2 Surface Wettability | 2 |
| 1.2.1 Ideal surface vs Real surface | 2 |
| 1.2.2 Contact angle | 3 |
| 1.2.3 Static contact angle/Young contact angle: | 3 |
| 1.2.4 Dynamic contact angle | 4 |
| 1.2.5 Superhydrophobicity | 5 |
| 1.3 Surface tension | 7 |
| 1.3.1 Surface tension/Equilibrium surface tension | 7 |
| 1.3.2 Dynamic surface tension | 7 |
| 1.4 Complex fluids | 8 |
| 1.4.1 Ferrofluids | 8 |
| 1.4.2 Dielectric fluids | 9 |
| 1.4.3 non-Newtonian fluids | 13 |
| 1.4.4 Electro and Magneto Rheology | 24 |
| 1.4.5 Surfactant solutions | 25 |
| 1.4.6 Bubble dispersions | 30 |
| 1.4.7 Nanocolloids | 32 |
| 1.5 Leidenfrost phenomenon | 33 |

| | | |
|----------|-----------------------------------------------------------------------------------------------------------|-----------|
| 1.5.1 | Why do water droplets dance on a hot surface? | 33 |
| 1.5.2 | Leidenfrost effect | 33 |
| 1.5.3 | Dynamic Leidenfrost effect | 34 |
| 1.5.4 | Origin of Leidenfrost point/Pool Boiling curve | 34 |
| 1.6 | Droplet impact | 36 |
| 1.7 | Motivation | 37 |
| 1.8 | Organization of the Dissertation | 39 |
| 2 | Literature Review | 43 |
| 2.1 | Introduction | 43 |
| 2.2 | Droplet impact | 43 |
| 2.3 | non-Newtonian fluids | 44 |
| 2.4 | Ferrofluids | 44 |
| 2.5 | Dielectric fluids | 45 |
| 2.6 | Leidenfrost droplets | 45 |
| 2.7 | Research Gap | 46 |
| 2.8 | Research Objectives | 47 |
| 3 | Magneto-elastic effect in non-Newtonian ferrofluid droplets impacting on superhydrophobic surfaces | 49 |
| 3.1 | Introduction | 49 |
| 3.2 | Materials and Methodologies | 51 |
| 3.2.1 | Non-Newtonian ferrofluids | 51 |
| 3.2.2 | Substrates | 52 |
| 3.2.3 | Experimental setup | 53 |
| 3.3 | Results and discussions | 56 |
| 3.3.1 | Droplet impact ferrohydrodynamics | 56 |
| 3.3.2 | Droplet rebound suppression kinetics | 58 |
| 3.3.3 | Droplet ferrohydrodynamics regimes | 65 |
| 3.4 | Conclusions | 70 |
| 4 | Triggering of electro-elastic anti-superhydrophobicity during non-Newtonian droplets collision | 71 |
| 4.1 | Introduction | 71 |
| 4.2 | Introduction | 71 |
| 4.3 | Materials and methods | 74 |
| 4.3.1 | Non-Newtonian dielectric fluids | 74 |
| 4.3.2 | Superhydrophobic surfaces | 75 |
| 4.3.3 | Experimental setup | 75 |
| 4.3.4 | Governing non-Dimensional numbers | 76 |
| 4.3.5 | Electrorheology of the experimental fluids | 77 |
| 4.4 | Results and discussions | 81 |

| | | |
|----------|------------------------------------------------------------------------------------------------------------------------|------------|
| 4.4.1 | Spreading electrohydrodynamics of non-Newtonian droplets | 81 |
| 4.4.2 | Droplet rebound suppression (anti-superhydrophobicity) kinetics . . . | 84 |
| 4.5 | Conclusions | 90 |
| 5 | Postponement of dynamic Leidenfrost phenomenon during droplet impact of surfactant solutions | 91 |
| 5.1 | Introduction | 91 |
| 5.2 | Materials and methods | 94 |
| 5.3 | Results and discussions | 95 |
| 5.3.1 | Influence of substrate temperature on spreading dynamics | 96 |
| 5.3.2 | Influence of We and surfactant concentration on spreading dynamics during Leidenfrost boiling (T_{DL}) | 96 |
| 5.3.3 | Role of surfactant concentration on dynamic Leidenfrost temperature (T_{DL}) | 100 |
| 5.3.4 | Scaling T_{DL} with Weber (We) and Ohnesorge (Oh) numbers | 103 |
| 5.3.5 | Influence of Bond number (Bo) on T_{DL} | 104 |
| 5.3.6 | Trampolining dynamics of the droplet at ($T_s > T_{DL}$) $\sim 400^0\text{C}$. . . | 105 |
| 5.3.7 | Fragmentation and jetting dynamics at ($T_s > T_{DL}$) $\sim 400^0\text{C}$. . . | 107 |
| 5.3.8 | Boiling regimes of impacting surfactant droplets | 108 |
| 5.4 | Conclusions | 110 |
| 6 | Morphed inception of dynamic Leidenfrost regime in colloidal dispersion droplets | 111 |
| 6.1 | Introduction | 111 |
| 6.2 | Materials and methods | 113 |
| 6.3 | Results and discussion | 115 |
| 6.3.1 | Transformation of contact boiling in nanocolloidal droplets($T_s \sim 150^0\text{C} < T_{DL}$) | 115 |
| 6.3.2 | Role of nanoparticle concentration on T_{DL} | 117 |
| 6.3.3 | Role of Weber number (We) on T_{DL} | 118 |
| 6.3.4 | Scaling correlation of T_{DL} with governing Weber number (We) and Ohnesorge number (Oh) | 120 |
| 6.3.5 | Boiling regimes of colloidal nanoparticle fluid droplets | 121 |
| 6.4 | Conclusions | 122 |
| 7 | Augmenting the Leidenfrost temperature of droplets via nanobubble dispersion | 123 |
| 7.1 | Introduction | 123 |
| 7.2 | Materials and methodologies | 125 |
| 7.2.1 | Experimental setup | 125 |
| 7.2.2 | Nanobubble generation | 126 |
| 7.3 | Results and discussions | 129 |

| | | |
|----------|-----------------------------------------------------------------------------------------------------------|------------|
| 7.3.1 | Contact boiling regime ($T_s \sim 150^0\text{C}$) < T_{DL} | 129 |
| 7.3.2 | Transition boiling regime ($T_s \sim 190^0\text{C}$) < T_{DL} | 130 |
| 7.3.3 | Dynamic Leidenfrost effect ($T_s \sim T_{DL}$) | 131 |
| 7.3.4 | Scaling T_{DL} with Weber (We) and Ohnesorge (Oh) numbers | 132 |
| 7.3.5 | Residence time of the droplets at T_{DL} | 135 |
| 7.3.6 | Bubble coalescence during the Leidenfrost regime ($T_s \sim T_{DL}$) | 136 |
| 7.3.7 | Droplet rebound dynamics at T_{DL} | 137 |
| 7.3.8 | Effect of impact momentum in post Leidenfrost regime ($T_s \sim 400^0\text{C}$) > T_{DL} | 138 |
| 7.3.9 | Boiling regime map | 138 |
| 7.4 | Conclusions | 140 |
| 8 | Conclusion | 141 |
| 8.1 | Conclusion | 141 |
| 8.2 | Future scope of the work | 143 |
| | References | 145 |
| | List of Publications | 171 |

List of Figures

| | | |
|------|--------------------------------------------------------------------------------------------------------------------------------------------------------------------------------------------------------------------------------------------------|----|
| 1.1 | (a) Pendant droplet, (b) Sessile droplet | 1 |
| 1.2 | Overview | 2 |
| 1.3 | Static contact angle (θ) of a water droplet | 3 |
| 1.4 | Dynamic contact angles of the water droplet on an inclined surface | 4 |
| 1.5 | (a) Hydrophilic surface (b) Hydrophobic surface (c) Superhydrophobic surface | 5 |
| 1.6 | Superhydrophobic surface with low adhesion-Lotus leaf effect (left wing), Superhydrophobic surface with high adhesion-Rose petal effect (right wing) | 6 |
| 1.7 | (a) water droplets (b) water strider (c) paperclip floating on water | 7 |
| 1.8 | Dynamic surface tension | 7 |
| 1.9 | Various complex fluids | 8 |
| 1.10 | Spikes of the ferrofluid | 9 |
| 1.11 | Classifications of the polar dielectric | 9 |
| 1.12 | Electronic polarization | 11 |
| 1.13 | Ionic polarization | 11 |
| 1.14 | Orientational polarization | 12 |
| 1.15 | Interfacial polarization | 12 |
| 1.16 | Stress components in the three-dimensional flow | 13 |
| 1.17 | Types of time-independent flow behaviour | 15 |
| 1.18 | shear stress–shear rate behaviour for time-dependent fluid behaviour | 16 |
| 1.19 | Schematic structure of the polymer | 17 |
| 1.20 | Classifications of the polymers | 17 |
| 1.21 | Classifications of the polymers based on the type of monomers | 18 |
| 1.22 | Classifications of the polymers based on the structure of the polymer | 18 |
| 1.23 | Classifications of the polymers based on the molecular forces of the polymer | 19 |
| 1.24 | Classifications of the polymers based on the mode of synthesis | 19 |
| 1.25 | Weissenberg effect (Rod climbing): The liquid in the photograph was prepared by dissolving a high molecular weight polyisobutylene (B200) in a low molecular-weight solvent of the same chemical nature (Hyvis 07, polybutene). | 20 |
| 1.26 | Barus effect (die swell): Die swell for a 2.0% aqueous solution of polyacrylamide. The liquid falls under gravity on exiting the capillary. (Photograph by Mr. R.E. Evans, University of Wales, Aberystwyth). | 21 |

| | | |
|------|--------------------------------------------------------------------------------------------------------------------------------------------------------------------------------------------------------------------------------------------------------------------------------------------------------------------------------------------------------------------------------------------------------------------------------------------------------------------------------------------------------------------------------|----|
| 1.27 | Kaye effect: (a) A solution of 5.7 g of polyisobutylene in 100 cm^3 of decalin is poured into a shallow dish filled with the same liquid, (b) Every few seconds, the falling stream on reaching the liquid in the dish 'bounces' and falls in an arc. The stream reaches the liquid surface at a distances of the order of a few centimetres from the starting point under the original falling stream. (From A.S. Lodge, Elastic Liquids, Academic Press, 1964, p. 251.) | 22 |
| 1.28 | The Open-Syphon effect: A 0.75% aqueous solution of Polyox WSR 301 fills a beaker. Only the slightest spilling will part empty the beaker. The sequence shows the development from the time soon after a small initial thread has been drawn over the side of the beaker to the stage where the part-emptying of the beaker is nearly complete. A high ratio of extensional viscosity to shear viscosity is a basic requirement in this experiment. (Photograph courtesy of Mr. R.E. Evans, University of Wales, Aberystwyth.) | 23 |
| 1.29 | Schematic of the surfactant | 25 |
| 1.30 | Classifications of the surfactant | 26 |
| 1.31 | Schematic of the Micelle | 27 |
| 1.32 | (a) low surfactant concentration($< CMC$)-moderate surface tension (b) surface saturation($\leq CMC$)-low surface tension, no micelles formation (c) critical micelle concentration($\sim CMC$)-low surface tension, micelle formation (d) high surfactant concentration($\geq CMC$)-low surface tension, micelle formation | 27 |
| 1.33 | Chemical structure of the SDS and CTAB | 27 |
| 1.34 | Tears of wine | 28 |
| 1.35 | some insects can jump on water | 29 |
| 1.36 | Nanobubbles | 30 |
| 1.37 | Bubbles in Champagne fizz up in a straight line | 31 |
| 1.38 | (a) Stable colloid (b)Unstable colloid | 32 |
| 1.39 | Classifications of the colloids | 32 |
| 1.40 | Leidenfrost effect (droplets dance on a hot surface) | 33 |
| 1.41 | Leidenfrost droplets | 34 |
| 1.42 | Pool boiling curve for water | 35 |
| 1.43 | Droplet applications | 36 |
| 1.44 | Inkjet printing | 37 |
| 1.45 | Magnetohydrodynamics(MHD) and Electrohydrodynamics(EHD) | 38 |
| 1.46 | Applications of Leidenfrost droplets | 38 |
| 1.47 | Organization of the Dissertation | 39 |
| 3.1 | Zeta Potential distribution of the highest concentration(5% w/w -F5) of the operating range of the ferrofluids used. | 51 |
| 3.2 | Microscopic structure of spray coated superhydrophobic surface using Scanning Electron Microscopy | 52 |

| | | |
|------|--------------------------------------------------------------------------------------------------------------------------------------------------------------------------------------------------------------------------------------------------------------------------------------------------------------------------------------------------------------------------------------------------------------------------------------------------------------------------------------------------------------------------------------------------------------------------------------------------------|----|
| 3.3 | Static equilibrium contact angles of different non-Newtonian ferrofluid droplets on spray coated superhydrophobic surface. | 53 |
| 3.4 | Schematic of the experimental setup. (a) Electromagnet power controller (b) droplet dispensing mechanism (DDM) unit (c) LED array for backlight illumination (d) DDM and LED array intensity controller (e) computer for data acquisition and camera control (f) micro-syringe (g) high speed camera (h) programmable electromagnet unit (i) spray coated superhydrophobic surface (j) bread board. | 54 |
| 3.5 | (i) top view and (ii) front view of the ferrofluid droplet under magnetic field. N and S represent the north and south poles of the electromagnet. | 54 |
| 3.6 | Rheological response of the non-Newtonian ferrofluid (P10-F5) in the presence of magnetic field. The sample with the highest polymer and Fe_3O_4 content has been chosen to explain the rheology in the context of the most viscous sample. It is noted that the non-Newtonian character of the ferrofluids is retained only up to shear rates of $\sim 50\text{--}100\text{ s}^{-1}$. This behaviour is also conserved in case of the magnetorheology. Beyond this regime, the fluids show nearly Newtonian behaviour, albeit with enhanced Newtonian viscosity due to the magnetic field. | 55 |
| 3.7 | Viscoelastic response of the non-Newtonian ferrofluid (P10-F2.5) due to increasing oscillatory angular frequency at 1 % oscillatory strain amplitude. A single case has been illustrated for representation purpose. The oscillatory frequency (ω) dependent values of G' and G'' are used to determine the frequency dependent complex viscosity as $\eta_c = \omega^{-1} \sqrt{G'^2 + G''^2}$, which is further used to estimate the relaxation time scales for the non-Newtonian fluids. | 55 |
| 3.8 | Temporal evolution of droplet impact ferrohydrodynamics for different Bo_m for (a) P0-F2.5 (b) P5-F2.5 and (c) P10-F2.5 fluids. The figure shows the role of increasing non-Newtonian fluid nature on the droplet impact ferrohydrodynamics. The scale bars represent 2.8 mm. The images are 1.6 ms apart. The magnetic field acts along the x-direction (coordinate axis shown in first row, first column of fig.3.8c) | 56 |
| 3.9 | The effect of magnetic Bond number (Bo_m) on the maximum non-dimensional orthogonal spreading (ξ_{max}) with (a) varying polymer concentration and (b) magnetic particle concentration | 57 |
| 3.10 | Effects of polymer concentration on the rebound kinetics of the ferrofluid droplets over SH surface for different magnetic Bond numbers at $We \sim 100$ for (a) P0-F2.5 (b) P5-F2.5 and (c) P10-F2.5. The scale bars represent 2.8 mm. From top to bottom, the rows represent $Bo_m = 0, 75, 300, 600$ and 1200. The region circumscribed by the dashed lines illustrates the regimes of rebound suppression. | 58 |

| | | |
|------|------------------------------------------------------------------------------------------------------------------------------------------------------------------------------------------------------------------------------------------------------------------------------------------------------------------------------------------------------------------------------------------------------------------------------------------------|----|
| 3.11 | Effects of magnetic particle concentration on the rebound suppression over SH surface for different magnetic Bond numbers, for (a) P10-F2.5 and (b) P10-F5, at $We \sim 100$. The scale bar represents 2.81 mm. From top to bottom, the rows represent $Bo_m=0, 75, 300, 600$ and 1200. The region circumscribed by the dashed lines illustrates the regimes of rebound suppression. | 59 |
| 3.12 | Effects of the impact Weber number on the impact events over SH surface for different Bo_m at $We \sim 40$ and ~ 100 . The scale bar represents 2.81 mm. From top to bottom, the rows represent $Bo_m=0, 75, 300, 600$ and 1200. The regions circumscribed by the dashed lines illustrate the regimes of rebound suppression. | 60 |
| 3.13 | Plot of the magnetic Weissenberg number (Wi_m) against the magnetic field intensity, for (a) P10-F2.5 droplets impacting at different velocities, and (b) for different non-Newtonian ferrofluid droplets impacting at velocity of 1.5 m/s. The horizontal dashed line indicated $Wi_m=1$. All points lying in the regime above this line exhibit rebound suppression triggered by the magneto-elastic effect | 64 |
| 3.14 | Demarcation of “rebound (combined RI and RII)” and “no rebound” cases of impacting non-Newtonian ferrofluid droplets in external magnetic field by changing both polymer concentration and magnetic nanoparticle concentration. | 66 |
| 3.15 | Scaling relationship between critical We and Bo_m to demarcate the “rebound” and “no rebound” behaviours of impacting non-Newtonian ferrofluid droplet for different concentrations of both polymer and magnetic nano particles. | 66 |
| 3.16 | (a) and (b) shows the critical We (across which We ferrofluid droplet “rebound” behaviour turns into “no rebound” and vice versa) over different polymer concentrations and magnetic nanoparticles concentrations respectively. | 68 |
| 3.17 | Phase maps indicating the different impact ferrohydrodynamic outcomes of non-Newtonian ferrofluid droplets in magnetic field ambience. The regimes 0, I, II, III, IV and V represent “ <i>non-experimental regime</i> ”, “ <i>rebound with pinch-off</i> ”, “ <i>complete rebound</i> ”, “ <i>breakup during retraction</i> ”, “ <i>fragmentation</i> ” (with orthogonal elongation) and “ <i>rebound suppression</i> ”, respectively. | 69 |
| 4.1 | Zeta Potential distribution of the highest concentration(10% w/w -T10) of the operating range of the dielectric fluids used. | 75 |

| | | |
|-----|----------------------------------------------------------------------------------------------------------------------------------------------------------------------------------------------------------------------------------------------------------------------------------------------------------------------------------------------------------------------------------------------------------------------------------------------------------------------------------------------------------------|----|
| 4.2 | Schematic of the experimental setup: (1) electrical wires (2) computer for data acquisition and camera control (3) DDM and backlight illumination controller (4) Droplet dispensing mechanism (DDM) unit (5) Microliter syringe (6) LED array (7) high speed camera (8) SH substrate (9) high voltage DC power supply unit (10) electrode assembly. | 76 |
| 4.3 | Shear viscosity of non-Newtonian dielectric fluid droplet with the variation of (a) polymer concentration and (b) dielectric particle concentration in the absence of an external electric field. | 77 |
| 4.4 | Shear viscosity of non-Newtonian dielectric fluid droplet in the presence of external DC electric field: (a) P20-T10 with the variation of DC electric field ranging from 0kV/mm to 0.5333kV/mm and in fig.4.4. (a), legend values are in kV/mm (b) effect of polymer concentration on shear viscosity against electric field strength 0.5333kV/mm and (c) effect of dielectric particle concentration with same polymer concentration on shear viscosity against electric field strength 0.5333kV/mm. | 78 |
| 4.5 | Small amplitude oscillatory shear (SAOS) electrorheological characterization over different electrical field strengths ranging from 0kV/mm to 0.5333kV/mm: (a) strain sweep of P20-T10 at a fixed angular frequency 1rad/s and (b) frequency sweep of P20-T10 at constant strain (c) Maxwell single-mode fit. In fig.4.5.a-c, all legend values are in kV/mm. . | 79 |
| 4.6 | Temporal evolution of the spreading electrohydrodynamics of non-Newtonian dielectric droplet for Eo_e ranging from 0-12, at $We \sim 65$ ($U=1.25\text{m/s}$), for different fluids as: (a) P5-T0 (b) P5-T2.5 (c) P5-T5 and (d) P5-T10. The scale bar represents 2.72 mm. Black dashes (—) represent the direction of electric field lines. | 81 |
| 4.7 | (a) Temporal evolutions of ξ from the instant of impact to the instant of attaining ξ_{max} at $We \sim 65$ and $Eo_e = 3.2$, (b) effect of dielectric particle concentration on ξ_{max} for a fixed polymer concentration P5 at $We \sim 65$ (i.e., at $U=1.25\text{ m/s}$). Black dashed line (—) in fig. 4.4.b. represent the best polynomial fit. | 83 |
| 4.8 | Effect of polymer concentration on non-Newtonian dielectric fluid droplet rebound for Eo_e ranging from 0-12, at $We \sim 85$ ($U=1.25\text{m/s}$) for fluids as: (a) P0-T10 (b) P5-T10 (c) P10-T10 (d) P20-T10. The scale bar represents 2.72 mm. The red outline represents the cases where complete suppression of droplet rebound (anti-superhydrophobicity) is observed. | 84 |
| 4.9 | Effect of fluid dielectric constant (particle concentration) on non-Newtonian fluid droplet rebound suppression for Eo_e ranging from 0-12, at $We \sim 85$ ($U=1.25\text{m/s}$) for fluids as: (a) P20-T0 (b) P20-T5 (c) P20-T7.5 (d) P20-T10. The scale bar represents 2.72 mm. The red outline represents the cases where complete suppression of droplet rebound (anti-superhydrophobicity) is observed. | 85 |

| | | |
|------|-------------------------------------------------------------------------------------------------------------------------------------------------------------------------------------------------------------------------------------------------------------------------------------------------------------------------------------------------------------------------------------------------------------------------------------------------------------------------------------------------------------------------------------------------------------------------------------|----|
| 4.10 | Effect of Weber number (We) on non-Newtonian dielectric fluid droplet rebound suppression over different Eo_e ranging from 0-12 for the case of P20-T10: (a) $We \sim 85$ ($U=1.25\text{m/s}$) (b) $We \sim 120$ ($U=1.5\text{m/s}$) (c) $We \sim 165$ ($U=1.75\text{m/s}$). The scale bar represents 2.64 mm. The red outline represents the cases where complete suppression of droplet rebound (anti-superhydrophobicity) is observed. | 86 |
| 4.11 | Electro-elasto-hydrodynamics of the non-Newtonian dielectric fluid droplet during the onset of retraction at $We \sim 85$: (a) role of fluid elasticity (polymer concentration) on Weissenberg number (Wi) for P2.5 to P20 with same dielectric particle concentration (T10) (b) map of Eo_e with Wi for different fluids, showing a best fit of power law scaling. | 87 |
| 4.12 | Regime map of droplet impact outcomes with proposed electric Weissenberg number (Wi_e) against Eo_e : (a) Map of Wi_e for different We for P20-T10 fluid (b) Map of Wi_e for different fluids at $We \sim 85$ | 88 |
| 4.13 | Demarcation of both rebound and no rebound (rebound suppression) regimes: (a) effect of Eo_e over polymer concentration at $We \sim 85$ (b) effect of Eo_e over dielectric nanoparticles concentration at $We \sim 85$, and (c) effect of Eo_e over We for a particular fluid P20-T10. | 90 |
| 5.1 | Schematic of the experimental setup: (1) Vibration free table-top (2) high-speed camera (3) hot substrate (4) microsyringe (5) droplet dispensing mechanism (DDM) unit (6) LED backlight (7) DDM and backlight illumination controller (8) hot substrate controller (9) computer for data acquisition and camera control. | 95 |
| 5.2 | Maximum spread state of SDS droplets for different impact velocities at (a) $T_a \sim 30^\circ\text{C}$, and (b) at their respective T_{DL} s (has been shown in the inset of each cell). The scale bar represents ~ 2.64 mm. The maximum spreading diameter (D_{max}) measurements with varying Weber number and surfactant concentration are shown in fig. 5.3. The transient dynamics of SDS droplets at 220°C (the temperature at which a water droplet attains Leidenfrost state at 0.5 m/s in the present study) is provided in fig. 5.6. | 97 |
| 5.3 | Variation in maximum spreading diameter (D_{max}) for different impact velocities of (a) SDS solution droplets at ambient temperature ($T_a \sim 30^\circ\text{C}$), (b) SDS solution droplets and (c) CTAB solution droplets at their respective T_{DL} | 97 |
| 5.4 | The maximum spread factor ($\beta_{max} = (D_{max}/D_o)$) at different We for surfactant solution droplets of (a) SDS (b) CTAB, respectively. In above figures, (\square) represents 0 CMC or water, (\triangle), (∇), (\diamond) and (\bigcirc) represent surfactant concentrations of 0.25 CMC, 0.5 CMC, 0.75 CMC and 1 CMC, respectively. The arrows represent increasing surfactant concentration. Fig. 5.5. shows the variation of $\beta_{max} = (D_{max}/D_o)$ for different impact velocities. | 98 |

| | | |
|------|-----------------------------------------------------------------------------------------------------------------------------------------------------------------------------------------------------------------------------------------------------------------------------------------------------------------------------------------------------------------------------------------------------------------------------------------------------------------------------------------------------------------------------------------|-----|
| 5.5 | Variation in non-dimensional maximum spreading diameter ($\beta_{max} = (D_{max}/D_o)$) over different impact velocities and different surfactant concentration of (a) SDS and (b) CTAB surfactant fluid droplets at their respective T_{DL} 's | 98 |
| 5.6 | Temporal evolution of the impacting SDS solution droplets with low impact velocity $U=0.5$ m/s at their respective T_{DL} : (a) side view (b) top view. For the same initial impact velocity, We is changing mildly due to variation in surfactant concentration. The scale bar represents 2.64 mm. The 3 rd column of each row represents the instant at which maximum spread occurs. The 4 th column of each row represents the instant at which the droplet begins to levitate for the first time. | 101 |
| 5.7 | The dynamic Leidenfrost temperature (T_{DL}) over surfactant concentration of (a) SDS and (b) CTAB fluid droplets. | 102 |
| 5.8 | Dynamic Leidenfrost temperature (T_{DL}) with respect to (a) Weber number (We) and (b) Ohnesorge number (Oh) for SDS solution droplets. The black dotted lines (4) in(a) and (b) represents the scaling behavior of T_{DL} with We and Oh respectively (as per given scaling in each figure). | 103 |
| 5.9 | Comparison between the calculated and experimental T_{DL} of impacting surfactant solution droplets with different concentrations. | 104 |
| 5.10 | Effect of Bond number (Bo) on dynamic Leidenfrost temperature T_{DL} of different concentrations of SDS solution droplet at impact velocity $U=0.5$ m/s. | 105 |
| 5.11 | Droplet trampolining dynamics of SDS solution droplets with low impact velocity $U=0.5$ m/s at the surface temperature of 400 ⁰ C. The scale bar represents 2.64 mm. The dynamics of 1 CMC SDS droplets at 0.5m/s, 0.75 m/s, and 1 m/s are presented in the supplementary section in movie format. | 106 |
| 5.12 | (a) Non-dimensional rebound height vs. SDS concentrations for different impact velocities. Trampolining dynamics over time is presented as 4.11. (b) coefficient of restitution, ε , for the same process in (a). | 107 |
| 5.13 | Jet ejection dynamics of SDS solution droplets at high impact velocity $U=1$ m/s for surface temperature $\sim 400^0$ C. The scale bar represents 2.64 mm. | 108 |
| 5.14 | Jet formation dynamics: (a) maximum jet height (b) critical substrate temperature (T_s) and (c) critical We with respect to SDS concentration of impinging droplets with high impact velocity $U=1$ m/s at surface temperature $\sim 400^0$ C. | 109 |
| 5.15 | Different boiling regimes impacting droplets of (a) water, (b) SDS, and (c) CTAB. The top row shows representative snapshots of the different boiling behaviors. | 110 |

| | | |
|-----|------------------------------------------------------------------------------------------------------------------------------------------------------------------------------------------------------------------------------------------------------------------------------------------------------------------------------------------------------------------------------------------------------------------------------------------------------------------------------------------------------------------------------------------------------------------------------------------------------------------------------------------------------|-----|
| 6.1 | Schematic of the experimental setup: (a) Motorized xyz stage (b) Droplet dispensing mechanism (DDM) unit (c) DDM controller (d) strobe light (e) Diffuser (f) Microliter syringe (g) Hot substrate (h) Hot substrate controller (i) High speed camera (j) Micron Lab jack (k) Computer for data acquisition and camera control (l) Vibration isolation table top | 114 |
| 6.2 | Zeta Potential distribution of the highest concentration(1% w/w) of the operating range of the nanocolloids used. | 114 |
| 6.3 | shows various transformations of contact boiling in nanocolloidal droplets at $We \sim 10$ at ($T_s \sim 150^0C$). In the array matrix (represented with gray colour dashed lines) of fig.6.3., the cluster of two images represents side view and top view respectively and all timeframe numbers (0, 100, 250, 500, 750 and 1012) above each cluster are in ms (milliseconds). The scale bar in the top-left corner of the first (side-view) and second (top view) columns represents 2.96mm. In fig.6.3., yellow, green and red color shaded regions represent spray boiling, bubbly boiling and residue deposition stage respectively. | 116 |
| 6.4 | Variation of non-dimensional residue diameter (D^*) of different concentrations of nanocolloidal droplets over different We at ($T_s \sim 150^0C$). The legend values represent %w/w concentration of nanoparticles of nanocolloids. | 117 |
| 6.5 | .(a) Temporal evolutions of the side-views of impacting nanocolloidal droplets with low $We \sim 10$ at their respective T_{DL} 's. All timeframe numbers (0, 5, 10, 15, 20 and 25) above each image in fig. 6.5a.are in ms (milliseconds). (b) Change in the T_{DL} over nanoparticle concentration ranging from 0.1% w/w to 1% w/w for different impact velocities. The scale bar represents 2.96mm. | 118 |
| 6.6 | .(a)Temporal evolutions of the side-views of impacting nanocolloidal droplets with 1% w/w nanoparticle concentration at their respective T_{DL} 's (b) Change in the T_{DL} over different We with the variation of nanoparticles concentration. In fig.6.5b., all legend values were represented as %w/w. All timeframe numbers (0, 5, 10, 15, 20 and 25) above each image in fig. 6.6a. are in ms (milliseconds).The above zoomed version of side view and top view snapshots evident the residue deposition during levitation of parent nanocolloidal droplet at their respective (T_{DL}). The scale bar represents 2.96mm. | 119 |
| 6.7 | .(a) Fitting of scaling correlation (calculated T_{DL})over experimental T_{DL} of various concentrations of the nanocolloids. The legend values represent %w/w concentration of nanoparticles of nanocolloids. Error bars represents the fluctuation of T_{DL} data point due to repeatability of the experiments. . | 120 |

| | | |
|-----|-----------------------------------------------------------------------------------------------------------------------------------------------------------------------------------------------------------------------------------------------------------------------------------------------------------------------------------------------------------------------------------------------------------------------------------------------------------------------------------|-----|
| 6.8 | Various boiling regimes of impacting nanocolloidal droplets with varied We of (a) deionized water (b), (c) and (d) shows nanocolloidal droplets with the concentration of 0.1%, 0.5% and 1% w/w respectively. The top row shows paradigmatic images of the different boiling behaviors: C-Contact boiling, S- Spray boiling, R-Rebounding Leidenfrost, RR-Residue-Rebounding Leidenfrost boiling and F-Fragmenting Leidenfrost. | 121 |
| 7.1 | Schematic of the experimental setup: (1) vibration-free table top, (2) computer for data acquisition and camera control, (3) high-speed camera with macro lens, (4) hot substrate, (5) droplet dispensing mechanism (DDM) unit, (6) DDM and backlight illumination controller, (7) hot substrate temperature controller, (8) micro liter-syringe, (9) backlight array. | 125 |
| 7.2 | (a) Experimental setup for nanobubble generation and (b) Bubble size distribution at different time interval. | 126 |
| 7.3 | Bulk nanobubbles generated at time intervals of 15, 30, 45, and 60 min; (a) Bubble number density (BND), (b) Bubble diameters, (c) Zeta potential, (d) Refractive index | 128 |
| 7.4 | Temporal evolution of the droplet during contact boiling stage. i.e., at $(T_s \sim 150^\circ\text{C}) < T_{DL}$ at a fixed impact velocity $U=0.5\text{m/s}$. Violet color inset represents the CCR mode of NB fluids in the Fig.7.4. The supplementary movies (figure7.4._water, figure7.4._104million) of each test fluid droplets illustrates the CCR mode in case of NB fluids. | 130 |
| 7.5 | Temporal snapshots of the splashing behaviour associated with thin jet ejection during Transition boiling stage. i.e., at $(T_s \sim 190^\circ\text{C}) < T_{DL}$ at a fixed impact velocity $U=0.5\text{m/s}$. Red color arrow in the inset of Fig.7.5. represents the jet ejection along with spraying. Supplementary video is added for further clarity (figure7.5.). | 131 |
| 7.6 | Influence of nanobubble concentration on T_{DL} : Temporal evolution (a) side-view and (b) top views of impacting droplets with a low impact velocity of $U=0.5\text{ m/s}$ at their respective T_{DL} s. The scale bar represents 2.64 mm and is the same for all cases. The first row with 0 million bubbles/ml shows water droplets and nanobubble dispersion concentration increases from top to bottom (the arrow at the extreme left shows concentration values). . . . | 133 |
| 7.7 | Effect of droplet impact velocity on dynamic Leidenfrost temperature (T_{DL}) for different nanobubbles concentrations. The error bars represent variation of $\pm 5^\circ\text{C}$ | 133 |

- 7.8 Relationship of T_{DL} with (a) We (In above Fig:7.8.a; the legend values represent million bubbles/ml, for instance legend value 214 represents the fluid with the dissolved oxygen nanobubbles concentration of 214 million bubbles/ml) and (b) Oh for different nanobubble concentrations. The dashed lines represent the scaling relationships obtained from the data. The lowest Oh value is of NB fluid 214 million bubbles/ml whereas the highest Oh value is of water. 134
- 7.9 The scaling correlation between the experimental and calculated T_{DL} of various nanobubbles concentrations. 135
- 7.10 The non dimensional residence time of different concentrations of nano bubbles dissolved water droplets (a) side view snapshots for varied bubble concentrations at an almost same We (b) over different Weber (We) numbers respectively. (b)The symbols (\square), (\triangle), (∇), (\diamond) and (\circ) represent different bubble concentrations of 0 (water), 87, 104, 158 and 214 million bubbles/ml respectively. The downward arrow is indicating increasing NB concentration. 136
- 7.11 Transformation of nanobubbles into macrobubble through microbubbles coalescence inside liquid droplet during dynamic Leidenfrost stage (i.e., at T_{DL}) at a fixed impact velocity $U=0.5\text{m/s}$. The scale bar represents 2.64 mm and is the same for all figures. The first row (0 million bubbles/ml) represents deionized water droplets and nanobubbles concentration increases from top to bottom rows. 137
- 7.12 The maximum nondimensional rebound height (h_{max}/R) of different concentrations of nanobubbles dispersed droplets during dynamic Leidenfrost stage (a) side view snapshots for varied bubble concentrations at an impact velocity $U=0.5\text{m/s}$ (b) maximum nondimensional rebound height (h_{max}/R) respectively. 138
- 7.13 Impact velocity dependence on different Leidenfrost states of nanobubbles dispersed fluid droplets with a particular concentration (87 million bubbles/ml) at a fixed elevated substrate temperature ($T_s \sim 400^\circ\text{C}$). . . . 139
- 7.14 Phase map of boiling regimes of impacting droplets with varied Weber (We) numbers of (a) deionized water and (b) NB fluid (concentration of 214 million bubbles/ml) drops. The top row shows representative snapshots of the different boiling behaviors. 140

List of Tables

| | | |
|-----|--------------------------------------------------------------------------------------------------------------------------------------------------------------------------------------------------------------------------------------------------------------------------------------------------------------------------|-----|
| 3.1 | Physical properties of impacting non-Newtonian dielectric fluid droplets: pre-impact droplet diameter D_o (mm), density ρ (kg/m^3), surface tension σ (mN/m) | 53 |
| 4.1 | Physical properties of impacting non-Newtonian dielectric fluid droplets: pre-impact droplet diameter D_o (mm), density ρ (kg/m^3), surface tension σ (mN/m) | 74 |
| 4.2 | Non-Dimensional numbers of impacting non-Newtonian dielectric fluid droplets | 76 |
| 4.3 | The relaxation time scales of non-Newtonian dielectric fluids for a particular polymer and dielectric nanoparticle concentration | 80 |
| 4.4 | The relaxation time scales of non-Newtonian dielectric fluids for different polymer concentrations | 80 |
| 4.5 | The relaxation time scales of non-Newtonian dielectric fluids for various dielectric particle concentrations | 80 |
| 5.1 | Experimental conditions and thermophysical properties of test fluid droplets: pre-impact droplet diameter D_o (mm), density ρ (kg/m^3), surface tension σ (mN/m), viscosity η (mPa-s), and capillary length λ_c (mm). In table.5.1 CMC represents critical micelle concentration. | 95 |
| 6.1 | Thermophysical properties of impacting nanocolloidal droplets at 25^0C : pre-impact droplet diameter D_o (mm), density ρ (kg/m^3), surface tension σ (mN/m), viscosity η (mPa-s). | 115 |
| 7.1 | Thermophysical properties of test fluid droplets at 25^0C : pre-impact droplet diameter D_o (mm), density ρ (kg/m^3), surface tension σ (mN/m), viscosity η (mPa-s), and capillary length λ_c (mm). | 129 |

List of Symbols

| | |
|-----------------|-------------------------------------------------------------------------|
| θ | static/Young contact angle, (degrees) |
| θ_A | advancing contact angle, (degrees) |
| θ_R | receding contact angle, (degrees) |
| θ | contact angle hysteresis, (degrees) |
| σ_{lv} | interfacial tension of the liquid-vapor, (N/m) |
| σ_{sv} | interfacial tension of the solid-vapor, (N/m) |
| σ_{sl} | interfacial tension of the solid-liquid, (N/m) |
| α | sliding angle/roll-off angle, (degrees) |
| ΔT | wall superheat/ temperature difference, ($^{\circ}C$) |
| T_L | Leidenfrost temperature/static Leidenfrost temperature, ($^{\circ}C$) |
| T_{DL} | dynamic Leidenfrost temperature, ($^{\circ}C$) |
| ρ | density, (kg/m ³) |
| V | impact velocity, (m/s) |
| V_o | impact velocity, (m/s) |
| U | impact velocity, (m/s) |
| D_o | pre-impact droplet diameter, (m) |
| σ_{lv} | surface tension, (N/m) |
| B | magnetic flux density, (Tesla) |
| μ_o | magnetic permeability of free space, (H/m) |
| η | viscosity of the fluid, (Pa-s) |
| m | magnetic moment per unit mass, (J/kg T) |
| G' | storage modulus/elastic modulus, (Pa) |
| G'' | loss modulus/viscous modulus, (Pa) |
| ω | angular frequency, (rad/s) |
| η_c | complex viscosity of the fluid, (Pa-s) |
| ξ_{max} | maximum non-dimensional orthogonal spreading (m) , |
| λ | polymer relaxation time , (s) |
| $\dot{\gamma}$ | shear rate , (1/s) |
| ϵ_o | electrical permittivity of free space/vacuum , (F/m) |
| ϵ | relative electrical permittivity of test fluids |
| E | electric field strength , (V/m) |
| σ_{drop} | surface tension of the droplet, (N/m) |
| ω_c | cross-over frequency (rad/s) |
| ξ_{max} | nondimensional maximum elliptical spreading |
| D_{major} | major axis diameter of the droplet (m) |
| D_{minor} | minor axis diameter of the droplet (m) |
| du/dy | shear rate (1/s) |

| | |
|---------------|----------------------------------------------------------------|
| R | liquid sheet radius during onset of retraction (m) |
| y | liquid sheet height (thickness) during onset of retraction (m) |
| t | time elapsed (s) |
| C | concentration (million bubbles/ml) |
| λ_c | capillary length (m) |
| β_{max} | maximum spread factor |
| D_{max} | maximum spreading diameter (m) |
| g | acceleration due to gravity (m/s ²) |
| ϵ | coefficient of restitution |
| $h_{rebound}$ | rebound height (m) |
| h_{impact} | impact height (m) |
| T_s | substrate temperature ($^{\circ}C$) |
| H | impact height (m) |
| D^* | non-dimensional residue diameter |
| t_f | lifetime of the bubble (s) |
| ρ_g | density of the gas bubble (kg/m ³) |
| C_s | saturation concentration of gas |
| f | gas saturation ratio |
| P_v | pressure inside the embryonic vapor bubble (Pa) |
| P_l | liquid pressure (Pa) |
| P_{sat} | saturation pressure (Pa) |
| p | Laplace pressure (Pa) |
| V_{re} | Rewetting velocity (m/s) |
| t_r | residence time (s) |
| t_i | impact time (s) |
| t_r^* | nondimensional residence time |
| h_{max} | maximum rebound height (m) |
| R | radius of the pre-impact droplet (m) |

List of Abbreviations

| | |
|--------------------------------|-----------------------------------|
| SDS | sodium dodecyl sulfate |
| SLS | sodium lauryl sulfate |
| SLES | sodium lauryl ether sulfate |
| CMC | critical micelle Concentration |
| CTAB | cetyltrimethylammonium bromide |
| TiO ₂ | Titanium dioxide |
| O ₂ | oxygen |
| MHD | magnetohydrodynamic |
| EHD | electrohydrodynamic |
| MRF | magnetorheological fluids |
| Fe ₃ O ₄ | iron (II, III) oxide |
| PEG | Polyethylene glycol |
| DI | deionized |
| SH | superhydrophobic |
| DDM | droplet dispensing mechanism |
| LED | light-emitting diode |
| PP | parallel plate |
| PAAM | polyacrylamide |
| DOD | droplet-on-demand |
| EWOD | electrowetting on dielectric |
| kV | kilo Volt |
| ER | Electrorheological |
| SAOS | small amplitude oscillatory shear |
| DC | direct current |
| E | electric field strength (V/m) |
| PIV | particle image velocimetry |
| TIR | total internal reflection |
| LFP | Leidenfrost point |
| DST | dynamic surface tension |
| LFT | Leidenfrost temperature |
| CCR | constant contact radius |
| Al ₂ O ₃ | Aluminium oxide |
| RR | Residue rebounding |
| NB | nanobubble |
| NTA | Nanoparticle Tracking Analysis |
| DLS | Dynamic Light Scattering |
| BND | Bubble number density |

| | |
|----|------------------|
| RI | Refractive index |
| DC | direct current |

List of non-dimensional numbers

| non-dimensional number | Definition | Expression |
|-----------------------------|-------------------------------------------------------------|----------------------------------------------------------|
| Weber number | $\frac{inertia\,force}{surf\,acetension\,force}$ | $We = \frac{\rho V^2 D_0}{\sigma_{lv}}$ |
| Reynolds number | $\frac{inertia\,force}{viscous\,force}$ | $Re = \frac{\rho V D_0}{\mu}$ |
| Capillary number | $\frac{viscous\,force}{surf\,acetension\,force}$ | $Ca = \frac{\eta V}{\sigma_{lv}}$ |
| Bond number/Eotvos number | $\frac{gravitational\,force}{surf\,acetension\,force}$ | $Bo/Eo = \frac{\rho g D_0^2}{\sigma_{lv}}$ |
| magnetic Bond number | $\frac{magnetic\,force}{surf\,acetension\,force}$ | $Bo_m = \frac{B^2 D_0}{\mu_0 \sigma_{lv}}$ |
| electric Eotvos number | $\frac{electric\,force}{surf\,acetension\,force}$ | $Eo_e = \frac{\epsilon_o \epsilon_r E^2}{\sigma_{drop}}$ |
| Weissenberg number | $\frac{elastic\,force}{viscous\,force}$ | $Wi = \lambda \dot{\gamma}$ |
| magnetic Weissenberg number | $\frac{magneto - elastic\,force}{visco - capillary\,force}$ | $Wi_m = Wi + Wi^{1/2} Bo_m^2$ |
| electric Weissenberg number | $\frac{electro - elastic\,force}{visco - capillary\,force}$ | $Wi_e = Wi + \frac{1}{2} Wi^{2/3} Eo_e^{1/5}$ |
| Hartmann number | $\frac{magnetic\,force}{viscous\,force}$ | $Ha = \frac{\rho m B D_0}{2 V_0 \eta}$ |
| Ohnesorge number | $\frac{viscous}{\sqrt{inertia \times surf\,acetension}}$ | $Oh = \frac{\eta}{\sqrt{\rho \sigma D_o}}$ |

Chapter 1

Introduction

1.1 Droplet

Drop is a globule of a liquid that accumulated enough volume or weight to maintain its shape before falling from its catch. “Droplet” (“let” stand for “smaller/lesser”) is smaller than a drop, which may adhere to or rest on a surface. A “droplet” is also defined as a small blob of liquid volume confined by its interfacial forces to minimize its surface energy. In general, droplets exhibit sessile form, where the droplet rests on some surface and pendant form (i.e., hanging droplet). Based on the interest of the interface, both forms of droplets are very important in their respective research problems. In sessile droplets, the “solid-liquid” interface plays a key role on the interfacial equilibrium of the surface (surface wettability) by changing its contact angles. Although the pendant droplet mimics a free form droplet, the “liquid-surrounding gas” interface of the pendant droplet has its own significance in the area of “droplet evaporation”.

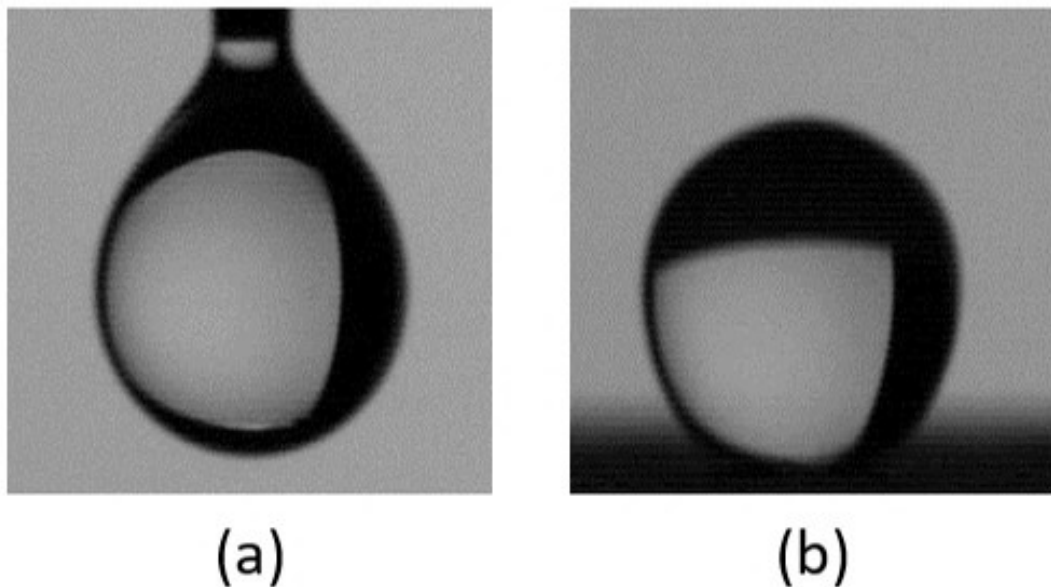


Figure 1.1: (a) Pendant droplet, (b) Sessile droplet

Drop dynamics is an area of research that has great potential in a wide range of applications in different scientific fields as shown in fig.1.2.

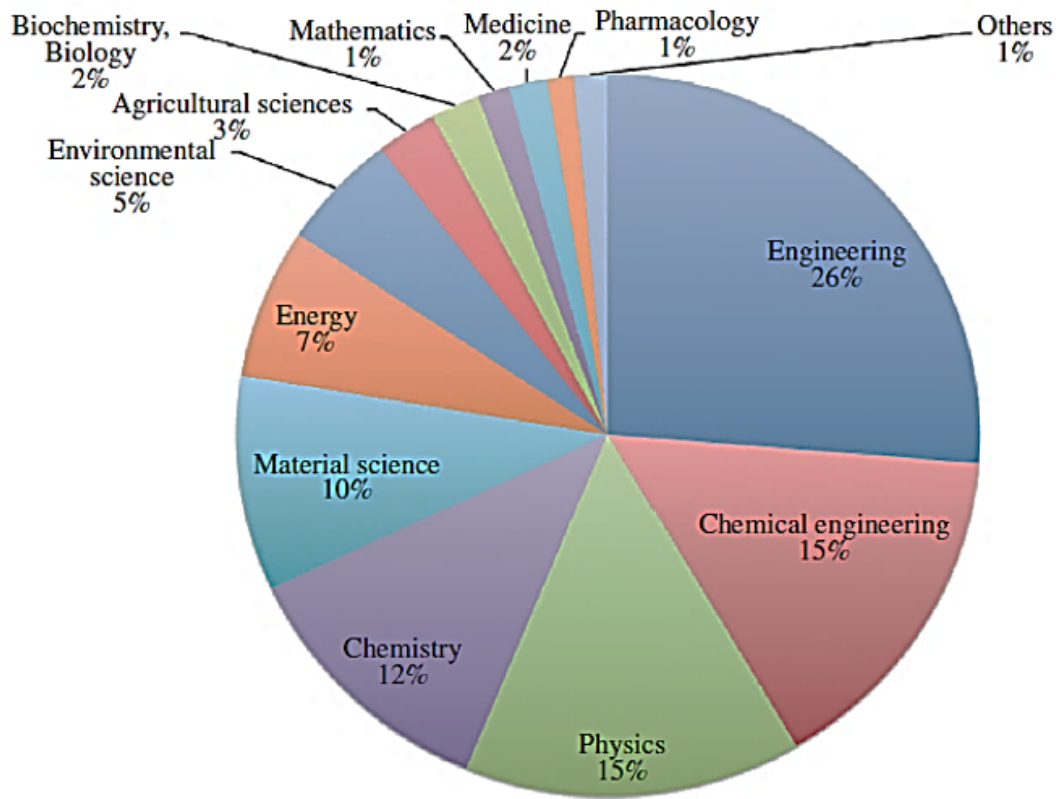


Figure 1.2: Overview

[Image source: google images/corresponding authors of the respective article/book]

1.2 Surface Wettability

Wettability : Wettability is an ability of a liquid to make contact with surface. Based on the spreading parameter, wetting behaviours have been categorized as partial wetting, complete wetting and complete dewetting. Droplet exhibit various shapes based on the wettability of the substrate. It mainly depends on the two major aspects, such as static equilibrium, which is the manifestation of the static equilibrium contact angle. Along with static contact angle, the dynamic contact angles such as advancing (θ_A) and receding contact angle (θ_R) also greatly alter the wettability nature of the surface.

1.2.1 Ideal surface vs Real surface

An ideal surface is an atomically flat, chemically homogeneous, isotropic, insoluble, non-reactive and non-stretched surface with zero contact angle hysteresis ($\Delta\theta = 0, i.e., \theta_A = \theta_R$). A surface which does not satisfy any of the above conditions is called a real surface. A real surface always maintains a non-zero contact angle hysteresis ($\Delta\theta \neq 0, i.e., \theta_A \neq \theta_R$).

1.2.2 Contact angle

Contact angle: Contact angle is the angle between a tangential line to the liquid surface from the three-phase contact line (shown as a yellow dot in fig.1.3.) and the plane of the solid surface on which the droplet rests or moves.

Equilibrium contact angle: It is the angle measured for the liquid surface at the solid surface at which the solid-liquid-gas system reaches an absolute minimum in its total free energy. Experimental access of equilibrium contact angle is rarely possible for real imperfect heterogeneous rough surfaces.

1.2.3 Static contact angle/Young contact angle:

The static contact angle is measured for a three-phase contact line, which is static/stationary. For an ideal smooth surface, the substrate contact angle can be estimated from Young's equation by balancing all specific interfacial energies at the triple contact line.

$$\sigma_{lv} \cos \theta = \sigma_{sv} - \sigma_{sl} \quad (1.1)$$

where, σ_{lv} , σ_{sv} and σ_{sl} denote interfacial tensions of the liquid-vapor, solid-vapor and solid-liquid respectively. θ represents the young contact angle or static contact angle.

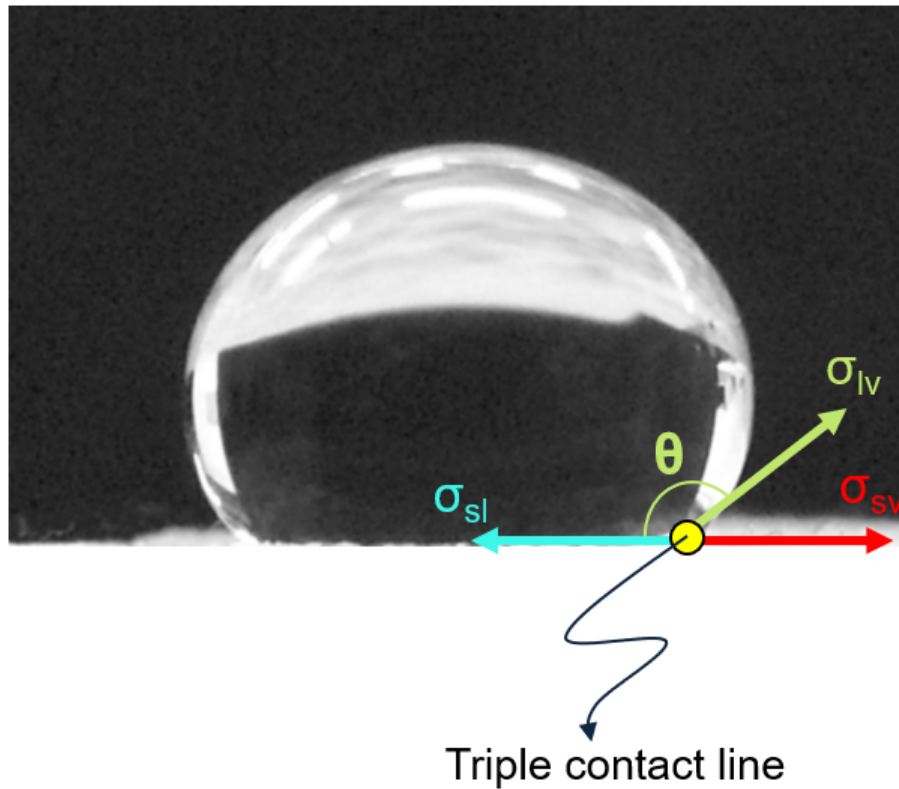


Figure 1.3: Static contact angle (θ) of a water droplet

1.2.4 Dynamic contact angle

Estimation of the contact angle of a liquid surface under the motion of its three-phase contact line associated with the advancing(θ_A) or receding(θ_R) of the contact lines (see fig. 1.4.). It is important to note that both advancing and receding contact angles refer to angles assessed under either static or dynamic conditions. If it is under static conditions, the angles for the liquid surface have recently developed on a dry surface or receded from a wet surface.

Contact angle hysteresis ($\Delta\theta$): It is the difference between the advancing and receding contact angles.

Contact angle hysteresis or CAH ($\Delta\theta$) = $\theta_A - \theta_R$

Sliding angle/Roll-off angle (α): The sliding/roll-off angle defined as the angle of inclination of a surface at which a water droplet begins to roll off it (see fig. 1.4.). The sliding angle plays a crucial role in superhydrophobic surfaces.

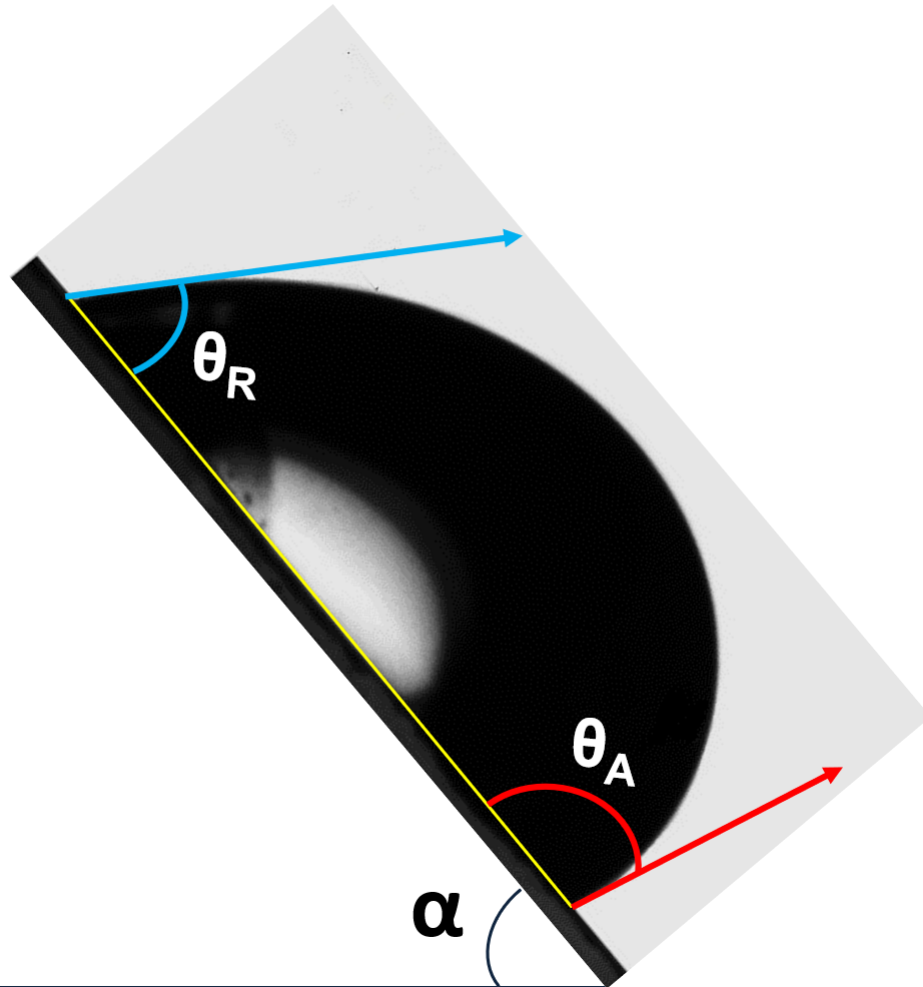


Figure 1.4: Dynamic contact angles of the water droplet on an inclined surface

1.2.5 Superhydrophobicity

Based on both static and dynamic contact angles, substrates have been mainly categorized into three categories, such as hydrophilic, hydrophobic and superhydrophobic surface (see fig. 1.5. a-c). As far as surface science is concerned the terms hydrophilicity and hydrophobicity play an important role in surface wettability. "Hydro" means water and "philicity" means affinity and "phobicity" means lack of affinity. In the scientific community, when a static water droplet maintains contact angle $\theta < 90^\circ$ is defined as a hydrophilic surface (see fig. 1.5.a). Similarly, if surface maintains the $90^\circ < \theta < 130^\circ$ and $\theta > 150^\circ$ are defined as hydrophobic (see fig. 1.5.b) and superhydrophobic (see fig. 1.5.c) surfaces respectively.

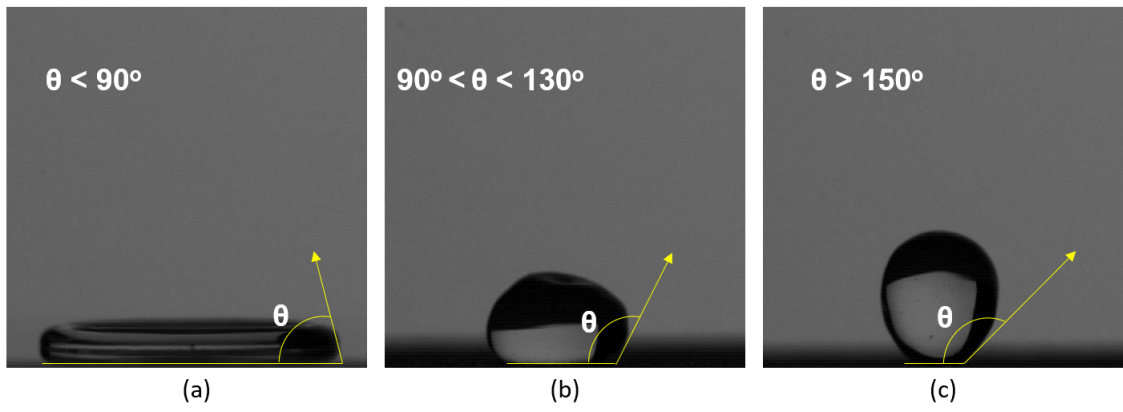


Figure 1.5: (a) Hydrophilic surface (b) Hydrophobic surface (c) Superhydrophobic surface

As mentioned above, the necessary condition for superhydrophobicity is $\theta > 150^\circ$, but it is not a sufficient condition to confirm the superhydrophobicity. We also need to check the adhesive behavior of the liquid droplet on the surface under a dynamic state (i.e., roll-off angle) through contact angle hysteresis. As earlier majority reported [1–4], if the surface maintains $\theta > 150^\circ$ with low contact angle hysteresis ($\Delta\theta \sim 5 - 7^\circ$) known as superhydrophobic surface. To explain the contrasting properties of superhydrophobicity with different adhesive behaviors, both rose petal and lotus leaf effects are further discussed. For instance, both lotus leaf and rose petal microscopic surface structures maintain $\theta > 150^\circ$, there is a great change in their adhesive nature which eventually resembles a significant difference in their roll-off angle. A superhydrophobic surface with low adhesion lowers the roll-off/sliding angle, which slides/rolls off the droplet easily on the surface. Similarly, the superhydrophobic surface with higher adhesion demands relatively more energy to move droplets over it, though it maintains the largest static contact angle. We may also understand this intriguing physics in another way such that the superhydrophobic surface with a lower contact angle hysteresis ($\Delta\theta < 10^\circ$) behaves as similar to the low roll-off angle case of lotus leaf effect. The superhydrophobic surface with a higher contact angle hysteresis ($\Delta\theta > 10^\circ$) exhibits similar physics of the higher roll-off angle case of the rose-petal effect. In the lotus leaf effect, the lotus leaf allows the

droplet to slide/roll easily on it, which eventually leads to clean the dirt or contaminants over it also called as self-cleaning droplets. This strategy has been used to create mirror coatings, when rainwater droplets fall on the window panes it produces a self-cleaning behavior.

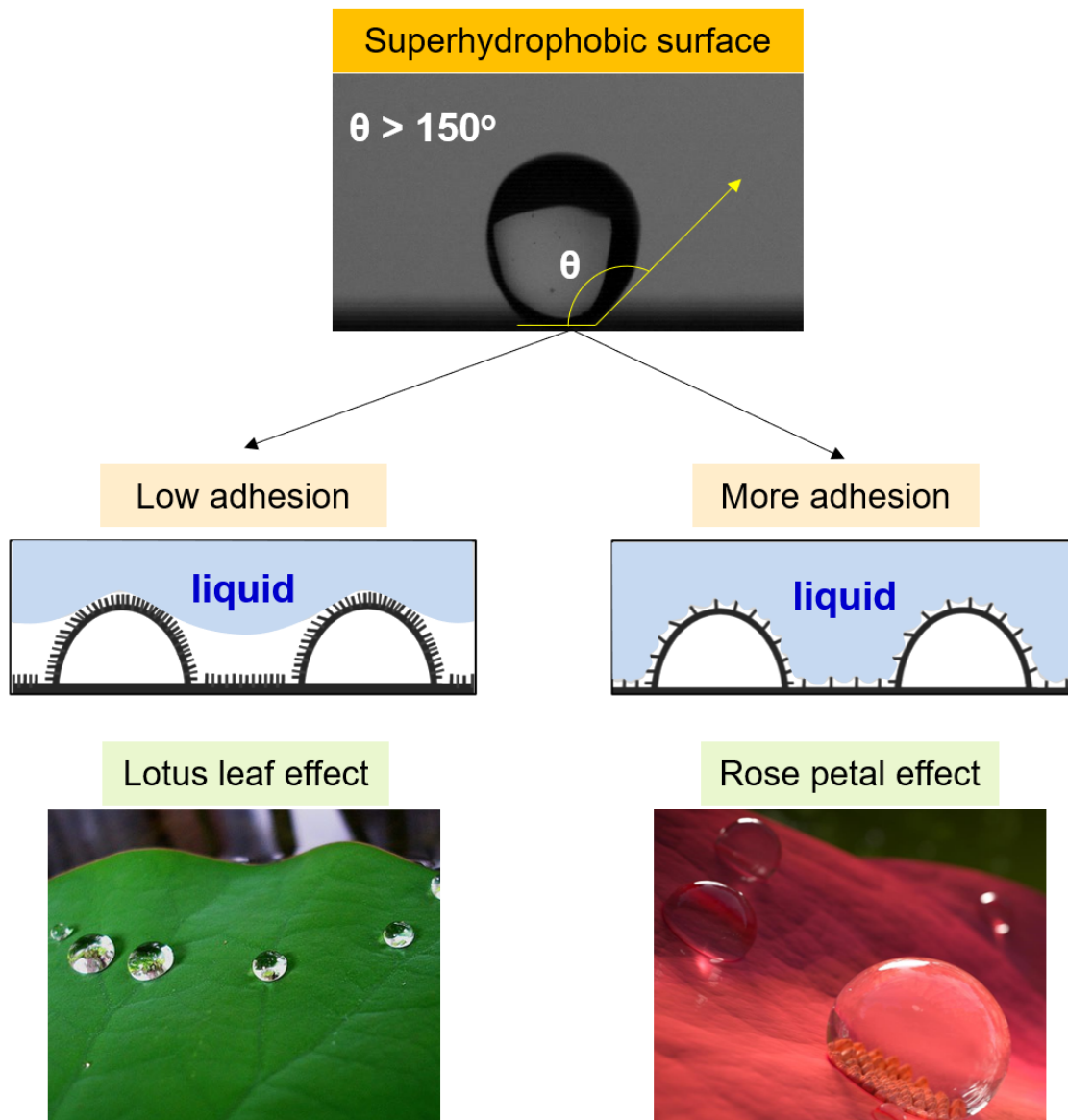


Figure 1.6: Superhydrophobic surface with low adhesion-Lotus leaf effect (left wing), Superhydrophobic surface with high adhesion-Rose petal effect (right wing)

[Image source: google images]

1.3 Surface tension

1.3.1 Surface tension/Equilibrium surface tension

Surface tension is a fluid property by virtue of which the free surface of liquid forms a minimum surface area by reducing its surface energy. Surface tension is also interpreted as the elastic tendency of a fluid that attains the least surface area as possible. Since all fluid molecules are at thermodynamic equilibrium, it can also be termed static surface tension. The role of surface tension becomes very important in a variety of studies like in drop impact dynamics, the motion of water striders on water, floating of needle on water surface etc.

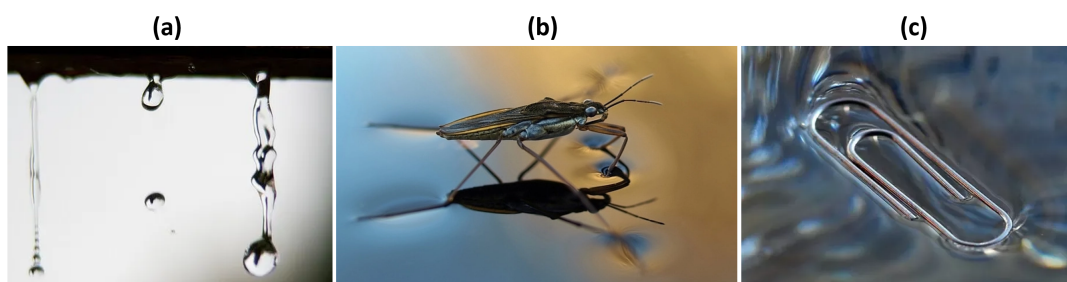


Figure 1.7: (a) water droplets (b) water strider (c) paperclip floating on water
[Image source: google images]

1.3.2 Dynamic surface tension

The dynamic surface tension [5–9] of an interface is the apparent surface tension that varies with surface age or interfacial age. Surface age is the age/time period from the start of the latest interface to the time of observation. The time-dependent surface tension of the interface is known as dynamic surface tension. It contrasts from equilibrium surface tension.

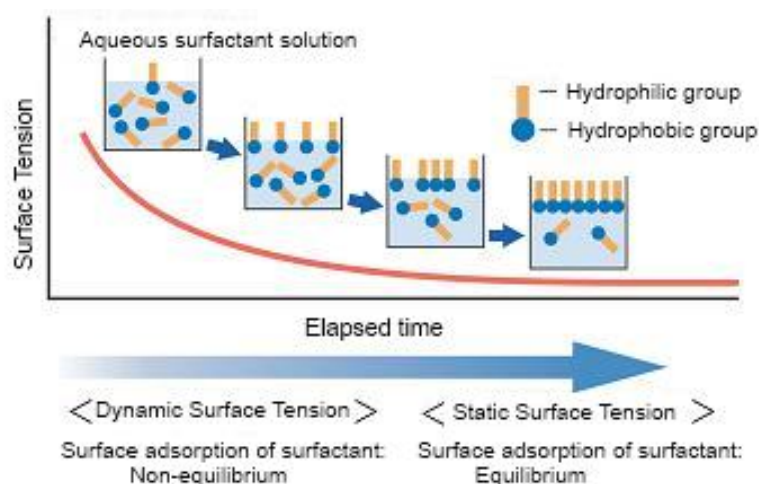


Figure 1.8: Dynamic surface tension
[Image source: Kyowa Interface Science Co.Ltd]

1.4 Complex fluids

Complex fluids are mixtures that coexist between two phases: solid-liquid (suspensions of the macromolecules, i.e., polymeric solution/colloidal solution/surfactant solution), liquid-gas (foams/bubbles dispersion in droplet) or liquid-liquid (emulsions/polymeric solution). In the present work, various kind of complex fluid droplets have been considered for their respective problems and thus current dissertation deals with the following complex fluids such as polymeric droplets, surfactant droplets, ferrofluid droplets, dielectric droplets, nanocolloidal droplets and nanobubbles dispersed droplets and so on.

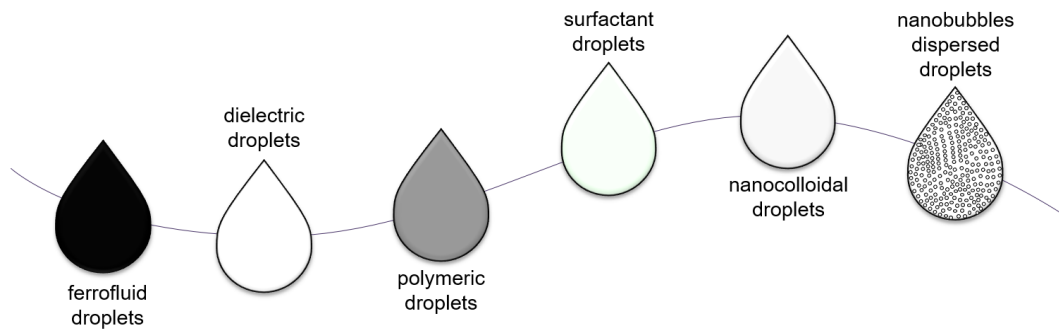


Figure 1.9: Various complex fluids

1.4.1 Ferrofluids

1.4.1.1 Ferrofluid:

A ferrofluid [10–14] is a colloidal liquid composed of nanoscale ferromagnetic or ferrimagnetic particles. Ferrofluid becomes highly magnetized in presence of the external magnetic field. Ferrofluids have great importance in a variety of applications such as magnetohydrodynamic inkjet printing, medical imaging, biosensing, magnetic manipulation, magnetic nanoemulsions, energy harvesting and vibration control etc.

Based on the method of colloidal stabilization, ferrofluids are classified as water-based ionic ferrofluids and surfacted organic media-based ferrofluids. Usually, the ionic ferrofluids were synthesized by surface treatment of particles. Surfacted ferrofluids keep their fluid properties over a wide range of temperatures. In this dissertation, Iron(II,III) oxide (Fe_3O_4) nanoparticles have been utilized to prepare the ferrofluids.

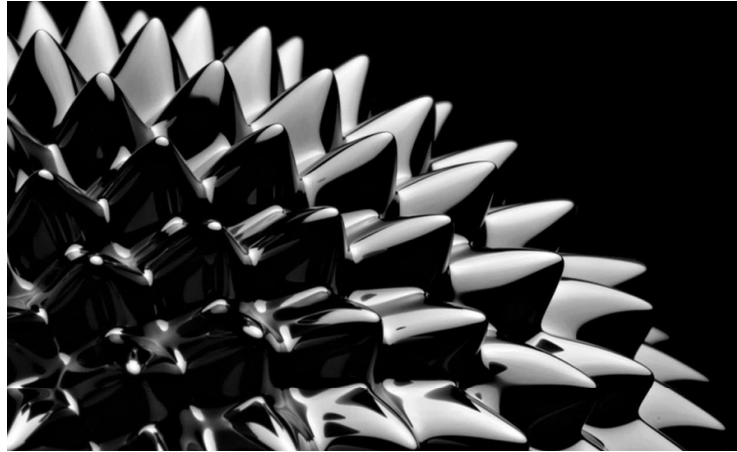


Figure 1.10: Spikes of the ferrofluid
[Image source: google images]

1.4.2 Dielectric fluids

1.4.2.1 Dielectric:

A dielectric(dielectric medium) is a material that acts as an electrical insulator when polarized by an external electric field. They do not have loosely bound or free electrons, which can flow through the material under electric polarization. Based on the nature of the type of molecules present in the material, dielectrics have been classified as polar dielectric (centre of the mass of both positive and negatively charged particles does not coincide with each other and forms a dipole moment) and non-polar dielectric(centre of the mass of both positive and negatively charged particles coincide with each other and does not have any dipole moment). Polar dielectrics are classified as follows

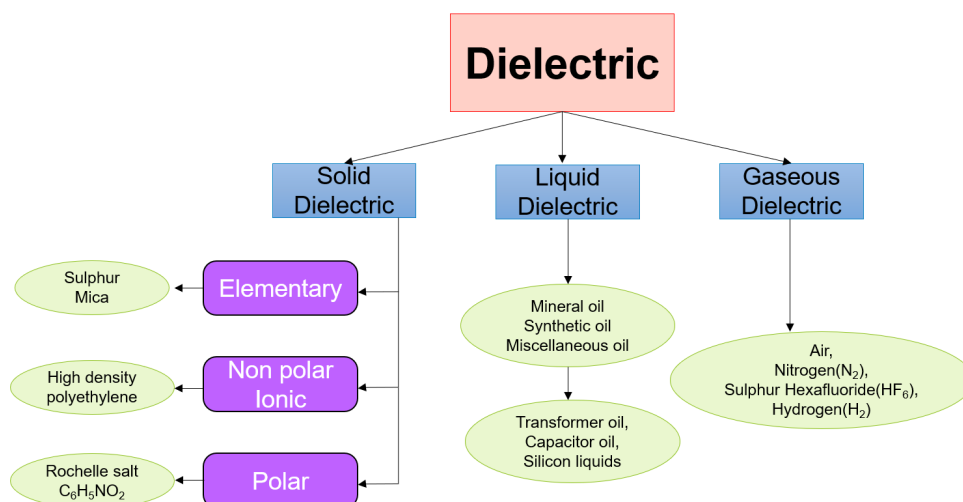


Figure 1.11: Classifications of the polar dielectric

1.4.2.2 Dielectric properties:

Dielectric properties are the elementary molecular properties that have been impending electron movement due to the induced polarization under the external electric field. The main dielectric properties are electric susceptibility, dielectric polarization, dielectric dispersion, dielectric relaxation, tenability etc.

1.4.2.3 Dielectric fluid:

A dielectric fluid (dielectric medium) is a liquid that acts as a poor electrical conductor with high dielectric strength. The most commonly used dielectric fluids include mineral oil, perfluoro alkanes and plant-based oils. Since dielectric fluids circulate through convective heating, they have been widely used in high-voltage applications such as transformers, capacitors, voltage cables etc. The main function of this dielectric is to suppress corona and arcing and provide cooling without electrical conductance. As this dissertation is concerned, the titanium dioxide(TiO_2) dielectric nanoparticles have been utilized to prepare the dielectric fluids.

1.4.2.4 Electric Susceptibility:

It is a property of a dielectric that measures the ability of a material to be polarized under an external electric field.

1.4.2.5 Dielectric Breakdown:

At higher electric fields, dielectrics begin to conduct themselves and act as electrical conductors by losing their dielectric properties. This process is irreversible, leading to the failure of the dielectric material. This phenomenon is described as a dielectric breakdown.

1.4.2.6 Dielectric polarization:

The change in the dielectric properties of a material is governed by the dipole moment(M) and the electric field(E) under an external electric field. Types of the dielectric polarization are as follows

1.4.2.6.1 Electronic polarization: In the presence of an external electric field the centres of positive charge and negative charge are displaced and create an atomic dipole called Electronic Polarization.

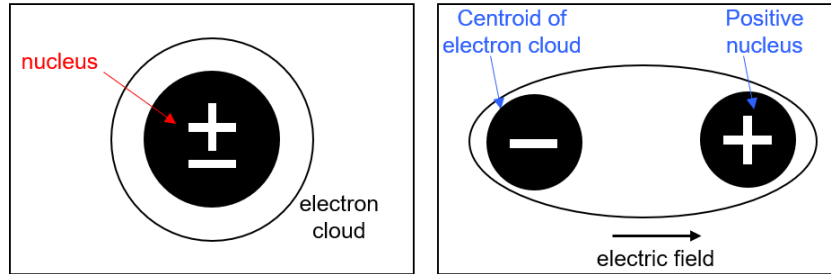


Figure 1.12: Electronic polarization

1.4.2.6.2 Ionic polarization: Ionic polarization occurs only in a dielectric material where the atoms have ionic bonds. When such a material is placed in an external electric field, the separation between the positive charge and the negative charge is separated by a large distance compared to the original length.

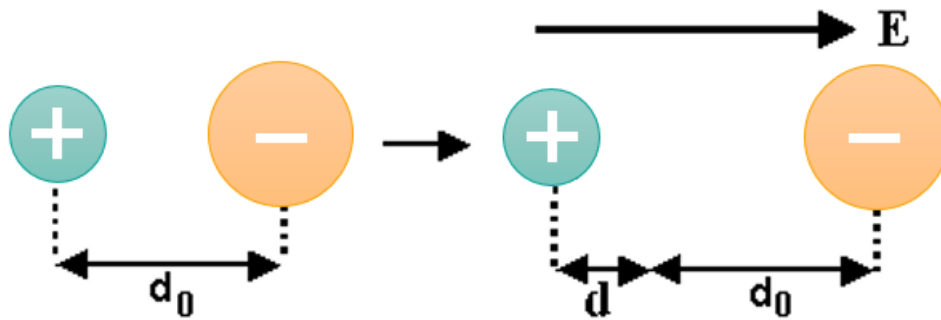


Figure 1.13: Ionic polarization

1.4.2.6.3 Orientational polarization: It occurs in polar dielectrics that have permanent dipole moments. The permanent molecular dipoles are randomly distributed in all directions so that their net dipole moment is zero in the absence of an electric field. But, once an external electric field is applied, the individual dipoles experience a torque, which tends to align them along the direction of the applied electric field. The number of dipoles oriented along the direction of the field will vary based on the applied electric field strength. For a very strong electric field, all molecular dipoles may completely align along the direction of the field.

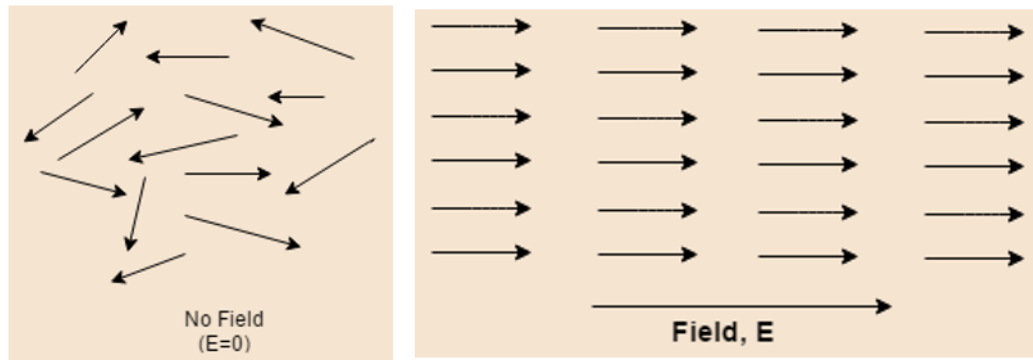


Figure 1.14: Orientational polarization

1.4.2.6.4 Space Charge (or Interfacial) Polarization: It occurs, when charge carriers migrate an appreciable distance through the dielectric, which becomes trapped/bound or not discharged at the electrode are called interfacial polarization.

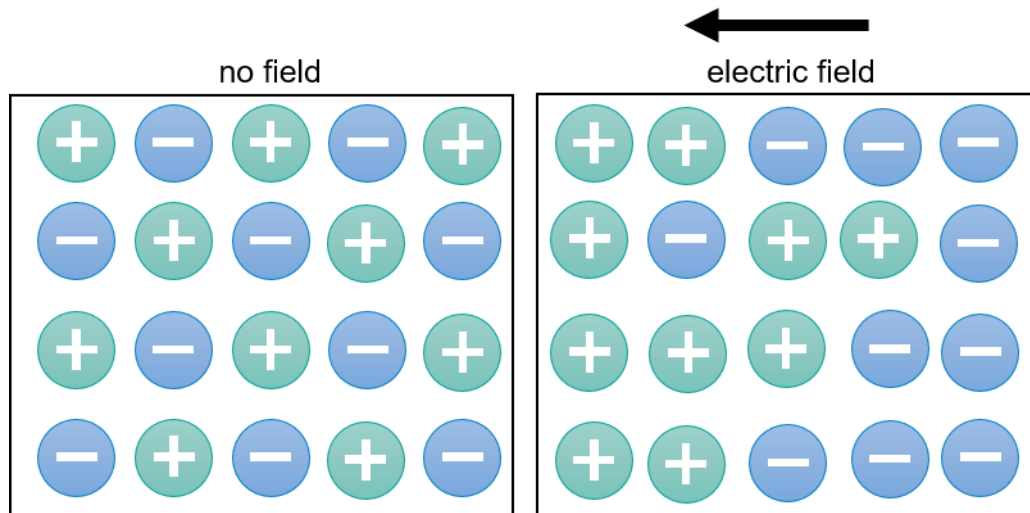


Figure 1.15: Interfacial polarization

1.4.3 non-Newtonian fluids

1.4.3.1 Fluid:

The fluid is a substance that continually deforms under an applied shear stress, no matter how small the shear stress may be.

1.4.3.2 What is a non-Newtonian fluid?

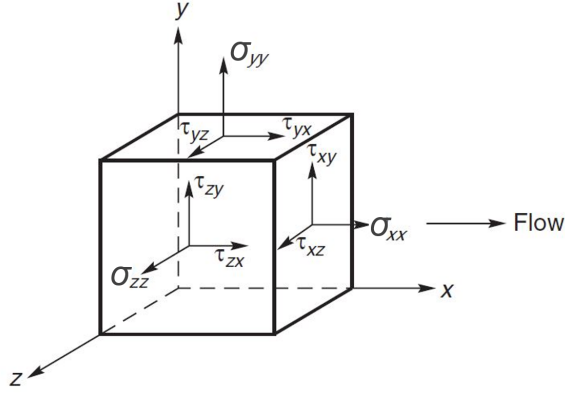


Figure 1.16: Stress components in the three-dimensional flow

[Image source: *Non-Newtonian Flow and Applied Rheology: Engineering Applications* by R.P.Chhabra and J.F. Richardson]

Fig.1.16 schematically shows the nine stress components of an infinitesimally small fluid element. The stresses in a fluid element decompose as two parts, known as hydrostatic stresses (not responsible for fluid deformation) and deviatoric stresses (responsible for fluid deformation and is a function of deformation).

$$\tau_{ij} = \tau_{ij}^{\text{hydrostatic}} + \tau_{ij}^{\text{deviatoric}} = -ps_{ij} + \lambda \frac{\partial V_k}{\partial x_k} s_{ij} + \mu \left(\frac{\partial V_i}{\partial x_j} + \frac{\partial V_j}{\partial x_i} \right) \quad (1.2)$$

where

$$\delta_{ij} = \begin{cases} 1 & i = j \\ 0 & i \neq j \end{cases} \quad (1.3)$$

When the fluid element is at an equilibrium state, the shear stress components can be shown that $\tau_{xy} = \tau_{yx}$, $\tau_{xz} = \tau_{zx}$, $\tau_{yz} = \tau_{zy}$.

$$\tau_{xy} = \mu \left(\frac{\partial V_x}{\partial y} + \frac{\partial V_y}{\partial x} \right) \quad (1.4)$$

$$\tau_{xz} = \mu \left(\frac{\partial V_x}{\partial z} + \frac{\partial V_z}{\partial x} \right) \quad (1.5)$$

$$\tau_{yz} = \mu \left(\frac{\partial V_y}{\partial z} + \frac{\partial V_z}{\partial y} \right) \quad (1.6)$$

The normal stresses can be described by summing up the two components such as isotropic pressure (p) and deviatoric stresses arises from fluid flow (τ_{xx}, τ_{yy} and τ_{zz})

$$\sigma_{xx} = -p + \tau_{xx} = -p + \lambda \frac{\partial V_k}{\partial x_k} + 2\mu \left(\frac{\partial V_x}{\partial x} \right) \quad (1.7)$$

$$\sigma_{yy} = -p + \tau_{yy} = -p + \lambda \frac{\partial V_k}{\partial x_k} + 2\mu \left(\frac{\partial V_y}{\partial y} \right) \quad (1.8)$$

$$\sigma_{zz} = -p + \tau_{zz} = -p + \lambda \frac{\partial V_k}{\partial x_k} + 2\mu \left(\frac{\partial V_z}{\partial z} \right) \quad (1.9)$$

$$\sigma_{xx} + \sigma_{yy} + \sigma_{zz} = -3p + (3\lambda + 2\mu) \frac{\partial V_k}{\partial x_k} \quad (1.10)$$

$$\frac{\sigma_{xx} + \sigma_{yy} + \sigma_{zz}}{3} = -p + \left(\lambda + \frac{2}{3}\mu \right) \frac{\partial V_k}{\partial x_k} \quad (1.11)$$

$$-p_{mechanical} = -p + \left(\lambda + \frac{2}{3}\mu \right) \frac{\partial V_k}{\partial x_k} \quad (1.12)$$

For an incompressible flow, the isotropic pressure is given by

$$p = -\frac{1}{3} (\sigma_{xx} + \sigma_{yy} + \sigma_{zz}) \quad (1.13)$$

Newtonian fluid: A Newtonian fluid can be defined as a fluid that not only maintains a constant viscosity but also fulfills either the flowing equation (1.14) or, in simpler terms, satisfies the entire set of Navier-Stokes equations. Consequently, fluids like the constant viscosity Boger fluids, which possess constant shear viscosity but do not conform to equation (1.14), are categorized as non-Newtonian fluids.

$$\tau_{xx} = \tau_{yy} = \tau_{zz} = 0 \quad (1.14)$$

non-Newtonian fluid: A non-Newtonian fluid exhibits a nonlinear flow curve (shear stress versus shear rate) or does not pass through the origin. where its apparent viscosity (shear stress/shear rate) is not constant at a given temperature and pressure. Instead, it varies based on different flow conditions, including flow geometry, shear rate, and sometimes even the kinematic history of the observed fluid element.

1.4.3.3 Classifications of non-Newtonian fluids:

1.4.3.3.1 Time-independent fluids : Fluids that exhibit a rate of shear at any given point solely determined by the shear stress value at that point and moment are referred to as "time-independent," "purely viscous," "inelastic," or "generalized Newtonian fluids" (GNF). Further time-independent fluids are categorized as follows:

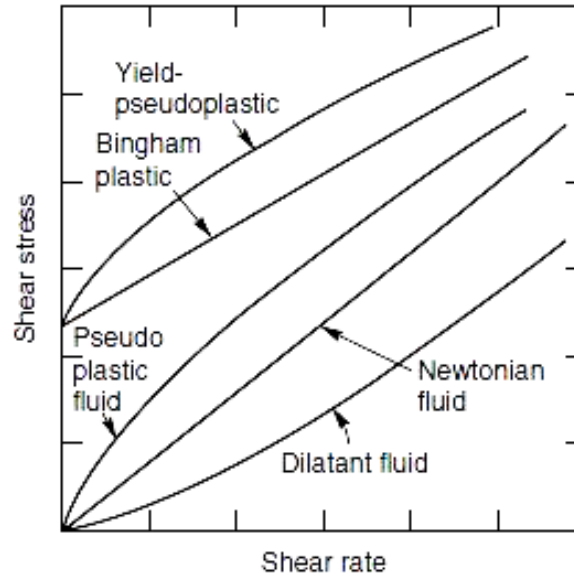


Figure 1.17: Types of time-independent flow behaviour

[Image source: *Non-Newtonian Flow and Applied Rheology: Engineering Applications* by R.P.Chhabra and J.F. Richardson]

a) shear thinning or pseudoplastic: The apparent viscosity of a shear-thinning fluid decreases from zero shear viscosity (μ_0) to infinite shear viscosity (μ_∞) with an increasing shear rate. Ex: polymer solutions and melts.

b) viscoplastic or Yield pseudoplastic: This fluid behavior is defined by the presence of a yield stress (τ_0), which must be surpassed for the fluid to deform or flow. Conversely, when the externally applied stress is below the yield stress, the material will exhibit elastic deformation (or flow as a rigid body). Once the external stress magnitude exceeds the yield stress value, the flow curve may exhibit linearity or non-linearity, but it will not intersect the origin.

c) Shear-thickening or dilatant fluid: The apparent viscosity of the dilatant fluid increases with increasing shear rate. These fluids are also called as shear-thickening fluids. Ex: cornstarch solution

1.4.3.3.2 Time-dependent fluids : In practical situations, the apparent viscosities of these materials may depend not only on the shear rate but also on the duration of time they have been subjected to shearing. Further the time-dependent fluids are categorized as follows:

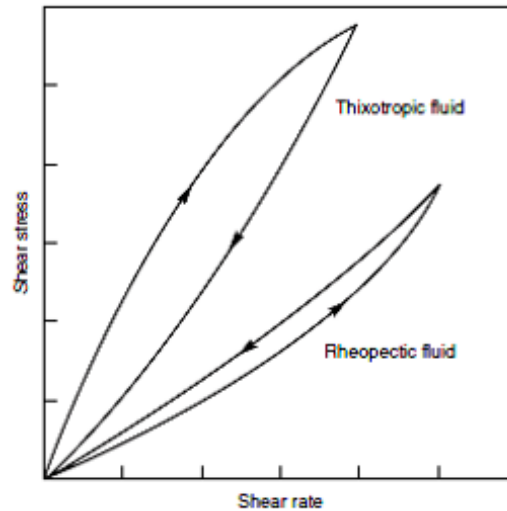


Figure 1.18: shear stress–shear rate behaviour for time-dependent fluid behaviour
 [Image source: *Non-Newtonian Flow and Applied Rheology: Engineering Applications* by R.P.Chhabra and J.F. Richardson]

a) Thixotropy: A material is considered to exhibit thixotropy if, when it is subjected to constant-rate shearing, its apparent viscosity (or the corresponding shear stress) decreases over time, as depicted in Figure 1.18 for a red mud suspension. When the flow curve of such a material is measured in a single experiment, where the shear rate is continuously increased at a constant rate from zero to a maximum value and then decreased back to zero at the same rate, a hysteresis loop is obtained, as shown in Figure 1.18. The characteristics of this hysteresis loop, including its height, shape, and enclosed area, are influenced by factors such as the duration of shearing, the rate of shear rate increase/decrease, and the material's previous kinematic history. In general, the larger the enclosed area of the hysteresis loop, the stronger the time-dependent behavior of the material. Conversely, time-independent fluids exhibit no hysteresis loop, resulting in an enclosed area of zero.

b) Rheopexy or negative thixotropy: Rheopexy, or negative thixotropy, characterizes the relatively few fluids whose apparent viscosity (or corresponding shear stress) shows an increase with the duration of shearing. In contrast to thixotropic materials, these fluids exhibit an inverted hysteresis effect in the flow curve, as illustrated in Figure 1.18.

1.4.3.3.3 Visco-elastic fluids : Many materials exhibit both elastic and viscous effects under specific conditions when the time-dependent behavior is absent, then the material is referred to as viscoelastic. Perfectly elastic deformation and perfectly viscous flow are, in essence, the limiting cases of viscoelastic behavior.

1.4.3.4 Polymers

Polymer: A polymer ("poly"=many "mer"=part/unit) is a substance composed of macromolecules with repeating units.

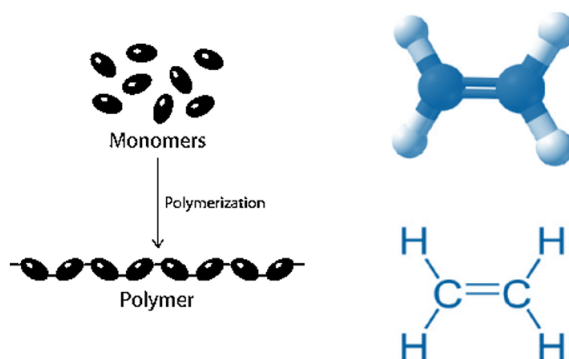


Figure 1.19: Schematic structure of the polymer
[Image source: google images]

Polymerization: Polymerization is the process of formation of the polymer by combining monomers.

Classifications of the polymers: Polymers were classified as based on different categories such as basis of source, based on type of monomers, based on structure, based on molecular forces and sequence of synthesis.

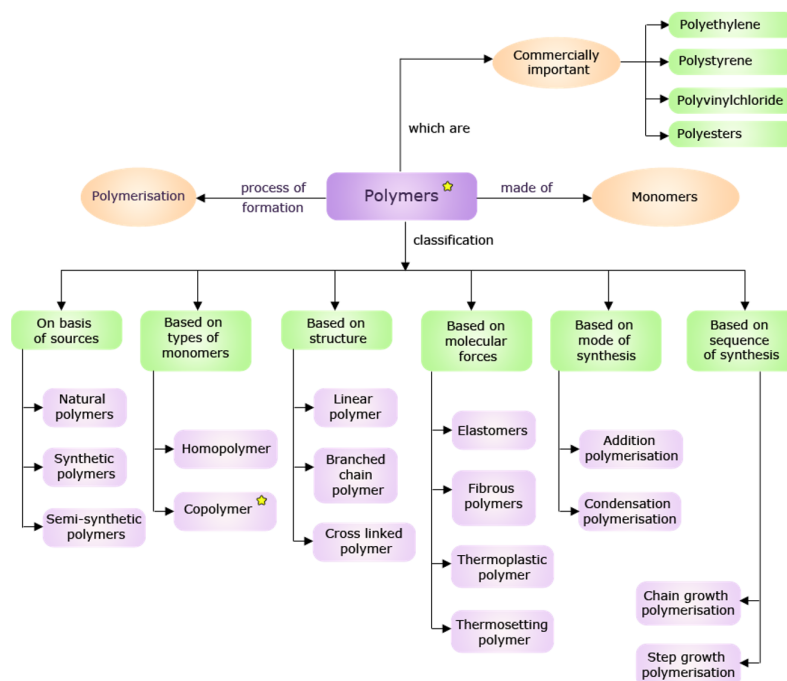


Figure 1.20: Classifications of the polymers
[Image source: google images/corresponding authors of the respective article/book]

Based on the source of the polymers, polymers can be classified into three categories such as natural(bio polymers, natural rubber, wool amber, silk etc.), semi-synthetic(cellulose nitrate and cellulose acetate) and synthetic(polyethylene, polypropylene, polystyrene, polyvinyl chloride, synthetic rubber, etc.). If the polymer is synthesized from a single type of monomer is known as Homopolymer(polyethylene, poly(vinyl chloride), etc.). If the polymer is formed from two or more different monomers is known as Copolymer(poly(ethylene-co-propylene), etc.).

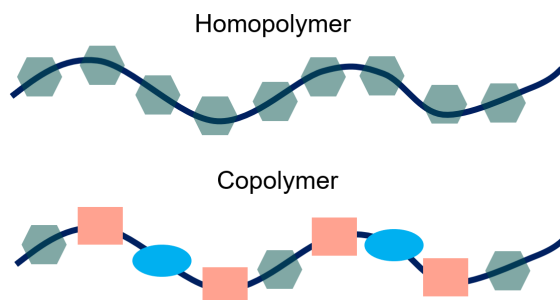


Figure 1.21: Classifications of the polymers based on the type of monomers

On the basis of the structure of the polymer, polymers were classified as linear, branched-chain, and cross-linked/network polymers. The polymers consist of long and straight chains known as line polymers. The polymers contain linear chains with branches known as branched-chain polymers. Similarly, polymers form bi-functional and tri-functional monomers and contain strong covalent bonds with various linear polymer chains known as cross-linked/network polymers.

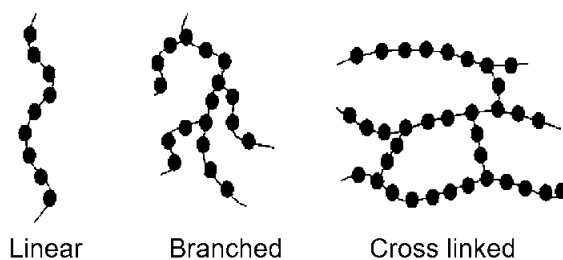


Figure 1.22: Classifications of the polymers based on the structure of the polymer
[Image source: google images]

Based on the molecular forces, the polymers were classified as elastomers, fibers, thermoplastics and thermosets. Elastomers are the polymers that can be easily stretchable with small amount stress(Natural rubber). Polymers that have strong intermolecular forces like hydrogen bonds or dipole-dipole interaction between the polymer chains called as Fibers(Nylon6,6). Polymers which can easily softenes upon heating called as Thermoplastics(polyethylene, polystyrene). Polymers that turns to be rigid and hard upon heating and cannot be reshaped is known as Thermosets.(Bakelite, Melamine formaldehyde).

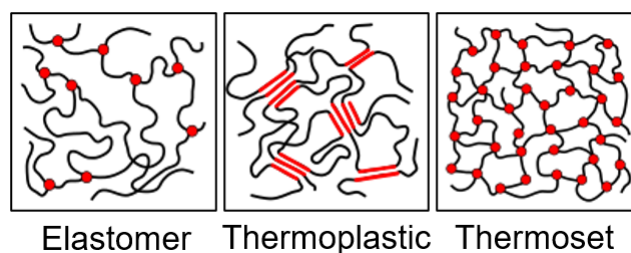


Figure 1.23: Classifications of the polymers based on the molecular forces of the polymer
 [Image source: wikipedia]

On the basis of the mode of synthesis, polymers were classified as addition polymers and condensation polymers. Addition polymers are the polymers that are formed by the repeated addition of the monomer molecules (ethene to polyethene). Addition polymers always have their empirical formula the same as their monomers. Condensation polymers are the polymers that are formed by the combination of the monomers, with the elimination of the small molecules like water, alcohol etc (Hexamethylenediamine and adipic acid to give Nylon – 66).

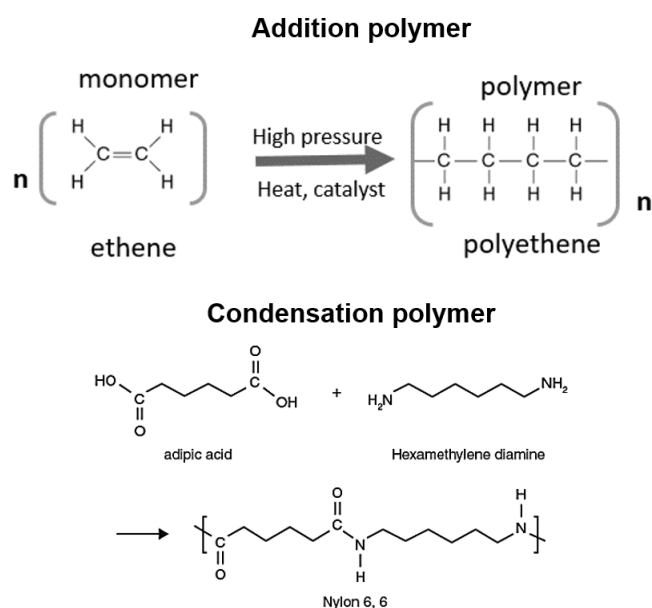


Figure 1.24: Classifications of the polymers based on the mode of synthesis
 [Image source: google images]

As this dissertation is concerned, Polyethylene glycol(PEG-400) has been utilized to prepare the non-Newtonian fluids.

PEG-400: Polyethylene glycol 400 (PEG 400) is a low molecular weight grade of the polymer with low level toxicity. It is hydrophilic in nature and can be used in water-soluble drugs. This polymer has great potential in various applications such as foods, cosmetics and medical applications, and so on.

1.4.3.5 Flow phenomena in non-Newtonian liquids

1.4.3.5.1 Weissenberg effect (Rod climbing): When a rod is rotated steadily in a vessel containing a Newtonian liquid, the free surface experiences depression near the rotating rod due to inertial effects. In contrast, when the rod is rotated in a non-Newtonian liquid with measurable normal stresses, the free surface can rise remarkably, as illustrated in figure 1.25. The rise in the free surface is a consequence of the normal stress component in the circular direction of flow resulting from the rod's rotation. If this normal stress component is greater in magnitude than the two perpendicular components, it generates tension in the flow direction. This tension increases as one approaches the surface of the rotating rod, leading to an inwardly directed pressure that grows closer to the axis of rotation. In certain cases, this pressure can be substantial enough to counteract centrifugal force effects, resulting in the upward movement of the rod. It's worth noting that this phenomenon is not exclusive to large polymer molecules and can also be observed in dilute fiber suspensions.

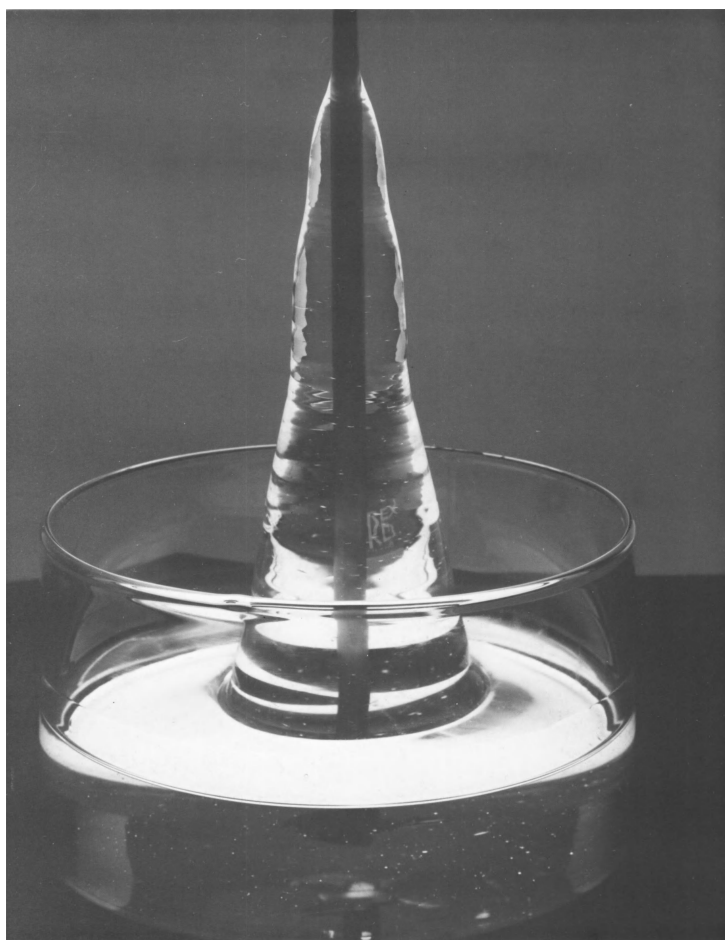


Figure 1.25: Weissenberg effect (Rod climbing): The liquid in the photograph was prepared by dissolving a high molecular weight polyisobutylene (B200) in a low molecular-weight solvent of the same chemical nature (Hyvis 07, polybutene).

[Image source: *Rheological Phenomena in Focus* by D.V.Boger and K.Walters FRS]

1.4.3.5.2 Barus effect (die swell): When a Newtonian liquid is extruded from a capillary, the diameter of the emerging liquid can either be slightly larger or slightly smaller than the capillary diameter, depending on the flow's Reynolds number, which considers the influence of fluid inertia. In contrast, with elastic liquids, a phenomenon called 'die swell' may occur, where the ratio of the diameter of the extruded jet to the capillary diameter can be as high as 3 or 4. In the case of a fully developed flow of an elastic liquid within the tube, tension is present along the streamlines associated with the normal stresses. As the fluid exits the tube into the atmosphere, it relaxes the tension along the streamlines by contracting in the longitudinal direction. In the case of an incompressible liquid, this results in lateral expansion, giving rise to the die-swell phenomenon.

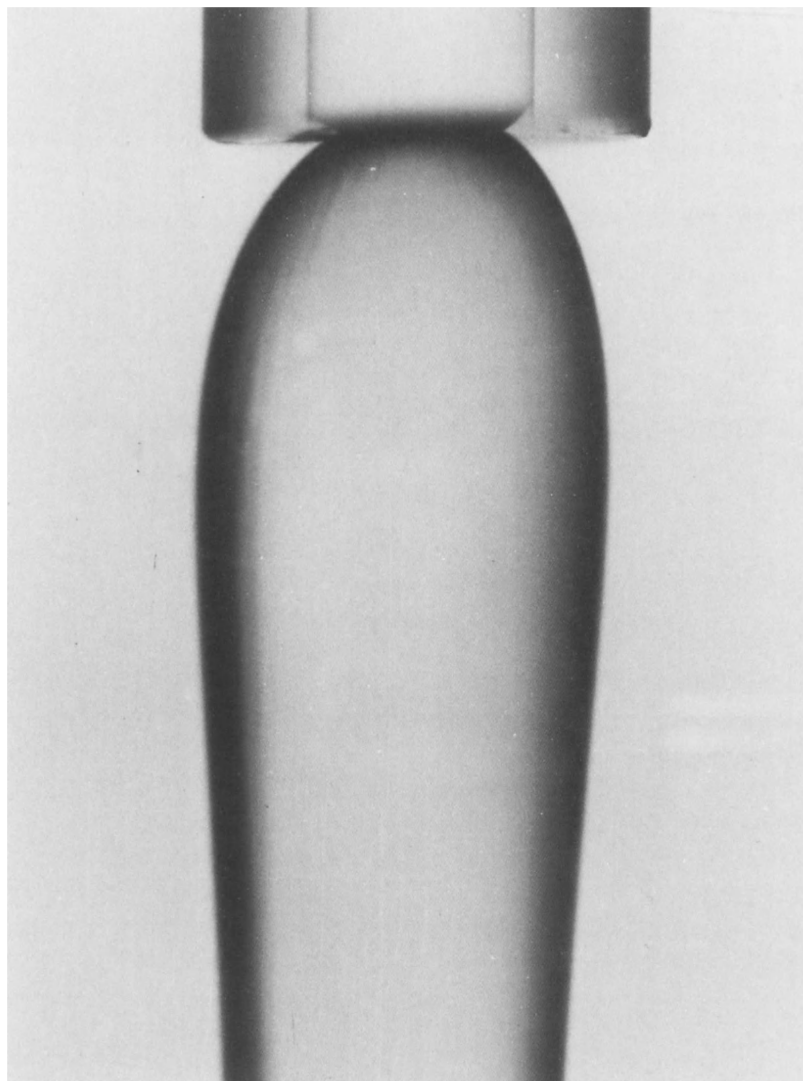


Figure 1.26: Barus effect (die swell): Die swell for a 2.0% aqueous solution of polyacrylamide. The liquid falls under gravity on exiting the capillary. (Photograph by Mr. R.E. Evans, University of Wales, Aberystwyth).

[Image source: *Rheological Phenomena in Focus* by D.V.Boger and K.Walters FRS]

1.4.3.5.3 Kaye effect: The Kaye effect is observed when a thin stream of shampoo or another suitable non-Newtonian liquid is poured onto a surface. Suddenly, a secondary jet emerges from the heap formed by the liquid and starts to 'dance' around the primary jet like a lasso. This captivating phenomenon continues until the 'dancing' jet eventually collides with the primary jet, causing both jets to collapse.

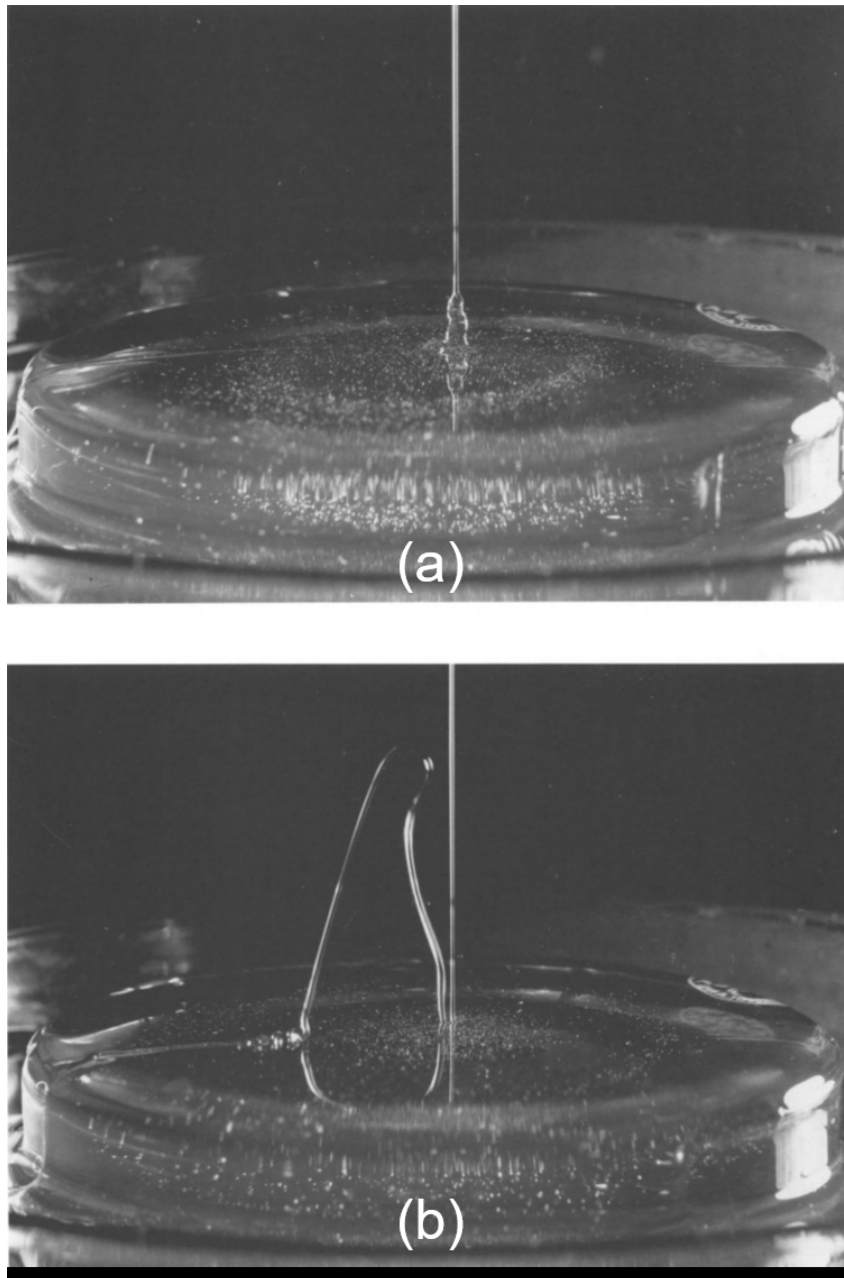


Figure 1.27: Kaye effect: (a) A solution of 5.7 g of polyisobutylene in 100 cm^3 of decalin is poured into a shallow dish filled with the same liquid, (b) Every few seconds, the falling stream on reaching the liquid in the dish 'bounces' and falls in an arc. The stream reaches the liquid surface at a distances of the order of a few centimetres from the starting point under the original falling stream. (From A.S. Lodge, *Elastic Liquids*, Academic Press, 1964, p. 251.)

[Image source: *Rheological Phenomena in Focus* by D.V.Boger and K.Walters FRS]

1.4.3.5.4 The Open-Syphon effect: The Open-Syphon effect, as depicted in figure 1.28, is a classical demonstration wherein the fluid, influenced by its extensional stresses in a gravitational field, pulls itself out of its containing beaker once the flow is initiated.

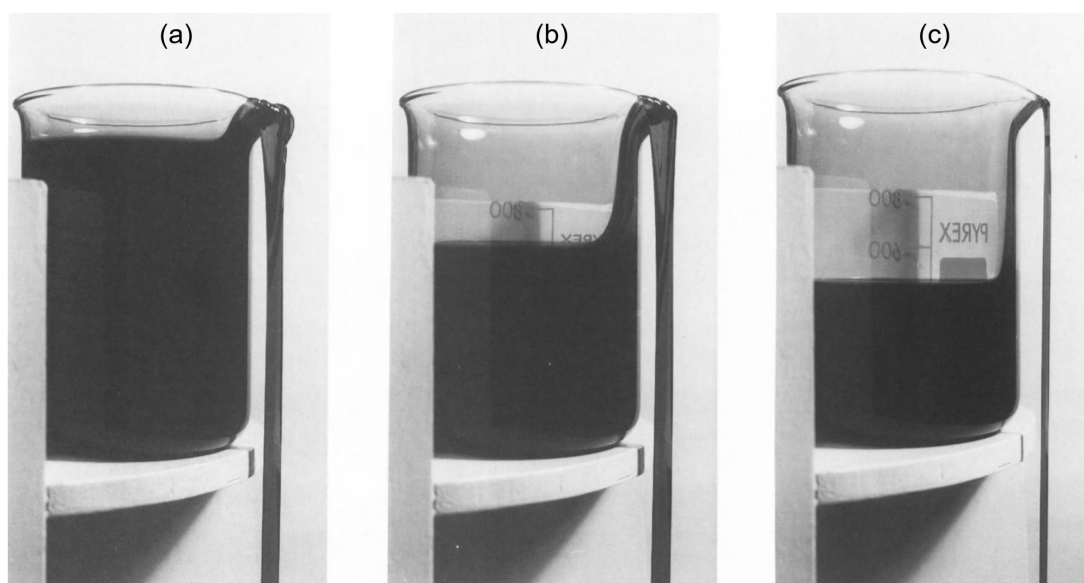


Figure 1.28: The Open-Syphon effect: A 0.75% aqueous solution of Polyox WSR 301 fills a beaker. Only the slightest spilling will part empty the beaker. The sequence shows the development from the time soon after a small initial thread has been drawn over the side of the beaker to the stage where the part-emptying of the beaker is nearly complete. A high ratio of extensional viscosity to shear viscosity is a basic requirement in this experiment. (Photograph courtesy of Mr. R.E. Evans, University of Wales, Aberystwyth.)

[Image source: *Rheological Phenomena in Focus* by D.V.Boger and K.Walters FRS]

1.4.3.5.5 Effects of polymer additives in drag reduction: In 1948, Tom et al. conducted an experiment [15] where they added a minute amount of polymethylmethacrylate (10 ppm by weight) to monochlorobenzene. Undergoing turbulent flow, the polymer solution exhibited a reduction in pressure drop compared to the pure solvent flowing at the same rate. This decrease in pressure drop in the presence of the polymer solution is known as drag reduction.

1.4.4 Electro and Magneto Rheology

Rheology: Rheology is the branch of science that deals with the flow and viscoelastic behavior of fluids and the deformation of solids. Rheology has great potential in a wide variety of applications such as polymer rheology, food rheology, cosmetics, energy materials, coatings and paints, petrochemicals, polymers and pharmaceuticals, etc. During the past few decades, researchers have explored and reported a class of fluids that greatly alters their flow properties under external field stimuli. For instance time-independent fluids, such as shear-thinning(pseudoplastic) fluids, shear-thickening (Dilatant) fluids and time-dependent fluids, thixotropic, negative thixotropic(rheopectic) fluids and so on. As per the classical theory of elasticity, viscoelastic materials play a crucial role under shear in above mentioned applications.

Electrorheological (ER) fluids: Since the nanostructural properties, crystal structure, cation composition, particle size, and organic and inorganic particles of various nanocolloidal complex fluids result in great change in their polarization ability under an external electric field, these colloidal systems can be used as ER fluids. For example, colloidal solutions of alumina, starch, silica, polyaniline(PANI), copolyaniline(COPANI), polypyrrole(PPy), poly(p-phenylene) etc.

Magnetorheological (MR) fluids: Suspended nanoparticles of colloidal solutions greatly change their magnetic properties such as magnetization, magnetic susceptibility, magnetic permeability, etc. when exposed to an external magnetic field. In the absence of a field, these fluids can flow with low viscosity, but if they are subjected to an external magnetic field, the suspended nanoparticles will reorient themselves in the direction of the magnetic field, which leads to results in a drastic change in its flow behavior like shear rate, viscosity etc. Since the choice of magnetic particles, the shape and size of suspended nanoparticles play a crucial role on the flow behavior of fluids under a magnetic field, colloidal solutions of magnetic nanoparticles are considered as MR fluids such as iron-cobalt alloy, carbonyl iron, nickel-zinc ferrites, ferrite-polymer, iron and its compounds and Magnetite (Fe_3O_4) and so on.

1.4.5 Surfactant solutions

1.4.5.1 Surfactants

Surfactant: Surfactant (surface active agent) is a chemical compound/substance that tends to reduce the surface tension of a fluid in which it is dissolved. Surfactants are organic compounds akin to the amphiphilic or amphipathic, which contain a hydrophilic group(head) and a hydrophobic group(tail) (see fig.1.8.)). Based on its chemical nature, the hydrophobic tail may be either lipophilic (oil-seeking) or lipophobic (oil- avoiding). Surfactant monomers have either one or two tails, those with two tails are known as double-chained.

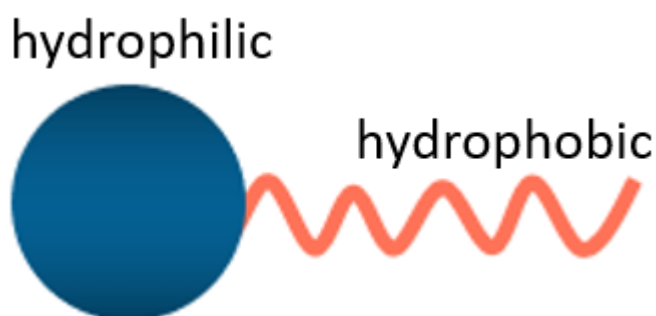


Figure 1.29: Schematic of the surfactant

Surfactants classification: Based on the polar group head, the surfactants are classified as non-ionic, anionic, cationic, and zwitterionic(amphoteric).

i) non-ionic surfactant: A surfactant that has no charged atoms in its head group is known as a non-ionic surfactant. These surfactants have covalently bonded oxygen-hydrophilic groups that are linked with the hydrophobic parent structures. In the case of aqueous surfactant solutions, these bonds reform into hydrogen bonding. Hydrogen bonds decrease with increasing temperature, so the tendency of non-ionic surfactants to dissolve in water decreases with increasing temperature. These surfactants have great potential applications in the manufacture of polishes, fragrances and cleaners.

ii) cationic surfactant: It has positively charged atoms in its head group. Based on the strong effect of its adsorption kinetics on negatively charged surfaces, these surfactants have been used in Antimicrobial and antifungal applications.

iii) anionic surfactant: It has negatively charged head group such as sulfate($-OSO_3^-$), sulphonate ($-SO_3^-$), phosphate, and carboxylates ($-COO^-$). Specifically, alkyl sulfates include ammonium lauryl sulfate, sodium lauryl sulfate(sodium dodecyl sulfate SLS or SDS) and the related alkyl-ether sulfates sodium laureth sulfate (sodium lauryl ether sulfate or SLES) and sodium myreth sulfate. These surfactants most widely used in detergents, toothpastes, shampoos, body soaps, and bath products etc.

iv) zwitterinoic(amphoteric) surfactant: It contains two oppositely(positive and negative) charged groups in its head. Both cationic and anionic centers are attached to its head. In general, The anionic part can be more variable and include sulfonates, as in sultaines CHAPS (3-[(3-cholamidopropyl)dimethylammonio]-1-propane sulfonate) and cocamidopropyl. Besides the cationic part is based on primary, secondary or tertiary amines or quaternary ammonium cations. But in biological zwitterionic surfactants contains phosphate anion with ammonium. These surfactants can be used in paints and cosmetics.

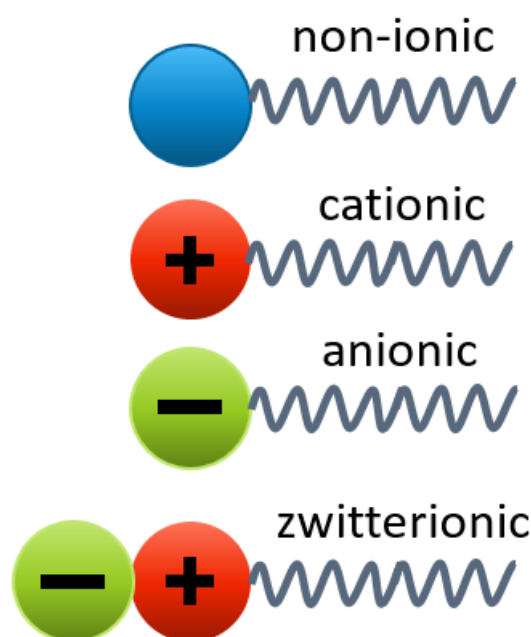


Figure 1.30: Classifications of the surfactant

Micelle: A micelle or micella is the smallest amphiphilic aggregate of surfactant molecules that forms a fluid-like with the non-polar portion of amphiphiles wrapped in a polar portion of the amphiphiles in contact with the dispersed in a liquid colloid. Based on their composition, micelles exhibits different shapes either spheroidal or rod-like.

Critical Micelle Concentration(CMC): It is defined as the critical concentration of the surfactant (amphiphilic molecules) beyond micelles that are formed. CMC is also intuited in such that the critical concentration of the surfactant above there is no change in its thermophysical properties (density, viscosity, surface tension, etc) of the dissolved liquid. The value of the CMC depends on the type of surfactant, solvent fluid, presence of electrolytes operating temperature and pressure. Micelles can only form beyond critical temperature known as krafft temperature, below that micelles cannot form.

In this dissertation, both sodium dodecyl sulfate (SDS)(anionic) and

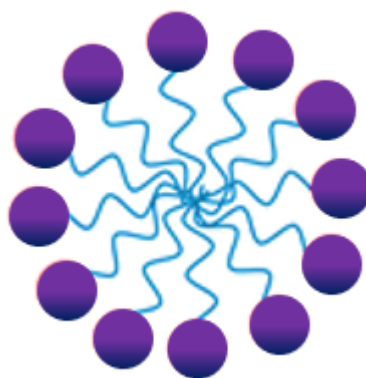


Figure 1.31: Schematic of the Micelle

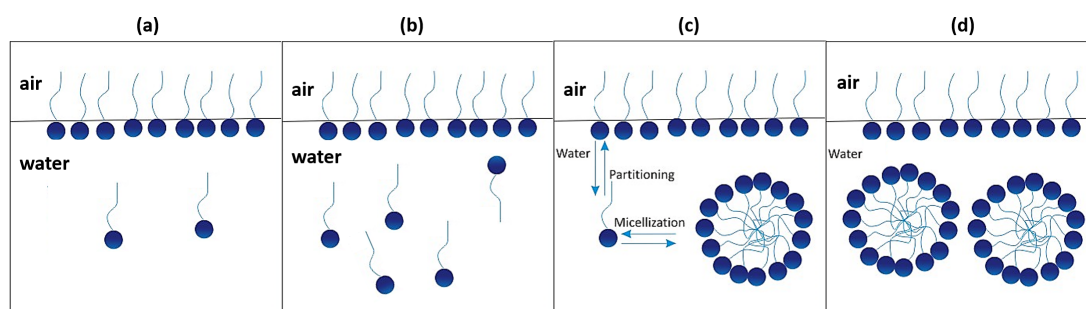
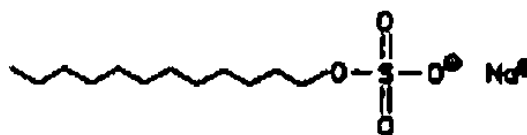


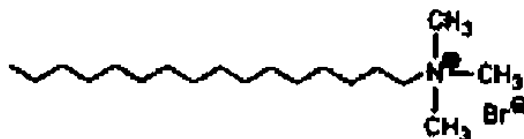
Figure 1.32: (a) low surfactant concentration($< \text{CMC}$)-moderate surface tension (b) surface saturation($\leq \text{CMC}$)-low surface tension, no micelles formation (c) critical micelle concentration($\sim \text{CMC}$)-low surface tension, micelle formation (d) high surfactant concentration($\geq \text{CMC}$)-low surface tension, micelle formation

[Image source: google images]

cetyltrimethylammonium bromide (CTAB)(cationic) have been utilized to prepare the surfactant solutions.



Sodium dodecylsulfate (SDS)



Cetyltrimethylammonium Bromide (CTAB)

Figure 1.33: Chemical structure of the SDS and CTAB

1.4.5.2 Interfacial phenomena of fluids

1.4.5.2.1 Marangoni effect (Why does wine cry?) The phenomenon of "tears of wine" is primarily due to the Marangoni effect, which results from differences in surface tension between the wine and the glass. When wine is swirled in a wine glass, ethanol evaporates from the surface of the wine. This leads to an increase in ethanol concentration at the liquid-air interface. Ethanol has a lower surface tension than water, and this increase in ethanol concentration reduces the surface tension of the wine at the top layer. At the same time, the surface tension at the lower part of the wine remains higher. The difference in surface tension between the top and bottom layers creates a gradient, causing the wine to flow back down along the inside surface of the glass in the form of "tears." These tears are essentially rivulets formed by the wine flowing back towards the bottom of the glass. The tears of wine phenomenon is not only visually appealing but also an interesting example of fluid dynamics and the interplay of surface tension and evaporation in liquids.



Figure 1.34: Tears of wine
[Image source: google images]

1.4.5.2.2 The water strider's leap (Does insects can jump on water?) Water striders, in fact, do possess the ability to jump straight into the air to escape from predators such as frogs, fish, and larger insects. This is an impressive feat considering their light weight, which allows the surface tension of water to support their easy horizontal movement. When a water strider takes off, it draws its legs inward and pushes down slowly on the water surface at first. As the leg motion speeds up, the insect never exerts enough force to break the surface tension of the water. This results in a stable launch platform, without any splash, allowing the water strider to take off efficiently and swiftly into the air.



Figure 1.35: some insects can jump on water

[Image source: *ScienceTake, The Water Strider's Leap* By DAVID FRANK and JAMES GORMAN]

1.4.6 Bubble dispersions

1.4.6.1 Bubble:

A bubble is a small spherical globule of a gas substance within a liquid.

1.4.6.2 Nanobubbles

Nanobubbles: Nanobubbles are typically nanoscopic gaseous cavities in water that change the characteristics of the water. Nanobubbles usually are less than $< 100nm$ in diameter. Nanobubbles are hydrophobic in nature that repel the water. Nanobubbles have their own importance in a wide range of applications such as water treatment, aquaculture, mineral preservation, mineral floatation, carbonated water, carbonated soft drinks, detergent products, fishery, food and in wastewater treatment and so on.

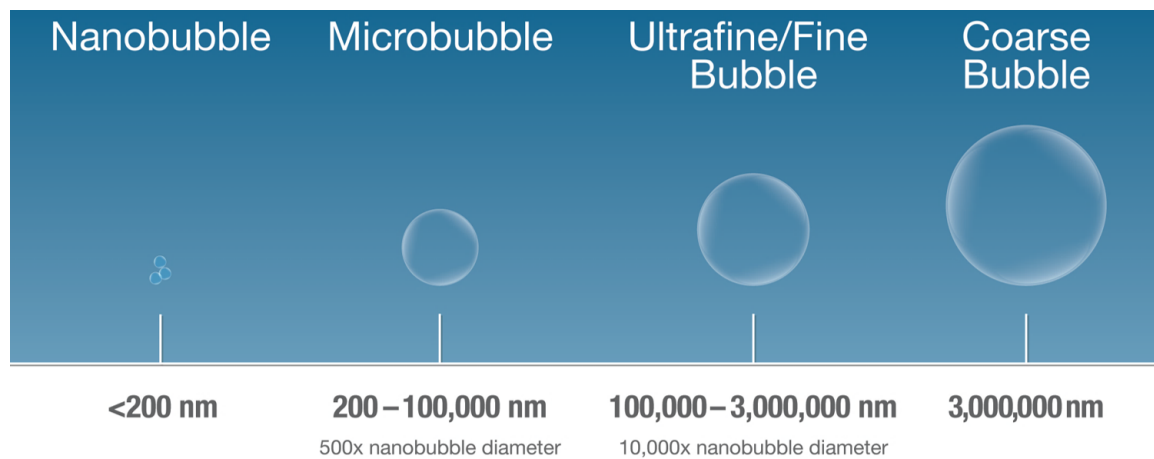


Figure 1.36: Nanobubbles
[Image source: google images]

In this dissertation, the oxygen nanobubbles (O_2) dispersion in water as a test fluid to investigate Leidenfrost droplet dynamics.

1.4.6.3 Why do Champagne bubbles rise in nice straight lines?

Champagne contains proteins that act as "surfactant" molecules, which play a crucial role in stabilizing bubbles and enabling them to rise in a straight line. Surfactants have two ends - one that is attracted to water (hydrophilic) and the other that repels water (hydrophobic). When gas is blown into a liquid containing surfactants, these molecules align themselves at the surface of the forming bubble. The hydrophilic end remains in the liquid, while the hydrophobic end extends into the gas, creating a barrier between the two phases. This stabilization process reduces the surface tension and prevents the bubble from popping, allowing it to rise smoothly and persistently. Fizzy drinks, like soda, beer, or Champagne, have bubbles due to dissolved carbon dioxide gas in the liquid. The carbon dioxide is added to create a fizzy texture, enhance flavor, and sometimes preserve shelf life by inhibiting bacterial growth. When the drink is opened, the release of pressure causes the dissolved carbon dioxide to come out of the solution in the form of bubbles. These bubbles rise to the surface, forming chains with a direction determined by the fluid dynamics of each beverage. In Champagne and sparkling wine, the gas bubbles rise in a single-file line that ascends straight upwards, forming what's known as a "stable" bubble chain. In contrast, in beer, sparkling water, and other carbonated drinks, the bubbles can veer off to the side, creating an "unstable" bubble chain. In an unstable chain, it appears as though multiple bubbles are rising simultaneously, deviating from the straight-line path.



Figure 1.37: Bubbles in Champagne fizz up in a straight line
[Image source: UK times report]

1.4.7 Nanocolloids

Colloid: A colloid is a heterogeneous mixture of micro/nanoscale insoluble particles of one substance dispersed in another substance.

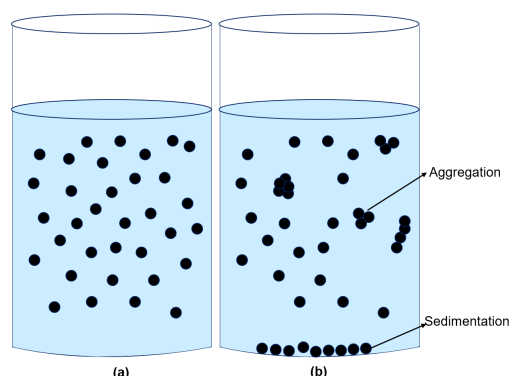


Figure 1.38: (a) Stable colloid (b) Unstable colloid

Classifications of the colloids:

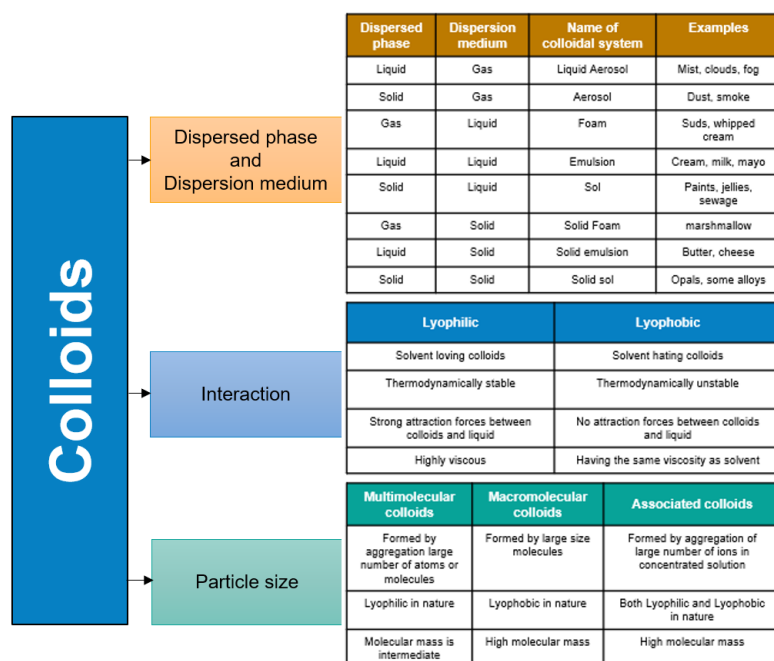


Figure 1.39: Classifications of the colloids

Colloids are of great importance in various industrial products like lotions, lubricants, coatings, toothpaste, paints, inks, etc. As far as this dissertation is concerned, different types of nanocolloids such as ferrofluids, dielectric fluids, surfactant solutions, nanocolloidal solutions and nanobubbles dispersed solutions have been used in various chapters.

1.5 Leidenfrost phenomenon

1.5.1 Why do water droplets dance on a hot surface?

Water droplets dance on a hot surface due to a phenomenon called the Leidenfrost effect. When a water droplet comes into contact with a surface significantly hotter than the boiling point of water, a thin layer of vapor forms between the droplet and the hot surface. This vapor layer insulates the droplet from direct contact with the surface, creating a cushion of steam that suspends the droplet above the hot surface.



Figure 1.40: Leidenfrost effect (droplets dance on a hot surface)

[Image source: *First synthesis of monodispersed microparticles of copper oxide films by pulsed spray pyrolysis (PSP): structural, optical, and morphological investigations*][16]

1.5.2 Leidenfrost effect

Leidenfrost effect(T_L): The Leidenfrost effect is, when a liquid contacts a surface that is significantly hotter than the liquid's boiling point, a vapor layer forms between the liquid and the surface that keeps the liquid suspended, delaying the rate of boiling. This effect is called as Leidenfrost effect. As far as the Leidenfrost effect in droplets is concerned, the Leidenfrost/static Leidenfrost temperature is defined as the minimum surface temperature at which the droplet shows the onset of rebound behavior on a smooth hydrophilic heated surface.

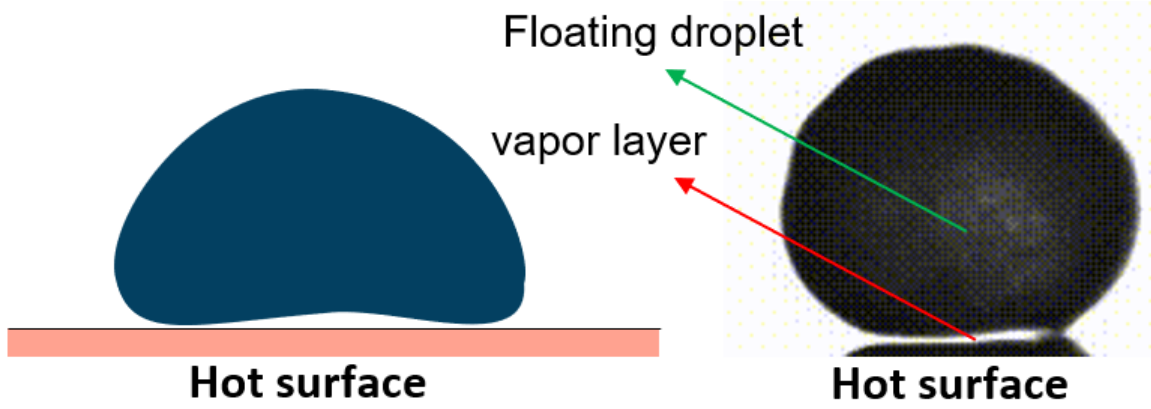


Figure 1.41: Leidenfrost droplets

1.5.3 Dynamic Leidenfrost effect

Dynamic Leidenfrost effect (T_{DL}): In this dissertation, since the droplet impact dynamics is conducted by varying different impact heights, the dynamic Leidenfrost temperature (T_{DL}) is defined as the surface temperature that shows the first onset of rebound behavior when the droplet is released from a certain height onto a smooth hydrophilic heated surface.

1.5.4 Origin of Leidenfrost point/Pool Boiling curve

When the liquid comes into contact with a heated solid surface maintained at a temperature higher than the saturation temperature of the liquid at existing pressure known as Boiling. If the heated surface is submerged below the free surface of the liquid referred to as pool boiling. (see fig.1.13.).

Water pool boiling undergoes various stages such as free convection boiling, nucleate boiling, transition boiling and film boiling respectively. When wall superheat or surface excess temperature is at $\Delta T \sim 5^\circ\text{C}$, the free convection currents are responsible for fluid motion near the surface called as Natural/Free convection boiling stage. If $\Delta T \sim 5\text{-}30^\circ\text{C}$, the liquid which is adjacent to the solid heated substrate shows the onset of the nucleation of the vapor bubbles (see point A in fig.1.13.) called as Nucleate boiling stage. Vapor bubbles nucleate from nucleation sites on the solid surface and some of them rise and rise to the free surface and the rest may collapse into the bulk liquid due to the pressure and temperature of the surrounding bulk liquid. Based on the change in ΔT , this regime (A-C, in fig.1.13) can be viewed as bubbles generation/collapse and bubbles columns in the bulk liquid respectively. At a certain ΔT (point C in Fig. 1.13), the heat transfer between the liquid and the hot surface reaches a peak called the maximum/critical heat flux. Further increase in $\Delta T \sim 30\text{-}120^\circ\text{C}$, the vapor bubbles begin to coalesce and try to form a sheet surrounded by a solid surface called as transition boiling stage. At this stage, part of the solid surface is covered by vapor bubbles and a sheet left over from the bubble's coalescence. At a particular $\Delta T \sim 120^\circ\text{C}$, the vapor bubbles exhibit the

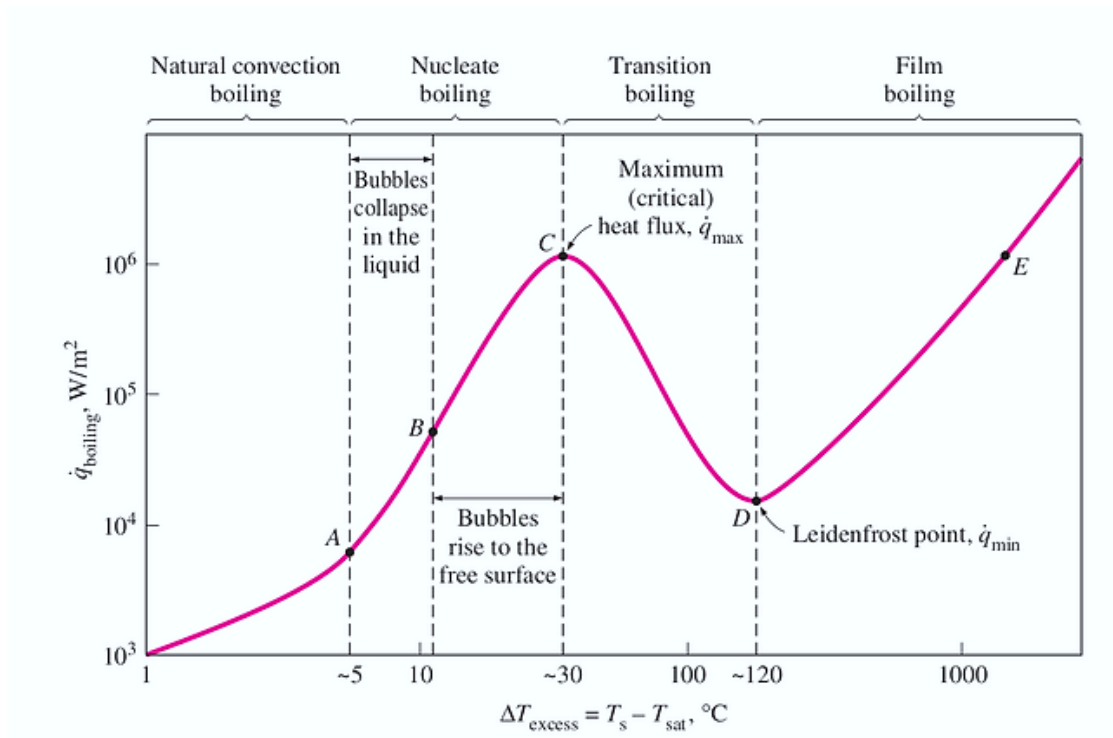


Figure 1.42: Pool boiling curve for water
 [Image source: Engineers edge website]

complete vapor layer shear formation from the coalescence and solid surface fully covered with the vapor layer sheet leads to transfer minimal heat transfer due to its poor thermal conductivity (disadvantageous in heat transfer applications). The onset of film boiling and the corresponding ΔT (point D in Fig. 1.13) is known as the Leidenfrost point. With further increase in $\Delta T \sim > 120^{\circ}\text{C}$, the heat flux enhances due to the more domination of the radiation.

1.6 Droplet impact

Droplet impact on a solid surface is an important area of research in nature and also decisive in various industrial applications, such as inkjet printing, spray cooling, microfluidics, surface wettability, combustion of fuel droplets during combustion in IC engines, droplet evaporation, pesticide droplets spraying on vegetation, spray painting/coating and so forth.

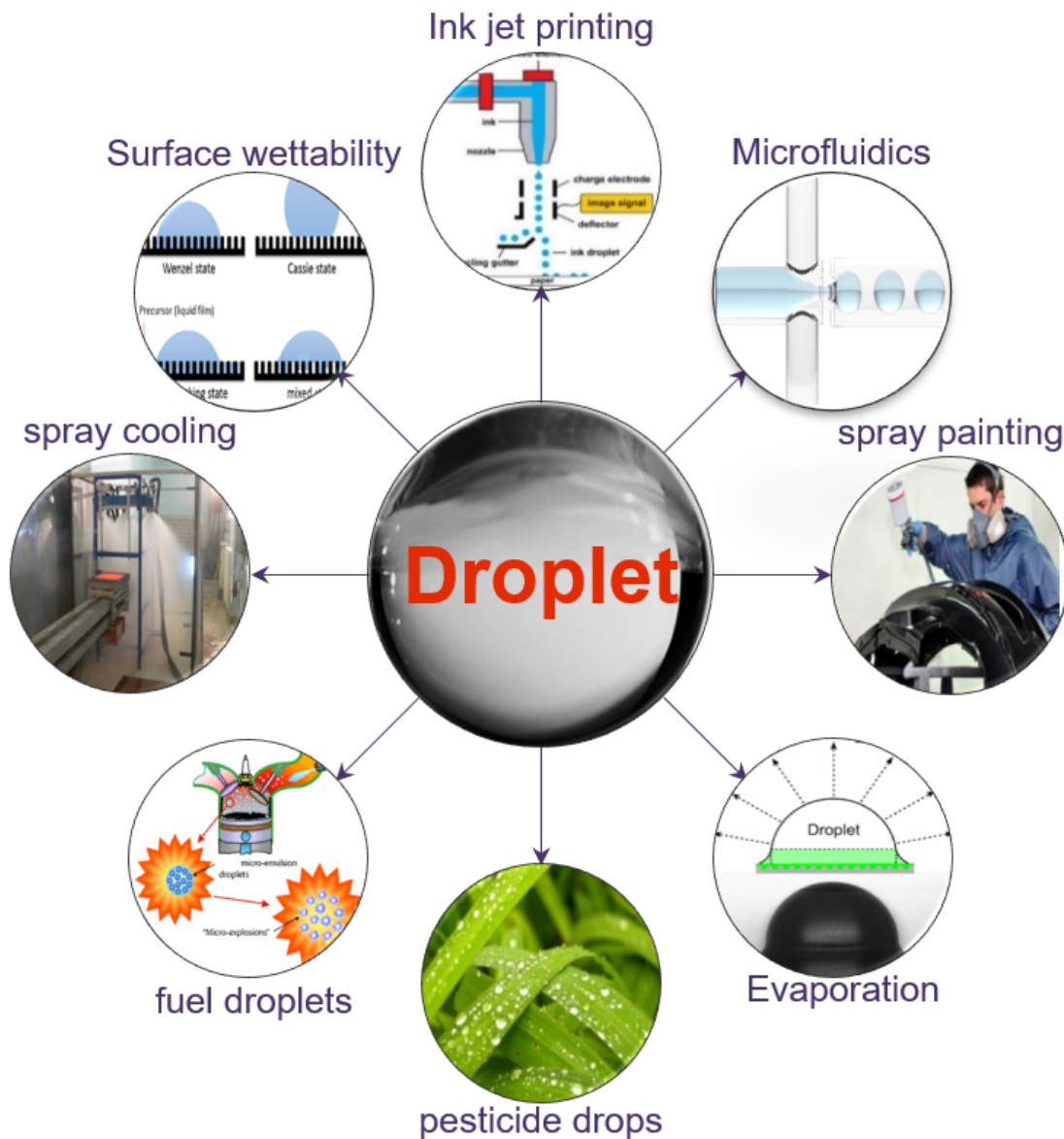


Figure 1.43: Droplet applications
[Image source: google images]

1.7 Motivation

It is true that research is often accompanied by critiques and challenges, but it is also associated with significant benefits and the potential for scientific discovery. The area of droplet research is particularly fascinating, as droplets play a critical role in many physical and biological processes. The doctoral research journey in this area demands a comprehensive and in-depth investigation to uncover new knowledge and drive scientific innovation. As the genesis of every living organism is rooted in a "drop," I am motivated to undertake a doctoral research journey that revolves around the exploration of "droplets." This domain necessitates exhaustive and meticulous examination to incite our cognitive faculties and unveil pioneering scientific breakthroughs. While this thesis provides noteworthy findings for forthcoming researchers, I acknowledge that it constitutes merely a "drop" in the boundless ocean of scientific research.

Recent investigations show the impact dynamics of droplets in current inkjet printing technology. Although earlier researchers have explored the drop impact dynamics, still there are a few problems such as drop rebound control, inkjet splash control, limitation of ink viscosity, clogging of small-size needles during the impact stage and generation of patterns smaller than nozzle size etc have not yet been resolved.

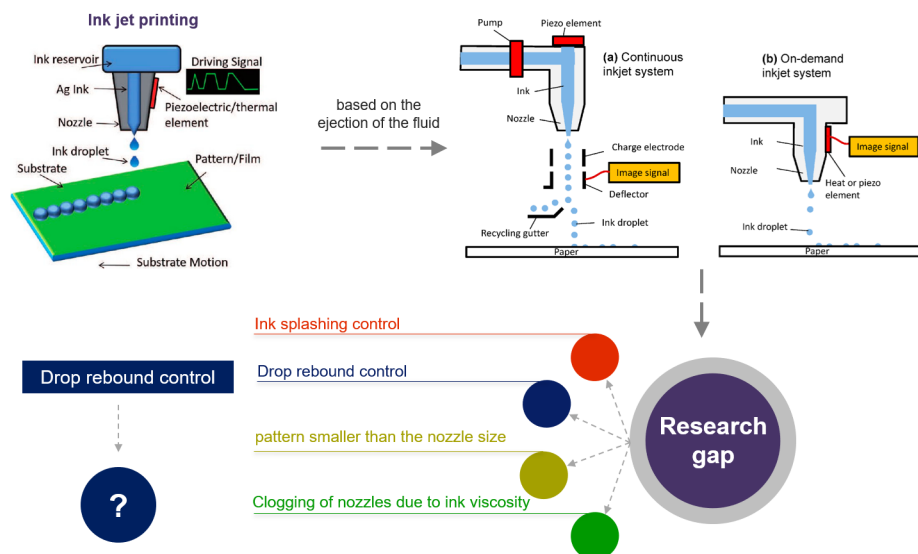


Figure 1.44: Inkjet printing
[Image source: google images]

As there is hardly any study handling non-Newtonian droplets, this dissertation addresses the impact dynamics of elastic(non-Newtonian) droplets in presence of magnetic field and electric field and targeted to provide feasible solutions for the above-mentioned (especially drop rebound and splash control) with magnetohydrodynamic(MHD) and electrohydrodynamic(EHD) inkjet printing technologies.

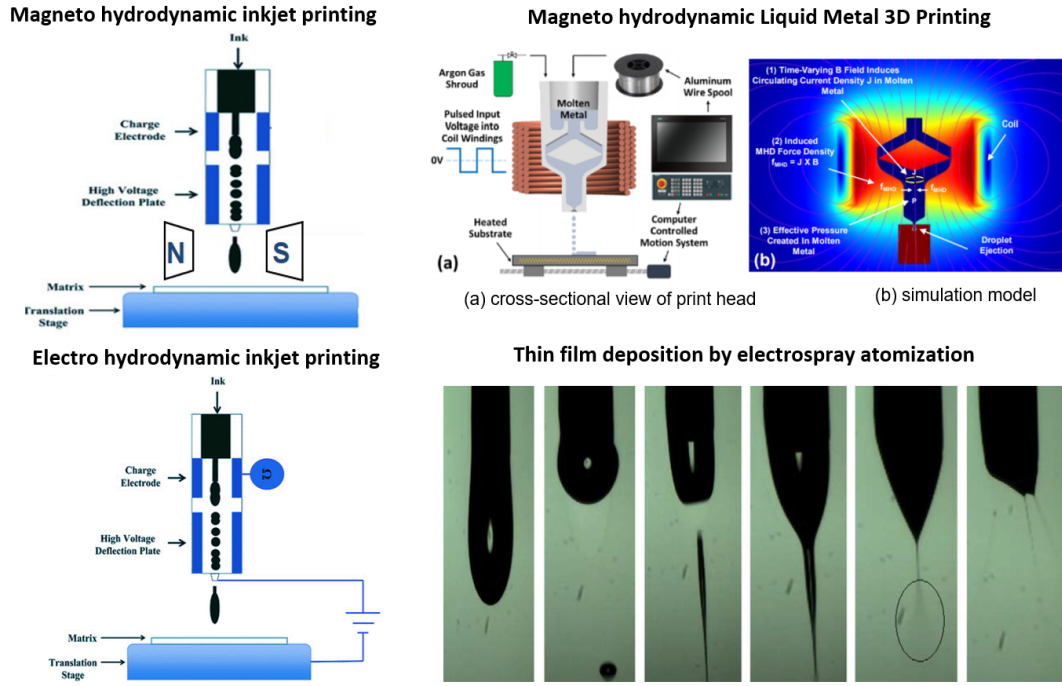


Figure 1.45: Magnetohydrodynamics(MHD) and Electrohydrodynamics(EHD)
[Image source: google images]

Additionally, the best utilization of novel coolants is also a highly demanding area in the current spray cooling industries. Therefore, to address this issue through thorough investigation, this dissertation proposes the best coolants with conclusive data that delay the Leidenfrost phenomenon more effectively than the traditional coolant water droplets.

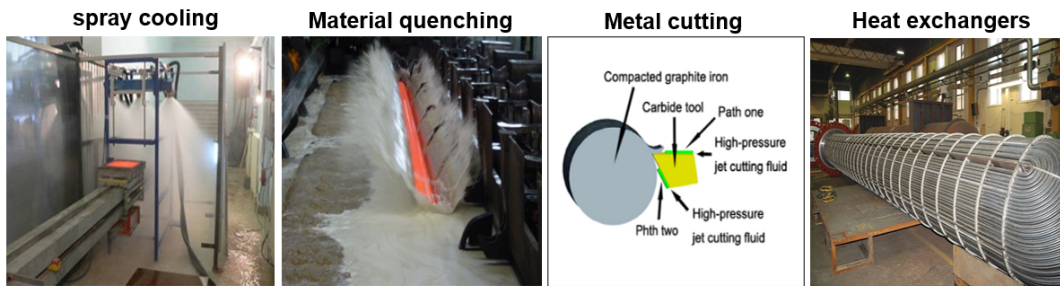


Figure 1.46: Applications of Leidenfrost droplets
[Image source: google images]

Therefore, in the above two research problems, on the one hand, this research focuses on the elastohydrodynamics of the non-Newtonian droplets (specifically on splash control during spreading regime, suppression of droplet rebound) on superhydrophobic surfaces in the presence of an external magnetic field and an electric field. On another hand, it targets to propose novel coolants such as surfactant droplets, nanocolloid droplets, and nanobubbles dispersed droplets with conclusive data.

1.8 Organization of the Dissertation

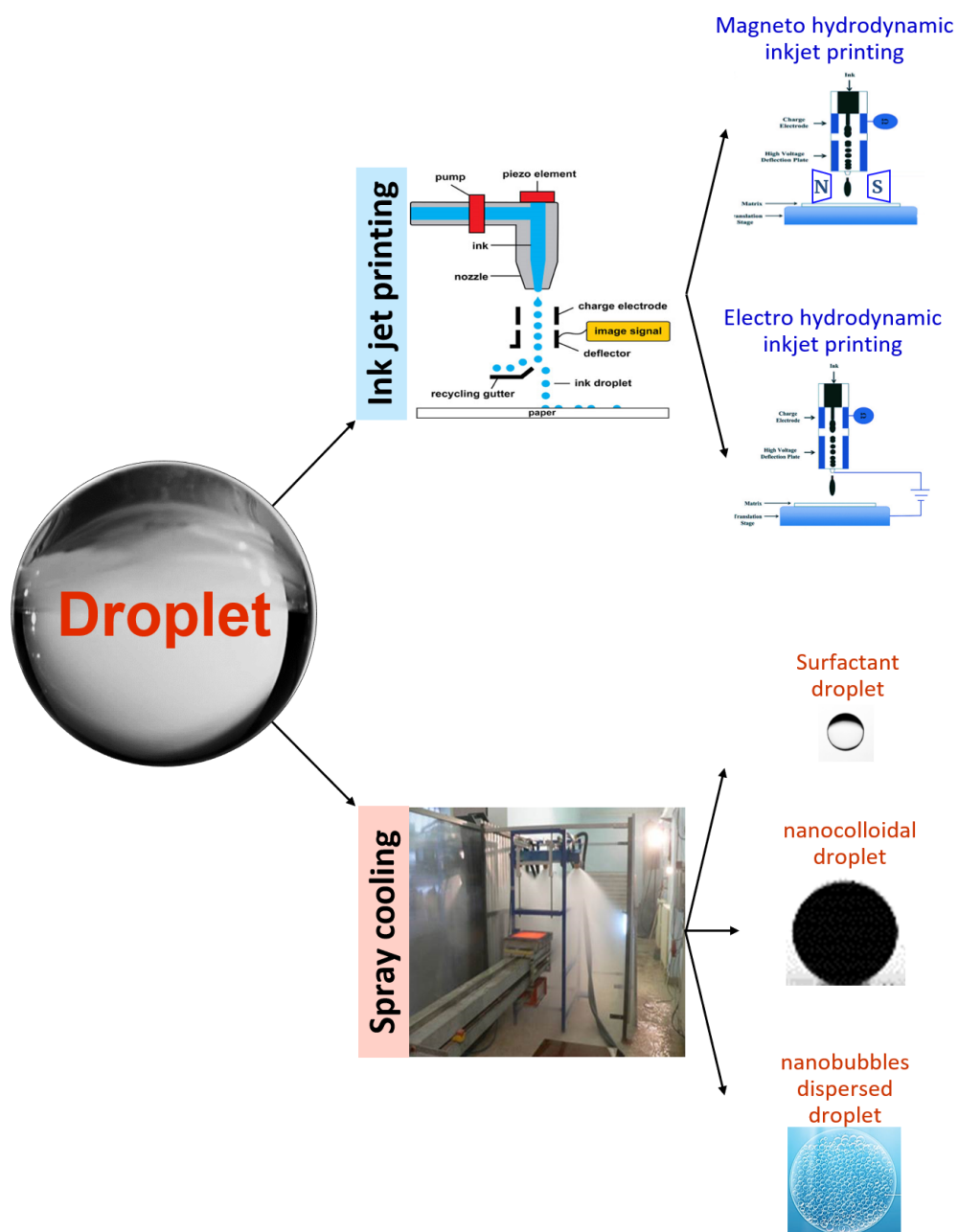


Figure 1.47: Organization of the Dissertation
 [Image source: google images]

Chapter1: Introduction

This chapter systematically introduces the fundamentals of droplets, surface wettability, surface tension, complex fluids and their wide range of applications in various industries, Electro and Magneto rheology and the Leidenfrost phenomenon.

Chapter2: Literature Review

This chapter presents a comprehensive literature survey on droplet impact dynamics, elastohydrodynamics and Leidenfrost dynamics of complex fluid droplets such as polymeric droplets, non-Newtonian ferrofluid droplets, non-Newtonian dielectric droplets, surfactant droplets, nanocolloidal droplets and nanobubbles loaded droplets under the external magnetic fields and electric fields. Out of this literature review, the research gap and research objectives are formulated in detail.

Chapter3: Magneto-elastic effect in non-Newtonian ferrofluid droplets impacting on superhydrophobic surfaces

This chapter reveals the role of magneto-elastic instability on the rebound suppression of a non-Newtonian ferrofluid droplet on superhydrophobic surfaces under an external magnetic field and further introduces the Weissenberg number (Wi) and the magnetic Weissenberg number (Wi_M) to explain the effects of magneto-elastic forces over visco-capillary forces on droplet rebound suppression.

Chapter4: Triggering of electro-elastic anti-superhydrophobicity during non-Newtonian droplets collision

This chapter discusses the impact dynamics of non-Newtonian dielectric droplets on superhydrophobic surfaces, which reveal anti-superhydrophobic behavior by arresting the rebound behavior of droplets under an external electric field. It further elucidates the effect of Eotvos number (Eo) and electric Eotvos numbers (Eo_e) to describe the electro-elastic effects on visco-interfacial forces.

Chapter5: Postponement of dynamic Leidenfrost phenomenon during droplet impact of surfactant solutions

This chapter presents the role of surfactants to enhance heat transfer during spray cooling by delaying the dynamic Leidenfrost temperature. This further invokes the effect of dynamic surface tension to explain the Taylor–Marangoni instability during the spreading and retraction phase of Leidenfrost droplets.

Chapter6: Morphed inception of dynamic Leidenfrost regime in colloidal dispersion droplets

This chapter reports the role of colloidal nanofluids on the suppression of the dynamic Leidenfrost regime. It also reveals the effect of residue deposition on the surface morphology during the spreading and retraction stages.

Chapter7: Augmenting the Leidenfrost temperature of droplets via nanobubble dispersion

This chapter introduces novel nanobubbles loaded droplets to increase the dynamic Leidenfrost temperature by revealing the nature of the dissolved gases of the nanobubbles dispersed droplets during the spreading and retraction stages.

Chapter8: Conclusion

This chapter summarizes the conclusions of this dissertation and possible extensions of the present work are suggested.

Chapter 2

Literature Review

2.1 Introduction

Droplets have attracted a lot of research interest in recent years because the impact thermo-hydrodynamics of a droplet is a crucial field of study in nature and has great potential in numerous industrial and biomedical applications such as inkjet printing [17, 18], spray coating [19], spray painting, spray cooling [20, 21], surface pattern, evaporation, surface wettability, fuel droplets in internal combustion engines, magnetic drug targeting in microfluidic applications [22], electrowetting [23], magnetohydrodynamic printing(MHD), electrohydrodynamic printing(EHD) [24], spray quenching [25], fire extinguishment in a sprinkler system [26], thermal management of nuclear power plants [27] and so on.

2.2 Droplet impact

The impact dynamics of droplets on solid and smooth surfaces have a strong influence on fundamental and applied studies in a wide variety of applications. Over the past decade, an enormous number of studies on drop dynamics have been reported as follows. Que´re´ et al. [28] have shown the steps to be followed to calculate the spreading diameter of the liquid droplet on the solid surface. Roisman et al. [29] introduced the theoretical model to predict the evolution of the droplet and explored both spreading and receding phases through liquid rim dynamics. Yongan Gu et al. [30] studied the spreading kinetics of the liquid drop on the solid surface at low impact velocities and proposed the theoretical spreading model. Besides few studies have explored the spreading dynamics and evaporation kinetics of liquid droplets on heated surfaces [31, 32]. Liang et al. [33] reviewed drop impact dynamics on heated walls and reported various aspects such as evaporation kinetics, different stages of boiling, drop rebound dynamics, secondary atomization of droplets and so on. Similarly, Tran et al. [34] have experimentally studied the drop impact dynamics of water droplets on superheated smooth surfaces and reported the various stages of boiling such as contact boiling, gentle film boiling and spray film boiling through interferometrical analysis. Additionally, few more researchers [35–40] have explored and reported the spreading dynamics of droplets during Leidenfrost boiling against micron vapor cushion, drop temporal evaporation and spreading dynamics on heated walls, fuel droplet impact during Leidenfrost stage, shape and stability of Leidenfrost droplets, Leidenfrost dynamics of liquid droplets on superhydrophobic heated surfaces respectively.

2.3 non-Newtonian fluids

Recent studies of the impact dynamics of non-Newtonian/polymeric droplets on a solid surface have received much research attention on drop rebound dynamics in pesticide spraying in agricultural sciences[41]. For instance, Bergeron et al.[41]explored the addition of polymers to an aqueous solution lead to effect the droplet rebound dynamics due to the elongational viscosity at the moving contact line during the spreading and retraction phases. Later, few studies [42, 43] have experimentally contradicted that polymers play a crucial role only during the retraction phase of the droplet. Similarly, Bonn et al.[44] revealed the role of dominant elastic normal stresses over surface tension forces on the droplet rebound behavior on superhydrophobic surfaces. Smith et al. explained the role of the stretchability of the flexible polymer chains during the retraction stage of the droplet on droplet rebound behavior. Smith et al. [45] showed that polymeric droplets with impact velocities lead to arrest the droplet rebound on the hydrophobic surface during the retraction state. Besides, few studies reported the reduced fragmentation of secondary droplets of polymeric jets due to the attachment of the filaments to the mother droplet [46, 47] .

2.4 Ferrofluids

Droplet post-impact hydrodynamics on a solid surface under external fields has attracted great attention because it shows strange physics from ordinary situations. On the one hand, recent studies have explored the role of ferrofluid droplets on drop rebound, splash, shape distortion and fragmentation dynamics under external magnetic field. visser et al. and Zenou et al. [19, 48] experimentally revealed that the droplet spreading dynamics promotes the shape distortion of metallic droplets in presence of the magnetic field during laser-induced curing. Ahmed et al. [49] discussed pre-impact droplet shape distortions from spheroidal to ellipsoidal under horizontal and vertical magnetic fields. Similarly, Yang et al. [50] reported the elliptical spreading of liquid metal (GaInSn alloy) droplets on the glass surface in presence of the horizontal magnetic field. Sudo et al. studied the effect of magnetic field strength on the spread factor and splash dynamics in presence of the magnetic field. Rahimi and Weihs [51] explored the impact dynamics of drops of magnetorheological (MR) fluids and showed that the spreading radius decreases with increasing magnetic field under the magnetic field. Besides, a few more studies [52, 53] investigated and reported the effect of rupture mechanics of fluid lamella for different impact velocities. Redon et al. analytically derived the growth rate of holes in the liquid lamella during the retraction stage of the liquid lamella on the mutual dominance of viscous forces and capillary forces.

2.5 Dielectric fluids

On the other hand, recent studies have examined the effect of dielectric droplets on rebound behavior, splash control, shape distortion and fragmentation dynamics under an external electric field. Yun and Lim [54] explored the effects of field strength on the shape eccentricity under an electric field. Deng et al. [55] and Yun et al. [56] showed the droplet rebound arrestment along with shape distortion under an external electric field. Khojasteh et al. [57] numerically showed that dielectric liquid droplet deformation triggers in the direction of the electric field. Ryu and Lee [58] experimentally showed the charge effect on the spreading dynamics of the droplets on the dielectric substrate. Later, Mohmoudi et al. [59] also experimentally investigated the charged droplet spreading achieves through the corona discharge-assisted technique. Yurkiv et al. [60] droplet impact hydrodynamics on both polarized and non-polarized dielectric surfaces under an external electric field. Besides, few more studies focus on electric field-embedded surface wettability techniques such as electrowetting [61–64] and dielectrowetting [65–67]. McHale et al. [65] reported the rate of spreading of dielectric liquid spreading on a partial wetting behavior under both external uniform and non-uniform electric fields. Zhang et al. [67] examined the droplet jumping motion in the presence of electric field.

2.6 Leidenfrost droplets

As surveyed above, the impact hydrodynamics of droplets, as well as the thermo-hydrodynamics of droplets, have attracted great research interest in a wide range of applications such as spray cooling and spray quenching etc. [20, 21]. In recent times, Leidenfrost dynamics of droplets play a crucial role especially in spray cooling due to the onset of the liquid-vapor interfacial cushioning dynamics. Quere and Clanet et al. [39] comprehend the droplet Leidenfrost dynamics on the heated solid substrate. Biance et al. [68] explored the dependence of the shape and size of the droplets on the cushioning dynamics of the vapor layer. Tran et al. [69] introduced a new scaling relation for the non-dimensional maximum spreading factor of droplets on heated surfaces with different Weber numbers. Khavari et al. [70] experimentally explored the impact dynamics and fingering patterns of the liquid droplets on heated substrate. Villegas et al. [71] numerically studied the temporal evolutions of the drop shape and vapor layer thickness using level set method. Later Qiao et al. [72] explored the Leidenfrost dynamics of droplets on liquid pools using Lattice Boltzmann method and reported the effect of various non-dimensional numbers such as Stefan number, Bond number, Ohnesorge number and pool depth on Leidenfrost dynamics.

In addition to the aforementioned droplet Leidenfrost effect, researchers have opened up new directions and tried to propose better complex fluids to cool the hot surface by delaying the onset of the Leidenfrost phenomenon. Dhar et al. [73] experimentally investigated the role of Weber number and polymer concentration on the Leidenfrost temperature due to the adhered long-lasting filaments at the heated surface. Qiao and Chandra [74] proposed the sodium dodecyl sulfate (SDS) surfactants to suppress Leidenfrost temperature and revealed the role of nucleation of vapor bubbles, reduced bubble coalescence on the increase of T_{DL} . In contrary to Qiao and Chandra's study, Chen et al. [75] tried with alcoholic surfactants (HAS) to increase the T_{DL} and established the empirical correlation between T_{DL} and maximum spread factor. Later, Ulahannan et al. [76] explored the role of nanoparticle shape and size on the shift of the nano colloidal droplets Leidenfrost point. Besides, further studies have revealed the role of surface roughness on the morph of the Leidenfrost temperature by introducing the microstructural surfaces with different surface engineering techniques etc [77–79]. Shi et al. [80] explored and reported the suppression of the Leidenfrost effect on superhydrophobic surfaces. They demonstrate that T_L of water on superhydrophobic surfaces with reentrant pillars can exceed than hydrophilic and superhydrophilic surfaces. Matsumoto et al. [81] experimentally investigated the levitation and self-propulsion of the droplets and reported the effect of pool temperature and thermophysical properties of droplets on the dynamics of self-propelled droplets on the heated pools. Talari et al. [82] comprehend the Leidenfrost drops on micro/nano textured surfaces and reviewed the influence of the various nano/micro-scale surface structures on the Leidenfrost temperature in detail. Wang et al. [83] examined the evaporation of Leidenfrost droplets on a thin soluble liquid bath with a thermal non-uniform effect and theorized that nonmonotonic variation of droplet temperature departs from the saturation temperature.

2.7 Research Gap

As per the extensive literature review that was described in the preceding sections, the important inferences regarding the state of knowledge regarding "droplets" can be summed up as follows:

1. The impact dynamics of droplets on hydrophilic and superhydrophobic surfaces with different parameters is well understood. Impact dynamics in inkjet printing still lack some major issues such as drop rebound control, drop splash control, ink viscosity effect, clogging of small nozzles, generation of patterns smaller than nozzle size and so on.
2. Recent research has shed light on the significance of the impact dynamics of polymeric droplets on superhydrophobic leaves during pesticide application and how these drop rebound control mechanisms are influenced by polymer chains in filamentous dynamics.

3. Similar to droplet impact dynamics, ferrofluids and dielectric fluids have shown great potential for drop rebound dynamics and splash control in the presence of external magnetic and electric fields, respectively.

4. Reports on Leidenfrost droplets have shown various strategies during droplet impact dynamics on a hot surface during the spray cooling process either surface morphology by developing functional surfaces with simple coolant or proposing novel complex fluids/coolants on a regular hot surface, etc. Detailed insight into complex fluids on surface morphology during the Leidenfrost phase is still lacking.

2.8 Research Objectives

The research objectives/goals for the current dissertation have been developed and listed as follows in light of the extensive literature review that was mentioned above and the significant knowledge gap that was described in the parts before it:

1. To examine the role of magneto-elastic effects of impact dynamics of non-Newtonian (polymer-based) ferrofluid droplets on superhydrophobic surfaces in presence of an external magnetic field and targeted to understand the elastic effects of the induced polymer chains of the non-Newtonian ferrofluid droplets on droplet rebound control under external magnetic field.
2. To investigate the role of electro-elastic effects of the impact dynamics of non-Newtonian (polymer-based) dielectric droplets on superhydrophobic surfaces in presence of an external electric field and aimed to explore the elastic effects of induced polymer chains of the non-Newtonian dielectric droplets on anti-superhydrophobicity through rebound suppression under external electric field.
3. To study the role of impact dynamics of surfactant droplets on the hydrophilic heated surfaces and target to enhance the heat transfer from the hot surface by suppressing the dynamic Leidenfrost phenomenon.
4. To explore the role of impact dynamics of nanocolloidal droplets on hydrophilic heated surfaces and aim to increase the heat transfer from the hot surface by delaying the onset of dynamic Leidenfrost temperature.
5. To investigate the role of impact dynamics of novel nanobubbles dispersed fluid droplets on hydrophilic heated surfaces and targeted to escalate the heat transfer from the hot surface by augmenting the dynamic Leidenfrost point.

Chapter 3

Magneto-elastic effect in non-Newtonian ferrofluid droplets impacting on superhydrophobic surfaces

3.1 Introduction

The dynamics and phenomenology of droplet impact on a solid or liquid surface is scientifically important due to the wide range of associated applications. Droplet impact dynamics comprises various physical phenomena, like deposition, rebound, partial rebound [17], splashing and fragmentation. Understanding the dynamics is a decisive factor in many applications like inkjet printing [18], spray coating and painting, spray cooling, and retention of pesticide sprays on vegetation to prevent groundwater contamination and pesticide over-use, etc. The manipulation of impact dynamics of ferrofluid droplets by magnetic field can lead to significant improvements in magnetic 3D printing [19] performance, and may also promote control of shape distortions in metallic droplets during welding or soldering. The magnetic force on ferrofluid droplets is important for handling magnetic beads and manipulating ferrofluid droplet transport and splitting in microfluidic devices [22]. Ahmed et al. [49] studied the maximum spreading dynamics of a ferrofluid droplet under the effect of vertically oriented magnetic field. The maximum spreading of the droplet was proportional to the corresponding non-dimensional numbers, like Weber number (We), magnetic Bond number (Bo_m), and Reynolds number (Re). Sudo et al. [84] explored the effect of magnetic field on the maximum spreading diameter and spike formation within the liquid lamella of impacting magnetic fluid droplets. Rahimi & Weihs [51] reported the droplet impact dynamics of magnetorheological fluids (MRF) and reported the dependence of maximum spreading factor on the magnetic field strength and Reynolds number (Re). Zhou and Jing [85] showed how magnetic field affects the collision characteristics, oscillation kinetics, maximum spreading factor, maximum recoiling height and the retraction height of ferrofluid droplets for different impact velocities. Sahoo et al. [86] experimentally investigated impact dynamics of ferrofluid droplets on superhydrophobic surfaces under the influence of horizontal magnetic field and reported that significant rebound suppression phenomena was observed at moderate

magnetic Bond numbers ($Bo_m \sim 300$). The ferrofluid droplet liquid lamella was shown to become largely unstable due to nucleation of holes during retraction stage at higher magnetic Bond numbers ($Bo_m > 300$), leading to distinct fragmentation kinetics fairly uncommon in droplet impact literature.

In recent years, elastic and viscoelastic effects during impact dynamics of non-Newtonian fluid droplets have gathered attention due to the observation of rebound suppression on superhydrophobic surfaces [44, 45, 87, 88]. It was shown that addition of minute amounts of flexible, very long-chain polymers like polyethylene oxide (PEO) or polyacrylamide (PAM) to water arrests the droplet rebound on superhydrophobic surfaces. Initially it was believed to be due to the higher energy dissipation caused by the elongational viscosity of the polymer solutions. Bartolo et al. [44] proposed that during retraction, the polymer chains generate a large amount of normal stresses, and slows down the moving contact line of the droplet. This opposes the capillary force and retraction kinetic energy, which ultimately leads to rebound suppression. Mao et al. [87] showed the dependence of rebound behavior on the spread factor and the static contact angle of the droplet. Smith et al. [45] showed the extensional deformation of solvated fluorescent dyed DNA molecules near the receding contact line of a droplet slows down the retraction process.

Later, Dhar et al. [88] showed the governing roles of the impact velocity and polymer concentrations as critical parameters to determine the onset of rebound suppression. Based on the shear rate during onset of retraction and the relaxation time scale of the elastic fluid, they showed that the onset of rebound suppression occurs only under circumstances where the governing Weissenberg number (Wi) exceeds one. They further showed that the change in retraction dynamics of the non-Newtonian droplets can be also used to morph the thermo-species transport behavior, such as delaying the droplet Leidenfrost effect [73]. Zang et al. [89] observed a transition from droplet rebound to sticking by the addition of PEO to Newtonian fluids and reported the importance of sliding angle of the fluid droplet, in addition to the contact angle. Yun et al. [56] reported the effect of electric field on non-axisymmetric droplets towards inhibiting droplet rebound and also investigated the impact dynamics of ellipsoidal drops as function of the geometric aspect ratio and impact Weber number [90]. Antonini et al. [91] showed the importance of the receding contact angle of the rebounding droplet on hydrophobic and superhydrophobic surfaces. Very recently a work revisited the role of elongational viscosity on rebound suppression event using advanced experimental techniques like total internal reflection microscopy [TIRM] [92].

In this article, we have explored a novel phenomenon in non-Newtonian ferrofluid droplets, which may be given a nomenclature of magneto-elastic effect. We have investigated the impact and rebound dynamics of polymer solution based ferrofluid droplets under the influence of a horizontal magnetic field, and the phenomenology of onset of conjugated magnetic and elastic instability, leading to suppressed droplet

rebound. The impact magneto-hydrodynamics of the droplet has been characterized by four dimensionless parameters, viz. the Weber number ($We = \rho V_0^2 D_0 / \sigma_{lv}$, defined as the ratio of inertial force to surface tension force), the magnetic Bond number ($Bo_m = B^2 D_0 / \mu_o \sigma_{lv}$, defined as the ratio of magnetic force to surface tension force), the magnetic capillary number ($Ca_m = \eta V_0 / \sigma_{lv}$, is defined as ratio of viscous force to surface tension forces under influence of magnetic field), and the Hartmann number ($Ha = \rho m B D_0 / 2 V_0 \eta$), [93], defined as the ratio of magnetic force to viscous force). Here ρ , V_0 , D_0 , σ_{lv} , B , m , μ_o and η denote the density, impact velocity, pre-impact diameter, surface tension, magnetic flux density, magnetic moment per unit mass, magnetic permeability of free space and viscosity of the ferrofluid droplet, respectively. Furthermore, we theorize and show that the onset of suppression of droplet rebound depends on the magneto-elastic effect, which is a conjugation of the polymer relaxation time, the shear rate at the contact line during the retraction stage, and the ferro hydrodynamics of the droplet. We have also highlighted the critical role of a proposed magnetic Weissenberg number in governing the onset criterion for droplet rebound suppression.

3.2 Materials and Methodologies

3.2.1 Non-Newtonian ferrofluids

The ferrofluids were synthesized using iron (II, III) oxide (Fe_3O_4) nanoparticles (Alfa Aesar India, >98.5% purity) of average particle diameter 20–30nm (noted from scanning electron microscopy images (not illustrated)). Polyethylene glycol (PEG 400, analytical grade, Finar Chemicals, India) was used to render the ferrofluids non-Newtonian. Initially, polymer solutions using PEG and deionized (DI) water were synthesized (5 and 10 % v/v of PEG). To these non-Newtonian fluids, the Fe_3O_4 nanoparticles are dispersed (2.5 and 5 wt. %) and stabilized following similarly reported protocol [94]. The polymeric ferrofluids

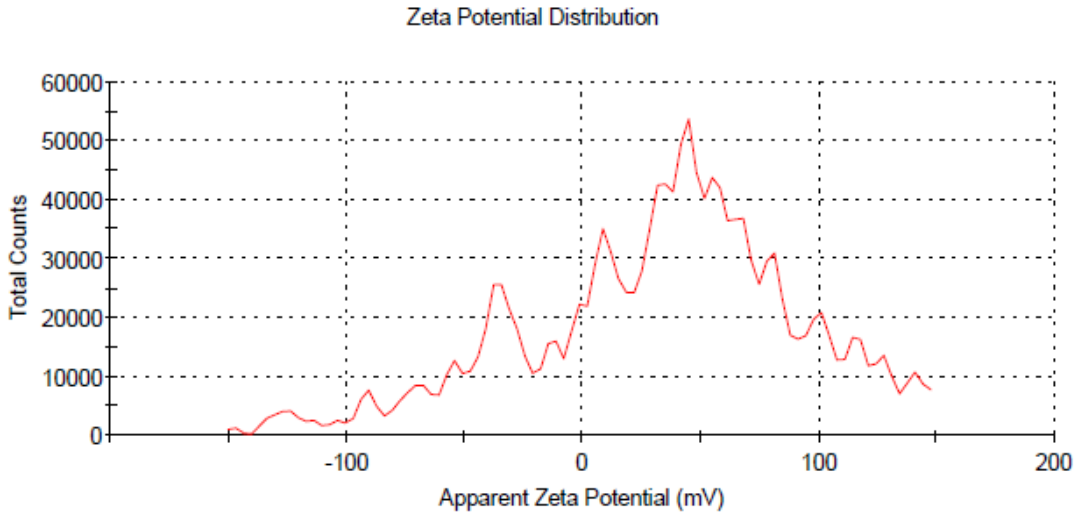


Figure 3.1: Zeta Potential distribution of the highest concentration(5% w/w -F5) of the operating range of the ferrofluids used.

were subjected to ultra-sonication for 2 hours to ensure colloidal stability. We adopt a nomenclature method for the polymeric ferrofluids: a sample containing ‘x’ % PEG in water, and ‘y’ % Fe_3O_4 particles is written as Px-Fy. Thus, sample P5-F2.5 contains 5 % v/v PEG in water with 2.5 w/w % particles dispersed in it. Any sample with P0 signifies Newtonian ferrofluid. To ascertain the stability of the colloidal dispersions, we followed the protocols outlined in previous references (94 and 183) for the preparation of colloidal solutions. Additionally, we performed a zeta-potential measurement using Zetasizer NanoZSP and observed a zeta-potential value of +23.9 mV at the highest particle concentration (refer fig.3.1.) This measurement confirmed the stability of the colloidal solutions .

3.2.2 Substrates

Glass slides coated with a commercial superhydrophobic (SH) coating (Neverwet Ultra Ever dry, USA) were used as substrates in the experimental study. The microscopic structure (noted from scanning electron microscopy images (refer fig.3.2.)) of the spray coated SH surface has been depicted in fig.3.2. The substrates were prepared by following

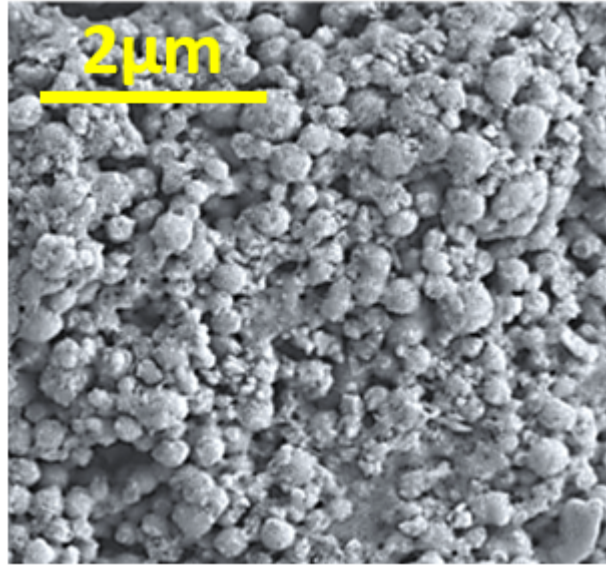


Figure 3.2: Microscopic structure of spray coated superhydrophobic surface using Scanning Electron Microscopy

previously reported protocol [95]. Before spray coating, each glass slide was cleaned with DI water followed by acetone and oven-dried thoroughly. The static equilibrium contact angles of the ferrofluid droplets are shown in Fig. 3.3. The static contact angle of non-Newtonian ferrofluid droplets on the SH surface is in the range of $155 \pm 3^\circ$. The surface tension of the ferrofluids (refer [Table. 3.1.]) was measured using the pendant drop method, and the equilibrium static contact angles were measured from image analysis. The surface tension values were noted to be minimally altered due to the magnetic field, and in the range of 76 ± 3 mN/m.

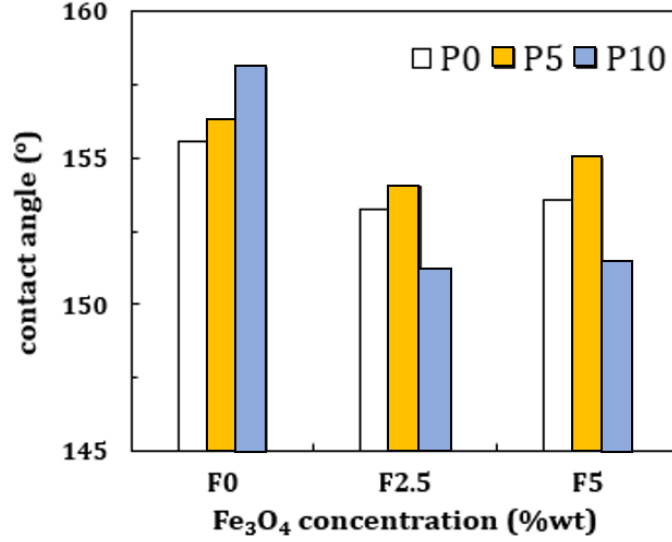


Figure 3.3: Static equilibrium contact angles of different non-Newtonian ferrofluid droplets on spray coated superhydrophobic surface.

Table 3.1: Physical properties of impacting non-Newtonian dielectric fluid droplets: pre-impact droplet diameter D_o (mm), density ρ (kg/m^3), surface tension σ (mN/m)

| Base fluid | Fe_3O_4 particles | surface tension (mN/m) |
|------------|---------------------|------------------------|
| P0 | F2.5 | 72.6 |
| P0 | F5 | 75.4 |
| P5 | F2.5 | 74 |
| P5 | F5 | 76 |
| P10 | F2.5 | 77.5 |
| P10 | F5 | 79 |

3.2.3 Experimental setup

The overall arrangement of the experimental setup is shown in Fig. 3.4. A digitized droplet dispensing mechanism (DDM) unit ($\pm 0.1 \mu l$ volumetric accuracy) was used to dispense droplets of fixed volume, via a glass micro-syringe with a flat head steel needle (22 gauge). The impact height of the droplet was adjusted to obtain different impact velocities, and different We . The droplet was allowed to fall freely on the substrate, which was placed between the poles of an electromagnet. An electromagnet (Holmarc Opto-Mechatronics Ltd., India) was used to generate the magnetic field, with controlled field strengths of 0–0.2 T. The field strength was varied by changing current input across the electromagnet pole windings using a direct current power supply (Polytonic Corp., India) unit. Flat face cylindrical iron billets of diameter 100 mm act as the magnetic pole shoes. The magnetic field strength near the substrate was calibrated by a Gauss meter (Holmarc Opto-Mechatronics Ltd., India) for different current inputs to the pole windings. Beyond 0.2 T, the free falling droplet shape is distorted by the field before impact, which induces artifacts to the post impact hydrodynamics. Accordingly, the experiments have been restricted to 0.2T. The micro-syringe needle and SH slides were positioned at the

center of the electromagnet poles to ensure that the droplet impact was in a uniform magnetic field. The droplet dynamics was recorded with a high-speed camera (Fastcam SA4, Photron, UK) attached with a macro lens of constant focal length of 105 mm (Nikkor, Nikon). All experiments were conducted at 3600 frames per second (fps) and 1024×1024 pixels resolution. For backlight illumination, an intensity-controlled LED array was used.

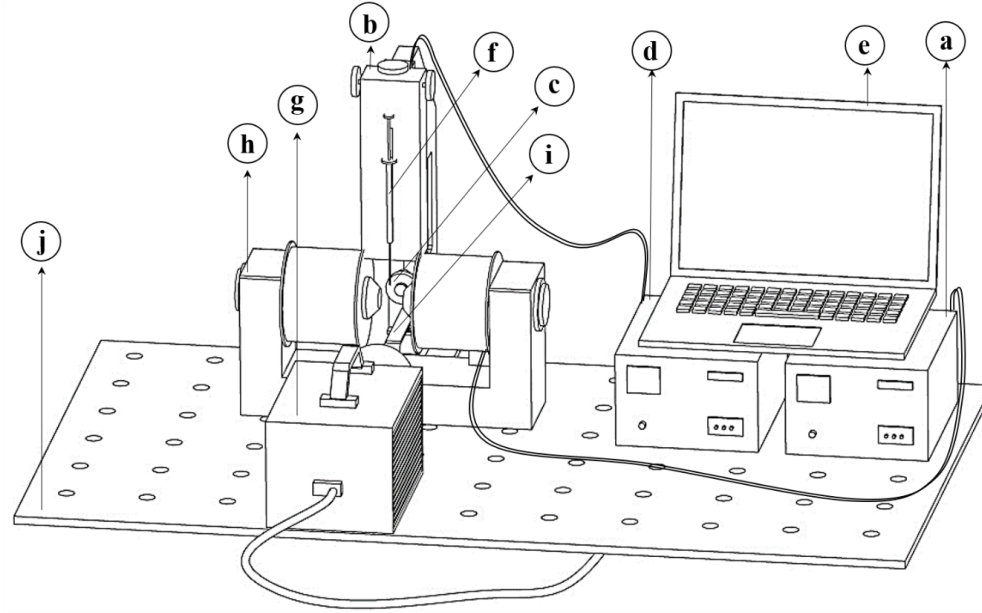


Figure 3.4: Schematic of the experimental setup. (a) Electromagnet power controller (b) droplet dispensing mechanism (DDM) unit (c) LED array for backlight illumination (d) DDM and LED array intensity controller (e) computer for data acquisition and camera control (f) micro-syringe (g) high speed camera (h) programmable electromagnet unit (i) spray coated superhydrophobic surface (j) bread board.

The schematic of the front and top views of positioning of the droplet, and the associated coordinate frame of reference are illustrated in Fig. 3.5.

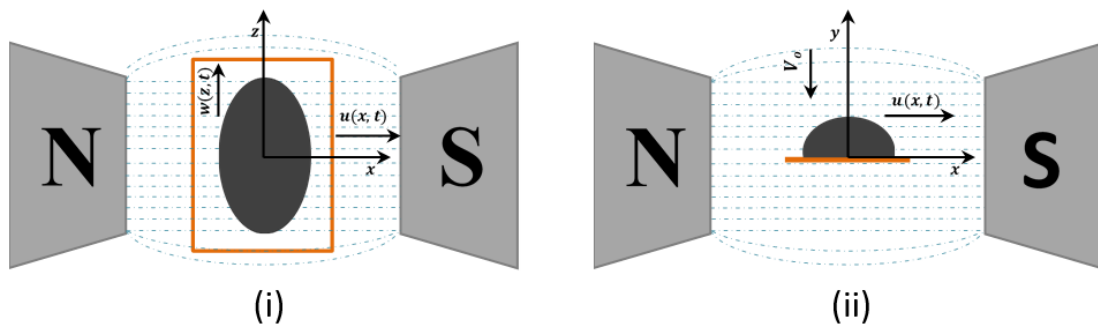


Figure 3.5: (i) top view and (ii) front view of the ferrofluid droplet under magnetic field. N and S represent the north and south poles of the electromagnet.

Rheological tests of the fluids were performed using a rotational rheometer (Anton Paar, Germany). A plate and plate geometry (PP-20) attached to a magnetorheological module

is used to determine the shear viscosity (η), elastic modulus (G') and viscous modulus (G'') (refer Fig. 3.6. and 3.7.) under influence of magnetic field. All tests and experiments were repeated thrice to check for repeatability.

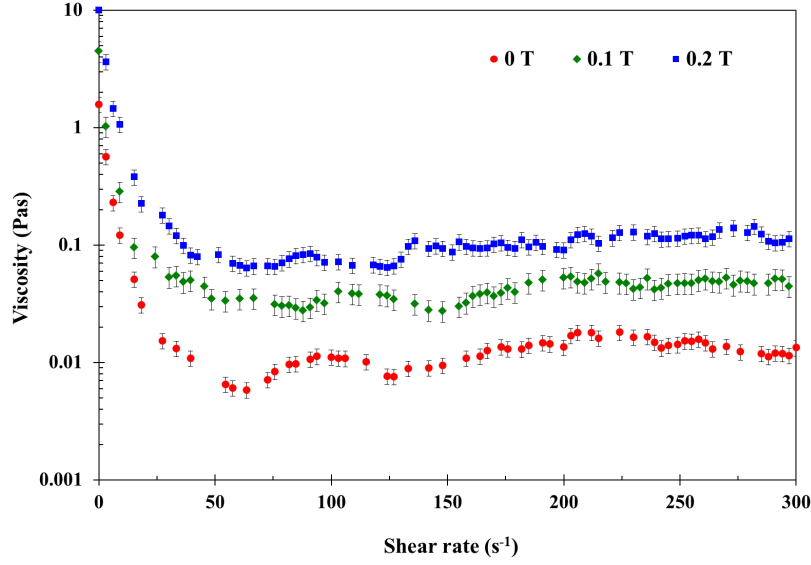


Figure 3.6: Rheological response of the non-Newtonian ferrofluid (P10-F5) in the presence of magnetic field. The sample with the highest polymer and Fe_3O_4 content has been chosen to explain the rheology in the context of the most viscous sample. It is noted that the non-Newtonian character of the ferrofluids is retained only up to shear rates of $\sim 50\text{--}100\text{ s}^{-1}$. This behaviour is also conserved in case of the magnetorheology. Beyond this regime, the fluids show nearly Newtonian behaviour, albeit with enhanced Newtonian viscosity due to the magnetic field.

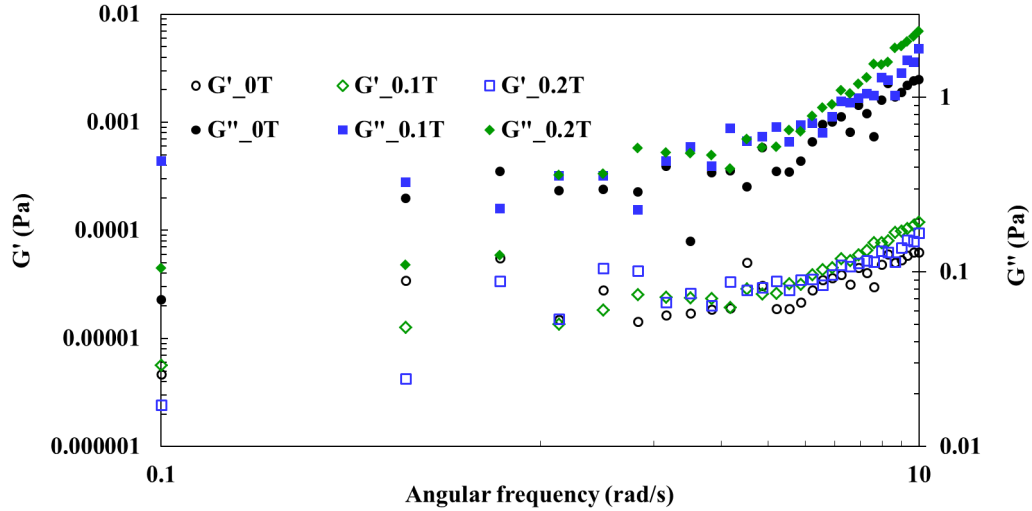


Figure 3.7: Viscoelastic response of the non-Newtonian ferrofluid (P10-F2.5) due to increasing oscillatory angular frequency at 1 % oscillatory strain amplitude. A single case has been illustrated for representation purpose. The oscillatory frequency (ω) dependent values of G and G'' are used to determine the frequency dependent complex viscosity as $\eta_c = \omega^{-1} \sqrt{G'^2 + G''^2}$, which is further used to estimate the relaxation time scales for the non-Newtonian fluids.

3.3 Results and discussions

3.3.1 Droplet impact ferrohydrodynamics

We start the discussions with the ferrohydrodynamics of the droplet impact event on SH surfaces. Fig. 3.8. (a), (b) and (c) show the effect of the magnetic Bond number on the ferrofluid droplet spreading due to increasing non-Newtonian nature (achieved by increasing polymer concentration) at $We \sim 100$. In both Newtonian (water based) and non-Newtonian (polymer solution based) ferrofluid droplet cases, the droplet spreads with radial symmetry intact in the absence of magnetic field ($Bo_m = 0$). For the Newtonian case (P0-F2.5), the droplets spread to a larger extent along the z direction compared to the x direction (refer fig. 3.8. c, 1st row, 1st column for the coordinate axis) with increasing magnetic Bond number (Bo_m) (fig. 3.8a). This is due to the interplay between magnetic forces and the surface tension force, and has been discussed in details in our previous report [86].

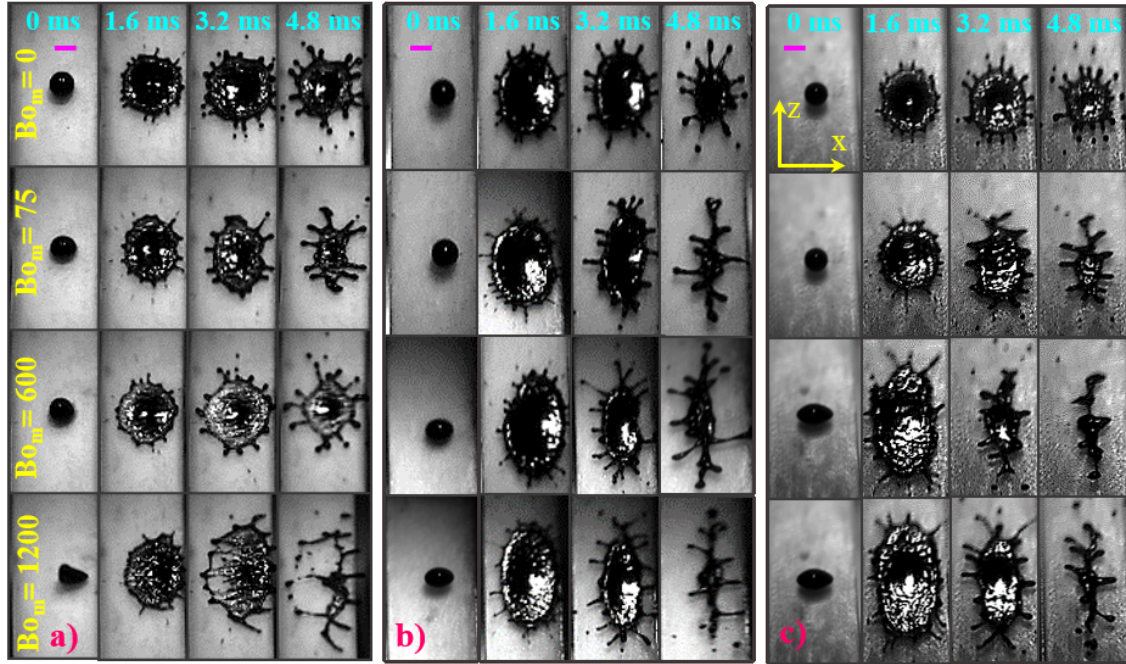


Figure 3.8: Temporal evolution of droplet impact ferrohydrodynamics for different Bo_m for (a) P0-F2.5 (b) P5-F2.5 and (c) P10-F2.5 fluids. The figure shows the role of increasing non-Newtonian fluid nature on the droplet impact ferrohydrodynamics. The scale bars represent 2.8 mm. The images are 1.6 ms apart. The magnetic field acts along the x-direction (coordinate axis shown in first row, first column of fig.3.8c)

As the droplet spreads in presence of the magnetic field, the rate of change of the magnetic force on the droplet increases. The Lenz's law, which suppresses the cause of change in the magnetic force in the system, thereby opposes the spread in the x-direction, while the droplet spreads unrestrictedly along the z-direction. Additionally, the liquid film formed and enclosed by the spreading rim (fig. 3.8a, 4th row, 3rd column) undergoes rupture due to nucleation and proliferation of holes at high values of magnetic Bond number (at

$Bo_m \sim 1200$) [86]. We have discussed the genesis of the rupturing instability from energy conservation considerations in the previous report [86]. Now we shift the focus to the non-Newtonian ferrofluids. The impact phenomenon is characterized by the formation of distinct filaments. This can be observed from fig 3.8b and c. With increase in either polymer concentration or the Bo_m , the rupturing instability of the spread droplet is noted to be seized. Also, the asymmetric elongation along the z-direction is notably pronounced, similar to the Newtonian drop impact dynamics in presence of magnetic field [86].

To quantify the asymmetric spreading kinetics, we define the maximum non-dimensional orthogonal spreading ratio as $\xi_{max} = (\frac{D_z}{D_x})_{max}$, and illustrate the same in fig. 3.9. Figure 3.9. illustrates the non-dimensional orthogonal maximum spreading ratio ξ_{max} for both Newtonian and non-Newtonian ferrofluid droplets for varied magnetic field intensity, quantified through the magnetic Bond number such as 0 T ($\xi_{max} = 0$), 0.05 T ($\xi_{max} \sim 75$), 0.10 T ($\xi_{max} \sim 600$) and 0.20 T ($\xi_{max} \sim 1200$). Fig. 3.9a shows the effect of ξ_{max} with varying polymer concentration on the ξ_{max} . Initially, the ξ_{max} increases linearly with ξ_{max} (~ 75) and then saturates to an almost constant value. It must be noted that the saturated value of ξ_{max} is increasing with the increase of polymer concentrations. One of the potential reason for the initial linear increase of ξ_{max} with Bo_m is due to the linear magnetization of the ferrofluid droplet [96, 97] in the low field regime. In a previous report [98] it has been shown that PEG chains may entangle Fe_3O_4 nanoparticles to form a particle-polymer chain mesh. We believe, in the non-Newtonian ferrofluids, the particles entangled to the fluid phase are able to arrest the spread along the x-direction to a greater extent. This is possible as the magnetic force acts on the whole fluid in a more uniform manner compared to the Newtonian case where the particles are dispersed, and prone to magnetophoretic drift with respect to the fluid. Consequently, the droplet spreads to a larger extent along the z-direction, thereby increasing the ξ_{max} . At the same time, for a fixed polymer (P10) concentration, ξ_{max} increases with increasing magnetic particle concentration (fig. 3.9b).

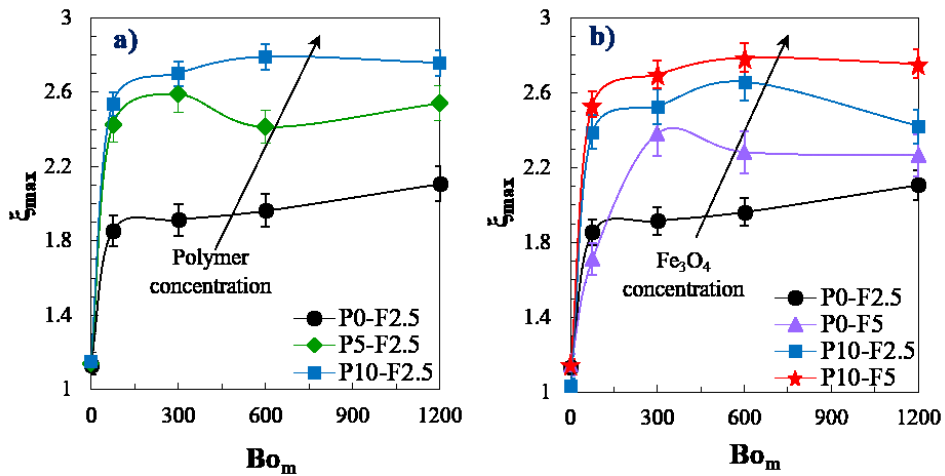


Figure 3.9: The effect of magnetic Bond number (Bo_m) on the maximum non-dimensional orthogonal spreading (ξ_{max}) with (a) varying polymer concentration and (b) magnetic particle concentration

3.3.2 Droplet rebound suppression kinetics

In this section, we discuss the phenomenology and physical mechanisms responsible for the suppression of rebound of the droplets under the effect of magnetic field.

3.3.2.1 Role of polymer concentration

The rebound phenomenology of the ferrofluid droplets in presence of horizontal uniform magnetic field on SH surfaces have been shown in Fig. 3.10. The set of experiments reported were done at fixed Weber number $We \sim 100$ and magnetic nanoparticle concentration (F2.5), and the figure illustrates the role of polymer concentration (non-Newtonian behavior). Additionally, as a set of control experiments (not illustrated), we performed the impact studies for only polymer solutions (P5-F0 and P10-F0) for different We and Bo_m , and no rebound suppression is noted at all. It can be readily observed that in absence of magnetic field ($Bo_m = 0$), both Newtonian and non-Newtonian ferrofluid droplets exhibit the usual droplet rebound behavior (fig. 3.10a, b and c, 1st row). In case of Newtonian ferrofluid, increasing the Bo_m reveals the following sequence of droplet impact outcomes, such as spreading, retraction, recoil, rebound and fragmentation. Under no circumstances the non-Newtonian ferrofluid exhibits rebound suppression for the studied range of Bo_m (fig.3.10a).

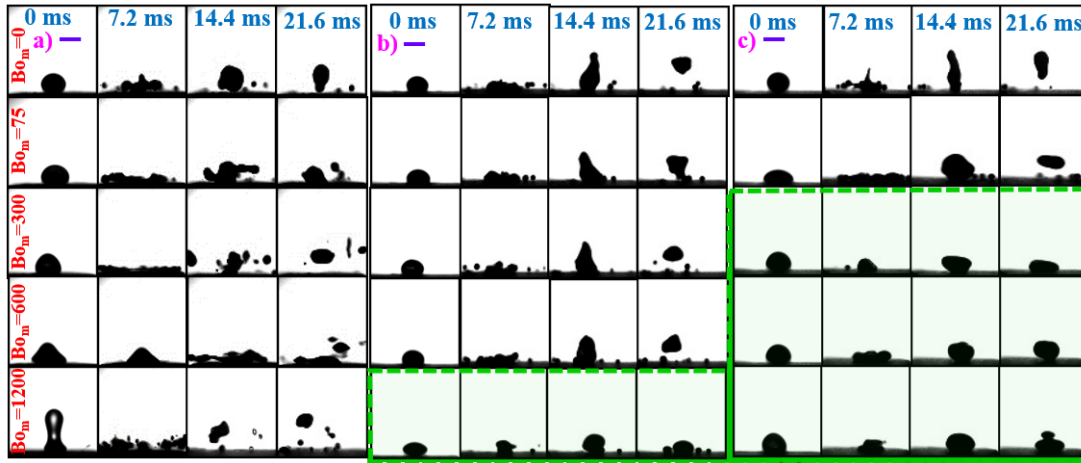


Figure 3.10: Effects of polymer concentration on the rebound kinetics of the ferrofluid droplets over SH surface for different magnetic Bond numbers at $We \sim 100$ for (a) P0-F2.5 (b) P5-F2.5 and (c) P10-F2.5. The scale bars represent 2.8 mm. From top to bottom, the rows represent $Bo_m = 0, 75, 300, 600$ and 1200 . The region circumscribed by the dashed lines illustrates the regimes of rebound suppression.

Next, we focus on the non-Newtonian ferrofluids, and keep the magnetic nanoparticle concentration fixed (F2.5) while varying the polymer concentration. The lower polymer concentration (P5) ferrofluid droplets also show similar impact phenomenology as the Newtonian ferrofluid droplets up to $Bo_m \sim 600$ (fig. 3.10b). But, at higher magnetic field strength ($Bo_m \sim 1200$), onset of rebound suppression of the droplet was observed (fig. 3.10b, 5th row). In the case of higher polymer concentrations (P10), post-impact stages

similar to P0 and P5 ferrofluids are noted in absence of magnetic field (fig. 3.10c 1st row). But interestingly, the P10 ferrofluids exhibit the onset of rebound suppression at much lower magnetic field strength regime ($Bo_m \sim 300$) (fig 3.10c, 3rd row) in comparison to the P5 fluid. For ease of illustration, we have enclosed the paradigms of rebound suppression in fig. 3.10 with dashed green lines. Thereby, we infer that at fixed impact We and magnetic particle concentration, the presence of certain non-Newtonian effect in conjunction with the magnetic force on the ferrofluid, triggers the rebound suppression phenomenon.

3.3.2.2 Role of magnetic particle concentration

Next, we probe the role of the magnetic particle concentration, which governs the magnetic force on the ferrofluid at a particular magnetic field (illustrated fig. 3.11). We fix the polymer concentration (P10) and the Weber number ($We \sim 100$), and vary the magnetic particle concentration (F2.5 and F5). In the absence of magnetic field, both the ferrofluid droplets (P10-F2.5 and P10-F5) show the typical rebound nature off SH surfaces (fig. 3.11a and b, 1st row). The low concentration (F2.5) non-Newtonian ferrofluid droplet shows onset of rebound suppression at moderate $Bo_m \sim 300$. But in case of a high concentration ferrofluid (F5) the same is noted at $Bo_m \sim 75$. Our control experiments using Newtonian ferrofluid droplets of F2.5 (fig. 3.11a) and F5 do not show any such rebound suppression events, even at $Bo_m \sim 1200$. Hence from the observations, we may

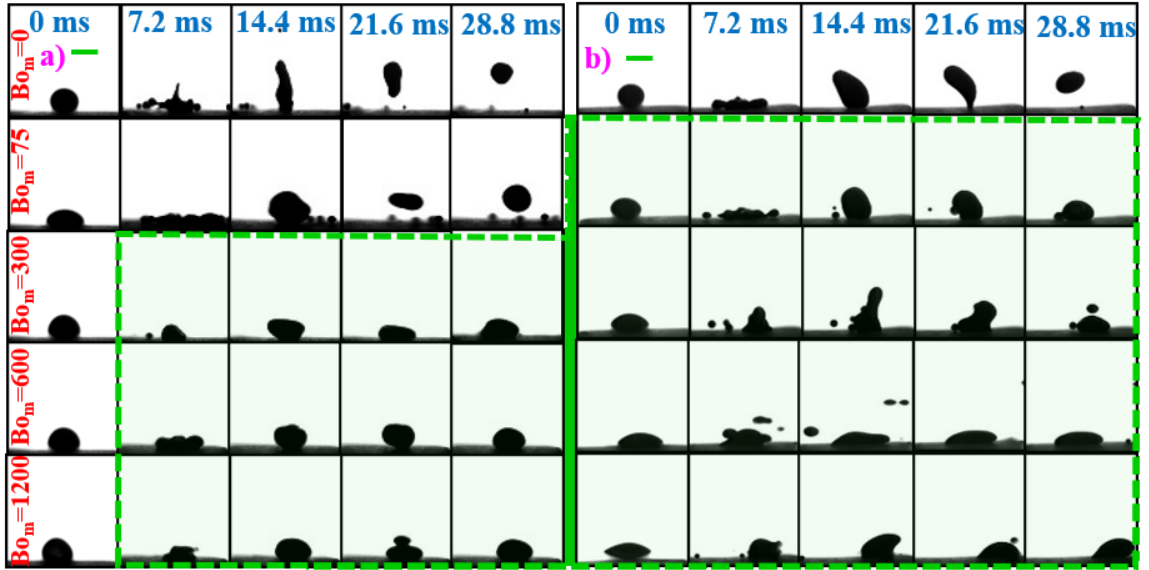


Figure 3.11: Effects of magnetic particle concentration on the rebound suppression over SH surface for different magnetic Bond numbers, for (a) P10-F2.5 and (b) P10-F5, at $We \sim 100$. The scale bar represents 2.81 mm. From top to bottom, the rows represent $Bo_m = 0, 75, 300, 600$ and 1200 . The region circumscribed by the dashed lines illustrates the regimes of rebound suppression.

further infer that the rebound suppression event is triggered by interplay of the magnetic and the non-Newtonian effects in the presence of a magnetic field. Compared to P10-F2.5; the droplet of higher magnetic particle concentration (P10-F5) exhibits fragmentation into

secondary droplets during receding and subsequent rebound inhibition. In case of P10-F5 drops, the magnetic force induced is greater (due to higher magnetic particle population) than P0-F2.5. The higher magnetic force overpowers the interfacial energy, leading to the breakage of finger like elements attached to the central portion from the main drop.

3.3.2.3 Role of impact Weber number

In this section, we discuss the role of the impact We . The impact phenomenology of different non-Newtonian ferrofluid droplets at two different $We \sim 40$ and ~ 100 have been illustrated in fig. 3.12. Our experiments show (not illustrated) that when the polymer concentration is kept constant and magnetic particle concentration is varied, the onset

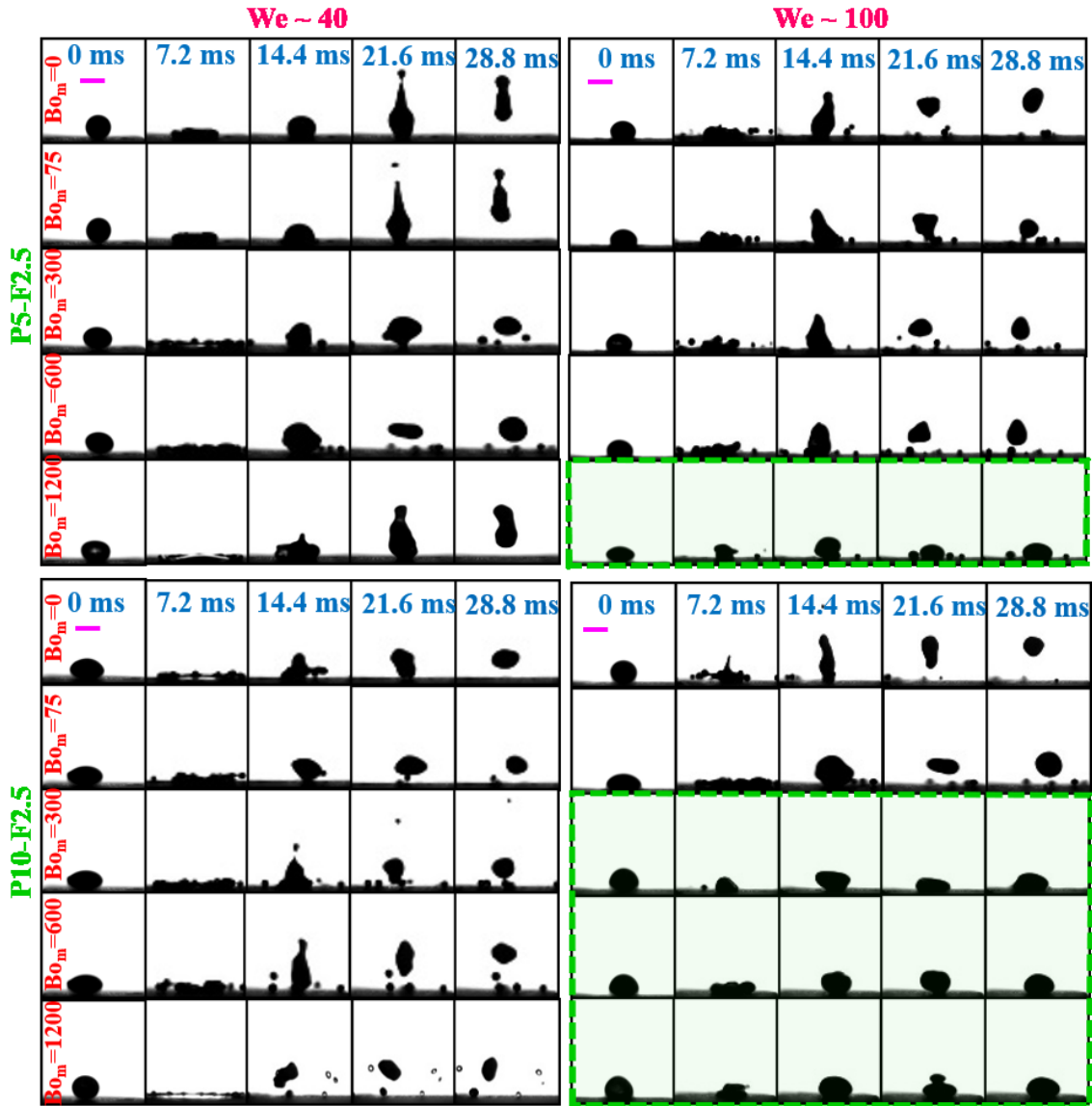


Figure 3.12: Effects of the impact Weber number on the impact events over SH surface for different Bo_m at $We \sim 40$ and ~ 100 . The scale bar represents 2.81 mm. From top to bottom, the rows represent $Bo_m = 0, 75, 300, 600$ and 1200 . The regions circumscribed by the dashed lines illustrate the regimes of rebound suppression.

of rebound suppression under magnetic field influence is not governed by the We . But the same is not true for the case where magnetic particle concentration is kept fixed, and the polymer concentration is varied (fig. 3.12). At a fixed $We \sim 40$, irrespective of the nature of the ferrofluid (Newtonian or non-Newtonian) and the Bo_m , the droplets do not exhibit any sign of rebound suppression. When the same set of impact experiments are conducted at $We \sim 100$, we note significant and drastic change in the associated hydrodynamics. At higher We , the onset of rebound suppression is observed at $Bo_m \sim 1200$ for low polymer concentration (P5), and at $Bo_m \sim 75$ for high polymer concentration (P10) cases. We therefore infer that the impact We and the non-Newtonian characteristics of the fluid (polymer concentration) also interplay, and higher We lead to triggering of the magneto-elastic effect. This observation is in agreement to our previous report on the elastic instability in non-Newtonian droplets [88].

3.3.2.4 'Magneto-elastic' effect and role of *magnetic Weissenberg number*

From the discussions in the previous three subsections, we infer that an interplay of the impact mechanics (manifested through the We , refer fig.3.12), the elasticity of the fluid (manifested through the polymer concentration, refer fig.3.10), and the ferrohydrodynamic forces (manifested through the Bo_m) are responsible for the triggering of the rebound suppression event. It is evident from fig. 3.10 that with increasing polymer concentration, rebound suppression is achieved at much lower Bo_m at a fixed $We \sim 100$. In absence of polymers (P0–F2.5), even at the highest $Bo_m \sim 1200$ no rebound inhibition was observed. On the other hand, for P5–F2.5 and P10–F2.5 the Bo_m at which the rebound suppression was observed were 1200 and 300 respectively. Clearly with increasing polymer concentration, the non-Newtonian effects are triggering the onset of rebound suppression at lower Bo_m . From figure 3.10, it was observed that for a fixed magnetic particle concentration, with increasing Weber number, the critical Bo_m for the rebound suppression is reduced. So, it is evident that the non-Newtonian effects responsible for droplet rebound suppression [44],[45, 73, 88] are becoming more potent with the increase of polymer concentration as well as We . In this context, it is worthwhile to mention that the relaxation time of the polymeric fluids increase with the polymer concentration. The role of We in setting up the critical shear rate required for non-Newtonian dynamics to be strong enough to slow down the retraction dynamics of the droplets during retraction is also well documented in earlier works [44],[45, 73, 88]. Now the product of the relaxation time and the shear rate (inverse of the flow time scale) is the classical Wi . Clearly, any phenomenon governed by Wi can be referred as elastic effects [99, 100]. The present study is also focusing the modulation of drop impact dynamics due to varying magnetic field strength (varying Bo_m). Since the suppression of drop rebound behaviour is simultaneously affected by elastic and magnetic field induced effects, the onset of droplet rebound was dubbed as the manifestation of “magneto-elastic” instability.

It is at this instance that the plausible role of viscosity of the fluids on the rebound suppression dynamics needs to be discussed. In our previous reports [73, 88] on elastic fluids, we have shown conclusively that the increase in viscosity of the fluids due to presence of polymer may alter the impact hydrodynamics, but does not trigger rebound suppression under any circumstances. In the present study, we have performed detailed rheology and magneto-rheology to understand the role played by viscosity (fig. 3.6.). As a representative case, we shall discuss the case for fluids P5-F2.5 at 0.1 T (corresponding to $Bo_m \sim 600$) and P10-F2.5 at 0 T ($Bo_m = 0$). From the magnetorheology studies, we have observed that the shear viscosities of these two fluids are within 3% of one another (for shear range of $0 - 300 \text{ s}^{-1}$). Next, we focus on the impact of these two fluids at $We \sim 100$ (fig. 3.12). Despite the similar viscosities, the P5-F2.5 exhibits rebound suppression at $Bo_m \sim 600$, whereas the P10-F2.5 exhibit the typical rebound of SH surface at $Bo_m \sim 0$. This clearly illustrates that the rebound suppression is not triggered by the increase in the viscosity of the ferrofluids due to the magnetorheological effect, and there is some other non-trivial mechanism at play.

For the explanation, we appeal to our previous report on rebound suppression of elastic fluid droplets on SH surfaces and the references within [88]. We showed that using very dilute polyacrylamide (PAAM) solution droplets, it was possible to induce elastic instability during the retraction phase after impact, which led to rebound suppression. During the spreading phase of the droplet, the long polymer chains unwind due to shear at the spreading contact line, and similar observations have been reported in literature [45]. During the retraction phase, the polymer chains recoil, and the recoiling dynamics is governed by the relaxation timescale of the polymer molecules. If the concentration of the polymer in the solution is such that the relaxation timescale of the non-Newtonian fluid is smaller than the timescale of retraction of the contact line, then the retracting contact line is not subjected to the normal stress generated against the retraction. In such cases, the droplet rebounds as typical on SH surfaces. In the event the polymer concentration is above the threshold, such that the relaxation timescale is greater than the retraction timescale, the triple line retracts faster than the polymer chains, leading to a normal stress generation which decelerates the retraction velocity. In absence of high retraction velocity, the rebound is suppressed. We have also shown that for all such cases of rebound suppression, the associated Weissenberg number ($Wi = \lambda \dot{\gamma}$, where λ is the relaxation time of the fluid, and $\dot{\gamma}$ is the shear rate at onset of retraction) is always greater than one. This signifies that the event is triggered by elastic instability within the fluid [88]. As the impact We increases, the retraction shear rate increases, and the droplets show higher propensity of rebound arrest. Needless to say, there may be an upper bound to the Weber number beyond which the drops may fragment upon impact on the ground. The present experimental study is performed at Weber number well below this upper bound.

At this juncture, it is noteworthy that such elastic instability can only be triggered in case of very long chain polymer molecules. In the present study, we have used PEG-400, which is a very short chain polymer, and thus the droplets cannot exhibit rebound suppression (via the route of elastic instability) for the range of impact We explored. We further confirm this using theoretical analysis and control experiments on the polymer solutions and non-Newtonian ferrofluids in absence of field. In the previous report [13], we have noted that for all cases of rebound suppression, $Wi > 1$ is satisfied signifying the onset of elastic instability. Following the same methodology, we deduce the approximate shear rates at the termination of spreading regime and onset of retraction regime from image processing. To determine the relaxation timescales for the polymer solutions, we take the aid of oscillatory rheometry. We first determine the viscoelastic signatures of the polymer solutions and non-Newtonian ferrofluids, and obtain the elastic (G') and viscous (G'') moduli of the fluids as function of oscillatory frequency (ω). From the viscoelastic response, we obtain the approximate relaxation times for the different fluids based on established theories [101–103]. While employing the theoretical framework to deduce the relaxation timescales for the non-Newtonian ferrofluids, we have assumed that the nanoparticle-based polymer solutions also conform to a similar viscoelastic model as the polymer solutions.

Based on the shear rates and relaxation timescales, we determine the Wi and observe that all the values (for different impact We) are well below one. This signifies that the elastic instability is absent in the droplets of only polymer solution and the non-Newtonian ferrofluids in absence of field. We have already ruled out the role of increased viscosity under magnetic field as a possible governing agent. Further, we have also noted that there is no rebound suppression in absence of field. Thereby, all evidences lead to the inference that a conjugal effect between the elastic and the magnetic forces is occurring, which leads to the rebound suppression. Next, we apply the same methodology to the different cases of non-Newtonian ferrofluid droplets impacting under field effect. To determine the relaxation timescales under the effect of one particular field strength, we perform frequency sweep oscillatory magnetorheology experiments at different field strengths (fig. 3.7.) and employ the methodology reported previously [73, 88]. We determine the values of the Wi for different impact velocity and magnetic field strength cases (here we use magnetic field strength instead of Bo_m as the wide range of properties in presence of field does not allow for the use of a single specific Bo_m value). Although the Wi values are greater than the zero-field cases, it is noted that the values of the Wi even for the cases of field induced rebound suppression are below one.

As the We cannot provide a valid physical picture of the proposed magneto-elastic effect, we propose a modified form of the non-dimensional number to incorporate the effects of the magnetic field. Based on the experimental observations, we propose a new non-dimensional variable, which we term as the magnetic Weissenberg number, expressed as $Wi_m = Wi + Wi^{1/2} Bo_m^2$. Physically, the number is the ratio of the magneto-elastic

forces to the visco-capillary forces within the non-Newtonian fluid, and we believe will be an improved non-dimensional number which shall be able to incorporate the magnetic effects within the gamut of the We . The exponents for We and Bo_m in the expression for Wi_m are based on detailed experimental data, and we have selected them in a manner such that the onset of magneto-elastic effect induced rebound suppression happens at the value of 1. The values of Wi_m for P10-F2.5 droplets for different impact velocity and different magnetic field strength have been illustrated in fig. 3.9a. We observe that the magnetic Weissenberg number criterion is able to segregate the regimes of rebound and rebound suppression ($Wi_m > 1$), with respect to both the impact velocity and applied magnetic field strength. The behaviour of the Wi_m with respect to the magnetic field strength for different non-Newtonian ferrofluid droplets impacting the SH surface at 1.5 m/s has been illustrated in fig. 3.13b. It can be seen that the proposed Wi_m is able to predict the paradigm of rebound suppression for different non-Newtonian ferrofluids. From the innate definition of the Wi_m and the fact that we can consistently predict rebound suppression at $Wi_m > 1$, our hypothesis on the presence of magneto-elastic effect in non-Newtonian ferrofluid impact dynamics is further cemented. Physically, fig. 3.13 highlights that for a given magnetic field strength, both polymer concentration and high impact velocity are essential to trigger the magnetic elastic effects to be dominant enough to cause rebound suppression. It must be noted that addition of polymers trigger the onset of instability at much lower Bo_m in comparison to the Newtonian counterpart (see fig.3.10) Hence, for a low polymer concentration fluid, at a given Bo_m , higher Weber number (higher impact velocity) is required to reach the critical shear rate required for non-Newtonian effects to be dominant in slowing down the retraction velocity. On the other hand, for the same Bo_m , for a high concentration polymer droplet, comparatively lower impact velocity (lower Weber number) is required to trigger the magneto-elastic effects.

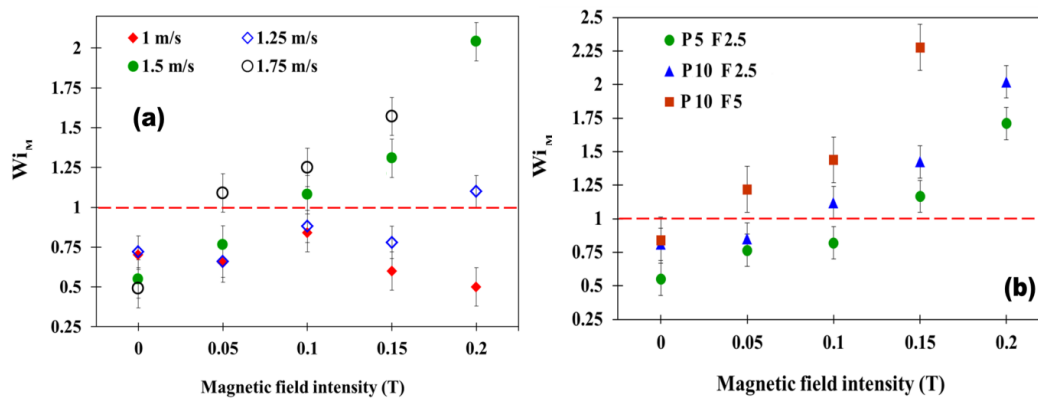


Figure 3.13: Plot of the magnetic Weissenberg number (Wi_m) against the magnetic field intensity, for (a) P10-F2.5 droplets impacting at different velocities, and (b) for different non-Newtonian ferrofluid droplets impacting at velocity of 1.5 m/s. The horizontal dashed line indicated $Wi_m = 1$. All points lying in the regime above this line exhibit rebound suppression triggered by the magneto-elastic effect

3.3.3 Droplet ferrohydrodynamics regimes

In this section, we elucidate various impact ferrohydrodynamic regimes of non-Newtonian ferrofluid droplets in presence of external uniform horizontal magnetic field. As evident from fig. 3.17, although the regime maps of the various drop impact outcomes for the three different test fluids (P5-F2.5, P10-F2.5 and P10-F5) are seemingly different from each other, we have tried to highlight the common features in the discussion of the five regimes represented in figure 3.17. The regime maps for Wi vs Bo_m and magnetic capillary number (Ca_m) vs Hartmann number (Ha) for different ferrofluids have been illustrated in fig. 3.17. In this study, the effect of We , Bo_m , and magnetic particle concentration was not sufficient to emphasize the impact hydrodynamic outcomes like breakup during retraction and rebound inhibition. The physical insight on the effect of relative dominance of magnetic force to viscous force and relative dominance of viscous force to surface tension force is also needed to explain the rebound suppression phenomenon of non-Newtonian ferrofluid droplet. Hence we have additionally introduced the Ca_m and Ha to predict the capillary driven hydrodynamic outcomes such as, breakup during retraction (receding breakup) and rebound suppression (at phase map section).

We discuss the various regimes in the phase map as follows:

Regime-0 (non-experimental regime): In this regime, the needle and droplet assembly lies within the direct influence of magnetic poles. The growing droplet is pulled away from the needle by the magnetic field and distorted largely before the impact, which does not lead to physically consistent observations. Thereby, experiments have not been done in this regime. For all the test fluids, this regime was observed for low We and low Ca , irrespective of Bo_m and Ha .

Regime-I (rebound with pinch-off): In this regime, the droplet rebounds with pinch-off (releasing a tiny droplet from the rebounding parent droplet). This rebound with pinch-off behavior exists due to the dominance of the inertial and capillary forces compared to the magnetic force. Accordingly, this regime is noted to occur at low Bo_m where the magnetic forces are weak, and at low to moderate We such that the impact process does not lead to shattering of the droplet due to high inertia.

Regime-II (complete rebound): Complete rebound takes place in this regime, due to the dominance of recoiling kinetic energy of the droplet over viscous dissipation during spreading and the magnetic body force. But in this regime, the capillary force is overshadowed by the rebound inertia, and pinch-off is absent. We presume that at relatively higher We , non-Newtonian effects are sufficiently strong to suppress the capillary instability induced pinch-off. Consequently, the regime appears in close conjunction with R-I, but extends to relatively higher We . If we club the regimes I and II as just rebound effect, it is evident that these two regimes are occurring in the bottom left corner above regime 0 of the regime maps i.e. for low We and low Ca . Low impact height is a prerequisite

for the rebound event of non-Newtonian ferrofluid droplets.

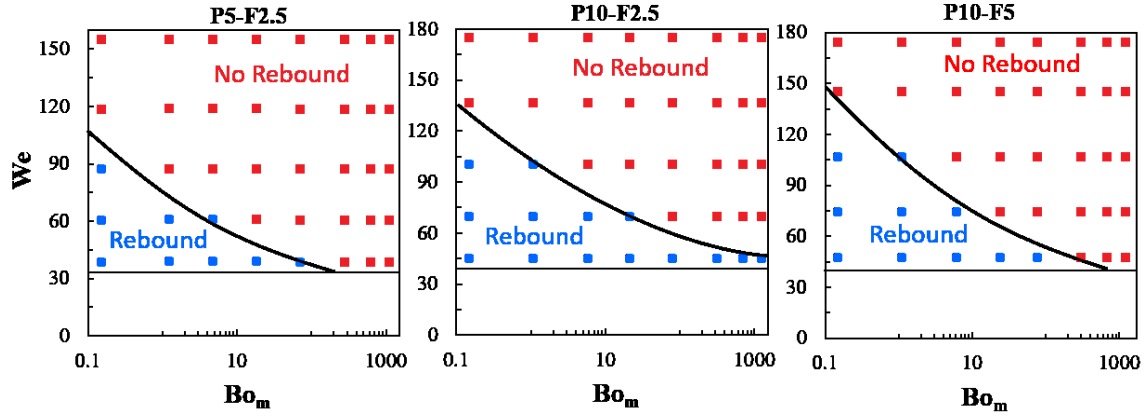


Figure 3.14: Demarcation of “rebound (combined RI and RII)” and “no rebound” cases of impacting non-Newtonian ferrofluid droplets in external magnetic field by changing both polymer concentration and magnetic nanoparticle concentration.

We have tried to establish the scaling relationship of the rebound regime (RI and R II combined) from the non-rebound regime in the form of $We \sim aBo_m^{-b}$, where a is the prefactor and b is the power law exponent (refer fig. 3.14. and 3.15. for the detailed fitting analysis). The power law exponents are approximately -0.123, -0.125 and -0.143 for the P5-F2.5, P10-F2.5 and P10-F5 respectively.

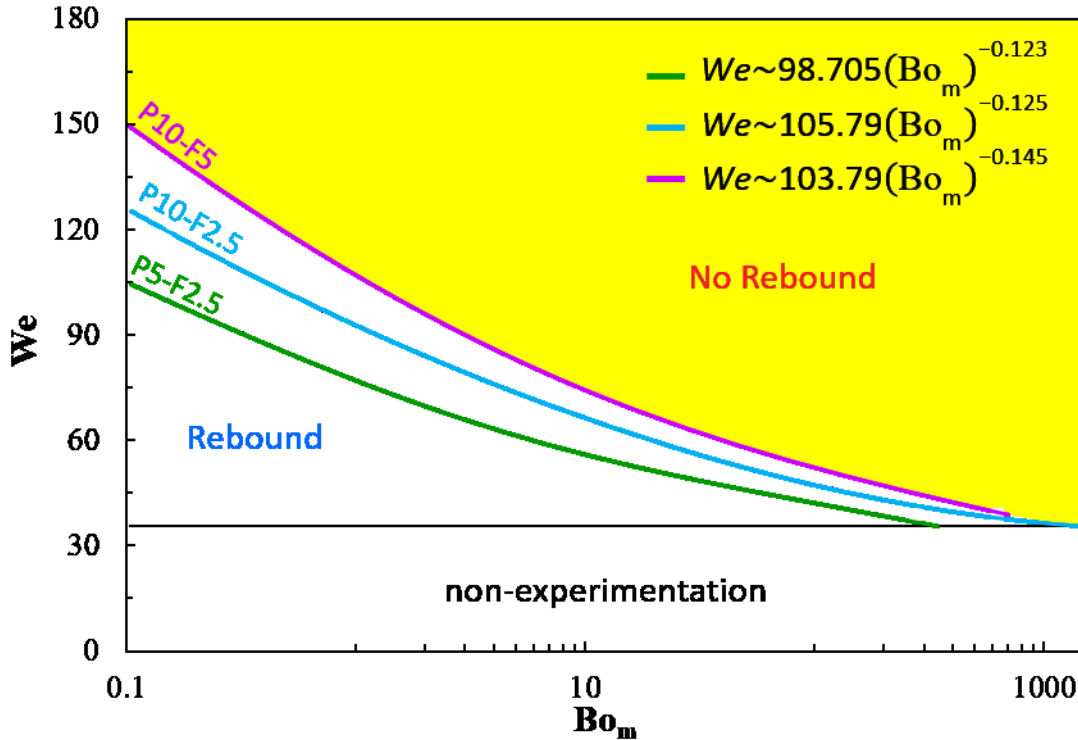


Figure 3.15: Scaling relationship between critical We and Bo_m to demarcate the “rebound” and “no rebound” behaviours of impacting non-Newtonian ferrofluid droplet for different concentrations of both polymer and magnetic nano particles.

Regime-III (breakup during retraction): The droplet breaks up during the

retraction stage in this regime [104]. In this regime, the droplet spreads to its maximum spread state, and forms radial filaments, which do not detach immediately as the capillary forces are dominated by the viscoelasticity of the fluid. The formation of the secondary droplets attached to the rim by thin filaments are referred as prompt splash [105]. At the maximum spread state, the magnetic force on the bulbs at the ends of the filaments is high at even moderate Bo_m . During the retraction stage, the recoil inertia is overcome by the magnetic force, and the bulbs detach off the retracting parent droplet to form smaller droplets. This regime occurs at higher We and moderate Bo_m as higher inertia ensures maximum spread state, and the moderate Bo_m ensures the detachment of the filamentous droplets at retraction. For P5-F2.5 and P10-F2.5, this regime is observed starting from the top left corner (high We , low Bo_m) extending upto the bottom right corner (low We and high Bo_m). However for P10-F5, this regime is only limited to the top corner due to the occurrence of rebound suppression (regime V) for a broader range of We and Bo_m .

Regime-IV (fragmentation): Fragmentation of the droplet into smaller secondary droplets occurs in this regime. This occurs at either high We or high Bo_m . At high We , the impact inertia is high enough to induce fragmentation of the droplet during the spreading state, caused by formation of large velocity gradients within the spreading droplet, which overcomes the capillary and viscous forces. At high Bo_m , the magnetic force on the spreading droplet is high enough to induce ferrohydrodynamic instability [86], which leads to rupturing of the spreading droplet as the magnetic forces overcome the capillary forces.

Regime-V (rebound suppression): In this regime, suppression of droplet rebound takes place due to the magneto-elastic instability, already explained in the preceding section. The requirements of the magneto-elastic instability to occur i.e. $Wi_m = (Wi + Wi_m^{1/2} Bo_m^2) > 1$, is ensured when the combined effect of We and Bo_m is sufficient to trigger the instability. This occurs at the junctions of R-III and R-IV, where the We is moderate enough to induce the elastic instability during the retraction process, and the Bo_m is moderate enough to induce the optimum ferrohydrodynamic force on the droplet. For the P5-F2.5 and P10-F2.5, the regime is sandwiched between regime III and IV. For the same particle concentrations (F2.5), the higher polymer concentration fluid P10-F2.5 has broader area of regime V than P5-F2.5. As evident from the fig.3.10 bottom row, the extent of the regime increases in size to a much greater extent in case of P10-F5, i.e. with increase in the elasticity of the fluid (polymer concentration) and magnetic moment of the droplet (magnetic particle concentration).

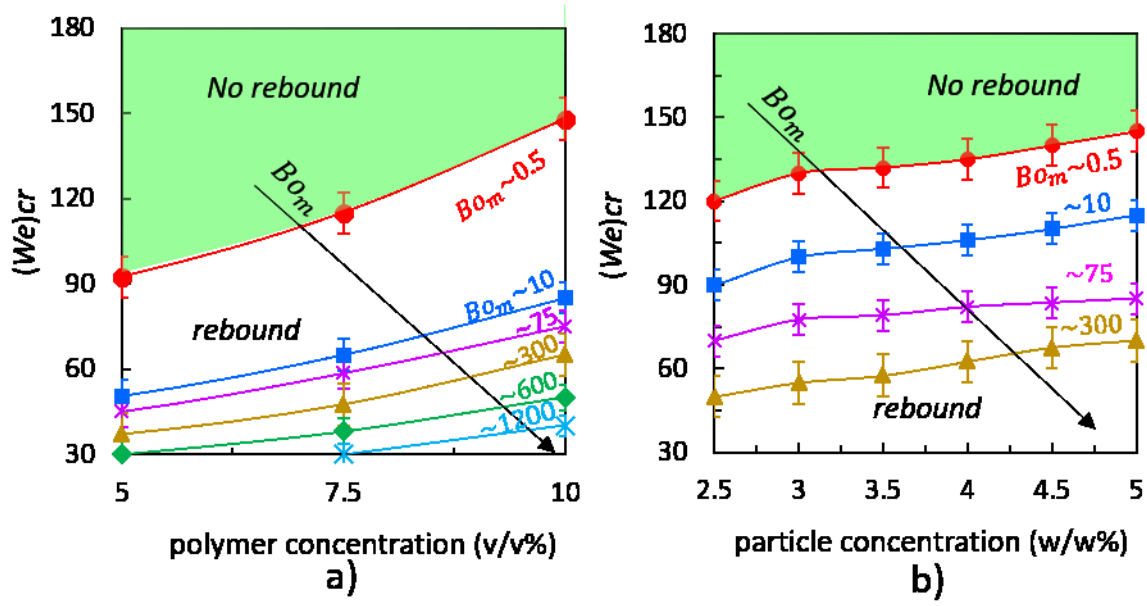


Figure 3.16: (a) and (b) shows the critical We (across which We ferrofluid droplet “rebound” behaviour turns into “no rebound” and vice versa) over different polymer concentrations and magnetic nanoparticles concentrations respectively.

In previous studies of drop impact on hydrophobic surfaces in absence of magnetic field [99, 100], it was observed that the impact outcomes varies from deposition (no rebound), partial rebound, complete rebound and finally fragmentation with the increasing We . Since our experimental study is incorporating the features of non-Newtonian effects and magnetic field, the impact outcomes are strikingly different with the increase of We . In our case, at the lowest We , rebound is observed and at higher We drop rebound is suppressed. In addition, with increase of Bo_m , even at the lower range of We rebound suppression was observed especially in case of P10-F5 (fig. 3.10 bottom row, left column). For a detailed regime map showing the role of We and Bo_m , and the segregation of the regimes based on the impact behavior and magnetic field constraints, refer fig. 3.16.

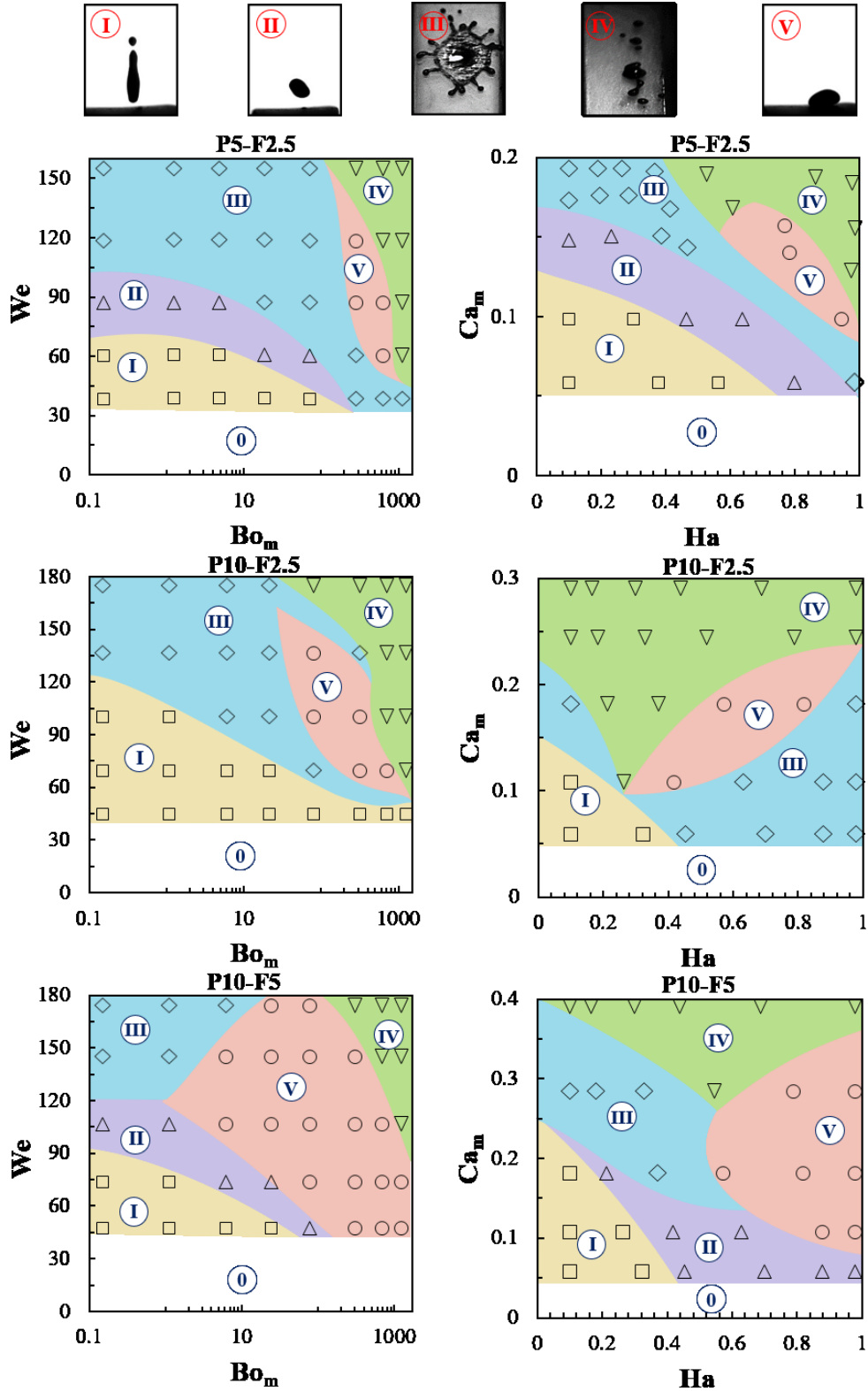


Figure 3.17: Phase maps indicating the different impact ferrohydrodynamic outcomes of non-Newtonian ferrofluid droplets in magnetic field ambience. The regimes 0, I, II, III, IV and V represent “non-experimental regime”, “rebound with pinch-off”, “complete rebound”, “breakup during retraction”, “fragmentation” (with orthogonal elongation) and “rebound suppression”, respectively.

3.4 Conclusions

In this study, we report an extensive experimental investigation on the impact ferrohydrodynamics of non-Newtonian ferrofluid droplets on a SH surface in the presence of a horizontal uniform magnetic field. We used stable colloidal solutions of magnetic nanoparticles dispersed in polymeric solutions as the non-Newtonian ferrofluids. The studies encompass a range of impact We up to ~ 180 and $Bo_m \sim 0$ to 1500. We noted that in the presence of magnetic field, the non-dimensional maximum spreading (ξ_{max}) increases compared to the Newtonian ferrofluids with increasing both polymer and magnetic particles concentration. Through experimental investigations, we have studied the effects of polymer concentration, magnetic nanoparticles concentration, Weber number and Bo_m on the impact dynamics of non-Newtonian ferrofluid droplet. Addition of polymers to the base Newtonian ferrofluid caused rebound suppression at lower Bo_m for fixed magnetic particle concentration and We . Similarly for fixed polymer concentration and We , increase of magnetic particle concentration triggered rebound suppression at lower Bo_m .

The combined effect of magnetic particles and elastic effects of polymer chains, together clubbed as magneto-elastic effect, similar to the coinage of elasto-inertial effect of earlier studies [88],[106] is shown to be responsible for the early onset of rebound suppression. We formed a non-dimensional number termed as magnetic Weissenberg number, Wi_m taking into account of the effect of classical Weissenberg number and the magnetic Bond number. Through the scaling analysis we showed that when $Wi_m \geq 1$ magneto-elastic instability is triggered and droplet rebound suppression is observed for the first time. This is analogous to the situations when purely elastic instability sets in [107, 108] or onset of drag reduction [109] for $Wi \geq 1$. Finally, ferrohydrodynamics of non-Newtonian ferrofluid droplet behavior regime phase maps over a wide range of corresponding dimensionless numbers such as We , Bo_m , Ca_m and Ha were presented. The present findings may have significant implications towards design and development of micro or macroscale systems and devices involving magnetic liquid droplets.

Chapter 4

Triggering of electro-elastic anti-superhydrophobicity during non-Newtonian droplets collision

4.1 Introduction

4.2 Introduction

The impact hydrodynamics of liquid droplets, Newtonian fluids or otherwise, on different surfaces in the presence of external electric or magnetic fields [11] has great importance in many applications, such as inkjet printing [17], ferrohydrodynamic 3D inkjet printing [110], magnetic drug targeting in microfluidic applications [22], spray painting, spray cooling [19], controlling the liquid metal droplet deposition during welding or soldering [111], electrohydrodynamic droplet-on-demand (DOD) inkjet printing [23], electro spraying [112, 113] electrowetting [23] electrohydrodynamic jet (E-jet)[114] printing and so forth.

Several theoretical and experimental works have reported the electrohydrodynamics of dielectric droplets under electric field in electrowetting and microfluidic applications. For instance, Nelson et al. [115] reviewed droplet actuation by electrowetting on dielectric (EWOD). They summarized the responsible forces which act on liquid droplets and their response in EWOD microfluidic devices. Torabinia et al. [24] proposed a new electromechanical model to predict the actuation of liquids in EWOD devices, and energy dissipation by contact line friction is treated in the form of a resistor, which explains contact angle hysteresis, line tension, etc. during EWOD. Wagoner et al. [116] theoretically studied the electrohydrodynamics of lenticular drops and equatorial streaming. They showed that a lenticular drop's equatorial profile can be a wedge due to normal current condition within the droplet. Mousavi et al. [117] numerically studied the dynamics of droplet detachment from hydrophilic and hydrophobic surfaces under electric field through used Lattice Boltzmann Method (LBM). Their findings highlighted the influence of several factors, including the Eotvos number (Eo), capillary number (Ca), Ohnesorge number (Oh) and the dielectric constant on the deformation of droplets (oblate/prolate) with varying degrees of wettabilities.

Pollack et al. [118] experimentally studied the actuation of microdroplets of aqueous electrolytes for integrated microfluidics based on electrowetting. They revealed that dependence of velocity on voltage is independent on droplet size and reported that using average velocities results in faster and more efficient droplet transport. Zeng et al. [119] investigated electrical controlled droplet based labs on chip device, working on the principles of electro-capillarity and dielectrophoresis. They conducted a study on the effects of electrowetting on dielectrics and electrophoresis on droplet generation and manipulation. Their findings revealed that dielectrophoresis resulted in a reduction of contact angles and wetting contribution. Park et al. [120] described the electro-hydrodynamically induced fluid flow through fine micro-nozzles for jet pattern printing with sub-micron resolution. They demonstrated the superiority of e-jet printing over traditional inkjet printing by achieving high levels of printing resolution. They suggested that reducing the nozzle dimensions further would allow for printing at even smaller scales, down to the nanoscale. Deng et al. [55] revealed the role of electric charge in microdroplets impacting on conducting surfaces, and reported sessile droplets with reduced contact angle and increased evaporation rates. Das et al. [121] numerically investigated the electrohydrodynamic interactions of a pair of leaky dielectric droplets in a uniform electric field, and discussed the stability of such compound droplets. They revealed that pair of droplets may coalesce or repel each other in presence of electric field. Additionally, they found that the stability of a compound droplet and the relative motion between a pair of droplets depend primarily on the charge relaxation time constant of both the ambient medium and the outer shell of the compound droplet.

Besides, many researchers have experimentally elucidated the impact or dynamic electrohydrodynamics of dielectric droplets. Sahoo et al. [122] experimentally investigated the impact electrohydrodynamics of dielectric liquid droplets on both hydrophilic and SH surfaces. They reported the influence of the electric Capillary number on the onset of droplet rebound suppression. Yun et al. [56] investigated and described the mechanism of droplet rebound suppression by inducing non-axisymmetric drop deformation and kinetic energy transfer between orthogonal coordinate axes. Tan et al. [123] revealed the control over drop impact on hydrophobic surfaces based on alternating current electrowetting-on-dielectric (AC EWOD). They studied the impact control mechanism of AC signal on droplets by analyzing changes in spread diameter and height under varying frequencies and amplitudes. They found that applying AC electrowetting on dielectric resulted in diameter oscillations during the retraction stage, which neutralized the kinetic energy and inhibited rebound.

Wang et al. [124] experimentally focused on the electrohydrodynamic atomization (EHDA) in a stable cone jet with a middle viscous liquid with low conductivity. They

reported that jet breakup with multi-jet, varicose, and kink instabilities are noted with an increased fluid flow rate. Sung et al. [58] experimentally investigated the maximum spreading of electrically charged droplets on dielectric substrates. They proposed a model to predict the maximum spreading ratio for electrically charged droplets using liquid-gas and liquid-solid interfacial tensions. Mahmoudi et al. [59] experimentally revealed the effect of interfacial electric pressure on the spreading of a dielectric droplet, and predicted the dynamics of film spreading owing to corona discharge through a simplified model. Yurkiv et al. [60] numerically simulated and modelled the drop impact on both polar and non-polar surfaces during EWOD.

Although earlier studies have focused on the influence of electric field on drop impact dynamics, the same for non-Newtonian droplets remain sparsely explored. Non-Newtonian droplets, especially elastic fluid or Boger fluids, have been shown known to arrest the droplet rebound on SH surfaces [125]. This has excellent potential towards the reduction of pesticide wastage and soil contamination during crop spraying. Various mechanisms, such as extensional viscosity [45], normal stress [126], and stretching of polymer chains near the receding contact line [127] were attributed to the slowdown of retraction dynamics and subsequent drop rebound suppression. Further studies [88] showed that polymer concentrations and impact velocity are critical parameters to trigger the regime of rebound suppression. Based on the shear rate near the contact line during the onset of retraction, they showed that the local Weissenberg number (Wi) exceeding 1 is an essential requirement for the elastic effects to dominate and lead to arrested rebound.

Recently, Gudlavalleti et al. [11] studied the effect of magnetic field on post impact non-Newtonian ferrofluid droplets of SH surfaces, and showed that droplet rebound suppression occurs earlier when in presence of a magnetic field. With increasing magnetic particle concentration, the rebound suppression starts at lower magnetic Bond numbers ($Bo_m = B^2 D_0 / \mu_o \sigma_{lv}$), defined as the ratio of magnetic force to surface tension force. Here, B , D_0 , μ_0 and σ_{lv} denote magnetic flux density, pre-impact droplet diameter, magnetic permeability of free space, and surface tension respectively.). The combined influence of non-Newtonian effects and magnetic field are together termed as magneto-elastic effect. Similar to the classical Weissenberg number ($Wi = \lambda \dot{\gamma}$; λ : is the relaxation time and $\dot{\gamma}$: shear rate, defined as the ratio of elastic forces to viscous forces), a magnetic Weissenberg number $Wi_m = Wi + Wi_m^{1/2} Bo_m^2$, defined in such that the ratio of magneto-elastic forces to visco-capillary forces) 1 was proposed as a threshold parameter to quantify the onset of droplet rebound suppression.

In the present article, we explore the combined effect of non-Newtonian effects and electric field on the droplet collision phenomena with SH surfaces. We have examined each aspect of impact dynamics of non-Newtonian dielectric fluid droplets, such as the role of impact spreading dynamics over external electric Eotvos numbers (Eo_e) ranging from 0-12.

Next, we have highlighted the role of fluid elasticity (polymer concentration), dielectric constant (nanoparticles concentration), and Weber number (We) on droplet rebound and its suppression kinetics, if any. We have formulated a modified form of the classical Weissenberg number, termed as electric Weissenberg number (Wi_e) to incorporate the influence of non-Newtonian effects and electric field as a threshold parameter to quantify the triggering of droplet rebound suppression on SH surfaces. Finally, we segregated both rebound and rebound suppression regimes as a function of polymer concentration, dielectric nanoparticle concentration, and We through a detailed regime map.

4.3 Materials and methods

4.3.1 Non-Newtonian dielectric fluids

The non-Newtonian dielectric fluids considered in this study were colloidal solutions of Titanium dioxide (TiO_2) nanoparticles dispersed in a non-Newtonian base fluid, composed of different polymer (PEG-400) concentrations in deionized (DI) water. First, different (%v/v) compositions of polyethylene glycol (PEG-400, Sigma Aldrich, India) were added to DI water and homogenized by stirring. Next, different (%w/w) compositions of Titanium dioxide (TiO_2) (Alfa Aesar, India, > 98.5% purity) nanoparticles were dispersed into the polymer solutions. Next, the colloidal polymeric solutions were subjected to mechanical stirring followed by ultrasonication for 2 hrs to ensure colloidal stability. Similar to an earlier study [9], the pendant drop method was used to measure the surface tension of the non-Newtonian dielectric fluid droplets. The physical properties of the different test fluids have been tabulated in Table. 4.1. We have adopted a nomenclature to distinguish the fluid samples: a non-Newtonian dielectric fluid containing “x” % (%v/v) polymer with “y” % (%w/w) TiO_2 nanoparticles dispersion is denoted as Px-Ty. For example, the sample P20-T10 contains 20 %v/v polymer in DI water, and with 10 %w/w of TiO_2 nanoparticles dispersed in it. The family of Newtonian dielectric fluid is denoted with P0-Ty. To ascertain the stability of the colloidal dispersions, we followed the protocols outlined in previous references (94 and 183) for the preparation of colloidal solutions. Additionally, We performed a zeta-potential measurement using Zetasizer NanoZSP and observed a zeta-potential value of +34.9 mV at the highest particle concentration (refer fig.4.1.). This measurement confirmed the stability of the colloidal solutions.

Table 4.1: Physical properties of impacting non-Newtonian dielectric fluid droplets: pre-impact droplet diameter D_o (mm), density ρ (kg/m^3), surface tension σ (mN/m)

| Base fluid (PEG-400 concentration) (%v/v) | (TiO_2 nanoparticles) (%w/w) | ρ | σ | D_o |
|-------------------------------------------------|------------------------------------|------------|-----------|-----------|
| 0 | 0-10 | 997-1320.2 | 71-68.4 | 2.72-2.75 |
| 5 | 0-10 | 1003-1326 | 70.6-68.2 | 2.72-2.75 |
| 10 | 0-10 | 1009-1331 | 70.4-68.1 | 2.73-2.75 |
| 20 | 0-10 | 1018-1339 | 70.2-68.2 | 2.73-2.75 |

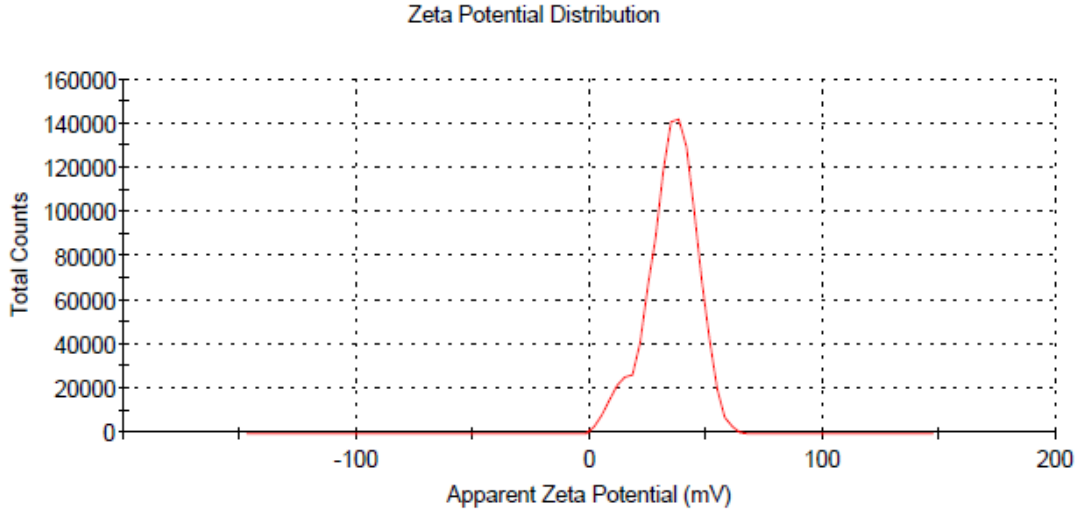


Figure 4.1: Zeta Potential distribution of the highest concentration(10% w/w -T10) of the operating range of the dielectric fluids used.

4.3.2 Superhydrophobic surfaces

The SH surfaces were fabricated by commercial spray (Neverwet Ultra Ever dry, USA) by following reported protocol [14, 86]. For the surface preparation, all glass slides were thoroughly cleaned with DI water and acetone and oven-dried carefully. Next, SH spray was used to create a uniform coated layer over the glass slides. We used a contact angle goniometer (Holmarc, India) to measure the static equilibrium contact angle, the advancing and receding contact angles of different dielectric fluids on these SH surfaces. Subsequently, we calculated the contact angle hysteresis (CAH) by following reported protocol [17]. The static equilibrium contact angles of water droplets and non-Newtonian dielectric fluid droplets on the spray-coated SH surfaces were measured to be $156 \pm 3^\circ$ and $153 \pm 2^\circ$ respectively. From four individual measurements, the average CAH was estimated to be $\sim 4^\circ$ - 6° .

4.3.3 Experimental setup

The experimental setup is similar to our earlier study on droplet impact [122]. Fig. 4.2. illustrates the schematic of the experimental setup, in which two aluminium strips ($50 \text{ mm} \times 20 \text{ mm} \times 2 \text{ mm}$) with attached wires were used as electrodes to generate a direct electric field of up to a maximum of 8 kV. Throughout this study, electrode gap of 15mm was maintained. A regulated, high voltage DC power supply unit (Ionics, India) is used to generate the high voltage between the two electrodes. A high-speed camera (Photron, UK) with a 105 mm macro lens (Nikon) was used to capture the images. All images were recorded at 4000 fps and at 1024×1024 resolution. An LED array was used for backlight illumination. To alter impact We , a digitized droplet dispenser unit (Holmarc, India) equipped with a chromatographic syringe with a 22-gauge needle (U-TEK, India) was used to release the droplets from different heights. The droplets were allowed to impact

on the SH surfaces such that it is equidistant from the two electrodes to ensure the impact was within a uniform electric field. All experiments were conducted at room temperature $\sim 25^\circ\text{C}$.

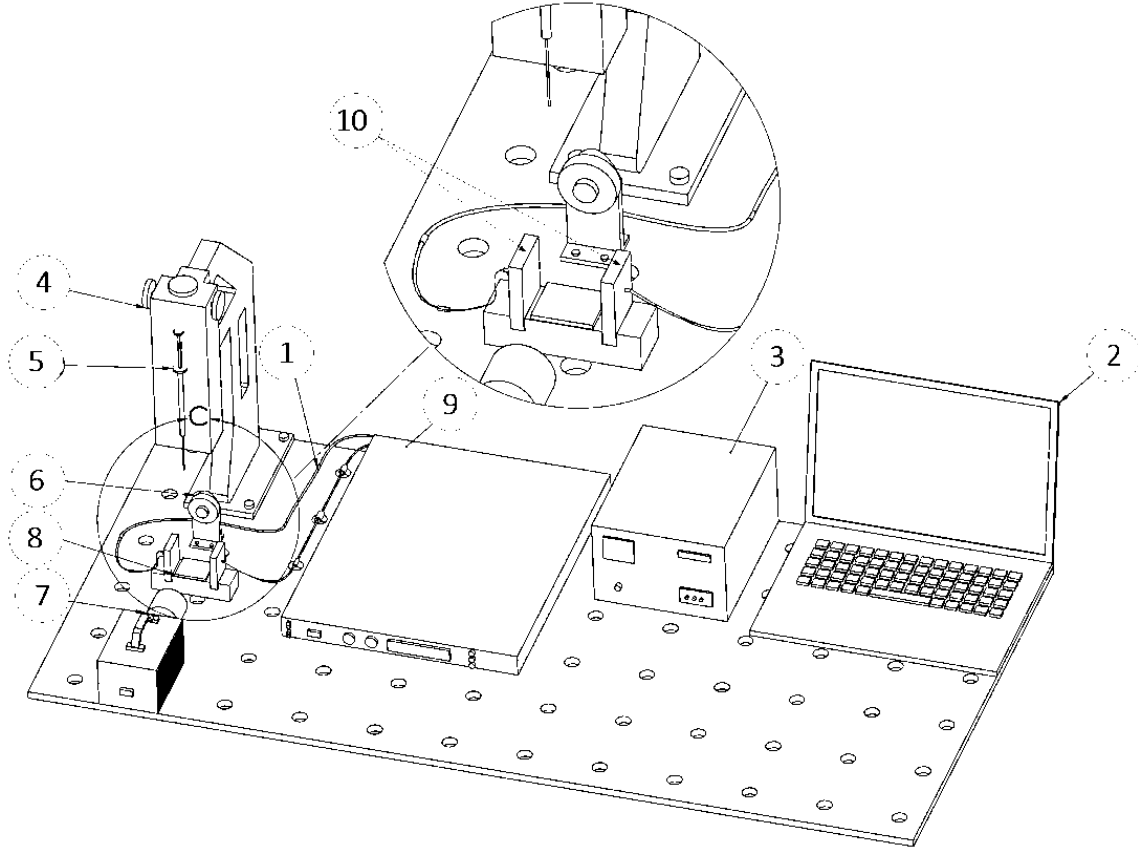


Figure 4.2: Schematic of the experimental setup: (1) electrical wires (2) computer for data acquisition and camera control (3) DDM and backlight illumination controller (4) Droplet dispensing mechanism (DDM) unit (5) Microliter syringe (6) LED array (7) high speed camera (8) SH substrate (9) high voltage DC power supply unit (10) electrode assembly.

4.3.4 Governing non-Dimensional numbers

The drop impact dynamics has been quantified using non-dimensional numbers. The maximum non-dimensional elliptical diameter (ξ_{max}) is defined as the ratio of major axis diameter (D_{major}) to minor axis diameter (D_{minor}) of elliptically spreading non-Newtonian dielectric fluid droplets.

Table 4.2: Non-Dimensional numbers of impacting non-Newtonian dielectric fluid droplets

| Dimensionless parameter | Expression | Range |
|---------------------------------------------|----------------------------------------------------|-------------|
| maximum non-dimensional elliptical diameter | $\xi_{max} = D_{major} / D_{minor}$ | 0.98 - 1.24 |
| Weber number (We) | $(We = \rho U^2 D_0 / \sigma_{drop})$ | 85 - 165 |
| electric Eotvos number (Eo_e) | $Eo_e = \epsilon_o \epsilon_r E^2 / \sigma_{drop}$ | 0 - 12 |

Weber number ($We = \rho U^2 D_0 / \sigma_{drop}$) quantifies the ratio of inertia force to surface tension force and electric Eotvos number ($Eo_e = \epsilon_o \epsilon_r E^2 / \sigma_{drop}$) quantifies the ratio of electric

force to surface tension force, where D_{major} , D_{minor} , ξ_{max} , ρ , U , D_o , ϵ_o , ϵ_r , E and σ_{drop} are the major axis diameter of elliptically spreading liquid lamella (considered only the liquid portion lies within the liquid rim) of the droplet, the minor axis of elliptically spreading liquid lamella, maximum non-dimensional elliptical diameter, density, impact velocity, pre-impact droplet diameter, the electrical permittivity of free space/vacuum ($\epsilon_o = 8.854 \times 10^{-12} F/m$), the relative electrical permittivity of test fluids, electric field strength (V/m) and surface tension of the fluids, respectively. The ranges of the non-dimensional numbers examined in this study are tabulated in table. 4.2.

4.3.5 Electrorheology of the experimental fluids

Electrorheological (ER) characteristics of the various test fluids were performed to estimate the effective relaxation timescales of the fluid system. Akin to reports [128–133], all ER measurements were conducted using a rotational rheometer (Anton Paar, MCR-102). The rheometer was fit with an ER unit and operated in parallel plate mode. The temperature of the sample was controlled by an inbuilt Peltier unit and maintained at 25°C. Firstly, we performed the shear dependent flow curve rheology tests of the test fluids for various electric field strengths, ranging from 0 – 0.5333 kV/mm. We observed that the degree of shear thinning increased with increase in both polymer and nanoparticle concentrations in absence of field (see figure 4.2. and 4.3. for flow curve behaviour of test fluids).

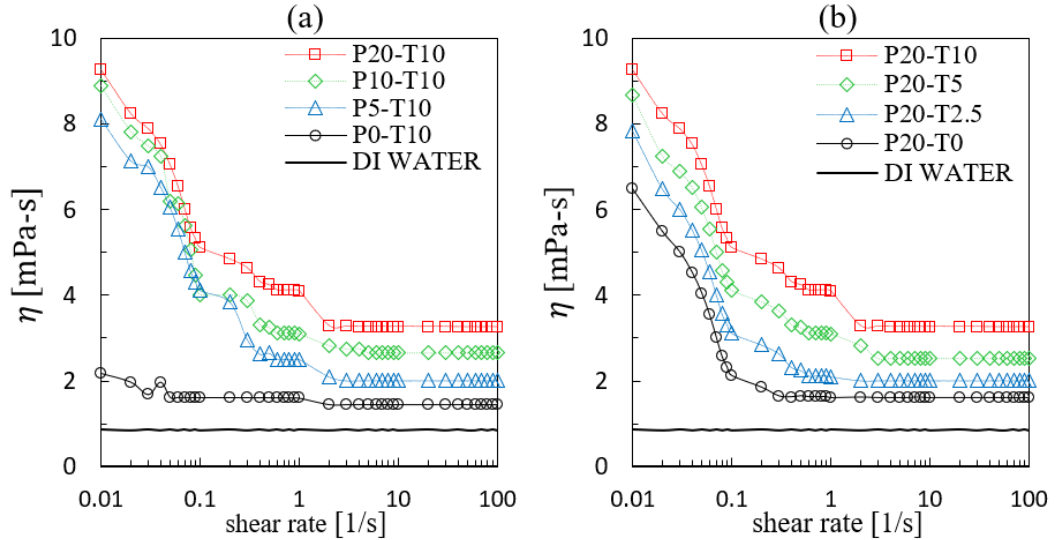


Figure 4.3: Shear viscosity of non-Newtonian dielectric fluid droplet with the variation of (a) polymer concentration and (b) dielectric particle concentration in the absence of an external electric field.

The variation of shear viscosity of non-Newtonian dielectric fluids with the variation of shear rate has been illustrated in figure 4.2. From fig. 4.3., it is evident that all concentrations of both polymer and dielectric particles of non-Newtonian dielectric fluid droplets display shear thinning behavior up to shear rate $\sim 1/\text{sec}$ in the absence of an external electric field. The degree of shear-thinning increased with an increase in particle concentration for a fixed nanoparticle concentration T10 (fig. 4.4.a). For a fixed polymer concentration of P20, the degree of shear-thinning increased with the nanoparticle concentration (fig. 4.4.b). Fluids devoid of polymer displayed Newtonian behavior for all concentrations of dielectric particle concentrations.

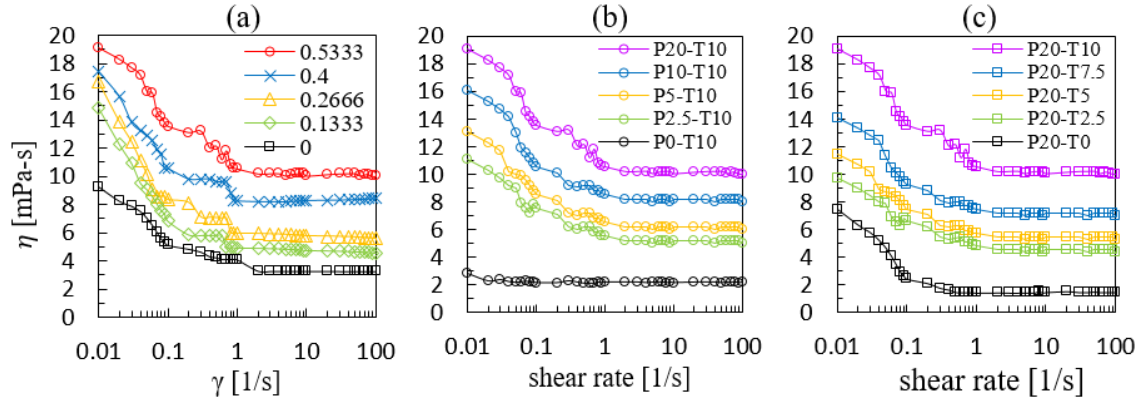


Figure 4.4: Shear viscosity of non-Newtonian dielectric fluid droplet in the presence of external DC electric field: (a) P20-T10 with the variation of DC electric field ranging from 0kV/mm to 0.5333kV/mm and in fig.4.4. (a), legend values are in kV/mm (b) effect of polymer concentration on shear viscosity against electric field strength 0.5333kV/mm and (c) effect of dielectric particle concentration with same polymer concentration on shear viscosity against electric field strength 0.5333kV/mm.

Subsequently, we investigated the impact of electric field strength ranging from 0-8kV/mm on the rheological properties of the non-Newtonian dielectric fluids. Similar to figure 4.2., figure 4.3. also shows that the shear-thinning regime is limited within the shear rate $\sim 1/\text{sec}$. However, for a fixed fluid P20-T10, both the transient (up to $\sim 1/\text{sec}$) and steady shear viscosity values ($1/\text{sec}$), it is also clear that all with an increment of electric field intensity. It is also evident that the shear-thinning behavior increases with increasing electric field intensity. A comparison of fig. 4.3.a and 4.4.a clearly show that both the transient and steady-state shear values got amplified in the presence of an electric field. For example, the P20-T10 fluid highest transient and steady-state shear viscosity values were ~ 9 and ~ 3 mPa-s respectively (fig. 4.3.a). Under the influence of electric field intensity, the same fluid 0.5333kV/mm showed the highest transient and steady-state shear values at ~ 19 and ~ 10 mPa-s respectively. The trends of shear-thinning with the change in polymer concentration for fixed dielectric particle concentration (fig. 4.4.b) or the change in particle concentration for fixed polymer concentration (fig. 4.4.c) were similar to the trends observed in fig. 4.3.

Next, oscillatory shear ER (frequency sweep, constant amplitude of 1%) is performed. Based on a single mode of Maxwell fit (refer figure 4.4.c.), the single relaxation time (τ_R) is estimated from the storage modulus G' (figure. 4.4.) and viscous modulus G'' (the figure. 4.4.) by using the following relations: $G'(\omega) = (G_0 \omega^2 \tau_R^2) / (1 + \omega^2 \tau_R^2)$ $G''(\omega) = G_0 \omega \tau_R / (1 + \omega^2 \tau_R^2)$. Based on reported studies [134–137], the plateau modulus was estimated from the fixed value of G' at a higher operating angular frequency (ω), and relaxation time estimated from the following relation, $\tau_R = 1/\omega_c$, where, ω_c is the cross-over frequency as shown in the figure. 4.4.c. The relaxation time scales of the test fluids are tabulated in tables 5.3-5.5. From table 4.3. it was observed that the relaxation time increases individually with increase in electric field strength, polymer concentration, and dielectric particle concentration provided the other two parameters were constant. As earlier reported [138, 139], many researchers have revealed that in presence of electric field, TiO_2 nanoparticles behave like dipoles due to the polarization and form an anisotropic thin chain-like structure along the streamlines of the electric field. When a shear (during the spreading and retraction phases of the droplet) is applied, it destroys the chain structure [140] and consequently may affect the elastic nature of the polymer chains due to the increment in the relaxation time of the polymer chains over an external field.

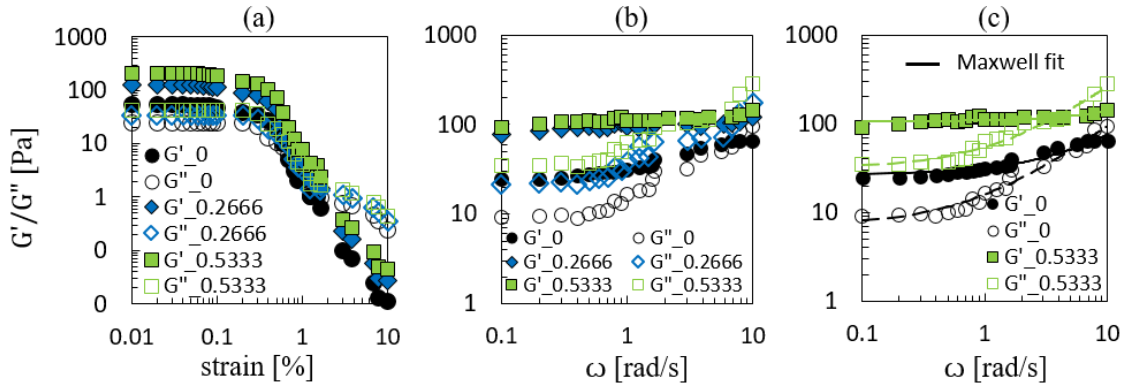


Figure 4.5: Small amplitude oscillatory shear (SAOS) electrorheological characterization over different electrical field strengths ranging from 0kV/mm to 0.5333kV/mm: (a) strain sweep of P20-T10 at a fixed angular frequency 1rad/s and (b) frequency sweep of P20-T10 at constant strain (c) Maxwell single-mode fit. In fig.4.5.a-c, all legend values are in kV/mm.

Apart from the flow curve test, to characterize the linear viscoelastic behavior of the non-Newtonian dielectric fluids, we conducted the small amplitude oscillatory shear (SAOS) rheology via relaxation time scales of different concentrations of non-Newtonian dielectric fluids. For that, we performed strain and frequency sweep over different external electric field strengths ranging from 0kV/mm to 0.5333kV/mm. The dynamic oscillatory shear electrorheology of non-Newtonian dielectric fluids exhibits the characteristics like Maxwell fluid at low shear frequencies (0.1-10rad/s). The relaxation time scales of non-Newtonian dielectric fluids with different polymer and dielectric particle

concentrations against varying DC electric field strengths were tabulated in tables 4.3.-4.5.

Table 4.3: The relaxation time scales of non-Newtonian dielectric fluids for a particular polymer and dielectric nanoparticle concentration

| Non-Newtonian dielectric fluid | Electric field strength (kV/mm) | Relaxation time |
|--------------------------------|------------------------------------|-----------------|
| P20- T10 | 0 | 125 |
| P20- T10 | 0 | 129.03 |
| P20- T10 | 0.26666 | 145.985 |
| P20- T10 | 0.4 | 190.476 |
| P20- T10 | 0.5333 | 222.22 |

Table 4.4: The relaxation time scales of non-Newtonian dielectric fluids for different polymer concentrations

| Non-Newtonian dielectric fluid | Electric field strength (kV/mm) | Relaxation time |
|--------------------------------|------------------------------------|-----------------|
| P0- T10 | 0.53333 | 0 |
| P5- T10 | 0.53333 | 193.42 |
| P10- T10 | 0.53333 | 205.33 |
| P20- T10 | 0.53333 | 222.22 |

Table 4.5: The relaxation time scales of non-Newtonian dielectric fluids for various dielectric particle concentrations

| Non-Newtonian dielectric fluid | Electric field strength (kV/mm) | Relaxation time |
|--------------------------------|------------------------------------|-----------------|
| P20- T0 | 0.5333 | 104.82 |
| P20- T2.5 | 0.5333 | 116.144 |
| P20- T5.0 | 0.5333 | 137.17 |
| P20- T7.5 | 0.5333 | 162.07 |
| P20- T10 | 0.5333 | 222.22 |

4.4 Results and discussions

4.4.1 Spreading electrohydrodynamics of non-Newtonian droplets

We begin the discussions with the spreading dynamics of the non-Newtonian dielectric fluid droplets on SH surfaces for different Eo_e . Fig. 4.6. a-d illustrates the influence of the Eo_e on the spreading behavior of non-Newtonian dielectric droplets by varying particle (TiO_2) concentration at constant polymer (5%v/v) concentration and $We \sim 65$.

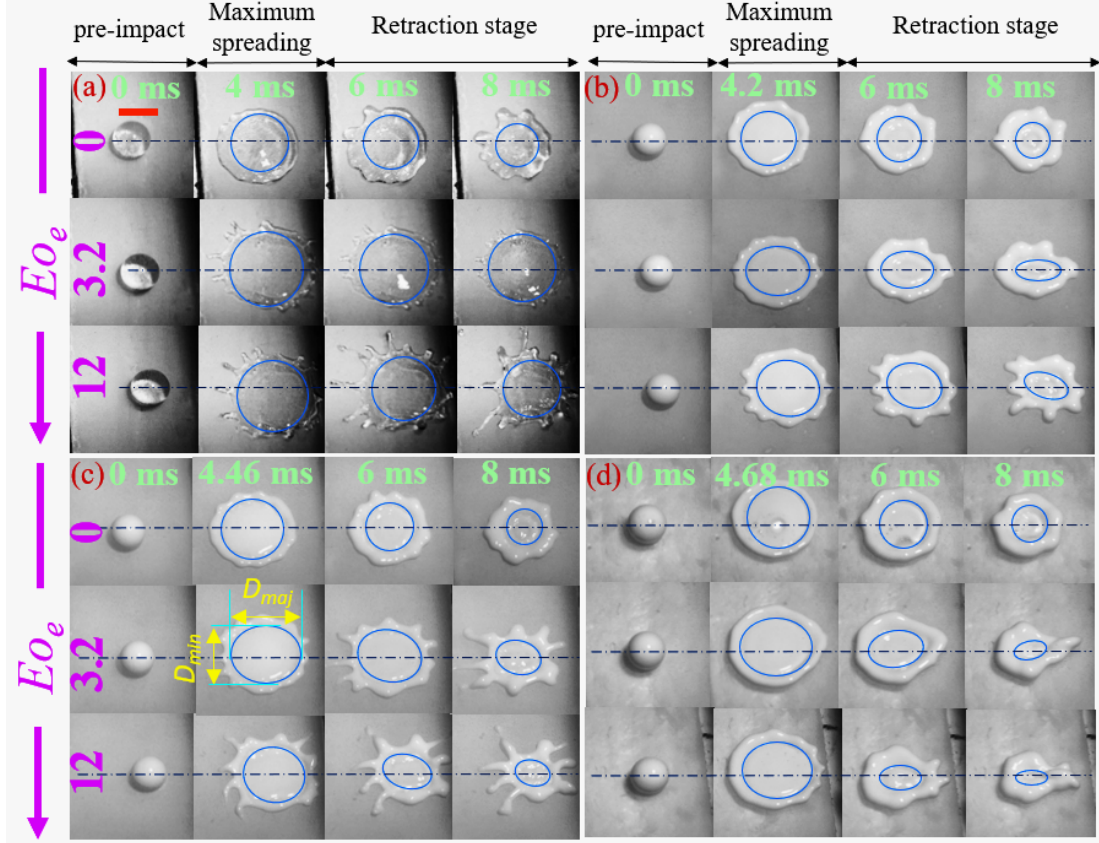


Figure 4.6: Temporal evolution of the spreading electrohydrodynamics of non-Newtonian dielectric droplet for Eo_e ranging from 0-12, at $We \sim 65$ ($U=1.25\text{m/s}$), for different fluids as: (a) P5-T0 (b) P5-T2.5 (c) P5-T5 and (d) P5-T10. The scale bar represents 2.72 mm. Black dashes (—) represent the direction of electric field lines.

In this work, we do not focus on the spreading electro-hydrodynamics of Newtonian dielectric droplets, as it has been discussed in details in our previous work [122]. Fig. 4.6.a. shows the spreading behavior of pure polymer (P5-T0) droplets. During spreading, a liquid sheet and rim spread due to capillary and inertial forces. We analyzed the shape of the sheet-rim (with a visible groove) during maximum spreading to measure non-uniform dynamics of electrically charged droplets. For each image, we attempted to fit the most appropriate circular or elliptical shape possible (blue color periphery). The droplet spreads with radial symmetry (throughout the study, we consider only the liquid lamella portion inside the liquid rim to describe the shape of spreading

symmetry; see blue-color peripheral boundary to identify the symmetry in Fig.4.6.). In the absence of electric field ($Eo_e \sim 0$), the P5-T0 droplets exhibit radial symmetry during spreading. The radius of the liquid lamella during the maximum spreading stage becomes larger with an increase in $Eo_e \sim 3.2$ and 12. This signifies that the electrical body force on the polymer droplet is potent enough to augment the spreading, especially via the formation of radial spikes (see fig. 4.6.a, for $Eo_e = 12$, at 6 ms to view the radial spikes).

When we increase the dielectric particle concentration at same polymer concentration (sample P5-T2.5), the droplet still shows radial symmetry (first row of Fig. 4.6. b) at $Eo_e \sim 0$. But Fig. 4.6. (row 2 and 3) reveals that the droplet shape transits from radial symmetry to elliptical symmetry with increasing $Eo_e \sim 3.2$ to 12. The droplets start to elongate along the direction of the electric field during the spreading process, assuming elliptical shapes. The elliptical spreading enhances with an increase of Eo_e . For non-Newtonian dielectric droplets (refer Fig. 4.6. b-c), we also observed that the formation of spokes or filaments in the radial direction is more vigorous with an increase of $Eo_e \sim 12$). Similarly, at higher dielectric particle concentration (at same polymer concentration (P5- T5)), the droplets still show the radial symmetry at $Eo_e = 0$. But, the same droplets exhibit elliptically spreading liquid lamella (refer second row and second column of Fig. 4.6.c) even at moderate $Eo_e \sim 3.2$. We infer that with an increase in Eo_e , the onset of elliptical spreading is triggered with increase in the dielectric constant of the fluid (caused by increased dielectric particle concentration).

Analogous to previous studies [141], it is noteworthy to elucidate the recoiling behavior of such non-Newtonian dielectric droplets during the retraction phase, against applied Eo_e . As depicted in fig.4.6. (a)-(c), the droplet exhibits radial spokes through the liquid rim due to the fingering instability [141] at the liquid rim against the applied Eo_e . Despite the induced corrugations or convolutions to the liquid rim during spreading and retraction stages, we believe that this may be due to the change in the dipole moment of the particles in the liquid sheet in presence of electric field. With increase of dielectric particle concentration, the fingering instability becomes more prominent. During early stages of spreading, the liquid rim displays the onset of fingers. These fingers may interact with each other to merge, or split based on the further expansion of the liquid rim [141]. But, at higher dielectric particle concentration (i.e., P5-T10), the transformation of spokes (fingers) into bulbous swelled liquid rim (refer fig. 4.6.(d), 2nd row and 3rd column to view the fingering instability of liquid rim) is noted. This is due to the merging of fingers during both spreading and retraction stages against external Eo_e .

To quantify the asymmetric spreading dynamics, we have defined the ratio of the major axis to the minor axis as $\xi_{max} = (D_{major} / D_{minor})_{max}$. Figure 4.6.a illustrates the temporal dynamics of ξ_{max} for different fluids at $Eo_e \sim 3.2$. From fig.4.7.a, it is observed that the droplet starts to elongate along the direction of the field within few milliseconds

of touching the substrate. In fig. 4.7. a and b, $\xi_{max} = 1$ implies radial symmetry for the whole range of Eo_e , and occurs when the working fluid is devoid of any dielectric particles. For a fluid droplet with certain (non-zero) dielectric particle concentration, the ξ_{max} increases monotonically from 1 with an increase in Eo_e . Also, for a fixed Eo_e , ξ_{max} increases with an increase in dielectric particle concentration. This is due to the increase in the electrohydrodynamic force in the droplets due to increase of dielectric constant of the fluid with increased dielectric particle population. Since pure non-Newtonian droplets do not exhibit elliptical spreading with an increase of Eo_e (fig. 4.7., 4.6.a and b), it can be concluded that the elliptical spreading is induced by the effect of the electric field on the dielectric particles. The dielectric force acting on the droplet [122] is proportional to square of strength of electric field (E^2) and the relative permittivity of the fluid, ϵ_r . Hence with increase of Eo_e ($\propto E^2$), the propensity to spread along the field direction increases. As noted from fig. 4.7.(b), the ξ_{max} of the non-Newtonian dielectric droplets over different Eo_e conforms to a third order polynomial with a measure of goodness of $R^2=0.9981$ as $\xi_{max}=1.0+0.0592(Eo_e)-0.0065(Eo_e)^2 + 0.0003(Eo_e)^3$.

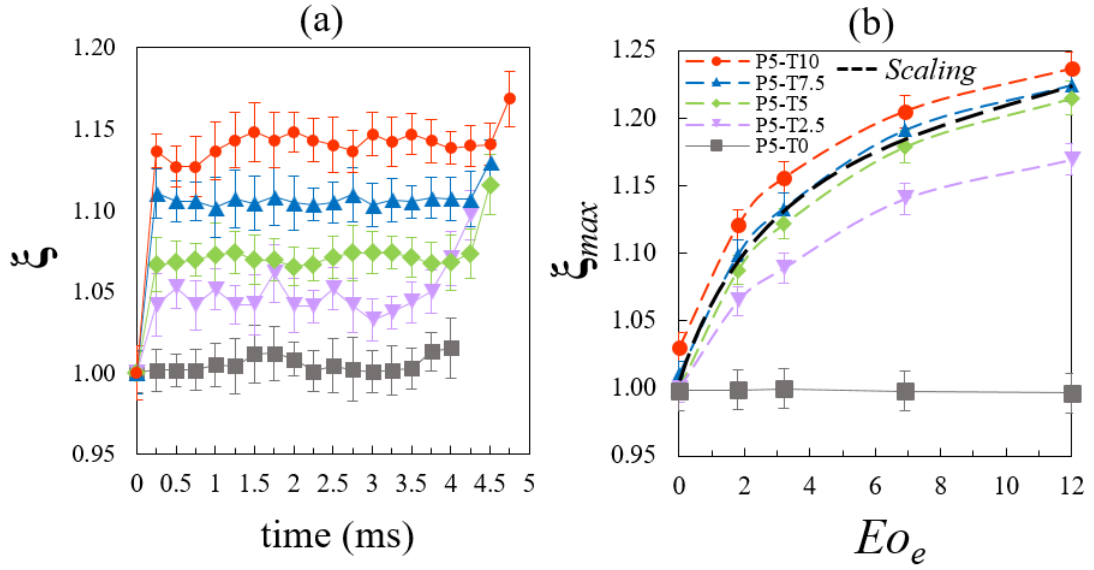


Figure 4.7: (a) Temporal evolutions of ξ from the instant of impact to the instant of attaining ξ_{max} at $We \sim 65$ and $Eo_e = 3.2$, (b) effect of dielectric particle concentration on ξ_{max} for a fixed polymer concentration P5 at $We \sim 65$ (i.e., at $U=1.25$ m/s). Black dashed line (—) in fig. 4.4.b. represent the best polynomial fit.

4.4.2 Droplet rebound suppression (anti-superhydrophobicity) kinetics

4.4.2.1 Role of fluid elasticity (polymer concentration)

This section discusses the role of fluid elasticity (polymer concentration varied from P0 to P20) on the droplet rebound behavior (for a fixed dielectric particle concentration T10) on SH surfaces for different Eo_e (fig. 4.8.) and at a fixed $We \sim 85$. The pure Newtonian droplets (P0, fig. 4.8.a) show no droplet rebound suppression for all Eo_e investigated. Also, droplet rebound suppression was never noted for the non-Newtonian droplets in case of zero electric field. It was evident that with an increase in polymer concentration (fluid elasticity), the droplet rebound suppression (anti-superhydrophobicity) was observed at lower Eo_e (red colored circumscribed area in figure.4.8. for droplet rebound suppression).

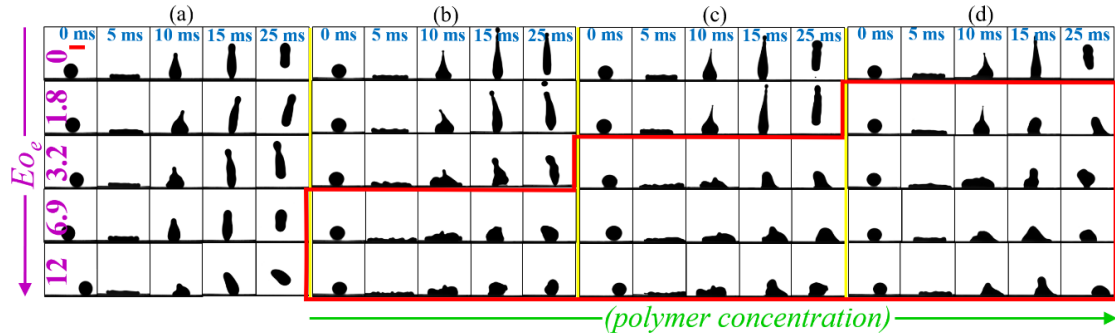


Figure 4.8: Effect of polymer concentration on non-Newtonian dielectric fluid droplet rebound for Eo_e ranging from 0-12, at $We \sim 85$ ($U=1.25\text{m/s}$) for fluids as: (a) P0-T10 (b) P5-T10 (c) P10-T10 (d) P20-T10. The scale bar represents 2.72 mm. The red outline represents the cases where complete suppression of droplet rebound (anti-superhydrophobicity) is observed.

For instance, rebound suppression was observed at $Eo_e \sim 6.9$ and 1.8 , for P5-T10 and P20-T10, respectively. Hence, experiments reveal that: (a) the coupled influence of fluid elasticity and electrohydrodynamic forces in the dielectric fluid leads to triggering of anti-superhydrophobicity effect, and (b) the rebound suppression is triggered at lower electric field strengths with increasing fluid elasticity. We believe, with increasing polymer concentrations, non-Newtonian effects such as the emergence of normal stresses slowing down the retraction dynamics gets augmented [88], resulting in lower threshold of Eo_e to trigger arrest of droplet rebound.

4.4.2.2 Role of fluid dielectric constant (particle concentration)

Figure 4.9. highlights the role of dielectric constant of the fluid (particle concentration ranging from T0-T10) for a fixed polymer concentration (P20) for varying Eo_e (0-12) on the droplet rebound behavior. The non-Newtonian droplets with no dielectric particles could not inhibit droplet rebound for all Eo_e (0-12). Droplet rebound

suppression occurred at lower Eo_e with the increase in dielectric particle concentration. Droplet rebound suppression was observed at $Eo_e \sim 6.9$ and 1.8 for P20-T5 and P20-T10 fluids (red colored circumscribed area in figure.4.9.) respectively. Therefore, from figure 4.9., it is evident that increase of dielectric particle concentration triggers rebound suppression at lower Eo_e .

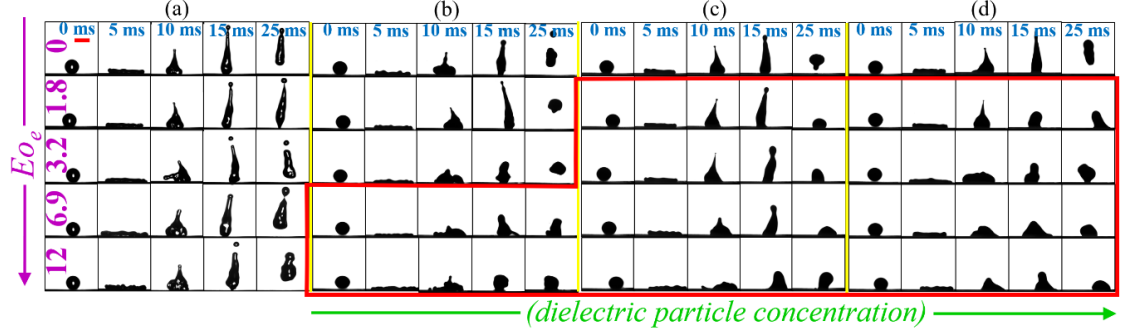


Figure 4.9: Effect of fluid dielectric constant (particle concentration) on non-Newtonian fluid droplet rebound suppression for Eo_e ranging from 0-12, at $We \sim 85$ ($U=1.25\text{m/s}$) for fluids as: (a) P20-T0 (b) P20-T5 (c) P20-T7.5 (d) P20-T10. The scale bar represents 2.72 mm. The red outline represents the cases where complete suppression of droplet rebound (anti-superhydrophobicity) is observed.

As discussed earlier [122], the dielectric force acting on the droplet is proportional to $(E^2 \epsilon)$. This dielectric force is responsible for elliptic spreading of the droplets. In contrast to radial spreading, the capillary force responsible for retraction is hindered by the dielectric force in case of elliptic spreading. As a result, the retraction velocity reduces with increase in $E^2 \epsilon$. This has been observed in our previous study [122], where rebound suppression on SH surface was observed with increase in electric field intensity for a Newtonian dielectric field. In the present scenario, we have noted that the onset of rebound suppression is largely reduced to lower values of Eo_e when the non-Newtonian component is present in the fluids. Further, the threshold Eo_e to trigger the rebound suppression is found to be decreasing with the increase in dielectric particle concentration.

This indicates the interactive role of non-Newtonian (elastic) effects with the electrohydrodynamic effects on rebound suppression kinetics. From Table 4.5., it is seen that for these set of fluids P20-T(0 to 10), the relaxation time increases with increase in the dielectric particle concentration. As we know with increase in relaxation time, fluid elasticity is increased. With increase in elasticity, emergence of non-Newtonian features such as stretching of polymer chains [126], normal stress [45] slowing down the retraction process initiates, and subsequent rebound suppression occurs. So, at lower Eo_e , for high dielectric particle concentration fluids, the elastic effects are already strong enough to hamper the receding dynamics. Therefore, the combined effect of polymers and increasing dielectric particle concentration leads to droplet rebound suppression at lower Eo_e .

4.4.2.3 Role of impact velocity (Weber number (We))

Next, we highlight the role of Weber number (85 to 165) for a fixed fluid P20-T10 on the rebound dynamics, for varying $Eo_e \sim 0$ to 12, in fig. 4.10. Rebound suppression was observed for higher Eo_e with the increase in We . For instance, the rebound suppression was observed at $Eo_e \sim 1.8$ and 6.9 for $We \sim 85$ and 165 respectively. With increasing We , higher impact kinetic energy translates to availability of higher surface energy during retraction phase, and hence a higher propensity of rebounding. Thus, higher electric field intensity is required to reduce the retraction kinetic energy to inhibit the droplet rebound as We is increased. The observations signify that the onset of rebound is governed by the magnitude of shear during the retraction phase (the shear during spreading and retraction is dependent on the impact We).

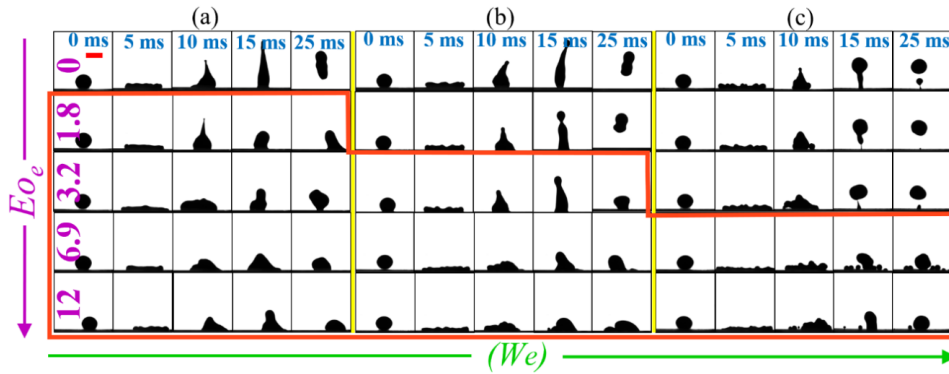


Figure 4.10: Effect of Weber number (We) on non-Newtonian dielectric fluid droplet rebound suppression over different Eo_e ranging from 0-12 for the case of P20-T10: (a) $We \sim 85$ ($U=1.25\text{m/s}$) (b) $We \sim 120$ ($U=1.5\text{m/s}$) (c) $We \sim 165$ ($U=1.75\text{m/s}$). The scale bar represents 2.64 mm. The red outline represents the cases where complete suppression of droplet rebound (anti-superhydrophobicity) is observed.

4.4.2.4 ‘Electro-elastic’ effect and role of electric Weissenberg number (We_e)

From the earlier subsections 3.2.1 - 3.2.3, it is evident that the onset of rebound suppression occurs at lower Eo_e and this increases with an increase in fluid elasticity (polymer concentration) (fig. 4.8.) as well as fluid dielectric constant (particle concentration) (fig. 4.9.). Again, from fig.4.10. it was concluded that with an increase of We , initiation of droplet rebound suppression was observed at higher Eo_e . The droplet impact dynamics depends on the electrorheological behavior (dependent on polymer concentration, particle concentration and electric field strength) of the fluids and Eo_e (taking into account the electric field intensity and surface tension effects). We first quantify the Weissenberg number to estimate the role of fluid elasticity during the droplet retraction phase. The Wi is calculated as the product of the relaxation time of the fluid and the average shear at the onset of retraction phase.

For the calculation of Wi , the relaxation time of the non-Newtonian solutions discussed

earlier in section 4.2.5 (table 4.3.-4.5.) was used. In addition, the shear rate was estimated at the moment of onset of retraction, based on protocol of previous studies on non-Newtonian droplets and flows [45, 88]. Due to the generation of normal stress during retraction [88] and stretching of polymer chains near the receding contact line [142], the shear rate was calculated at the onset of retraction from image processing. To estimate the average shear rate during the onset of droplet retraction, we adopted the expression, $\dot{\gamma} = du/dy = (\Delta R/(\Delta t/\Delta y))$, where $\dot{\gamma}$, R, y and t represent the retraction shear rate, liquid sheet radius during onset of retraction, liquid sheet height (thickness) during onset of retraction, and time elapsed, respectively.

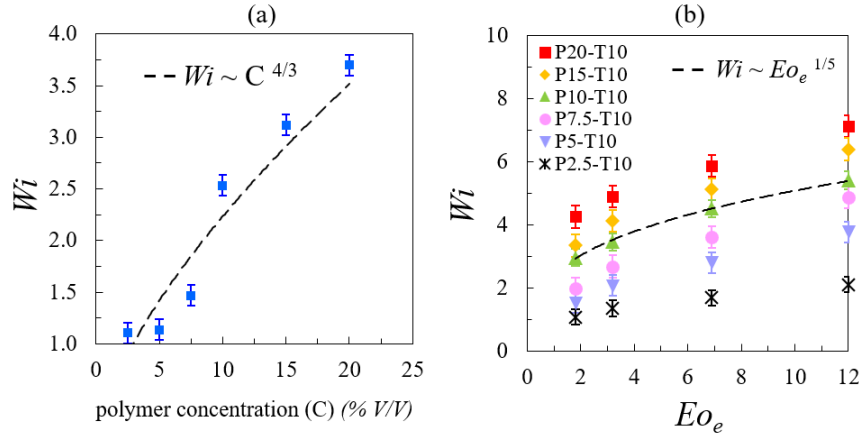


Figure 4.11: Electro-elasto-hydrodynamics of the non-Newtonian dielectric fluid droplet during the onset of retraction at $We \sim 85$: (a) role of fluid elasticity (polymer concentration) on Weissenberg number (Wi) for P2.5 to P20 with same dielectric particle concentration (T10) (b) map of Eo_e with Wi for different fluids, showing a best fit of power law scaling.

Figure 4.11. (a) shows the influence of polymer concentration on Wi at a fixed We . Since the non-Newtonian effects hardly affect the spreading dynamics [45, 88], the shear rate estimated during the onset of retraction (at fixed We) will be of almost the same magnitudes for different polymer concentrations. Since the relaxation times usually increase with polymer concentration, it is evident that for a fixed We and consequently fixed shear rate, Wi will increase with concentration (C), with an approximate scaling of $Wi \sim C^{(4/3)}$ as obtained from fig. 4.11.a. Next, we tried to probe the influence of Eo_e on the Wi during the onset of retraction of non-Newtonian dielectric droplets for different concentrations (figure 4.11.(b)). It can be observed that for a fixed We , Eo_e and nanoparticle concentration, the Wi increased with the polymer concentration. Similarly, for a fixed We and any particular fluid, the Wi increased with the increase in Eo_e (since the fluids show different retraction dynamics in presence of field). Since the Wi at a fixed We is dependent on relaxation time behavior, the trends of figure 4.11.b can be explained through the relaxation time trends presented in table 4.3.-4.5. (in the supplemental document). From figure 4.11.(b), Wi was observed to scale in the best fit of power law fashion as $Wi \sim Eo_e^{1/5}$.

The *electro-elastic effect* is defined as the result of the combined effect of both elastic effects of induced polymer chains and electrohydrodynamics of dielectric nanoparticles under external electric field. Since the pure elastic effects of polymer dynamics through the manifestation of Wi and the pure electrohydrodynamics of dielectric particles through Eo_e cannot provide a complete picture of the electrohydrodynamics of non-Newtonian dielectric droplets, it is essential to provide the overall justification by joining both effects.

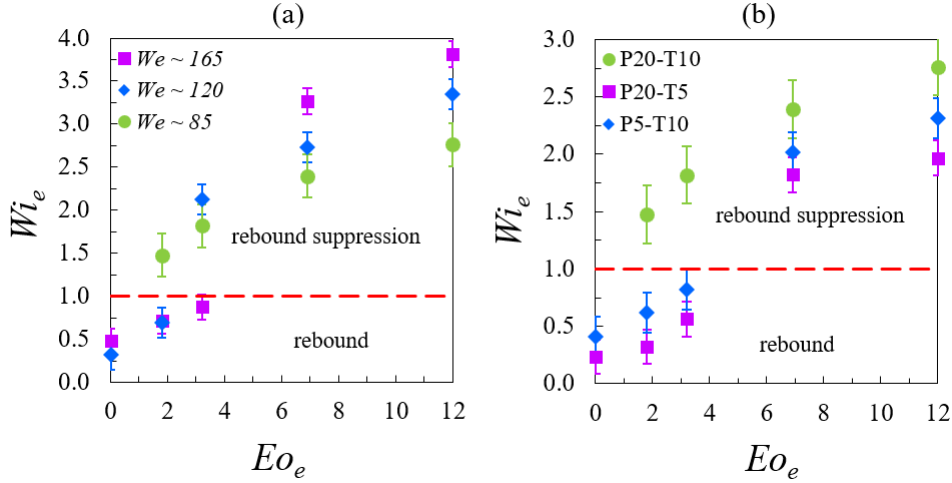


Figure 4.12: Regime map of droplet impact outcomes with proposed electric Weissenberg number (Wi_e) against Eo_e : (a) Map of Wi_e for different We for P20-T10 fluid (b) Map of Wi_e for different fluids at $We \sim 85$.

In order to quantify the electro-elastic effect, we need to combine both elastic effects due to polymer dynamics and the electrohydrodynamic behavior. With the aid of scaling analysis, we propose a new non-dimensional number, the electric Weissenberg number ($Wi_e = Wi + 1/2 (Wi^{2/3} Eo_e^{1/5})$). The Wi_e and the exponents of its constituents are defined in such a fashion that the onset of electro-elastic rebound suppression is demarcated by the regime $Wi_e \geq 1$. This is analogous to our earlier observed criteria of $Wi \geq 1$ for rebound arrest in case of pure non-Newtonian droplets [88], and magnetic Weissenberg number ($Wi_M \geq 1$) in the case of non-Newtonian ferrofluid droplet rebound suppression [11] by magneto-elastic phenomenon. The values of Wi_e for P20-T10 droplets with different impact We against varied Eo_e have been illustrated in fig. 4.12. (a). We emphasize that the threshold electric Weissenberg number ($Wi_e > 1$) criterion can segregate the regimes of rebound and rebound suppression (inhibition) with respect to both impact We and applied Wi_e and has been highlighted in the figure. 4.12. (a-b). Hence, based on this proposed non-dimensional number, the electro-elastic paradigm and its manifestation of anti-superhydrophobic behavior by the non-Newtonian dielectric droplets can be quantified and mapped.

Figures 4.10. and 4.12.a summarize the influence of impact We on non-Newtonian

dielectric droplet rebound suppression. For a fixed working fluid P20-T10, it is evident that for lower $We \sim 85$, rebound suppression was observed for the whole range of Eo_e measured in our study. The rebound suppression was observed at higher Eo_e at higher We only. The low electric field strength was reasonably sufficient to inhibit the dielectric droplet rebound against low retraction shear rates by overcoming stored kinetic energy. But, when the same droplet impacts with a higher We , the droplet needs higher electric field strengths to overcome the higher retraction shear rates. Thus, from the figure.4.12.(a), we confer that the non-Newtonian dielectric droplet of the case P20-T10, the droplet impacts relatively with higher We (i.e., ~ 165) needs higher electric field strength (i.e., higher Eo_e) to suppress the droplet rebound. From figures 4.8. and 4.12.(b), it is clear that the probability of rebound suppression increases with the increase in polymer concentration (P5 and P20) for a fixed dielectric particle concentration (T10). This is obvious as the relaxation time increases with polymer concentration and subsequently Wi . Consequently, the chance of $Wi_e > 1$ is higher with increased polymer concentration for a fixed dielectric particle concentration (refer to table 4.4. in the supplemental document). Similarly, in reference to table 4.5. in the supplemental document, relaxation time increased with an increase in dielectric particle concentration for a fixed polymer concentration. So, at a fixed polymer concentration of P20, the higher dielectric particle concentration fluid P20-T10 tends to inhibit droplet rebound compared to P20-T5.

4.4.2.5 Regime map of rebound and rebound suppression in drop impact dynamics

Finally, we have prepared the phase maps highlighting the demarcation zone of drop rebound and rebound suppression as a function of Eo_e vs. polymer concentration, dielectric particle concentration and We in fig. 4.13.a, b and c, respectively, from figure 4.13.a, it is evident that the probability of rebound suppression at lower Eo_e increases with an increase in polymer concentration. Again, for a fixed polymer concentration, the probability of rebound suppression increases with an increase in Eo_e . Figure 4.13.b shows similar trends as fig. 4.13.a. The onset of rebound suppression was observed at lower Eo_e with an increase in TiO_2 concentration. At a particular Eo_e and We , the rebound suppression phenomena trigger an increase in polymer concentration. The droplet with low polymer concentration needs higher electric Eo_e to get rebound suppression (refer fig.4.13.(a) to view the rebound arrestment of the droplet). On the other hand, the dielectric particle concentration of a droplet of the same polymer concentration at a fixed Eo_e and We triggers rebound suppression phenomena. The droplet with high dielectric particle concentration requires higher Eo_e . We also investigated for a particular case of non-Newtonian dielectric fluid droplets of P20-T10, the influence of We on droplet rebound suppression against external Eo_e and infer that droplet has higher propensity to exhibit rebound suppression relatively at lower We . Since droplet impacts with lower We , contains

develop lower shear rates during retraction. Hence, the lower electric field strength is quite sufficient to retard the drop retraction by overcoming the stored kinetic energy. But, in the case of the droplet with higher We needs more electric field strength to retard the drop retraction at higher shear rates due to the larger amount of stored kinetic energy of the droplet (refer fig.4.13.(c) to view the segregation of both rebound and no-rebound behaviours of the droplet).

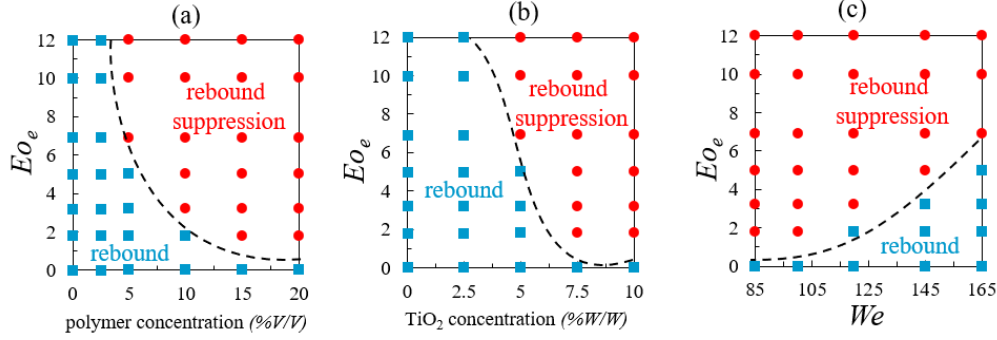


Figure 4.13: Demarcation of both rebound and no rebound (rebound suppression) regimes: (a) effect of Eo_e over polymer concentration at $We = 85$ (b) effect of Eo_e over dielectric nanoparticles concentration at $We = 85$, and (c) effect of Eo_e over We for a particular fluid P20-T10.

4.5 Conclusions

In this study, we report an experimental investigation of the electrohydrodynamics of non-Newtonian dielectric droplets on SH surfaces in the presence of an external DC electric field. We used stable colloidal solutions of dielectric particles (TiO_2) dispersed in polymeric solutions as the non-Newtonian dielectric fluids. This study encompasses a range of $We \sim 85-165$ and $Eo_e \sim 0-12$. We observed that the non-dimensional maximum elliptical spreading (ξ_{max}) increases with dielectric particle concentration at a fixed polymer concentration and We against external electric Eo_e . Through the experimental investigations, we examined the effects of polymer concentration, dielectric particle concentration, We and Eo_e on the impact electrohydrodynamics of non-Newtonian dielectric droplets. We also emphasized the role of polymer concentration, dielectric particle concentration and We on non-Newtonian droplet rebound suppression kinetics over external DC electric field in terms of Eo_e . With the thorough experimental examination, increasing polymer and dielectric particle concentration, the drop rebound suppression triggers with an increase of Eo_e . But decreasing We for a particular polymer and dielectric particle concentration triggers the onset of rebound. The findings of this research could assist future researchers in developing new strategies to minimize ink wastage caused by droplet rebound suppression from external fields in alternative printing techniques such as electrohydrodynamic inkjet printing (EHD), magnetohydrodynamic inkjet printing (MHD) and so on.

Chapter 5

Postponement of dynamic Leidenfrost phenomenon during droplet impact of surfactant solutions

5.1 Introduction

Liquid-vapour phase change is ubiquitous in several natural phenomena and man-made utilities. Under its broad aegis, the Leidenfrost effect is an atypical phenomenon where the liquid may levitate above its own vapor cushion at temperatures significantly higher than its boiling point [39]; often observed in day-to-day life when water droplets come in contact with superheated kitchen-ware. The corresponding temperature at which the onset of the effect occurs is the Leidenfrost point (or temperature). At this juncture, the heat transfer rate between the fluid and the heated surface drops significantly as the vapor cushion formed beneath the fluid droplet is a poor thermal conductor. The impact of liquid droplets on such superheated surfaces is of prime relevance to many industrial processes such as spray quenching of alloys, fire extinguishment by sprinkler systems [26], additive manufacturing, and coatings [27], and turbine blade cooling [27]. The reduction in heat transfer can be detrimental in several such cases, for example, in the thermal management of nuclear power plants [27] or metallurgical treatments. The droplet Leidenfrost effect also has great potential in drag reduction [143] and nanoscale manufacturing processes [143].

In recent times, there have been significant strides in the field of droplet Leidenfrost dynamics. Quere and Clanet et al. have made seminal contributions in this field [39], [68, 144–146]. Biance et al. studied the shape of Leidenfrost droplets and their dependence on the dynamics of the vapor layer beneath it [68]. They also characterized the lifetime of the Leidenfrost droplets. Self-propulsion of Leidenfrost drops [144] or solids (those which directly sublime overheated substrates [145]) can be controlled with specially designed ratcheted surfaces. Directed motion in Leidenfrost drops can be helpful for efficient heat transfer [144, 145] and targetted hot-spot cooling. Dupeux et al. [146] incorporated crenulations on the surface to increase friction and control the mobility of Leidenfrost

droplets. Bouillant et al. [147] performed particle image velocimetry (PIV) within the Leidenfrost droplets (at 300°C) and established that mobility is dependent on the droplet sizes. They showed that if the droplet diameters are lesser than the capillary length scale, only one vortex exists within the drop. On the contrary, larger diameter droplets showed the presence of two internal vortices. Shirota et al. [69] explored the relevant length and time scales vital for the transition from the fully wetted to the fully levitated (i.e., Leidenfrost) state of droplets on an isothermal hot substrate using total internal reflection (TIR) imaging technique.

Tran et al. [69] proposed a new scaling relationship for dimensionless maximum spreading (γ) of impacting droplets on the heated surfaces in both gentle and spray film boiling regimes with Weber number ($\gamma \sim We^{0.4}$). They showed that the spreading dynamics for heated conditions is higher compared to that for ambient conditions ($\gamma \sim We^{0.25}$). Khavari et al. [70] experimentally investigated the impact dynamics of droplets on sufficiently heated surfaces and, based on the fingering patterns of the post-impact droplet, classified the boiling into four regimes, viz. spreading (negligible heating effect), bubbly boiling (activated nucleate boiling at the solid-liquid interface), fingering boiling, and Leidenfrost regime, respectively. Villegas et al. [71] performed direct numerical simulations of the Leidenfrost state. Using the level set and ghost fluid methods, they studied the temporal evolution of drop shapes and vapor layer thickness. Qiao et al. [72] used lattice Boltzmann techniques to simulate the Leidenfrost dynamics of droplets on overheated liquid pools. They explored the effect of various non-dimensional parameters like vapor Stefan number, Bond number (Bo), Ohnesorge number (Oh) and releasing height, and pool depth on the Leidenfrost dynamics.

In addition to the research aimed at understanding of fundamental aspects of the droplet Leidenfrost effect, there have been efforts to modulate the dynamic Leidenfrost temperature (T_{DL}) of fluids via the addition of non-Newtonian additives [73, 148, 149, 149]. It has been shown by Dhar et al [88] that when long-chain polymers are dissolved in Newtonian fluids, the resultant elastic fluid droplets exhibit rebound suppression on superhydrophobic surfaces. This rebound suppression behavior has been exploited in the case of Leidenfrost droplets to arrest rebound and thereby delay the reduction of heat transfer calibre of the droplets. Secondary atomization of droplets and increase of T_{DL} was observed by Bertola and his co-workers [148, 149, 149] with polymer additives in the droplet fluid. Dhar et al. [73] highlighted the role of Weber number and polymer concentration on the Leidenfrost point (LFP). They showed that the long-lasting filaments attached to the substrate are responsible for the increase of T_{DL} . The elastic effects of polymer chains in suppressing the droplet rebound at heated [73] and ambient conditions [88] were explored by Dhar et al. and was shown to be potential method to delay the Leidenfrost effect in droplets.

Another route to morph the T_{DL} is through the addition of surfactants, which can alter the surface tension and the wetting characteristics of the fluid. Qiao and Chandra [74] performed one of the earliest studies on the effect of typical surfactants (sodium dodecyl sulfate, SDS) on drop impact behavior at high surface temperatures. The addition of surfactants enhanced the nucleation of vapor bubbles, reduced bubble coalescence, and promoted foaming in the liquid. An increase in surfactant concentration led to a decrease in the T_{DL} . The surfactants could not affect the evaporation time of the droplets in the film boiling regime, but spray cooling regime was enhanced by addition of surfactants [150]. In contrary to Qiao and Chandra's observations [74], Chen et al. [75] reported the increase of T_{DL} by addition of high alcohol surfactants (HAS). They established an empirical correlation between T_{DL} and the maximum spreading factor. Zhang et al. [151] reported that T_{DL} was reduced by use of SDS and cetyl tri-methyl-ammonium bromide (CTAB), while use of PEG-1000 (a polymer) increased T_{DL} . They concluded that the occurrence of bubble jet and bubble explosion processes on superheated hydrophilic surfaces enhanced the heat transfer efficiency and delayed LFP. Similarly, Moreau et al. [152] showed that Leidenfrost droplets of aqueous solution of SDS at high temperatures undergo violent explosion. The explosion was attributed to the Plateau-Marangoni-Gibbs effect [153]

In this article, we aim to understand the effect of surfactants on the dynamic Leidenfrost phenomenon, when droplets of aqueous surfactant solutions impact superheated substrates. We focus on understanding the intricacies of the hydrodynamics of the processes, which lead to morphed thermal aspects of the Leidenfrost behavior in surfactant solution droplets. In our study, we explore the role of two common laboratory surfactants, SDS and CTAB. Initially, we investigated the role of surfactant concentration, We , Oh , and spreading hydrodynamics on the T_{DL} during Leidenfrost boiling ($T_s \sim T_{DL}$) regime. We have invoked the concept of dynamic surface tension (DST) to explain the spreading dynamics. The spreading behaviour was counterintuitive where the non-dimensional maximum spread factor (refer sec. 3.2) was decreasing in spite of increasing surfactant concentration. Based on the previous studies [154–156], we have invoked the concept of dynamic surface tension (DST) to explain the anomalous spreading dynamics. The T_{DL} was increasing with increase in both SDS and CTAB concentration, which was contrary to earlier studies by Qiao and Chandra [74] and Zhang et al [151]. We have done a comparative study with these existing studies [74, 151] and justified our experimental findings. Based on operating impact velocities, at temperatures higher than the T_{DL} ($T_s \sim 400^\circ\text{C}$ in the present study), droplets exhibited trampoline-like behavior and a central-jet formation during explosive boiling ($T_s > T_{DL}$). We explore the dynamics of such bouncing and jetting behavior at superheated states with different impact velocities. The role of substrate temperature, Weber number and surfactant concentration on the formation of a central jet at higher temperatures than T_{DL} was reported for the first time, to the best of our knowledge. Finally, we have

presented a phase map of the different boiling regimes like transition boiling ($T_s < T_{DL}$), Leidenfrost boiling ($T_s \sim T_{DL}$) and explosive boiling ($T_s > T_{DL}$) as a function of substrate temperature and We . We believe that, this study shall provide a comprehensive and mechanistic picture on the delaying of the Leidenfrost effect using surfactant solution droplets.

5.2 Materials and methods

The experimental setup is similar to our earlier works on droplet impact thermo-hydrodynamics [11, 73]. A schematic diagram of the experimental setup is illustrated in fig. 5.1. We have used a precision control heater plate (Holmarc Opto-Mechatronics Ltd., India), with digitized temperature control to heat the substrates to temperatures ranging from 150⁰C to 400⁰C and maintain near isothermal conditions on the substrate during the experiments. The test surface was a square stainless-steel block (80mm \times 180mm) mounted on the heating element. A T-type thermocouple probe was inserted into the stainless-steel substrate. The thermocouple measured the temperature of the substrate 1 mm below the top surface and was connected to the digitized temperature controller. The temperature controller can maintain isothermal conditions at the heating element accurate to ± 2 –3⁰C. A height-adjustable droplet dispensing mechanism (Holmarc Opto-Mechatronics Ltd., India) with digitized control was used to release the droplet from different heights, thereby allowing different impact We based experiments. A micro-syringe (± 0.1 l volumetric accuracy) enclosed to the droplet dispenser is used to dispense droplets of fixed volume through a flat head steel needle (22 gauge). A high-speed camera (Photron, UK) was used to capture the images of droplet impact on the hot substrate. All experiments were recorded at 4000 frames per second using a 105 mm macro lens (Nikon).

Before each experiment, the stainless-steel hot substrate was properly cleaned with DI water, followed by acetone, to remove dirt and contaminants from the heated surface. The substrate is heated to a particular temperature using the digitized controller and allowed to attain a steady-state. At a steady-state, the substrate temperature may vary within ± 2 –3⁰C of the set value. In this study, DI water, and aqueous solutions of SDS and CTAB (Sigma Aldrich India) were used as fluids. All surfactant solutions were prepared by continuously stirring at 600 rpm with a mechanical stirrer. In this study, we have used different concentrations of surfactant concerning its critical micelle concentration (CMC). We have tested solutions with 0.125, 0.25, 0.5, 0.75 and 1 times the CMC concentration. The relevant thermophysical properties [69, 152] of these fluids have been tabulated in Table. 5.1. To characterize the impact hydrodynamics and surface interactions of the impacting droplets, we use certain conventional non-dimensional parameters, as shown in Table. 5.2.

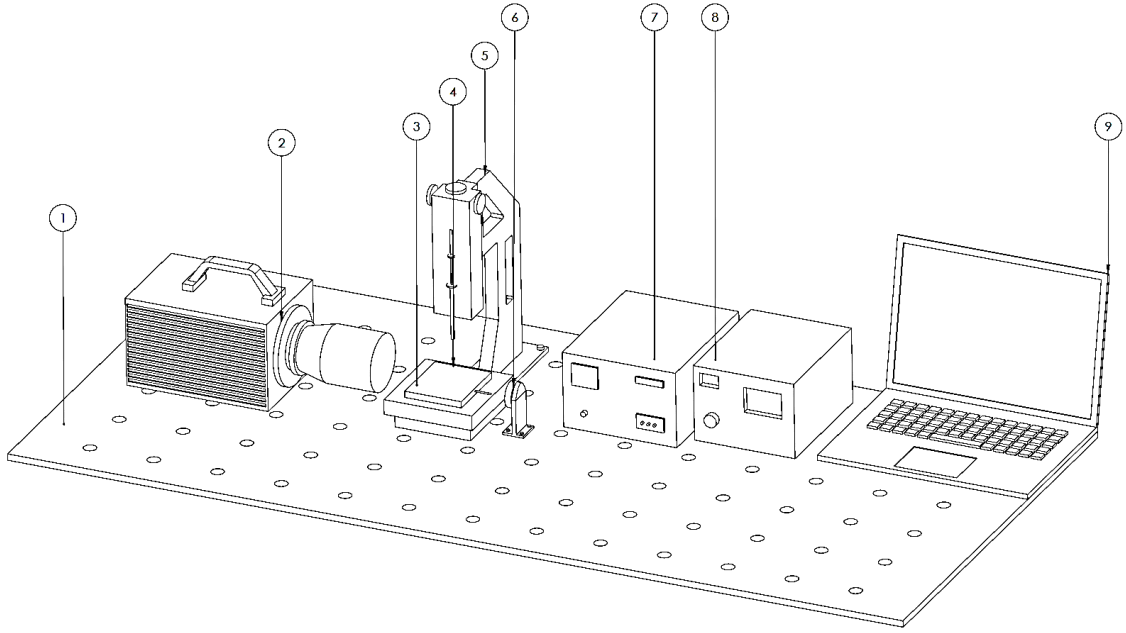


Figure 5.1: Schematic of the experimental setup: (1) Vibration free table-top (2) high-speed camera (3) hot substrate (4) microsyringe (5) droplet dispensing mechanism (DDM) unit (6) LED backlight (7) DDM and backlight illumination controller (8) hot substrate controller (9) computer for data acquisition and camera control.

Table 5.1: Experimental conditions and thermophysical properties of test fluid droplets: pre-impact droplet diameter D_o (mm), density ρ (kg/m^3), surface tension σ (mN/m), viscosity η (mPa-s), and capillary length λ_c (mm). In table.5.1 CMC represents critical micelle concentration.

| Liquid | D_o | ρ | σ | η | λ_c |
|-----------------------|-----------|---------------|---------------|---------------|-------------|
| DI water | 2.64 | 995.67 | 71.03 | 0.791 | 2.69 |
| SDS (0.125-1 CMC) | 2.55 – 2 | 972.15 - 1010 | 67.725 - 39.8 | 0.792 - 0.802 | 2.66 – 2.0 |
| CTAB (0.125-1 CMC) | 2.53–2.34 | 994 - 994.25 | 49.31 - 33.53 | 0.731-0.732 | 2.24 - 1.85 |

5.3 Results and discussions

In this section, the drop impact dynamics at high substrate temperatures will be discussed. We have varied the impact We by changing the release height of the droplets, the drop sizes, and the surface tension (due to different concentrations of the surfactants). The variation of drop diameters and surface tension was mentioned in table 5.2. The impact dynamics behavior has been classified along the lines of previous reports [75], [157, 158]. The minimum temperature at which the drop levitates over a stable, thin vapor layer without splashing is considered as the Leidenfrost temperature (T_L) [18-24]. When the droplet is gently placed ($We \sim 0$) over the heated substrate, then the Leidenfrost temperature (LFT) is termed as the static Leidenfrost temperature. However, when a

droplet is released from a certain height, the influence of initial impact velocity (quantified through We) also becomes an important factor in the Leidenfrost dynamics. Since the LFT changes with the We , it is common practice to term it as the dynamic Leidenfrost temperature (T_{DL}) [69, 143]. We have considered the T_{DL} as the substrate temperature at which the impacting fluid droplet displays onset of intact rebound off the hot surface, and the corresponding boiling state is denoted as Leidenfrost boiling.

5.3.1 Influence of substrate temperature on spreading dynamics

The change in surface tension (due to the addition of surfactant) and the thermal condition of the substrate subsequently affect the spreading behavior on the hot surface. As mentioned in earlier studies [27], [143] on many applications, it is essential to understand the spreading dynamics to estimate the heat transfer rate of droplets during the Leidenfrost stage. This section shall discuss how surfactant concentration and substrate temperature interplay to bring about changes in the spreading hydrodynamics. Fig. 5.4a and 5.4b illustrate the maximum spread state of impacting DI water and surfactant droplets on a substrate at ambient temperature $T_{DL} \sim 30^0\text{C}$, and at their respective dynamic Leidenfrost temperatures (T_{DL}) respectively. In this context, it must be noted that due to variation in equilibrium surface tension, the droplet diameter varies with the surfactant concentration (droplet size impacting the surface decreases with an increase in surfactant concentration).

As seen from table 5.1, the highest concentration (1 CMC SDS) has a droplet diameter ~ 2 mm, whereas the lowest concentration (0.125 CMC SDS) solution has a droplet diameter of ~ 2.5 mm. At 0 CMC (i.e., water) the droplet diameter is ~ 2.6 - 2.7 mm. Since the initial drop diameters are different, it is cumbersome to quantify the effect of surfactants on the spreading diameter directly from fig. 5.2. However, the effect of impact velocity for a fixed surfactant concentration is readily evident from fig. 5.2. For a fixed surfactant concentration, maximum spreading diameter increases with increased impact velocity at both ambient conditions and at the corresponding Leidenfrost state. It is noted from fig.5.2b that compared to water at its Leidenfrost state, the tendency of crown formation and fragmentation of secondary droplets decreases with the addition of surfactants. We further note that the vigorous boiling during impact at the corresponding Leidenfrost state is reduced with surfactants, as evident from the reduction in the splashing behavior at impact (fig.5.2b, 1st column).

5.3.2 Influence of We and surfactant concentration on spreading dynamics during Leidenfrost boiling (T_{DL})

As both maximum spreading diameter (D_{max}) and initial droplet diameter (D_o) changes with increasing surfactant concentration, we have quantified the spreading dynamics by defining the non-dimensional maximum spread factor $\beta_{max}=(D_{max}/D_o)$. This section highlights the role of We on the spreading dynamics at the Leidenfrost state

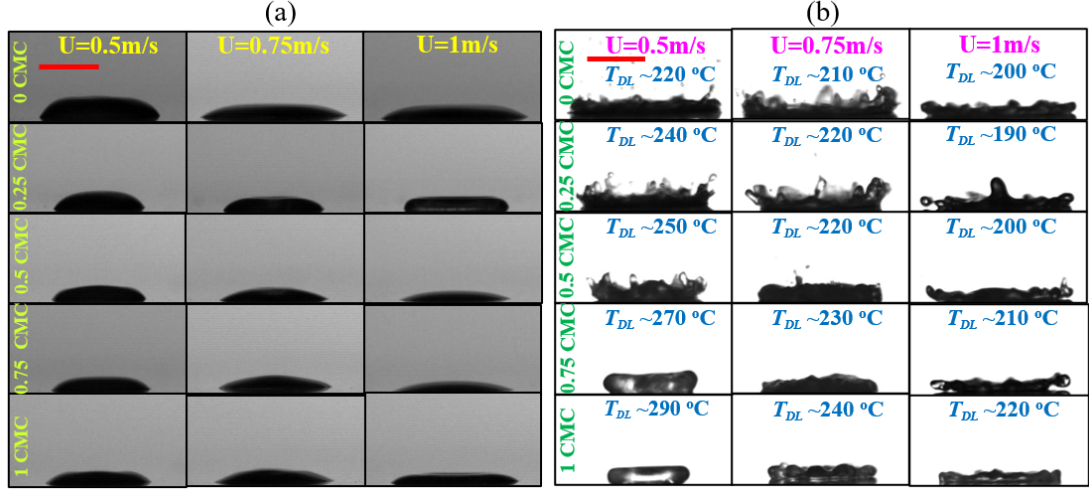


Figure 5.2: Maximum spread state of SDS droplets for different impact velocities at (a) $T_a \sim 30^\circ\text{C}$, and (b) at their respective T_{DL} s (has been shown in the inset of each cell). The scale bar represents ~ 2.64 mm. The maximum spreading diameter (D_{max}) measurements with varying Weber number and surfactant concentration are shown in fig. 5.3. The transient dynamics of SDS droplets at 220°C (the temperature at which a water droplet attains Leidenfrost state at 0.5 m/s in the present study) is provided in fig. 5.6.

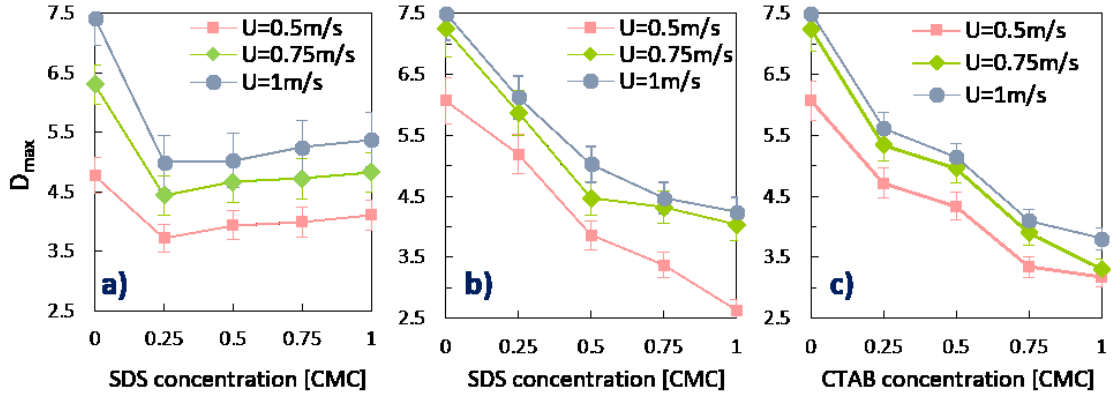


Figure 5.3: Variation in maximum spreading diameter (D_{max}) for different impact velocities of (a) SDS solution droplets at ambient temperature ($T_a \sim 30^\circ\text{C}$), (b) SDS solution droplets and (c) CTAB solution droplets at their respective T_{DL} .

of each fluid i.e., at T_{DL} . The We based on impact velocity at the moment of impact is governed by the droplet release height, droplet diameter, as well as surface tension. For the sake of simplicity, we have considered the equilibrium surface tension at ambient temperature [24] for calculation of the We . Fig. 5.4(a) and (b) show the variation of $\beta_{max}=(D_{max}/D_o)$ for different concentrations (0 to 1 CMC) of both SDS and CTAB solution droplets at their respective T_{DL} over different We . For a given test fluid, the We is increased by increasing the drop release height. Consequently, the $\beta_{max}=(D_{max}/D_o)$ (for a particular fluid) also increases due to the dominance of the stored kinetic energy of impacting fluid droplet against the surface energy.

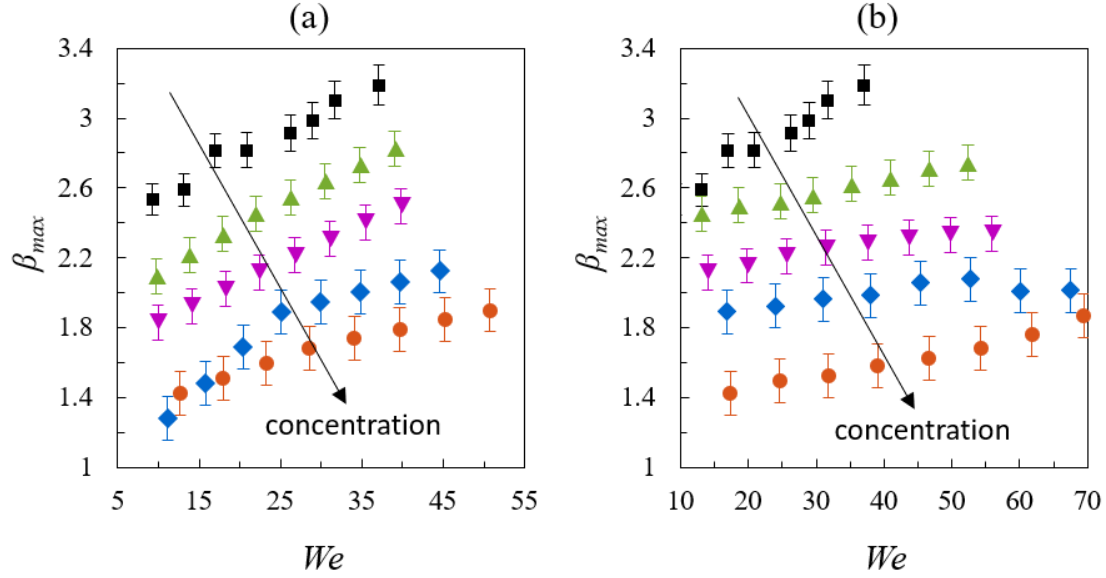


Figure 5.4: The maximum spread factor ($\beta_{max} = (D_{max}/D_o)$) at different We for surfactant solution droplets of (a) SDS (b) CTAB, respectively. In above figures, (\square) represents 0 CMC or water, (\triangle), (∇), (\diamond) and (\circ) represent surfactant concentrations of 0.25 CMC, 0.5 CMC, 0.75 CMC and 1 CMC, respectively. The arrows represent increasing surfactant concentration. Fig. 5.5. shows the variation of $\beta_{max} = (D_{max}/D_o)$ for different impact velocities.

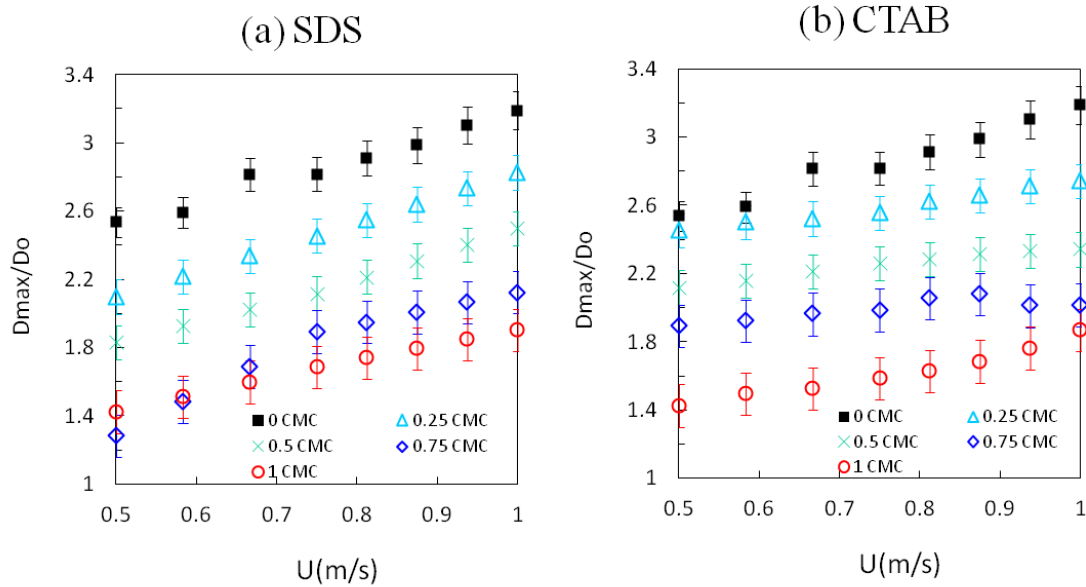


Figure 5.5: Variation in non-dimensional maximum spreading diameter ($\beta_{max} = (D_{max}/D_o)$) over different impact velocities and different surfactant concentration of (a) SDS and (b) CTAB surfactant fluid droplets at their respective T_{DL} 's

From fig. 5.4a and 5.4b, it is observed that $\beta_{max} = (D_{max}/D_o)$ decreases with an increase of surfactant concentration, at a particular We . The decreasing trend of spreading diameter with increasing surfactant concentration (which reduces equilibrium

surface tension) is counter-intuitive [73], [157, 158]. Recent studies have shown the role of dynamic surface tension (DST) in the case of determining maximum spreading [154, 155]. These studies have put forward that during the fast-spreading dynamics (occurring in the order of milliseconds), the DST should be considered instead of the equilibrium surface tension. In the initial phase after impact on the substrate, the surfactant molecules require certain time to diffuse from the bulk of the drop to the recently formed interfaces to initiate the process of reduction in surface tension. The surface tension in this phase could be higher than the equilibrium surface tension with surfactants. We can interpret the equilibrium surface tension as the steady state value surface tension value for non-deforming interfaces whereas DST is the instantaneous surface tension for the temporally varying interfaces. The temporal evolution of the freshly formed interfaces is referred as surface ageing. Since the timescale for attainment of equilibrium surface tension values is higher than the time scale of spreading dynamics, the role of DST in spreading dynamics is important. The surfactants were categorized as “fast” and “slow” depending upon the adsorption-desorption kinetics of the surfactant molecules from the bulk of the fluid to the liquid-air interface and resultant transient reduction in surface tension. The role of DST on maximum spreading is more prominent at higher impact velocities [156]. At higher impact velocities it was observed that maximum spreading diameter of the surfactant solution droplets were less than that of water drops. Previous studies [156] have suggested that for high impact velocities and resultant smaller time scale of spreading process, the occurrence of non-uniform distribution of surfactant molecules at the air-liquid interface may give rise to Marangoni stresses, which may impede the process of droplet spreading.

CTAB was shown to be a “slow” surfactant in a study by Hoffman et al. [154]. Based on these studies, we hypothesize that both the surfactants (CTAB and SDS) used in our experiments are “slow” to reduce the interfacial force, thereby failing to increase (D_{max} to the intuitive levels at their respective dynamic Leidenfrost temperatures (T_{DL}). In addition to the potential role of DST [154–156], the atypical decreasing trend of spreading factor with increasing surfactant concentration may also be due to thermo-capillarity driven Marangoni flows [159–161]. Due to the high-temperature gradient between the bottom and top surface of the droplets at the T_{DL} , and the resultant surface tension gradient, a toroidal convection sets in the droplet [36]. Fluid motion starts along the spherical periphery and sequentially accelerates downward to the contact point near the center. This internal convection impedes the spreading process, as the flow tries to curl up in the opposite direction instead of advancing horizontally towards the spreading contact line. Hence, we believe that such thermo-capillarity induced internal and interfacial convection becomes stronger with increasing surfactant concentration (due to additional solutal Marangoni effect [162, 163]) and results in the decreasing trend of spreading factor with increasing surfactant concentration for a fixed We .

5.3.3 Role of surfactant concentration on dynamic Leidenfrost temperature (T_{DL})

The dependence of dynamic Leidenfrost temperature (T_{DL}) on surfactant concentration is discussed in this section. Figure 5.6 (a) and (b) illustrate the side view and top view of the impact dynamics of various concentrations of SDS droplets at their corresponding Leidenfrost state. From fig. 5.6, it can be readily observed that at a fixed velocity of $U=0.5\text{m/s}$, the time to attain the maximum spreading diameter decreases with the increase of surfactant concentration. This effect is obvious as the droplet size decreases with the increase in surfactant concentration (refer table 5.1). The residence time (time from moment of impact to onset of lift-off) decreases with the surfactant concentration (4th column of fig. 5.6 a, b). The Leidenfrost temperature T_{DL} was denoted as the temperature at which the droplet showed rebounding off the surface for the first time [73]. At a slightly lower temperature than T_{DL} , the droplets were in always contact wholly or partially with the heated substrate. The droplets, with increasing surfactant concentration, exhibit mode shapes characterized by an undulating interface (fig. 5.6b, 2nd and 3rd column). Such prominently distorted interface during the spreading and boiling phenomena is akin to the Taylor-Marangoni instability discussed in the literature [164]. In the present case, the presence of the surfactants augments the thermal Marangoni instability due to the addition of the solutal counterpart, which leads to such prominently distorted interface of the droplet due to thermo- and soluto-capillary disturbances.

Figure 5.7 a, and b show the variation of T_{DL} with variation of impact velocity and surfactant concentration, for both SDS and CTAB solution droplets, respectively. For a fixed impact velocity, T_{DL} increases with an increase in surfactant concentration. The increasing trend is more prominent for SDS solutions (fig. 5.7 a). At the lowest impact velocity (0.5 m/s), the T_{DL} for 1 CMC SDS solution is higher than water droplets by almost $\sim 70^\circ\text{C}$, which is a high delay of the onset of Leidenfrost effect, and may have strong implications for several utilities. In the case of CTAB solutions, T_{DL} initially increases with increasing surfactant concentration up to 0.25 CMC and then maintains a near-constant value at a higher temperature compared to water (0 CMC) (fig. 5.7 b). For both the solutions, at fixed surfactant concentration, T_{DL} decreases with an increase in impact velocity. This trend is similar to the Leidenfrost phenomena studies with water and polymer droplets [73]. With an increase in impact velocity, due to higher inertia, droplets spread to a greater distance radially (as long as the impact velocity is low enough not to induce splashing/fragmentation). The subsequent increase in the contact area between the spreading droplet and the heated surface promotes the formation of nucleation sites at the liquid-solid interface to form vapor pockets. The enhanced rate of vapor formation beneath the drop helps in stable vapor layer formation and results in droplet levitation above it. Hence with increasing impact velocity, the propensity for attaining Leidenfrost state onsets at a lower temperature [73]. Following this argument,

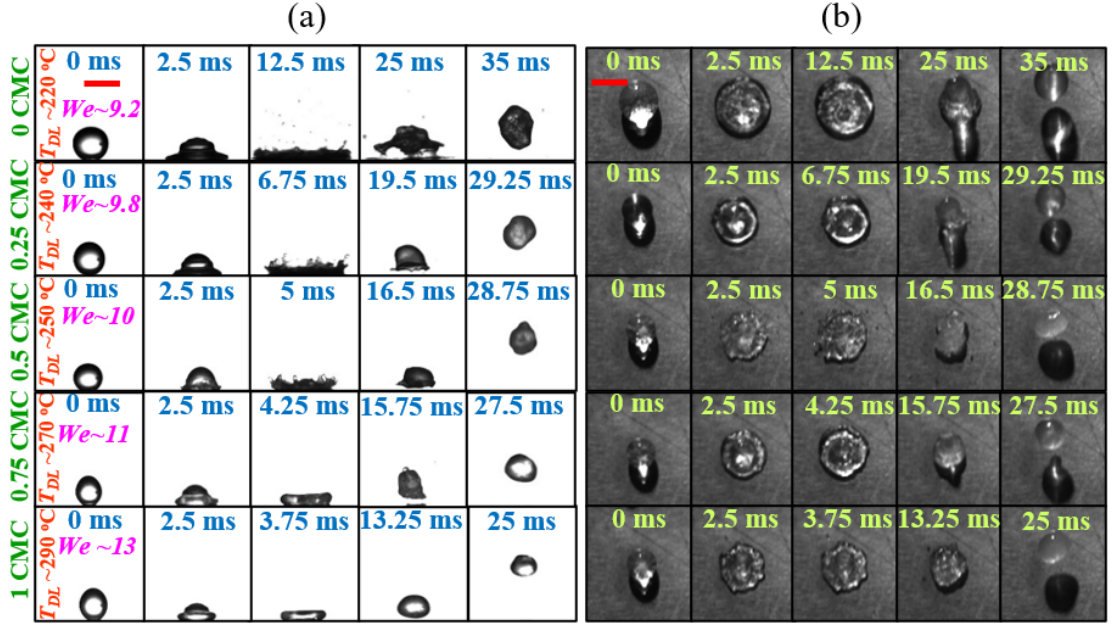


Figure 5.6: Temporal evolution of the impacting SDS solution droplets with low impact velocity $U=0.5$ m/s at their respective T_{DL} : (a) side view (b) top view. For the same initial impact velocity, We is changing mildly due to variation in surfactant concentration. The scale bar represents 2.64 mm. The 3rd column of each row represents the instant at which maximum spread occurs. The 4th column of each row represents the instant at which the droplet begins to levitate for the first time.

the increasing trend of T_{DL} with an increase in surfactant concentration can be explained. Since on heated surfaces, the radial spreading is observed to decrease with the surfactant concentration, the propensity of achieving the Leidenfrost state also reduces compared to water.

Our findings are in contrast with previous studies where T_{DL} was observed to decrease with increasing concentrations of SDS [74],[151] and CTAB [151]. One of the possible reasons could be the type of substrate. We have performed the Leidenfrost dynamics experiments on smooth stainless steel whereas previous studies were done on unmodified and modified (trimethoxy silane) smooth silicon surfaces [151]. However, this reasoning is inconclusive as the types of surfaces (smooth stainless steel) were similar for our studies and work by Qiao and Chandra [74]. Another reason could be the variation in droplet size. The previous studies had droplets of diameter $\sim 2.05 \pm 0.03$ mm [74] and 2 mm [151] whereas our experiments involved greater variation (0.125CMC and 1CMC SDS droplets were of 2.55 mm and 2 mm diameter respectively. We have tried to perform the experiments with the droplet sizes selected in such a way that the capillary and gravitational effects are almost balancing one another. For droplets size less than capillary length (λ_c), the droplets can retract easily and assume the spherical shape [165] quickly. Due to lower contact surface area as well as contact time with the heating substrate, the

vapor can easily cushion the droplet and attains dynamic Leidenfrost stage at a lower temperature. Similarly, if the droplet size is more than its λ_c , due to greater effect of gravitational force over capillary force, droplets tend to form puddle structure in the spreading state and has lesser propensity to assume a spherical shape during retraction [68]. Due to higher area of the flattened puddle structure, it is difficult for vapor to levitate the droplet. Consequently the dynamic Leidenfrost state is achieved at a higher temperature. For instance, the capillary length (λ_c) of SDS droplet with 0.125 CMC is 2.66 mm (refer Table.5.1.). If we operate the same 0.125 CMC SDS droplet with diameter of 2mm, the droplet will attain spherical shape easily during retraction and achieve the Leidenfrost state at lower temperature due to the predominance of capillary effects. Moreover, if we maintain all SDS surfactant droplets with diameter of 2 mm [74], [151] for all concentrations, for most of the concentrations it will be gravity dominated regime. Hence, we operated all concentrations of both SDS and CTAB surfactant droplets near capillary length scale (i.e., 0.125CMC SDS droplet operating diameter $D=2.55\text{mm}$, which is very near to its capillary length scale, i.e., 2.66 mm).

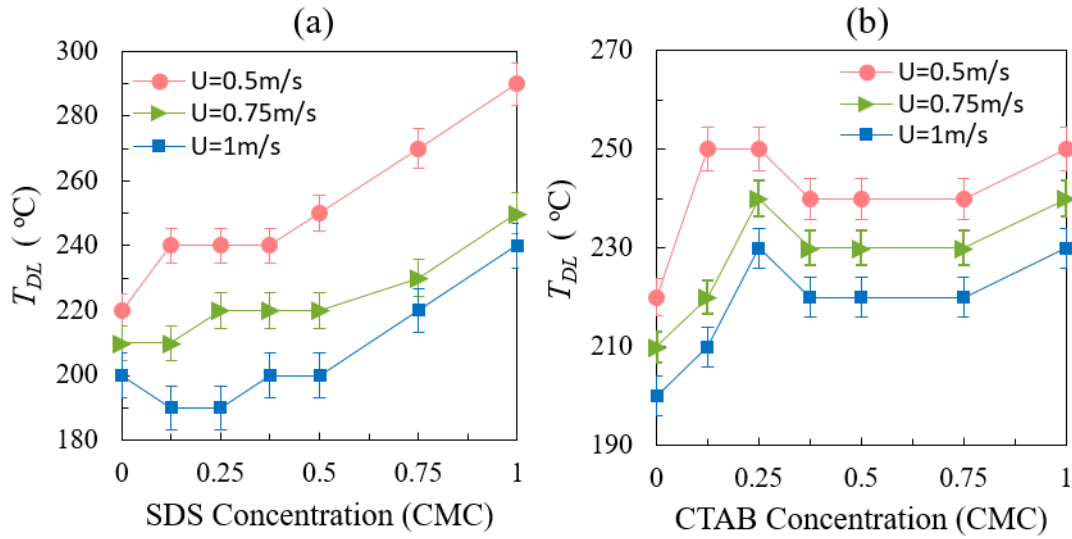


Figure 5.7: The dynamic Leidenfrost temperature (T_{DL}) over surfactant concentration of (a) SDS and (b) CTAB fluid droplets.

For further insight, we emphasized the influence of Bond number (mutual competition between both capillary forces and gravitational forces) on T_{DL} in the section 6.3.5. The droplet sizes were reducing with the increase in surfactant concentration. The variation of Bond number due to size variation may be another potential reason for the contrasting results. In addition, although the equilibrium surface tension for a specific type of surfactants are generally same, the role of DST in the first few milliseconds may vary from one batch of surfactants to another as the manufacturers were different in each other (Sigma Aldrich for our studies, Malinkrodt Speciality Chemicals [74] and Shanghai Aladdin Biochemical Technology Co., Ltd [151]).

5.3.4 Scaling T_{DL} with Weber (We) and Ohnesorge (Oh) numbers

Subsequently, based on the information highlighted in figure 5.7 a and b, the dependence of T_{DL} on We for SDS solution droplets is shown in fig. 5.8(a). It is evident that the T_{DL} decreases with an increase of We for all solution concentrations. Since the $\beta_{max} = (D_{max}/D_o)$ (refer fig. 5.6.) increases with the increase of We , heat transfer from the hot substrate occurs over a larger area of the thin liquid disc formed by the droplet at maximum spread state. As a result, the formation of a stable vapor cushion is more favorable at lower temperatures, resulting in decreasing trend of T_{DL} with increasing We . At the same We , the T_{DL} increases with an increase of surfactant concentration. This reveals that We alone is not enough to explain the effect of surfactant concentration on the T_{DL} . To improve upon this observation, we introduce another non-dimensional number, the Ohnesorge number ($Oh = \sqrt{We}/Re$). Oh is the ratio of viscous forces to both surface tension and inertial forces. Fig. 5.8 (b) reveals that T_{DL} vs. Oh reflects the increasing trend of T_{DL} with surfactant concentration at a fixed impact velocity (fig. 5.9) as in both cases, the equilibrium surface tension decreases with the increment of Oh and surfactant concentration. From figure 5.8, it is visually evident that T_{DL} is dependent on both We and Oh .

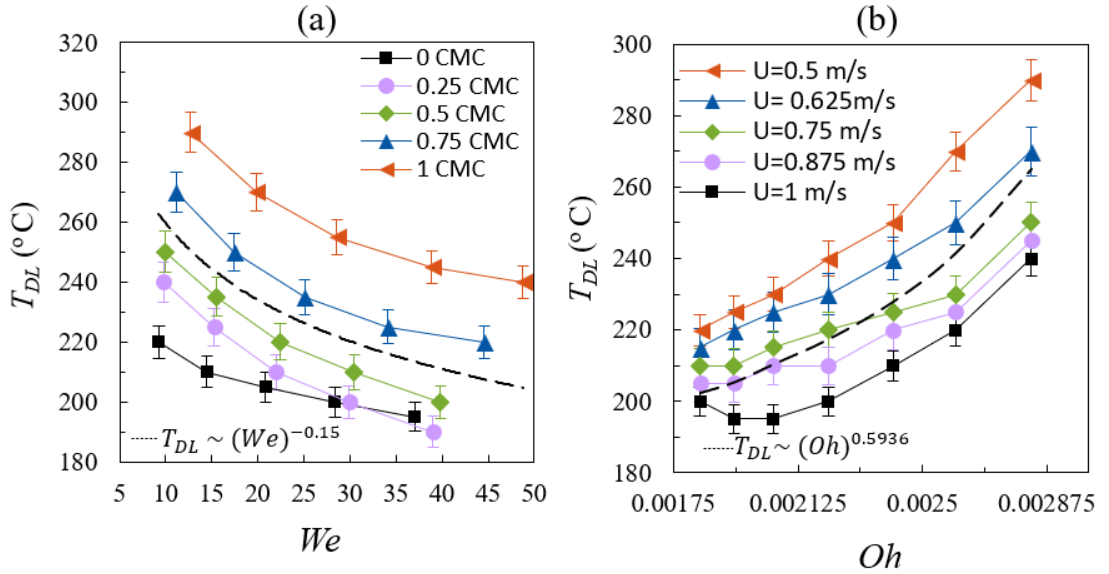


Figure 5.8: Dynamic Leidenfrost temperature (T_{DL}) with respect to (a) Weber number (We) and (b) Ohnesorge number (Oh) for SDS solution droplets. The black dotted lines (4) in(a) and (b) represents the scaling behavior of T_{DL} with We and Oh respectively (as per given scaling in each figure).

Analogous to a previous study of the Leidenfrost effect with high-alcohol surfactants (HAS) [24], we have attempted to introduce a scaling relationship of T_{DL} with We and Oh . The T_{DL} converges to static Leidenfrost temperature (T_{SL}), when We approaches

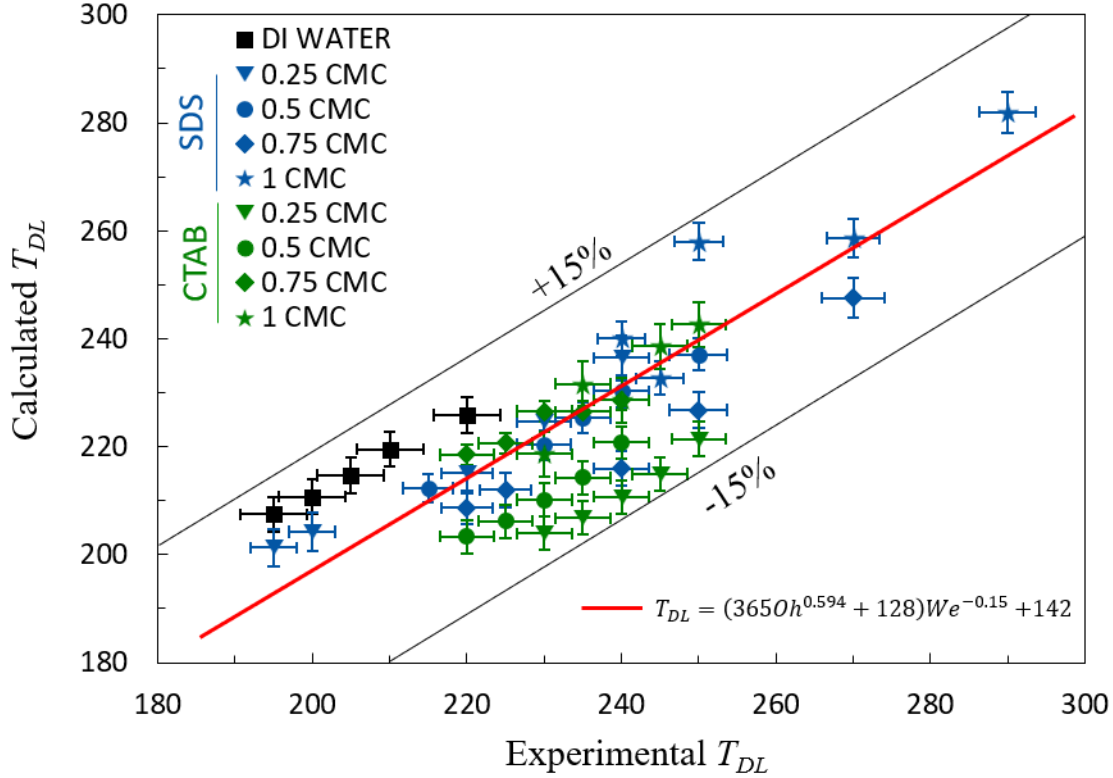


Figure 5.9: Comparison between the calculated and experimental T_{DL} of impacting surfactant solution droplets with different concentrations.

zero. The experimental results of T_{DL} are fit to conform to the following relationship: $T_{DL} = (aOh^b + c)We^{-d} + e$. Through least squares regression, the scaling correlation of T_{DL} in terms of We and Oh (with $\pm 15\%$ confidence interval, refer fig. 5.9) is obtained as: $T_{DL} = (365Oh^{0.594} + 128)We^{-0.15} + 142$. We believe that this scaling correlation will be of valuable reference for future researchers in this field.

5.3.5 Influence of Bond number (Bo) on T_{DL}

From the expression of Bond number, $Bo = (\rho g D_o^2 / \sigma)$, it is evident that there are two parameters (D_o and σ) which are varying with surfactant concentrations. With increasing surfactant concentration, the equilibrium surface tension value decreases. Since σ is in the denominator, due to its decreasing nature with increasing surfactant concentration, Bo values will increase if other parameters are same. On the other hand, due to reduction in equilibrium surface tension, our initial diameters of the droplets hanging from the syringe were also decreasing. As D_o is in the numerator, Bo will decrease with increase in surfactant concentration, provided other parameters are constant. Due to this contrasting impact of these two quantities on Bond number, the dependence of Bo during the levitation state at T_{DL} on varying concentrations at a fixed impact velocity $U=0.5\text{m/s}$ is presented in fig.5.10. In figure 5.7, it was already observed that the T_{DL} increases with the surfactant concentration. Due to reduced droplet diameters for higher surfactant concentration, Bo is decreasing with increasing surfactant concentration, in

spite of the reduction in equilibrium surface tension. As a result, figure 5.10. highlights that T_{DL} decreases with increasing Bo . This figure may provide relevant information on the dynamics of the Leidenfrost droplets only in terms of the droplet and its physical properties.

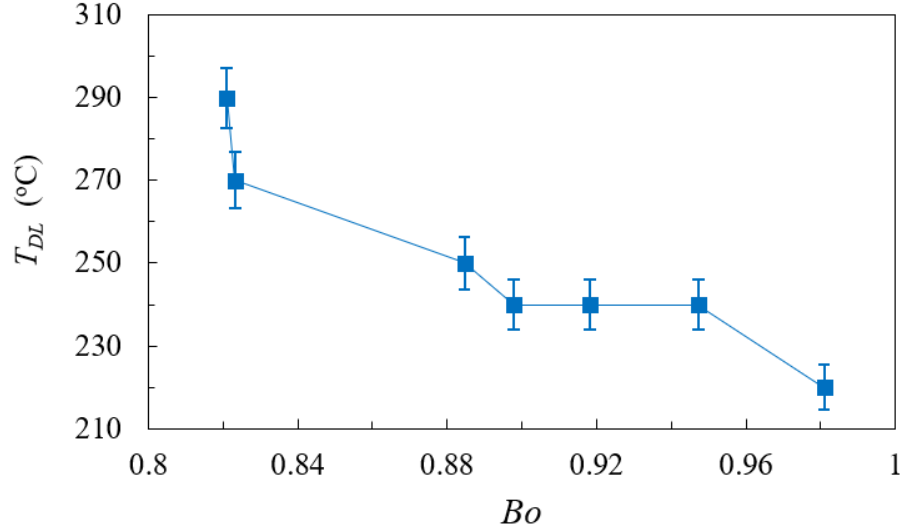


Figure 5.10: Effect of Bond number (Bo) on dynamic Leidenfrost temperature T_{DL} of different concentrations of SDS solution droplet at impact velocity $U=0.5\text{m/s}$.

5.3.6 Trampoline dynamics of the droplet at $(T_s > T_{DL}) \sim 400^{\circ}\text{C}$

At temperatures significantly higher than T_{DL} (i.e., at $T_s \sim 400^{\circ}\text{C}$ in the present discussion), droplet impact behavior is significantly changed with impact velocity. Similar to the rebound height at T_{DL} (fig. 5.12.), rebound height reduces with increasing impact velocity for 0.5 m/s . At lower impact velocity $\sim 0.5\text{m/s}$, droplets display a series of bouncing off dynamics on the substrate. This type of behavior is termed trampolining dynamics, as described in the literature [73, 145, 147, 164]. On the further increase of impact velocity to 1m/s , a central jet formation and ejection was observed during the retraction phase. In this section, we will discuss trampolining behavior. The time-dependent bouncing behavior of the droplets at different SDS concentrations is presented in fig. 5.11. At significantly high temperature $\sim 400^{\circ}\text{C}$, prompt formation of the stable vapor layer (just after $\sim 10\text{ ms}$, refer to 3^{rd} and 4^{th} column of fig.5.11) enhances the cushioning effect, and the rapid vapor generation leads to the ejection of the droplet from the surface in a nearly intact manner. The sustained oscillations are possible due to the thermo-capillarity induced flow and vapor generation during the contact, energizing the flow [161–164]. This is a significant deviation from the impact dynamics at their corresponding T_{DL} (refer to fig. 5.12.). At T_{DL} , for all impact velocities, droplets rebounded off the surface. For a fixed test fluid, rebound height decreased with increasing impact velocity. This is consistent with a previous study, highlighted [166] the increase of viscous dissipation and the resultant reduction in retraction kinetic energy with increasing

impact velocity.

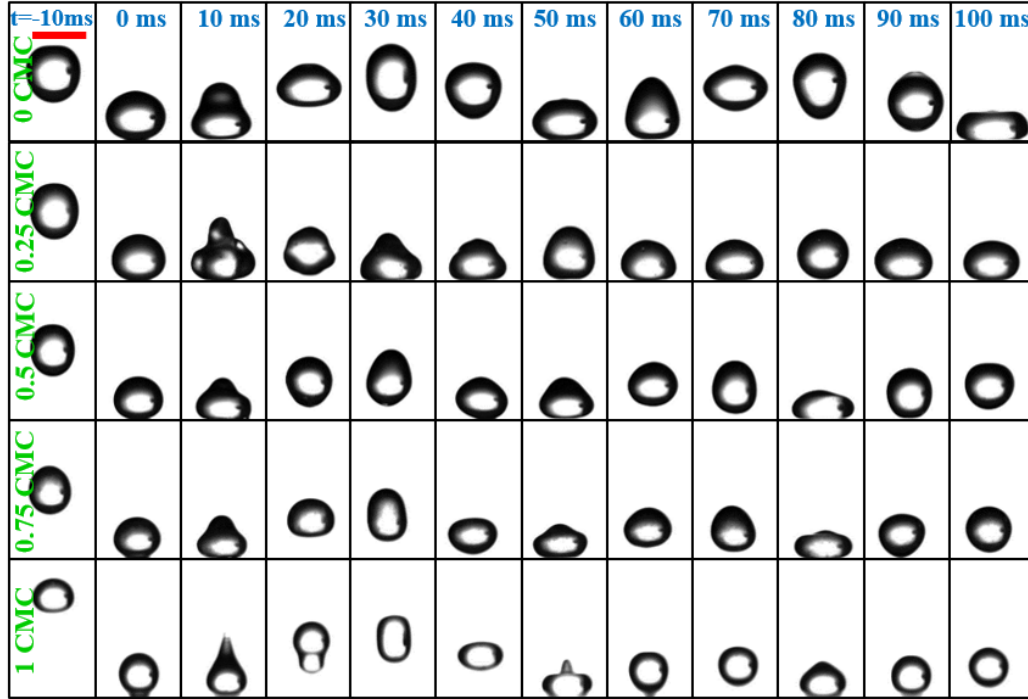


Figure 5.11: Droplet trampolining dynamics of SDS solution droplets with low impact velocity $U=0.5\text{m/s}$ at the surface temperature of 400°C . The scale bar represents 2.64 mm. The dynamics of 1 CMC SDS droplets at 0.5m/s , 0.75 m/s , and 1 m/s are presented in the supplementary section in movie format.

Subsequently, the non-dimensional rebound height (rebound height/ drop radius) for the 1st rebound and the coefficient of restitution (rebound height/initial height)^{0.5} for 0.5, 0.625, and 0.75 m/s were presented in figure 5.12 a and b, respectively. We have tried to observe the trampolining behaviour at impact velocity lesser than 0.5 m/sec. However, for lower velocity like 0.4 m/sec, the needle is too close to the substrate. For example, at 0.4 m/sec, the equivalent distance from the needle tip is around 8.15 mm. The water droplets are of 2.64 mm diameter. The remaining 5.51 mm height was insufficient to avoid the disruption of trampolining behaviour by the needle. As a result, we haven't reported the measurements for lower impact velocities. At velocities higher than 0.75m/s and $T_s \sim 400^\circ\text{C}$, for some surfactant concentrations, instead of trampolining dynamics, the drops displayed jet formation and fragmentation. So, we have reported for a limited range of impact velocities of 0.5 to 0.75 m/sec. The non-dimensional rebound height for 0.5 and 0.625 m/sec initially decreases at 0.25 CMC and then increases with increase in concentration. This trend is similar to the trends of rebound heights presented in fig. 5.12. (0.5 m/sec). However, the rebound height measured for higher velocity (0.75 m/s) shows a monotonically decreasing trend with increasing surfactant concentration. Also, the non-dimensional rebound height is higher for 0.75 m/s velocity, unlike the trend presented in 4.12. at respective T_{DL} s. Compared to both 0.5 m/s and 0.625 cases, the frequency of rebound is reduced for 0.75 m/s (refer supplementary movies).

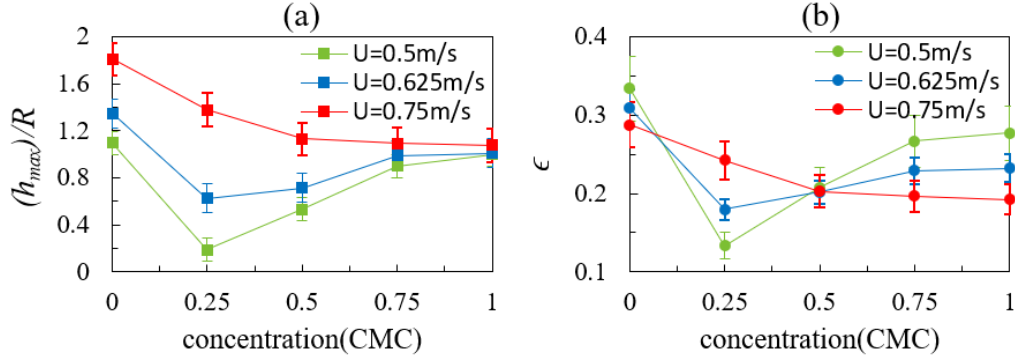


Figure 5.12: (a) Non-dimensional rebound height vs. SDS concentrations for different impact velocities. Trampolining dynamics over time is presented as 4.11. (b) coefficient of restitution, ϵ , for the same process in (a).

The coefficient of restitution is defined as $\epsilon = \sqrt{h_{rebound}/h_{impact}}$. Fig. 5.12b presents the coefficient of restitution with variation in impact velocity and varying SDS concentrations. The ϵ is much less compared to the previous studies on Leidenfrost trampolining behavior where the ϵ was almost equal to 1 [166]. At a lower impact velocity, the coefficient decreases with concentration and then increases, and this behavior is observed in repeated experiments. At lower impact velocity, the low kinetic energy allows for better heat transfer and vapor generation due to greater contact time, which in turn promotes the Taylor instability at the droplet interface (refer fig. 5.6b) [164]. Taylor instability promotes the formation of vapor dome and overall increase of vapor layer thickness. We speculate that the onset of this instability reduces the available kinetic energy during cushioning and rebound, leading to a reduced coefficient of restitution at lower concentrations. As the surfactant concentration increases, the effective spreading reduces. Consequently, the available interfacial area for the instability to manifest reduces, thereby reducing its strength. We postulate that, for this reason, the droplet is further able to exhibit an increased coefficient of restitution.

5.3.7 Fragmentation and jetting dynamics at $(T_s > T_{DL}) \sim 400^\circ\text{C}$

At higher impact velocity ~ 1 m/s and very high surface temperature, the droplets no longer stay intact and fragment into secondary droplets during the recoiling process after maximum spreading. This impact outcome is termed as explosive boiling. During retraction, the droplets undergo fragmentation into smaller droplets. The formation of a central jet was noticed and the height of the jet was observed to increase with the increase in SDS concentration (refer fig. 5.13). It is noteworthy that due to higher impact velocity, the process of jet formation has started just after ~ 5 ms from the instant of the droplet touching the substrate, even before the attainment of maximum spread state. A previous study by Siddique et al. [167] showed that the jet formation was due to the inertial collapse of the air cavity formed beneath the droplet, caused by the rapid vaporization at the point

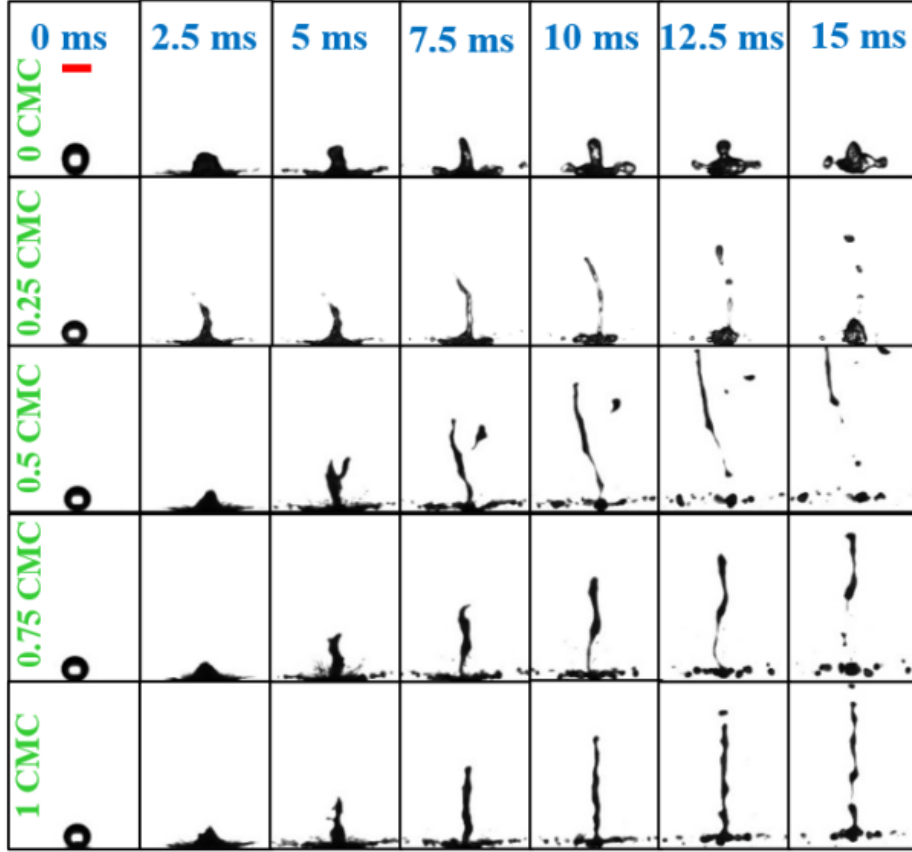


Figure 5.13: Jet ejection dynamics of SDS solution droplets at high impact velocity $U=1$ m/s for surface temperature $\sim 400^{\circ}\text{C}$. The scale bar represents 2.64 mm.

of contact due to very high surface temperature. From fig. 5.13 and fig. 5.14 a, it is evident that the central jet height increases with the increase of SDS concentration. For further description of jet ejection dynamics, the role of critical substrate temperature (T_s) and We at which the jet formation was observed for the first time has been highlighted in fig.5.14 b and 6.14 c, respectively. Fig. 5.14 (b) reveals that the critical T_s increases with an increase of surfactant concentration. Fig. 5.14(c) shows that the critical We increases with an increase of surfactant (SDS) concentration. The higher surfactant concentration droplet has less surface tension than the low surfactant concentration droplet. When a droplet has low surface tension, it needs more stored kinetic energy to propagate the jet during the retraction phase. Similarly, the lesser stored kinetic energy is quite sufficient to support the onset of central-jet formation. Thus, higher surfactant (SDS) concentration droplets need higher critical T_s and large critical We to exhibit the onset of central jet-formation.

5.3.8 Boiling regimes of impacting surfactant droplets

Finally, we have presented the phase maps of different boiling regimes of the impacting water, SDS and CTAB solution droplets in fig. 5.15 a, b and c respectively. In case of SDS solution droplets (fig. 5.15 b), Leidenfrost temperature was attained at 240°C for 0.125 CMC and 290°C for 1 CMC concentration. For CTAB solution droplets

the Leidenfrost temperature variation had a narrower range of 250⁰C (1 CMC) and 225⁰C (0.125 CMC). The parametric dependence of substrate temperature (150⁰C - 400⁰C) and Weber number based on the impact velocities (0.5 to 1 m/s) on the various boiling regimes is presented in fig. 5.15. The surfactant concentrations ranged from 0.125CMC-1CMC for both CTAB and SDS solutions. The boiling regimes were distinguished into transition boiling, Leidenfrost state, trampolining behavior, and explosive boiling, marked with colored letters I (blue), II (red), III (pink), and IV (green), respectively in fig. 5.15. In comparison to DI water droplets (see fig.5.15 (a)), the phase diagram of SDS and CTAB droplets boiling behavior (presented in fig.5.15 b c respectively) highlights the greater coverage of transition boiling regime due to an increment of the T_{DL} with the addition of surfactants. In case of SDS solution droplets (fig. 5.15 b), the T_{DL} was attained at 240⁰C for 0.125 CMC and 290⁰C for 1 CMC concentration.

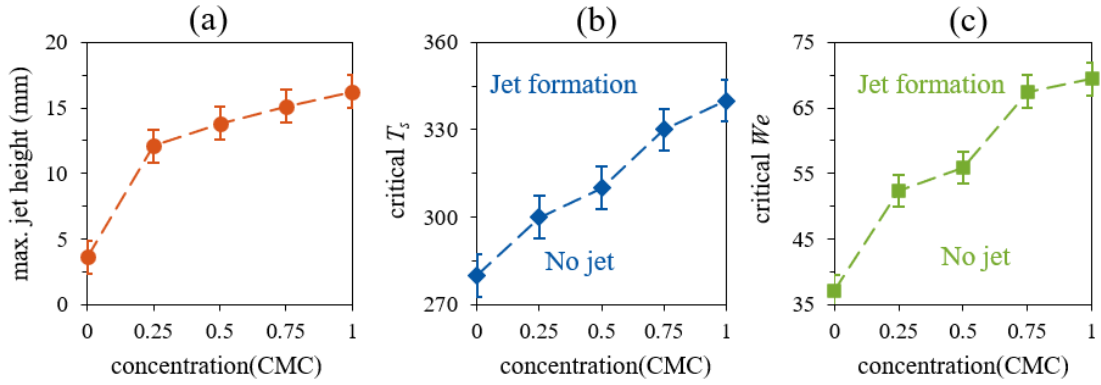


Figure 5.14: Jet formation dynamics: (a) maximum jet height (b) critical substrate temperature (T_s) and (c) critical We with respect to SDS concentration of impinging droplets with high impact velocity $U=1\text{m/s}$ at surface temperature $\sim 400^0\text{C}$.

For CTAB solution droplets the T_{DL} variation had a narrower range of 250⁰C (1 CMC) and 225⁰C (0.125 CMC). Also, the upper temperature limit of transition boiling reduces with We as T_{DL} was observed to decrease with We . Similarly, the explosive boiling region with central jet ejection is also occurring over a wider phase space due to higher chances of jet formation and fragmentation in the surfactant solutions. In this context, it is worthwhile to discuss the competition between both transition boiling and explosive boiling regimes against impact We . On the one hand, we notice that both SDS and CTAB solution droplets show the onset of transition boiling at lower substrate temperature even at higher We . On the other hand, explosive boiling exhibits at higher substrate temperatures even at low We . Thus, finally, from fig.5.15., the overall Leidenfrost regime is suppressed with an increase of surfactant concentration. For a specific fixed surfactant concentration, the Leidenfrost regime also shrinks (reduced shaded area) further with an increase in impact We .

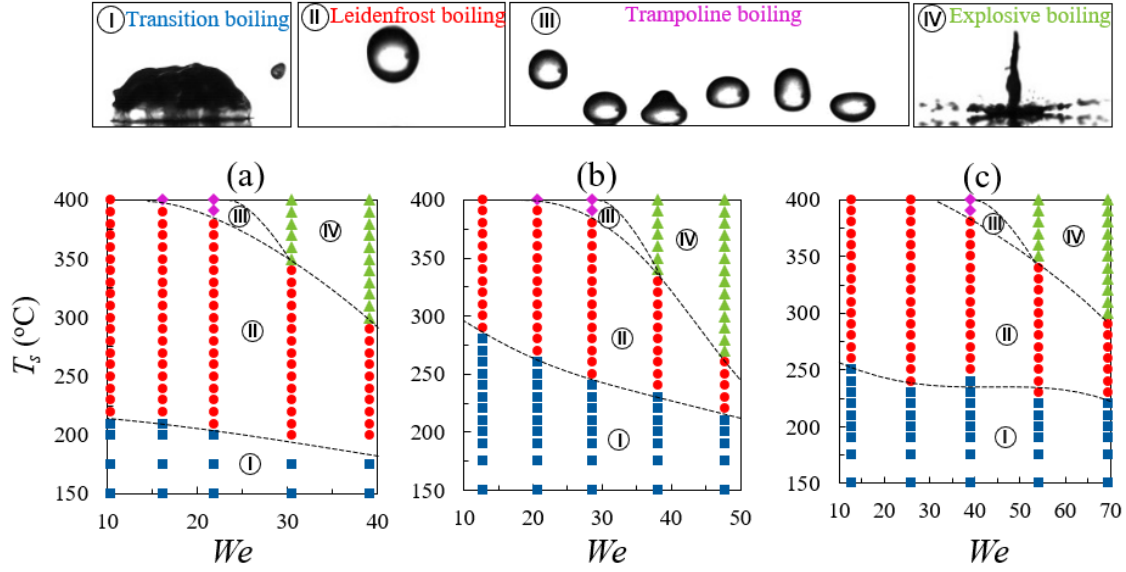


Figure 5.15: Different boiling regimes impacting droplets of (a) water, (b) SDS, and (c) CTAB. The top row shows representative snapshots of the different boiling behaviors.

5.4 Conclusions

The present study showed that both the surfactants (SDS and CTAB) are effective in increasing the Leidenfrost point T_{DL} compared to water. The T_{DL} was decreasing with Weber number for a fixed concentration, whereas, the T_{DL} was increasing with surfactant concentration. Scaling relationships of T_{DL} with We and Oh was proposed. At temperature significantly higher than T_{DL} (400°C), the drop impact behavior was shown to be dependent on the impact velocity. At lower impact velocity ~ 0.5 m/s, the droplets exhibited trampolining dynamics. On increasing the impact velocity ~ 1 m/s, droplets fragmented into secondary droplets along with the emergence of a vertical jet in the central region during the recoiling process. Finally, we have prepared a phase map of the different boiling states like transition, Leidenfrost, trampolining dynamics, and explosive boiling (with fragmentation and central jet formation) as a function of temperature and We . We believe our study will be helpful and instrumental in carrying out experiments and numerical simulations of surfactant droplet dynamics on heated substrates with further details. Also, the findings may have substantial implications in the design and development of safer and more reliable high-temperature thermal management strategies in certain niche utilities.

Chapter 6

Morphed inception of dynamic Leidenfrost regime in colloidal dispersion droplets

6.1 Introduction

When a droplet is deposited on a surface heated at temperatures much higher than the liquid's boiling point, the droplet levitates on its own vapour cushion, and this is known as the Leidenfrost effect [168]. Droplet impact on superheated surfaces find direct implications towards utilities in various domains, like spray cooling[20], fire suppression [169], electronics cooling[170], material quenching [25] , cooling of nuclear fuel rods [171], and so forth. The thin, micron-scale vapor layer acts as a thermal insulator at the solid-liquid interface, and significantly affects the heat transfer from the heated substrate to the fluid droplet. At the same time, it propels the droplet away from the surface via intermittent levitation. Hence, often it is desirable to delay the onset of the Leidenfrost effect for better thermal management of overheated components. Researchers have explored in various directions and targeted to increase the Leidenfrost point by different techniques, viz., addition of nanoparticles [172], [173], polymers[73, 149], surfactants [9, 75], nanobubbles [174]and use of an external electric field [175]. Duursma et al. observed and reported the effect of droplet receding breakup and recoiling height on the rebounding nature during Leidenfrost stage [172]. Similarly, Paul et al. reported that the influence of nanoparticle deposition on the vapor layer formation and the disruption of Leidenfrost state[173]. Bertola et al. observed and reported the behavior of polymeric non-Newtonian fluid droplets and the shift of the Leidenfrost point [149].

Dhar et al. showed the behavior of polymeric droplets during the droplet's retraction phase and the effect of threshold impact velocity and polymer concentration on the increase of the Leidenfrost point [73]. Chen et al. have shown that adding alcoholic surfactants may delay the Leidenfrost effect . Both 1-octanol and 2-ethyl-hexanol alcoholic surfactant droplets greatly affect the spreading dynamics on a superheated surface. They observed that an increase in the alcoholic surfactant concentration led to increase in the maximum spreading factor and shortens the maximum spreading time at a particular impact height due to great reduction in equilibrium surface tension. Similarly,

they have also revealed and reported the effect of bubble bursting and bubble coalescence behaviour on the shift of the Leidenfrost point[75].

Similarly, Gudlavalleti et al. experimentally aimed to postpone the dynamic Leidenfrost temperature by adding anionic and cationic surfactants to water droplets. They invoked the role of dynamic surface tension on the maximum spread factor during Leidenfrost stage. They reported the effect of Taylor-Marangoni instability on the shift of T_{DL} with various surfactant concentrations at a fixed We . They have also revealed the effect of novel thermohydrodynamic events like Trampoline and Jetting dynamics during droplet impact on superheated surfaces[9]. Later, Gudlavalleti et al. introduced a novel methodology of oxygen nanobubbles dispersed droplets on the augmentation of dynamic Leidenfrost point. They discussed the effect of CCR mode of contact boiling stage for different nanobubble concentrations with various We . Next, they noticed that thin cylindrical jet splashing behaviour of nanobubble dispersed droplets during transition boiling stage. They have also revealed and reported the role of rewetting velocity on the delay and suppression of Leidenfrost effect[174]. Besides, Villegas et al. executed numerical simulations to examine the shape and spreading behaviour of a droplet during the Leidenfrost state, for different Weber numbers ($We = (\rho U^2 D_o / \sigma)$, represents the ratio of inertial force to surface tension force) and validated with experimental observations. They have also explained the influence of loss of momentum due to viscous dissipation inside the droplet on the droplet shape evolution and on the satellite droplet formation[71]. Qiao et al. performed numerical simulations of the Leidenfrost droplet (using the Lattice Boltzmann method) on liquid pools and reported the role of different non-dimensional numbers such as Stefan number (is defined as the ratio of sensible heat to latent heat), Bond number (described as the ratio of gravitational force to capillary force) and Ohnesorge number (is defined as the ratio of viscous forces to inertial-capillary forces), pool depth and impact height on droplet impact hydrodynamics. They have also numerically examined and reported the role of Stefan flow on the generation of strong airflow between drop and the heated pool during Leidenfrost state [72].

Later, Ulahannan et al. [76] studied the effect of the shape of nanoparticle on the shift of Leidenfrost point. They conducted experiments of nanocolloidal droplet impact on aluminum heated surface with cylindrical rod shape and spherical shape. They observed that colloidal droplets with rod-shaped nanoparticles dispersion exhibit a larger spread factor than droplets with spherical-shaped nanoparticles dispersion. They have also reported that Leidenfrost point is lesser for nanofluid droplets than water droplets. Further, experimental studies have also highlighted the role of surface roughness on the modulation of the Leidenfrost point, by providing different geometries of the various microstructures [77–79] with different surface engineering techniques viz., polished, particle blasted, porous ceramics [176], particle coated [177] and rough sanded surface finish[68]. Along a different approach, Biance et al. examined and reported the effect

of droplet size and shape on the stability of the vapor layer formation during the Leidenfrost state [34]. Tran et al. showed the scaling analysis for the maximum spreading of the impacting droplet on the both hydrophilic and hydrophobic heated surfaces, and distinguished the different boiling regimes as contact boiling, gentle, and spray film boiling [70]. Next, Khavari et al. experimentally examined and segregated the different boiling regimes as spreading regime, bubbly boiling, fingering boiling and Leidenfrost regime based on the various fingering patterns of the droplet during the Leidenfrost regime [178]. Nanocolloids have great potential on the efficiency of cooling in various thermal engineering applications, such as emergent core cooling of nuclear reactors in nuclear powerplant, electronics cooling and material quenching etc. The enhanced thermal properties of nanocolloids play a vital role in thermal management systems [179], [180] and in spray cooling and drop-wise cooling applications [11, 181, 182]. Some of the earlier studies have reported various mechanisms on the shift of T_{DL} with different kinds of fluids like polymers, surfactants, and nanobubbles [9, 73, 75, 149, 174]. Though, previous studies [173], [76] have examined the effect of size and shape of nanoparticles on the Leidenfrost temperature a clear insight into the mechanism responsible for the change in T_{DL} with nanocolloidal droplets is still lacking. In this present article, we mainly focus on understanding the impact thermo-hydrodynamic behaviour of the nanocolloidal droplets during dynamic Leidenfrost state with different We ranging from 10-168 in detail and targeted to delay the Leidenfrost regime.

6.2 Materials and methods

A schematic of the experimental setup used in this study is illustrated in fig.6.1. We used a smooth polished square (180mm \times 180mm) stainless-steel plate, mounted over heating coils, as a hot substrate (Holmarc Opto-Mechatronics Ltd., India). Similar to our previous studies [9], [174] substrate temperatures ranging from 150°C to 400°C was altered by using a digitized temperature controller. A T-type thermocouple was installed into the substrate and was used to measure and control the temperature at ~ 1 mm below that of the top surface (where drop impacts). The temperature controller maintained the substrate at near isothermal conditions ($\pm 2 - 3^\circ C$ deviations) from the set temperature point. In order to change the We ($We = (\rho U^2 D_o / \sigma)$), where ρ , U , D_o and σ represents the density, impact velocity, pre-impact droplet diameter and surface tension respectively. We measured the impact velocity by using following relation $U = \sqrt{2gH}$, where g , H denotes acceleration due to gravity and the impact height from the droplet to targeted heated substrate. The release height of the droplet was changed by a droplet dispenser with a digitized controller [94]. A microliter syringe (± 0.1 l volumetric accuracy) attached to the droplet dispenser was utilized to dispense the droplets of required volume through a flat head steel needle (22 gauge). A high-speed camera (Fastcam Mini-100, Photron, UK) was utilized to capture the hydrodynamic events of Leidenfrost phenomenon. All the experiments were recorded using a macrolens (Nikon) of 105mm focal length by

maintaining 4000 frames per second and 1024×1024 resolution with the spatial resolution of $8.47 \mu\text{m}$ per pixel and shutter minimum exposure time of $2.7 \mu\text{s}$.

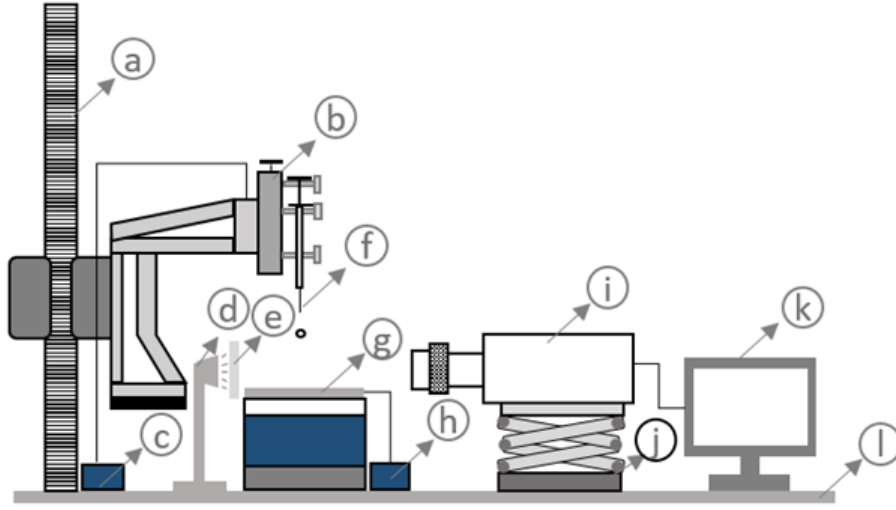


Figure 6.1: Schematic of the experimental setup: (a) Motorized xyz stage (b) Droplet dispensing mechanism (DDM) unit (c) DDM controller (d) strobe light (e) Diffuser (f) Microliter syringe (g) Hot substrate (h) Hot substrate controller (i) High speed camera (j) Micron Lab jack (k) Computer for data acquisition and camera control (l) Vibration isolation table top

Before carrying out each experiment, we cleaned the test substrate with acetone to remove dirt and contaminants from the surface. In this present study, we used colloidal dispersions of aluminium oxide (Al_2O_3) nanoparticles (Alfa Aesar India, $> 98.5\%$ purity, average particle size of $20\text{-}30\text{nm}$) in deionized (DI) water as the test fluids. To prepare nanocolloids, we have dispersed different weight percentages of nanoparticles ranging from 0.1% to 1% into water.

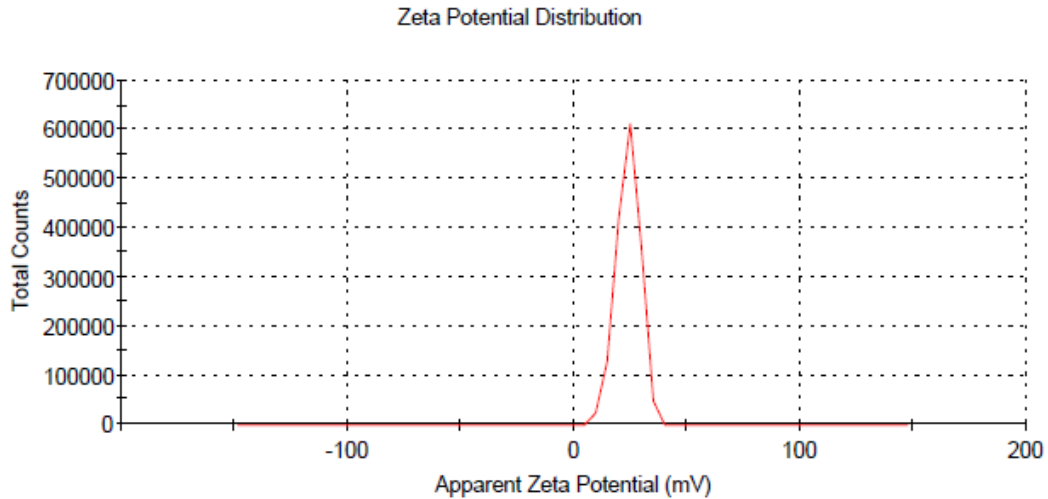


Figure 6.2: Zeta Potential distribution of the highest concentration(1% w/w) of the operating range of the nanocolloids used.

As earlier reported [183], the nanofluids were mechanically stirred for 30mins and further subjected to ultra-sonication for 2 hours to disrupt the agglomeration of nanoparticles. The

synthesized colloids were observed to be stable for over 24-36 hours, which surpasses the experimental timescales by a large margin. We performed a zeta-potential measurement using Zetasizer NanoZSP and observed a zeta-potential value of +28.8 mV at the highest particle concentration (1%w/w Al_2O_3 , refer fig.6.2.). This measurement confirmed the stability of the colloidal solutions. We adopt pendant drop method to measure the surface tension of the nanocolloidal droplets. We have conducted Rheological flow curve test with parallel plate geometry (PP-20) to determine the shear viscosity of nanocolloidal solutions. Similarly, we measured both $(D_r)_{max}$ and D_o through image processing by using ImageJ software. All thermophysical properties of nanocolloids have been tabulated in table.6.1.

Table 6.1: Thermophysical properties of impacting nanocolloidal droplets at $25^{\circ}C$: pre-impact droplet diameter D_o (mm), density ρ (kg/m^3), surface tension σ (mN/m), viscosity η (mPa-s).

| Liquid/particles | D_o | ρ | σ | η |
|-----------------------|-----------|--------------|-----------|-------------|
| DI water | 2.64 | 995.67 | 71.03 | 0.791 |
| Al_2O_3 (0.1-1%w/w) | 2.78-2.96 | 997.9-1024.7 | 70.8-69.7 | 0.806-0.807 |

6.3 Results and discussion

In this section, we discussed the impact dynamics of the nanocolloidal droplets for different We and for different substrate temperatures ($150^{\circ}C$ to $400^{\circ}C$). The minimum temperature at which the droplet showed rebound behavior for first time, with minimal spraying was considered as the dynamic Leidenfrost temperature (T_{DL}). The corresponding boiling state is defined as the rebounding Leidenfrost state and residue-rebounding Leidenfrost state for water and nanocolloidal droplets respectively.

6.3.1 Transformation of contact boiling in nanocolloidal droplets ($T_s \sim 150^{\circ}C < T_{DL}$)

At the lower end of the substrate temperatures tested ($T_s \sim 150^{\circ}C$), the contact boiling stage was observed along with residue formation from the nanocolloidal droplets. Fig.6.3., first (side view) and second (top view) columns in the array matrix represented with dashed lines illustrates the temporal evolutions of the nanocolloidal droplets during the contact boiling ($T_s \sim 150^{\circ}C < T_{DL}$) regime. Unlike DI water droplets, the nanocolloidal droplets shows various transformations in the contact boiling with an increase in contact time. We categorized the transformations in such that, where parent nanocolloidal droplet maintains contact with heated substrate along with secondary droplets spraying termed as spray boiling [184], [185] (yellow color shaded region in fig.6.3.). After attainment of spray boiling regime, as similar to earlier reported [178], nanocolloidal droplet also exhibits contact boiling together with foamy kind of bubbles nucleation with an increase in contact time is defined as bubbly boiling [186] (green color circumscribed region in fig.6.3.).

With furthermore increase of contact time, the contact boiling regime of nanocolloidal droplets left thin residue disk over the hot surface before complete evaporation of liquid is described as residue deposition stage. The diffusion of the nanoparticles also plays a vital role on residue formation and affects the amount of residue left on the hot surface before evaporation[187]. Fig.6.3.(see even columns)shows the size of residue changes with nanoparticle concentration. Such residue formation was not observed in case of water droplets (fig. 6.3. 1st row, 11 – 12th columns). With an increase in concentration of nanoparticles, the boiling period decreased. Consequently, the disk containing the nanoparticles is also deposits sooner may be due to the more conduction from the residue disk to the liquid. For instance, the 1%w/w nanoparticle concentration forms residue on the heated substrate at 679.5 ms at a fixed $We \sim 10$. But, at a same We , low nanoparticle concentration (0.1%w/w) deposits residue on the heated substrate at 1018 ms.

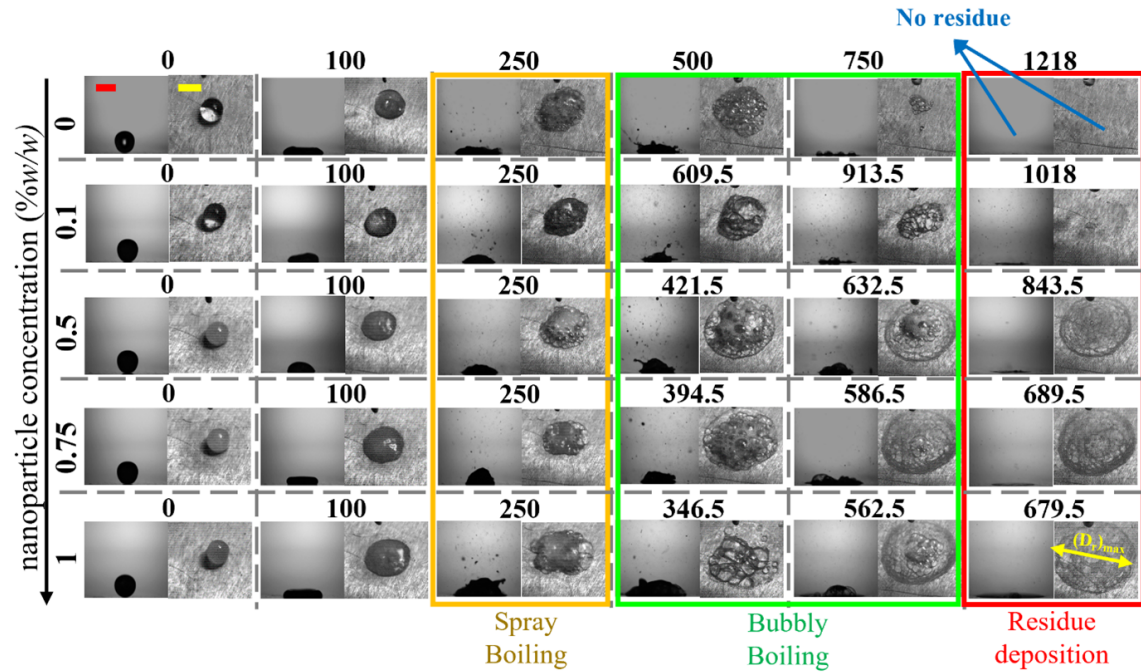


Figure 6.3: shows various transformations of contact boiling in nanocolloidal droplets at $We \sim 10$ at ($T_s \sim 150^0C$). In the array matrix (represented with gray colour dashed lines) of fig.6.3., the cluster of two images represents side view and top view respectively and all timeframe numbers (0, 100, 250, 500, 750 and 1012) above each cluster are in ms (milliseconds). The scale bar in the top-left corner of the first (side-view) and second (top view) columns represents 2.96mm. In fig.6.3., yellow, green and red color shaded regions represent spray boiling, bubbly boiling and residue deposition stage respectively.

Fig.6.4. represents the variation of non-dimensionalized residue disk $D^* = (D_r)_{max}/D_o$; where $(D_r)_{max}, D_o$ denotes the maximum diameter of the residue disk on the heated substrate and pre-impact droplet diameter respectively. We have considered the residue diameter(D_r) of nanocolloidal droplet as the diameter of the thin residue disk left over the hot substrate after complete evaporation of the liquid droplet. The residue resembling a thin disk increased in size with an increase in nanoparticle concentration at a fixed We

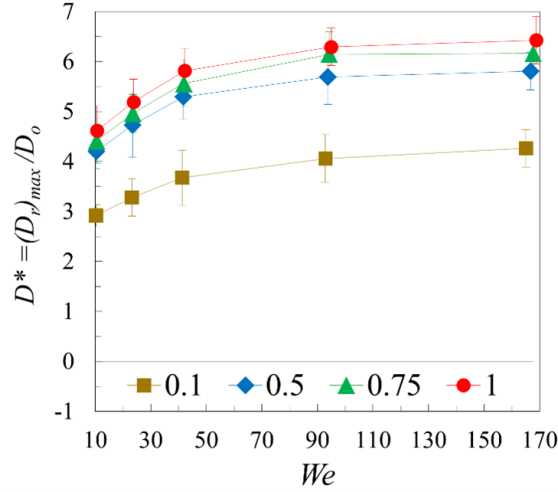


Figure 6.4: Variation of non-dimensional residue diameter (D^*) of different concentrations of nanocolloidal droplets over different We at ($T_s \sim 150^\circ\text{C}$). The legend values represent %w/w concentration of nanoparticles of nanocolloids.

(fig.6.4.) due to the more robust bubbly and foaming kind of behavior (see 7–10th columns of fig.6.3). Similarly, it is also noticed that for a particular nanoparticle concentration, the D^* increases with an increase of We due to higher impact momentum of the droplet.

6.3.2 Role of nanoparticle concentration on T_{DL}

Fig.6.5a. shows the temporal evolution of nanocolloidal droplets of varying concentration at their corresponding T_{DL} . In fig.6.5a., unlike water droplets, it was observed that the onset of the Leidenfrost phenomenon was accompanied by the minimal spraying of secondary droplets. We presented the effect of nanoparticle concentration on T_{DL} in fig.6.5b. and observed that T_{DL} increases with an increase in nanoparticle concentration at a particular We .

Further, it is also noted that the onset of T_{DL} decreases with the rise in We for the same nanoparticle concentration. We performed experiments with the temperature difference of 5°C . To ensure the repeatability of the experiments, we have provided the vertical error bars on main T_{DL} data point in fig. 6.5b. Based on earlier studies [173], [184] we noticed that the residue deposition on the heated surface during the spreading stage of the nanocolloidal droplet affects the retraction and bouncing behavior of the droplet. The deposited thin residue disk morphs the heated substrate roughness, and enhances the generation of bubble nucleation sites. Although, the diffusion of nanoparticles play a crucial role on the shape, thickness, and amount of residue disk left on the heated substrate, we believe that the additional provision of nucleation sites beneath the droplet due to the residue left on the heated substrate play more dominant role on the bubble coalescence. On the one hand, the hot surface wettability greatly alters due to the deposition of the residue beneath the droplet during the spreading stage. It strongly influences the bubble formation, number of bubble nucleation sites, bubble growth and detachment behaviour of vapor bubbles. It consequently affects the retraction and rebounding behaviour of

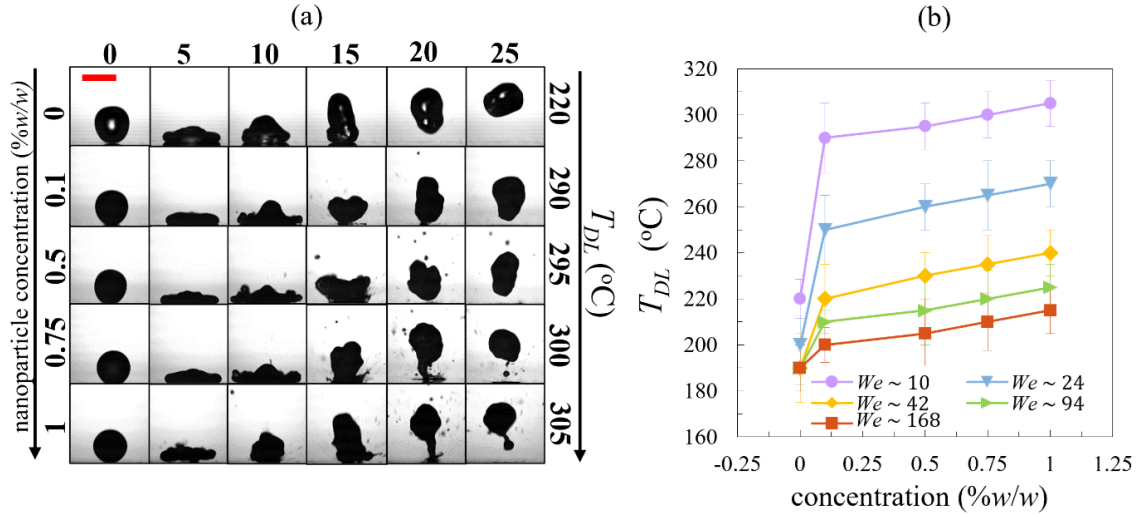


Figure 6.5: (a) Temporal evolutions of the side-views of impacting nanocolloidal droplets with low $We \sim 10$ at their respective T_{DL} 's. All timeframe numbers (0, 5, 10, 15, 20 and 25) above each image in fig. 6.5a are in ms (milliseconds). (b) Change in the T_{DL} over nanoparticle concentration ranging from 0.1% w/w to 1% w/w for different impact velocities. The scale bar represents 2.96mm.

nanocolloidal droplet during Leidenfrost regime. On another hand, the critical bubble radius and critical distance between two nucleation sites also affect the bubble coalescence behavior [173], [184]. From earlier works [173], [184], it was noticed that the bubble departure diameter is below the half of the threshold nucleation sites gap, it is difficult for bubbles to coalesce to form stable vapor layer.

Thus, a higher substrate temperature is required to accelerate more vapor bubbles to achieve the Leidenfrost state. Apart from that, generation of the nucleation sites beneath droplet also depends on the nanoparticle concentration and its diffusive nature. From the fig.6.5a, the thin residue left on heated substrate during spreading state strongly affects the retraction behavior of nanocolloidal droplets by forming more nucleation sites beneath the droplet with increase in nanoparticle concentration. We believe that the departure diameter of the vapor bubbles from residue becomes smaller than the half of the critical nucleation site gap with increase in nanoparticle concentration. If the departure diameter of vapor bubbles from residue nucleation sites during retraction is less than the threshold nucleation site gap, it will fail bubbles coalescence and not support the formation of a stable vapor layer due to Taylor instability. [173]. Therefore, a higher surface temperature is required to intensify bubble coalescence and generate more nucleation sites for the formation of a stable vapor layer. Hence, T_{DL} was delayed with increasing nanoparticle concentration at constant We .

6.3.3 Role of Weber number (We) on T_{DL}

Next, in this section, the role of We on the T_{DL} of nanocolloidal droplets is discussed in detail. Fig.6.6a. shows the temporal evolutions of the nanocolloidal droplets

of 1% w/w nanoparticle concentration with different We at their respective T_{DL} s. It is observed from the fig.6.6a., that the nanocolloidal droplet undergoes vigorous spraying during the onset of the Leidenfrost regime. When nanocolloidal droplet impacts with low impact momentum, the droplet bounces off the surface with very minimal splashing (see the 1st row of fig.6.6a., but in higher impact momentum case, the parent droplet bounces off with vigorous spraying and secondary droplet atomization (see the 5th row of fig.6.6a.) From fig.6.6a., it was noticed that the spreading diameter of the liquid droplet increases with impact momentum (impact velocity) and lead to form a larger residue disk beneath the nanocolloidal droplet. The significant increment in the nucleation sites beneath the droplet during retraction promotes higher rate of bubble coalescence and quicker vapor layer formation relatively at lower substrate temperatures [187].

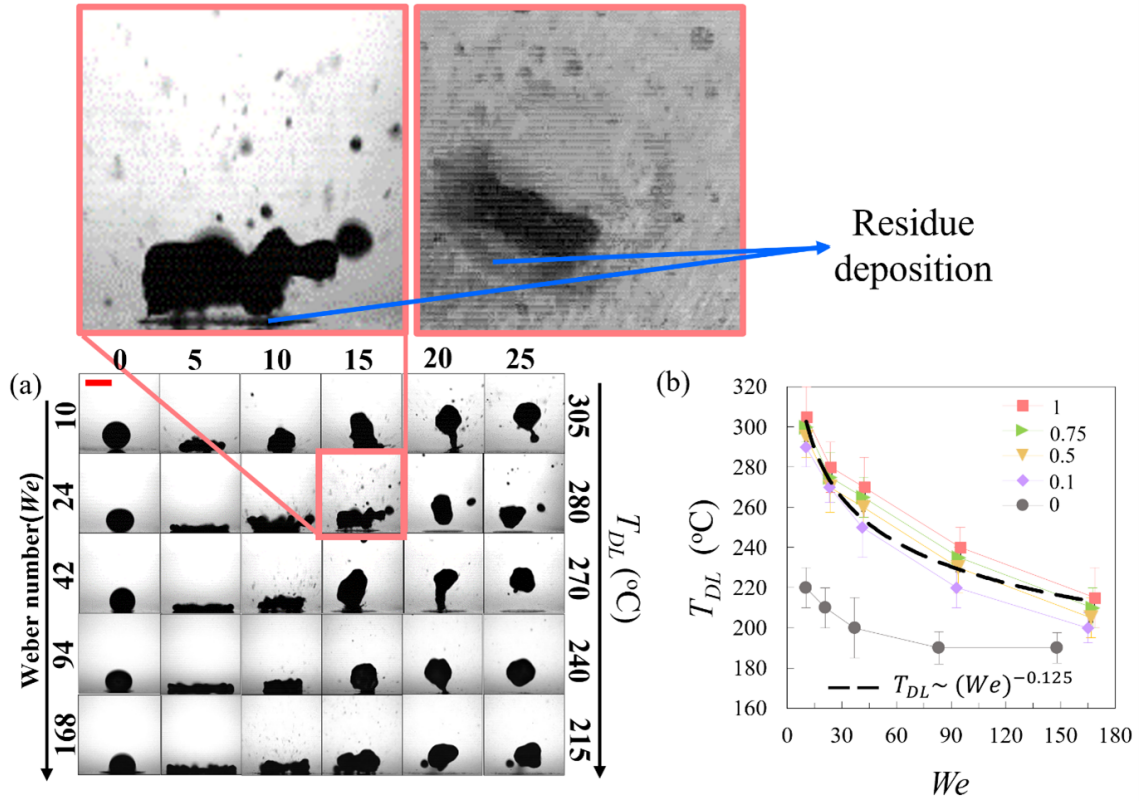


Figure 6.6: (a) Temporal evolutions of the side-views of impacting nanocolloidal droplets with 1% w/w nanoparticle concentration at their respective T_{DL} 's (b) Change in the T_{DL} over different We with the variation of nanoparticles concentration. In fig.6.5b., all legend values were represented as %w/w. All timeframe numbers (0, 5, 10, 15, 20 and 25) above each image in fig. 6.6a. are in ms (milliseconds). The above zoomed version of side view and top view snapshots evident the residue deposition during levitation of parent nanocolloidal droplet at their respective (T_{DL}). The scale bar represents 2.96mm.

Further, we depicted the role of impact We on the T_{DL} in fig.6.6b. From fig.6.6b., it is noted that the T_{DL} decreases with an increase of impact We for a particular nanoparticle concentration. This decreasing trend of T_{DL} with increasing We was similar to the Leidenfrost studies with other aqueous solutions of polymers, surfactants and

nanobubbles[10], [9, 174]. In fig. 6.6b., we have provided the vertical error bars on main data point to ensure the repeatability of the experiments. The propensity of the generation of the more nucleation sites may increased due to larger size of residue disk with an increase in We . Hence, we theorize that the increment in the nucleation sites lead to enhance the probability of the bubble coalescence and form stable vapor sheet relatively at low substrate temperatures due to larger residue disk formation. Thus, T_{DL} decreases with an increase in We for a particular nanoparticle concentration. With the aid of scaling analysis, the effect of T_{DL} with impact We yield $T_{DL} \sim We^{-0.125}$.

6.3.4 Scaling correlation of T_{DL} with governing Weber number (We) and Ohnesorge number (Oh)

From the earlier subsection 3.3., it has been revealed that change in the T_{DL} with We as follows $T_{DL} \sim We^{-0.125}$. In this section, we tried to develop the scaling correlation over experimental T_{DL} values with the minimum possible error band through the least square regression method. Along with the dominance of inertial and surface tension forces, it is also essential to consider another non-dimensional number called the Ohnesorge number($Oh = \sqrt{\rho\sigma D} = We/Re$), reflects the mutual dominance of viscous and inertial-capillary forces of nanocolloids.

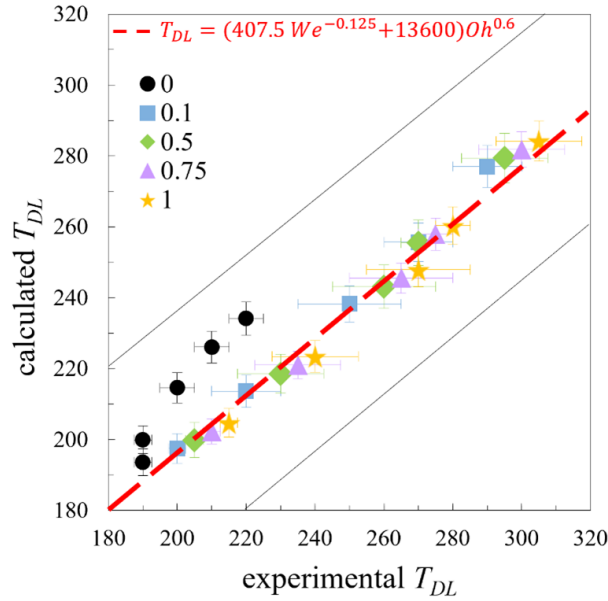


Figure 6.7: (a) Fitting of scaling correlation (calculated T_{DL}) over experimental T_{DL} of various concentrations of the nanocolloids. The legend values represent %w/w concentration of nanoparticles of nanocolloids. Error bars represent the fluctuation of T_{DL} data point due to repeatability of the experiments.

We tried to fit the experimental results of T_{DL} in terms of We and Oh with the minimum possible confidence interval yields the following relationship: $T_{DL} = (aWe^{-b} + c)Oh^d$. Through least squares regression, we proposed the scaling correlation of T_{DL} in terms of We (almost with $\pm 20\%$ error band, refer to fig.6.7.) is reflected as: $T_{DL} = (407.5We^{-0.125} +$

13600) $Oh^{0.6}$. We believe that this developed correlation helps future researchers in this field.

6.3.5 Boiling regimes of colloidal nanoparticle fluid droplets

In this section, we present the different boiling regimes [187] of nanocolloidal droplets at various impact We in fig.6.8. The segregated boiling regimes were named as contact boiling (C), spray boiling (S), rebounding Leidenfrost (R), Residue-rebounding Leidenfrost (RR) and Fragmenting boiling (F) respectively.

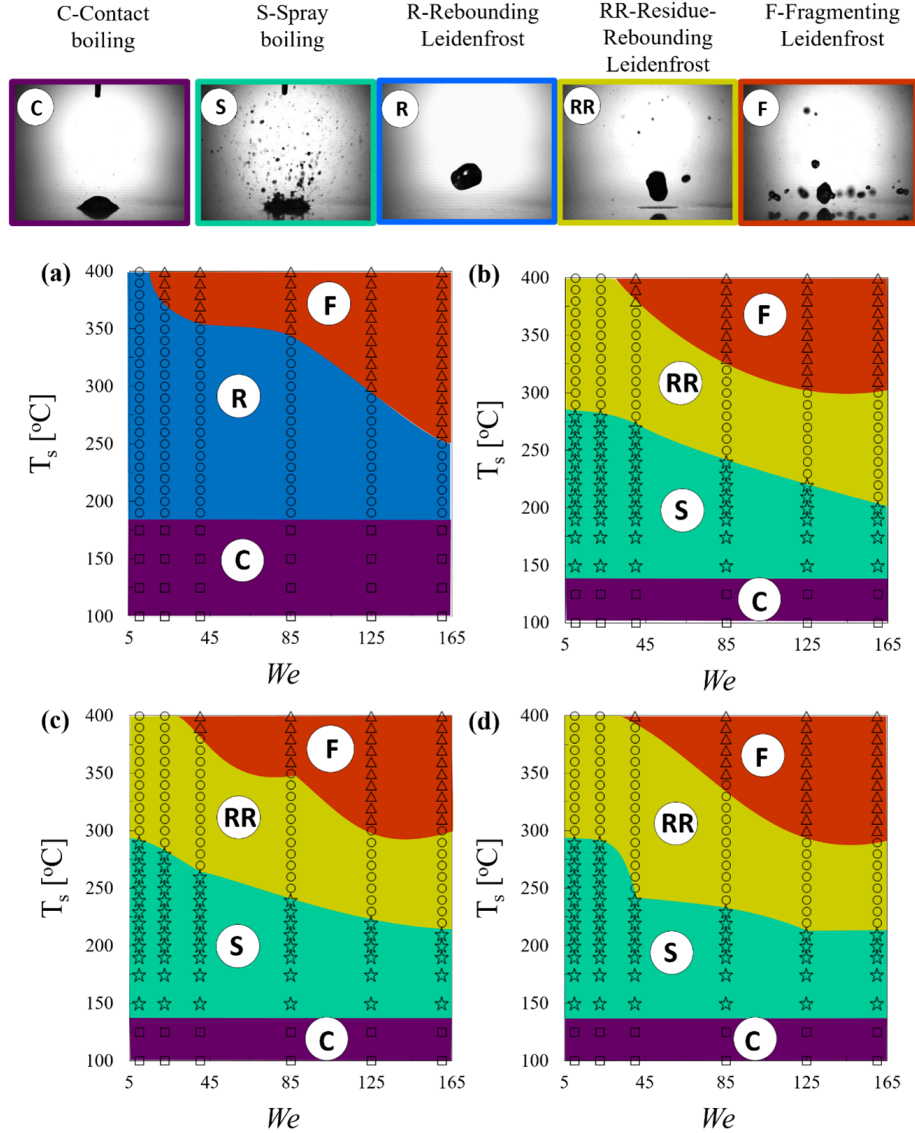


Figure 6.8: Various boiling regimes of impacting nanocolloidal droplets with varied We of (a) deionized water (b), (c) and (d) shows nanocolloidal droplets with the concentration of 0.1%, 0.5% and 1% w/w respectively. The top row shows paradigmatic images of the different boiling behaviors: C-Contact boiling, S- Spray boiling, R-Rebounding Leidenfrost, RR-Residue-Rebounding Leidenfrost boiling and F-Fragmenting Leidenfrost.

Contrary to the DI water droplets, spray boiling and Residue-rebounding Leidenfrost (RR) behaviors have been exhibited during the droplet impact of nanocolloidal droplets

on hot surface. Unlike in DI water droplet case, the nanocolloidal droplet regime phase map shows the rebounding Leidenfrost regime with residue deposition (see yellow color shaded regime area) has been suppressed and compensated with contact boiling and spray boiling. Compared to DI water droplets, the addition of nanoparticles lead to increase the T_{DL} as high as $70^{\circ}C$ at a particular $We \sim 10$. In spite of pure rebound behavior, both spray boiling (see green color shaded region) and residue-rebounding Leidenfrost boiling regimes trigger more with an increase in impact We of nanocolloids for a specific concentration of 1% w/w and results in suppressing the rebounding Leidenfrost boiling behavior. Vigorous spraying of nanocolloids attains Leidenfrost state relatively at higher temperatures than DI water droplets at a fixed We . Although both rebounding Leidenfrost and residue-rebounding Leidenfrost behaviors are qualitatively different, in the end, they fall into the same Leidenfrost (rebound of parent droplet maybe with an additional residue deposition) state. In this context, it is imperative to discuss the mutual dominance of residue-rebounding Leidenfrost regime and fragmenting Leidenfrost regime in nanocolloidal droplets against different impact We . Unlike the DI water droplet case, the nanocolloidal droplets residue-rebounding Leidenfrost regime transform into fragmenting Leidenfrost regime relatively at higher substrate temperatures at a fixed $We \sim 160$ due to the lack of retraction surface energy against stored impact energy. Thus, finally, from fig.6.8., we emphasize that the overall Leidenfrost (rebounding) regime is suppressed and compensated by spray boiling with an increase in nanoparticle concentration for a fixed We and the Leidenfrost (rebounding) regime shrinks more (see yellow colored shaded area) with a rise in impact We .

6.4 Conclusions

In summary, we have shown that nanoparticles can be effective in enhancing the T_{DL} . We have shown the onset of residue deposition of nanocolloidal droplets and their vigorous spraying behavior during the contact boiling stage. Next, we reported the role of residue deposition on both bubble coalescence and vapor layer formation against Taylor instability during the Leidenfrost regime. Next, we noticed that an increment in T_{DL} with an increase in nanoparticle concentration at a fixed We and further report the decrement in the T_{DL} with an increase of impact We . With the aid of scaling analysis, we have also elucidated the role of impact We on the T_{DL} and tried to compare the experimental and fitted T_{DL} with the possible least error band. Finally, based on the rebounding nature of the parent nanocolloidal droplet at different substrate temperatures, we demarcated the boiling regimes of the nanocolloidal droplets as contact boiling, spray boiling, rebounding Leidenfrost, residue-rebounding Leidenfrost and fragmenting Leidenfrost. We believe this study will be relevant for researchers using the efficacy of nanocolloids in heat transfer applications.

Chapter 7

Augmenting the Leidenfrost temperature of droplets via nanobubble dispersion

7.1 Introduction

The Leidenfrost effect is the phenomenon wherein a droplet levitates above its vapor cushion, formed on a substrate heated to a temperature sufficiently high above the saturation temperature [33, 39]. The heat transfer rate substantially drops at the Leidenfrost state as the vapor cushion is a bad conductor of heat. Discovered by (in the vicinity of the 1750's) a German doctor, Johann Gottlob Leidenfrost [188], the phenomenon holds significance in the modern applications involving liquid-vapor phase change and multiphase thermo-hydrodynamics. In today's world, the Leidenfrost effect is of prime concern for the safety and management of nuclear reactors and power plant systems. Also, the study of droplet impact on heated substrates is useful in optimal performance of myriad applications like spray cooling in fire-fighting, sprinkling, and electronic cooling [21], combustion dynamics of direct fuel injection [189], drag reduction [143] or directed motion [144]. Thus, the Leidenfrost effect also holds importance in droplet, spray and jet impingement systems operating at high temperatures.

With the advancements in high-speed photography, laser based optical diagnostics, and interferometry, experimentalists have been able to unravel various features of the Leidenfrost dynamics. Self-propulsion dynamics of drops of various sizes at high temperatures ($\sim 300^\circ\text{C}$) was explored using Particle image Velocimetry [147]. The vorticity distribution within the drop was noted to vary depending upon the capillary length scale of the fluid. Droplets with a diameter lesser than the capillary length of the droplet fluid showed the existence of one vorticity, whereas larger droplets displayed the existence of two internal vortices. Also, it was shown that propulsion mobility is dependent on the droplet size. The dynamics of the self-propelling droplets may be due to the vapor film whose flow can entrain fluid due to viscous effect as well as thermal gradient induced Marangoni effect [190]. Star-shaped droplets with arms (4, 6 and 8 in number) were observed in the Leidenfrost state. The formation of these transient states was attributed to the Faraday instability triggered by the vibrations of the vapor cushion [191]. Tran

et al. [34] performed interferometry measurements to reveal the structure of the vapor layer beneath the droplets. They showed that the nondimensional maximum spreading diameter during gentle and spray boiling regimes scales with the Weber number ($\sim We^{0.4}$), which is steeper than the power-law scaling at ambient temperatures ($\sim We^{0.25}$).

Enhancement of Leidenfrost point or temperature (LFT) can be achieved by various methods, viz. dispersion of polymer additives [73, 149], surfactants [9, 75] or nanoparticles [173, 192]. Other avenues of LFT enhancement were achieved by substrate modification using femtosecond laser-based surface processing [193, 194] or by the use of an electric field [175]. The aim of this thesis is to augment the LFT of fluids by generating and dispersing stable nanobubbles (NB) in the fluid. Fluid dispersions of nanobubbles have recently emerged in the limelight [195–199] due to their potential in water treatment, food processing and sonochemistry.

The nanobubbles possess high surface to volume ratio (the ratio varies as $6/d$ for spherical shapes, where d is diameter) and high mass transfer coefficient. The surface zeta potential [197] of nanobubble dispersions is observed to be approximately -33 mV which is well within the colloidal stability regime of nano-suspensions. One of the peculiar properties of nanobubbles is high longevity and thermodynamic and colloidal phase stability, and it has been experimentally shown that nanobubble dispersions can be stable for more than 2-4 months [196].

As per Epstein and Plesset's theory [200], the lifetime [201] of a bubble is expressed as :

$$t_f = (R^2 \rho_g) / (2C_s (1-f)) \quad (1)$$

where, t_f , R , ρ_g , C_s and f represents the lifetime of the bubble, radius of the bubble, density of the gas bubble, saturation concentration and gas saturation ratio respectively. For nanobubbles [202], the lifetime turns out to be in microseconds (for ~ 100 -200 nm diameter bubbles dispersed in water, $t_f = 20$ -80 μ s), considering that Henry's law and Young-Laplace equation are valid at the nanoscale. In stark contrast, multiple experimental results show evidence of the existence of the nanobubbles [196–198] for a very long time. The extra-longevity of nanobubbles is still puzzling and there is no universal theory to explain the behavior of nanobubbles. Some of the recent works demonstrated that the ion-enrichment at the interface may plausibly be responsible for such extraordinary stability [196]. The extra-longevity and homogeneously dispersed gaseous phase ensures that nanobubble dispersions have several utilities, like waste-water treatment [203], ultrasound contrast agent [204], therapeutic drug delivery [205], drag reduction in micro-channels [206], promotion of the physiological activity of living organism [207], enhanced germination rate of seeds [208], improved blood oxygenation [209], etc. In this work, we explore how dispersions of nanobubbles in liquids may augment the dynamic LFT of the fluid. We test the premise using deionized water based stable nanobubble dispersions and experimentally explore the droplet impact Leidenfrost dynamics. We further direct the study towards understanding the effect of governing parameters, viz. nanobubble concentration, impact Weber number (We) and Ohnesorge number (Oh) and determine their roles towards the Leidenfrost behavior and other boiling regimes.

7.2 Materials and methodologies

7.2.1 Experimental setup

The schematic view of the experimental setup used in this study has been illustrated in figure.7.1. The setup is similar to our previous reports on Leidenfrost dynamics [9, 73, 75]. We have utilized a programmable hot plate (Holmarc Opto-Mechatronics Ltd., India), with a digitized temperature controller to heat the substrate to temperatures ranging from 150°C to 350°C , and to maintain near-isothermal conditions on the substrate during the experiments. In this study, a square stainless-steel plate ($80\text{mm} \times 180\text{mm}$) mounted on the heating element was used as the substrate. A T-type thermocouple probe was inserted into the stainless-steel hot plate. The thermocouple measures the temperature of the substrate $\sim 1\text{ mm}$ below that of the top surface (where the droplet impacts) and is connected to the programmable temperature controller. The controller maintains the hot plate temperature at near-isothermal conditions ($\pm 2 - 3^{\circ}\text{C}$ deviations from the set temperature data point).

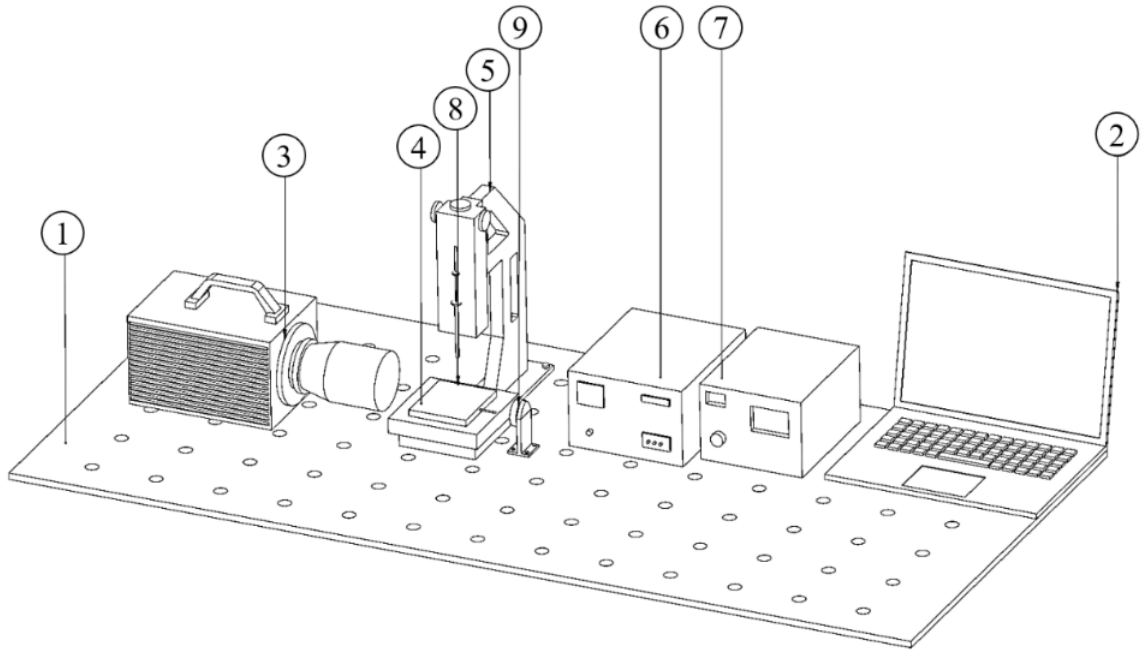


Figure 7.1: Schematic of the experimental setup: (1) vibration-free table top, (2) computer for data acquisition and camera control, (3) high-speed camera with macro lens, (4) hot substrate, (5) droplet dispensing mechanism (DDM) unit, (6) DDM and backlight illumination controller, (7) hot substrate temperature controller, (8) micro liter-syringe, (9) backlight array.

A height alterable droplet dispenser, coupled with a digitized controller unit has been used to generate and release the droplets from different heights. As similar to our previous studies [9],[11], we have performed experiments at different Weber numbers ($We = \rho U^2 D_o / \sigma$) i.e., the ratio of inertial forces to surface tension forces and Ohnesorge number ($Oh = \mu / \sqrt{(\rho \sigma D_o)} = \sqrt{We} / Re$) i.e., the ratio of viscous forces to both inertial

and capillary forces. where, ρ , U , D_o , and σ represent density, impact velocity, pre-impact droplet diameter and surface tension of the fluid respectively. Reynolds number is denoted as Re in the definition of Ohnesorge number. The Weber number (We) is changed by altering the heights to obtain different impact velocities.

A micro-syringe (± 0.1 l volumetric accuracy) attached to the droplet dispenser is used to dispense the fluid droplets of required volume through a flat head steel needle (22 gauge). In this study, we have utilized a high-speed camera (Photron, UK) to capture the droplet impact hydrodynamic events during the Leidenfrost stage. All experiments were recorded at 4000 frames per second at 1024×1024 resolution using a macro lens (Nikon) of constant focal length of 105 mm. Before each experiment, the stainless-steel substrate was cleaned with deionized water followed by acetone to remove the dirt particles and contaminants from the hot surface. The heater was heated to a set temperature data point and allowed to attain a steady-state and then each impact experiment was conducted.

7.2.2 Nanobubble generation

In this study, we used nanobubble dispersed deionized (DI) water as the test fluid. Nanobubbles are ultrafine bubbles with diameters in the submicron range and the mean diameter ranging from 100-200 nm [202]. Oxygen nanobubbles are generated using nanopore gas diffusion method in deionized water as shown in Fig. 7.2.(a) [210]. High pressure oxygen gas was introduced through nanopores and nanobubbles were generated due to the shear force exerted by the water flowing in a milli channel in a cross-flow configuration. The volumetric flow rate of gas and pressure plays an important role in controlling the mean diameter of nanobubbles and concentration of nanobubbles. The optimum flow rate and gas pressure used in this work are 2 lpm and 3 bar respectively. The experimental set was run for 60 mins only as there is no further significant increase in the concentration.

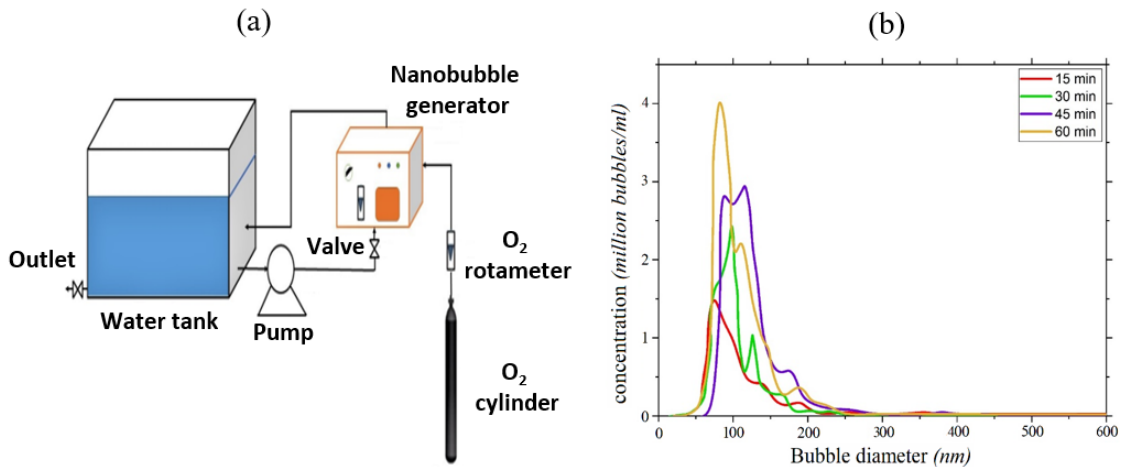


Figure 7.2: (a) Experimental setup for nanobubble generation and (b) Bubble size distribution at different time interval.

The experimental rig for the measurement of volumetric mass transfer coefficient consists of a water tank made up of acrylic sheet with dimensions (49 cm x 29 cm x 30 cm; l x b x h) filled with 20 L of distilled water with 140 mm of liquid height. The oxygen gas is injected into the membrane module by an oxygen generator which continuously provides the oxygen with more than 90% purity. The gas flow rate is measured by the rotameter in the gas line. The pore size of the membrane module used is 30 nm. The dissolved oxygen (DO) probe is installed in the water tank to measure the dissolved oxygen level in the water. The temperature of the water is also measured by the oxygen probe. Further, the NTA (Nanoparticle Tracking Analysis) and DLS (Dynamic Light Scattering) techniques have been adopted to characterize the nanobubbles samples at atmospheric conditions[211]. For the nanobubbles loaded droplets, Zeta potential cannot be measured directly due to its high instability, but it can be derived using a theoretical model and an experimentally determined electrophoretic mobility of charged entities under an applied electric field. The electrophoretic mobility, μ_e , is defined as: $\mu_e = u/E$. where u and E are the drift velocity of the dispersed particle and the strength of the applied electric field. Thus, the zeta potential, ζ , can be calculated from: $\mu_e = \frac{2}{3} \frac{\epsilon_o \epsilon_r \zeta f(Ka)}{\eta}$. where, ϵ_r , ϵ_o , ζ , η and $f(Ka)$ are, respectively, the relative permittivity or dielectric constant of the dispersion medium, the permittivity of vacuum, the dynamic viscosity of the dispersion medium at the experimental temperature and Henry's function which describes the electrophoretic mobility of a spherical colloidal particle in the limit of low surface potentials. The results were presented in terms of bubble size distribution, concentration of nanobubbles, bubble diameters, and zeta potential. The concentration of nanobubble increases monotonically with time and the mean diameter lies in the range 100-120 nm as shown in Fig. 7.2.(b). The maximum concentration of nanobubbles occurs at 60 min with 214 million bubbles per mL whereas the mean diameter is observed in the range of 100-140 nm, as shown in Fig. 7.3.(a) and Fig. 7.3.(b), respectively. The nanobubbles are observed to have negative zeta potential of -28 mV as shown in Fig. 7.3.(c). The high negative zeta potential around the nanobubbles helps make them stable in suspension for a longer time duration, leading to long-term stability.

The bubble generation was performed carefully to avoid contamination in the liquid. The possibility of the contamination could be the metals used in the nanobubble generator. The refractive index of nanobubbles is estimated in order to make sure that the possible chances of contamination. Evidently, the refractive index of solid particles and drops must be always higher than 1.33, while the refractive index of nanobubbles lies close to 1. We have calculated the refractive index of nanobubbles using the Mie scattering theory method [195] based on scattering intensity measurement. Clearly, the refractive index of nanobubbles in all the cases, shown in Fig. 7.3.(d), was very close to one (RI of air = 1), which confirms that these are gas nanobubbles.

In this study, different concentrations of oxygen gas nanobubbles dispersed solutions were used to generate droplets. The thermophysical properties such as density, surface tension and viscosity of the test solutions significantly varies with increasing oxygen

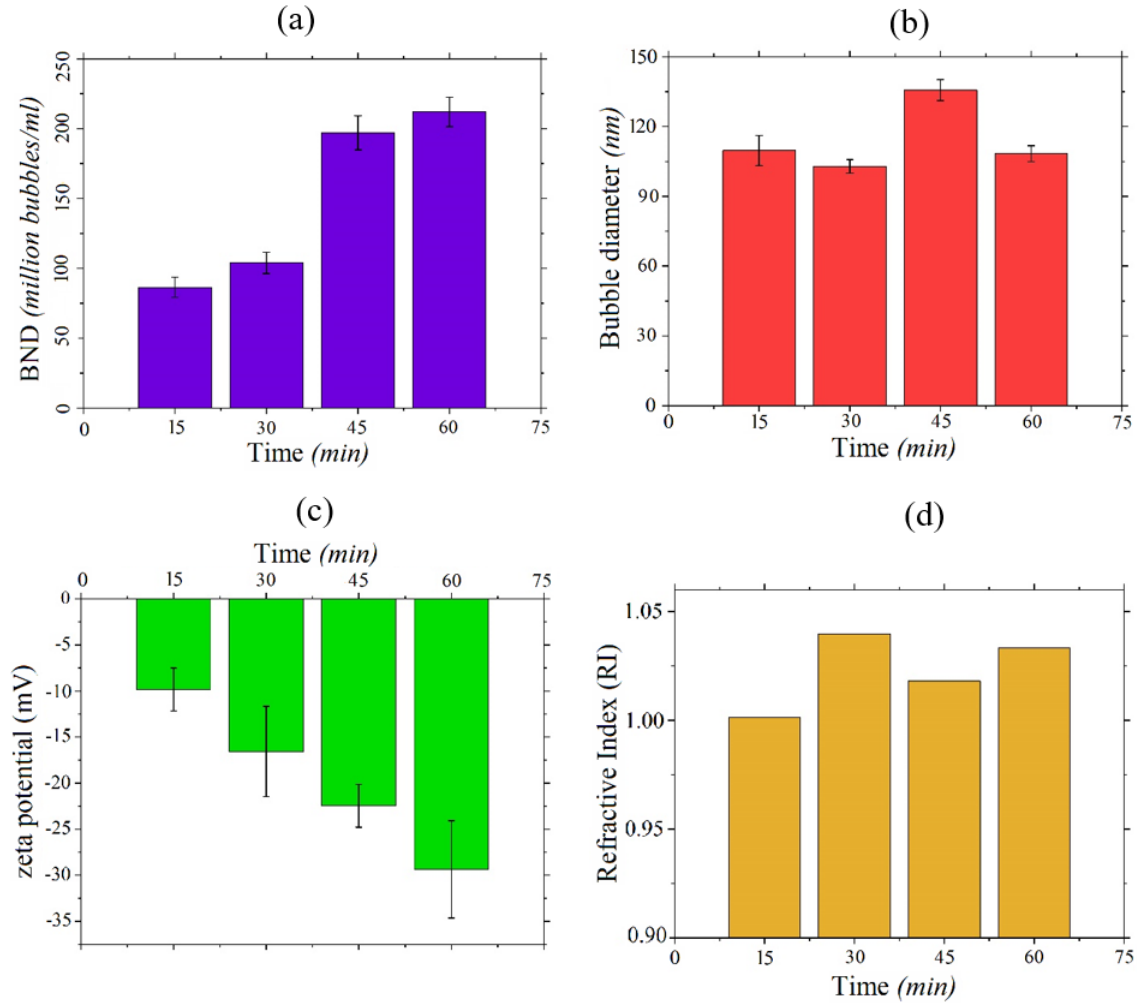


Figure 7.3: Bulk nanobubbles generated at time intervals of 15, 30, 45, and 60 min; (a) Bubble number density (BND), (b) Bubble diameters, (c) Zeta potential, (d) Refractive index

nanobubbles concentration. Increase in concentration of solid particles will lead to increase in viscosity. However increase in concentration of nanobubbles may not necessarily lead to increase in viscosity. The increase in liquid-gas interface due to the increase in NB concentration in the bulk of the liquid leads to increase slip between surfaces and therefore, the measured shear force decreases in nanobubble suspension [212]. The decreasing trend of density with increase in NB concentration is obvious due to increase of gaseous phase in the NB fluids. Surface tension is the tangential force acting on the interface per unit length that can also be expressed by Gibbs free energy per unit area at constant temperature and pressure. Clearly, Gibbs free energy expected to be minimum both in the bulk and the interface of the system at thermodynamic equilibrium. The interfacial area of the system boundary may increase by migration of nanobubbles towards the interface. Therefore, the nanobubble contribute to decrease in the surface tension.

We adopted Wilhelmy plate method to measure the surface tension of the test fluids at the temperature 25°C. All thermophysical properties of nanobubbles dispersed fluid solutions have been tabulated in table.7.1.

Table 7.1: Thermophysical properties of test fluid droplets at 25⁰C: pre-impact droplet diameter D_o (mm), density ρ (kg/m³), surface tension σ (mN/m), viscosity η (mPa-s), and capillary length λ_c (mm).

| nanobubbles concentration (million bubbles/ml) | D_o | ρ | σ | η | λ_c |
|---------------------------------------------------|---------|--------|--------------|-------------|-------------|
| 0 | 2.6 | 995.6 | 71.8 | 0.8 | 2.7 |
| 87 | 2.6 – 2 | 993.3 | 69.9 - 39.8 | 0.9 - 0.802 | 2.6 |
| 104 | 2.8 | 992.7 | 68.1 - 33.53 | 0.8 | 2.6 |
| 158 | 2.8 | 992.2 | 66.7 - 33.53 | 0.8 | 2.6 |
| 214 | 2.9 | 991.2 | 62.3 - 33.53 | 0.8 | 2.5 |

7.3 Results and discussions

In this section, we have discussed the impact hydrodynamics of the nanobubble dispersion droplets over hot surfaces with varying impact Weber numbers (We). The different regimes of boiling and phenomenology of nanobubble dispersion droplets are discussed one after another.

7.3.1 Contact boiling regime ($T_s \sim 150^0\text{C}$) < T_{DL}

Fig.7.4. illustrates the temporal snapshots of the droplets with different nanobubble concentration at a fixed impact velocity $U=0.5\text{m/s}$. The advection of the bubbles in NB fluid droplets was observed inside liquid droplet during contact boiling [$(T_s \sim 150^0\text{C}) < T_{DL}$] stage. From Fig.7.4. it has been noticed that no such advective motion exists in case of de-ionized water droplet. From the Fig.7.4., it has been noticed that the dissolved oxygen nanobubbles coalesce and transform to bigger bubbles in the lower half of the droplet adjacent to the heated substrate (see the 3rd column of 2nd, 3rd and 4th row of Fig.7.4.). Subsequently due to buoyancy and thermal Marangoni effect due to the surface tension gradient induced by temperature variation existing between the heated droplet bottom surface and relatively less heated top portion [212, 213], these bubbles travel in vertical direction away from the heated surface. It is also noticed that the vigorousness of the advective motion of the bubbles is enhanced with an increase in nanobubble concentration.

Di-water droplets exhibit contact boiling (see 1st row and 3-5 columns of Fig.7.4.) phenomenon through bulging its volume up to a contact time of 107.5ms. The contact boiling was followed by nucleate boiling due to the vigorous nucleation of vapor bubbles beneath the droplet. Unlike DI water droplets, the nanobubbles dispersed fluid droplets interestingly exhibits CCR (constant contact radius) mode (see 3-5th column of the NB fluid droplets in Fig.7.4.) with no shift of its triple line during boiling. This behaviour is analogous to the constant contact radius mode observed in evaporation of droplets [214, 215]. On further magnification of the Fig.7.4., 2nd row and 3-5 columns in the top row of the figure 7.4., it is readily evident that the nanobubble fluid droplets undergoes CCR mode via change in its contact angle (see red, yellow and green color droplet curvature profiles

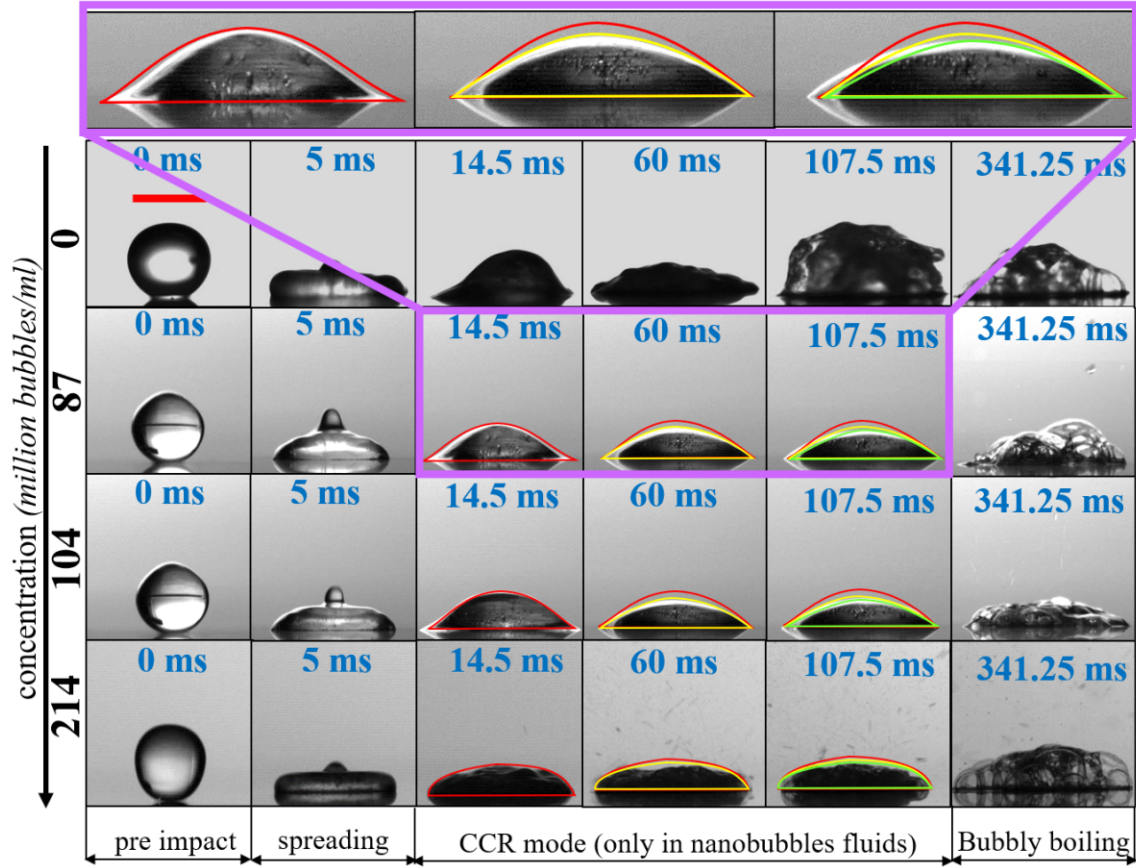


Figure 7.4: Temporal evolution of the droplet during contact boiling stage. i.e., at $(T_s \sim 150^\circ\text{C}) < T_{DL}$ at a fixed impact velocity $U=0.5\text{m/s}$. Violet color inset represents the CCR mode of NB fluids in the Fig.7.4. The supplementary movies (figure7.4._water, figure7.4._104million) of each test fluid droplets illustrates the CCR mode in case of NB fluids.

in the inset of Fig.7.4.) without losing its pinning effect. The CCR mode was lasting for ~ 245 ms for 87 million and 104 million bubbles/ml. But, for higher NB concentration (i.e., 214 million bubbles/ml), droplet displays CCR mode along with ejection of secondary droplets. Eventually, this nanobubble fluid droplets enters into contact boiling stage and transforms to bubbly boiling (nucleate boiling) with increase in time.

7.3.2 Transition boiling regime ($T_s \sim 190^\circ\text{C}) < T_{DL}$

Next, we shift our focus on splashing behaviour of droplet during transition boiling $[(T_s \sim 190^\circ\text{C}) < T_{DL}]$. The splashing behaviour of impinging droplets of both water and NB solutions have been illustrated in Fig. 7.5. From Fig.7.5., it has been noticed that all deionized water droplets show usual secondary droplet atomization during transition boiling due to the onset of the coalescence of the vapor bubbles of the liquid beneath the droplet. But, in case of droplets with NB solutions, droplets display vigorous ejection of thin cylindrical jets or elongated secondary droplets (see red color arrows in the Fig.7.5.). No such onset of thin cylindrical jet ejection was observed in case of pure deionized water droplets. With increase in contact time as well as NB concentration, the vigorousness of

these thin jet ejection is increased.

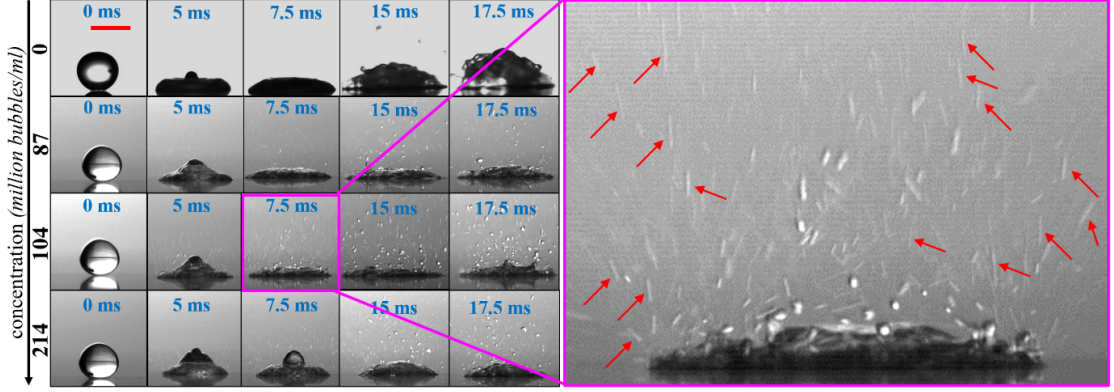


Figure 7.5: Temporal snapshots of the splashing behaviour associated with thin jet ejection during Transition boiling stage. i.e., at $(T_s \sim 190^\circ\text{C}) < T_{DL}$ at a fixed impact velocity $U=0.5\text{m/s}$. Red color arrow in the inset of Fig.7.5. represents the jet ejection along with spraying. Supplementary video is added for further clarity (figure7.5.).

7.3.3 Dynamic Leidenfrost effect ($T_s \sim T_{DL}$)

Next, we shift our attention to major focus of present work on understanding how the presence of nanobubbles affects the droplet Leidenfrost regime. The substrate temperature at which the droplet exhibits onset of rebound with minimal spraying is noted as the dynamic Leidenfrost temperature (T_{DL}) [73],[9]. Figure 7.6. a and b illustrate the temporal evolution of NB droplets of different concentration and their corresponding dynamic Leidenfrost temperature T_{DL} at a fixed impact velocity of $U=0.5\text{m/s}$. From the first column of Fig. 7.6.a, it is evident that the increase of nanobubble concentration leads to increase in T_{DL} at $U=0.5\text{ m/s}$. Compared to pure DI water, the increase in T_{DL} was as high as $\sim 100^\circ\text{C}$ for this same impact velocity (4th and 5th row of figure 7.6.). For all the ranges of impact velocities tested, at any fixed velocity, the T_{DL} was observed to increase monotonically with an increase in nanobubble concentration (Fig. 7.7.). At a fixed nanobubble concentration, the T_{DL} decreased with the increase of impact velocity. Contrary to the previous studies where fizzy (carbonated) droplets levitated on superhydrophobic surfaces at ambient temperature [216] and Leidenfrost temperature decreases with increase of dissolved gas concentration in water [217], the oxygen nanobubbles of the NB fluids are altering the T_{DL} in a counterintuitive manner.

A recent study [218] has shown that near the transition Leidenfrost point, oscillatory boiling occurs. Oscillatory boiling signifies the alternate occurrence of boiling and rewetting over time. The study reports the rewetting velocity of the form

$$v_{re} = ((P_v - P_l) / 4\rho_l F)^{1/2} \quad (2)$$

Here, P_v and P_l are the pressure inside the embryonic vapor bubble, and liquid pressure respectively. ρ_l is the liquid density and F is a correction factor for partial spherical

shape of the vapor embryo. The P_v is estimated as:

$$P_v = P_{sat}(T_l) \exp(v_l \{P_l - P_{sat}(T_l)\} / (RT_l)) \quad (3)$$

Where, P_{sat} is the saturation pressure at liquid temperature T_l and v_l is the specific volume of the liquid. We have taken $T_l = 200^\circ\text{C}$ as a reference since for water T_{DL} was observed at temperatures as high as $\sim 220^\circ\text{C}$. Now, at $T_l = 200^\circ\text{C}$ we have taken the saturation pressure and specific volume from steam tables and estimated the rewetting velocity as ~ 16.23 m/sec. This is the same order of magnitude as the reported study [218]. Similarly for NB fluids, the highest T_{DL} was observed at $\sim 320^\circ\text{C}$. Hence $T_l = 300^\circ\text{C}$ was taken as a reference point. For $T_l = 300^\circ\text{C}$, the rewetting value is a complex number since P_l (1 atmospheric pressure) is less than P_v . Hence the unrealistic value is an indicator that for water, 300°C is already past the Leidenfrost state, and not in the oscillatory phase.

We hypothesize that for NB fluids, the nanobubbles act as the embryos for the nucleation sites. If we consider the physical properties of the NB fluid (214 millions/ ml) from Table 7.1. and the mean NB radius to be 100 nm (refer Fig. 7.2.(b)), by using the Laplace equation $\Delta p = 2\sigma/r$, we can substitute the Δp value in the equation of V_{re} and get a realistic value of 20 m/sec. We can hypothesize that due to the higher-pressure difference within the bubble and the liquid, there exists a realistic possibility of rewetting to happen which basically disrupts continuous vapor formation, and thereby causing higher T_{DL} . We further theorize that upon contact of the NB fluid droplet with the superheated surface, the nanobubbles at and near the liquid–solid interface is thermally destabilized, and expand rapidly. This leads to the release of the gas from the nanobubbles at and near the heated interface, leading to the formation of a micron scale thin gas layer between the NB droplet and heated surface. We hypothesize that this gas layer reduces effective contact area between the droplet and the hot surface, thereby delaying formation of the stable vapour cushion which signifies the onset of the Leidenfrost regime.

7.3.4 Scaling T_{DL} with Weber (We) and Ohnesorge (Oh) numbers

In this section, we have presented the scaling relations of T_{DL} with two different nondimensional parameters, the Weber number ($We = \rho U^2 D_o / \sigma$) and Ohnesorge number ($Oh = \mu / \sqrt{(\rho \sigma D_o)} = We / Re$). Physically the Weber number represents the ratio of inertial force to surface tension. Figure.7.8. (a) exhibits the decreasing trend of the T_{DL} with increasing impact We for a fixed nanobubble concentration ($T_{DL} \sim We^{-0.15}$). The decreasing trend of T_{DL} with increase in Weber number is similar to the Leidenfrost phenomenon studies for polymer droplets [73] and surfactant droplets [9]. At higher We , due to higher inertia, drops attain higher spreading. Due to the higher area of contact between the spreading droplet and heated substrate, higher proliferation of nucleation sites at the fluid-solid interface leads to quicker vapor formation. The augmented rate of vapor layer formation leads to droplet rebound at lower temperature and consequently the T_{DL} .

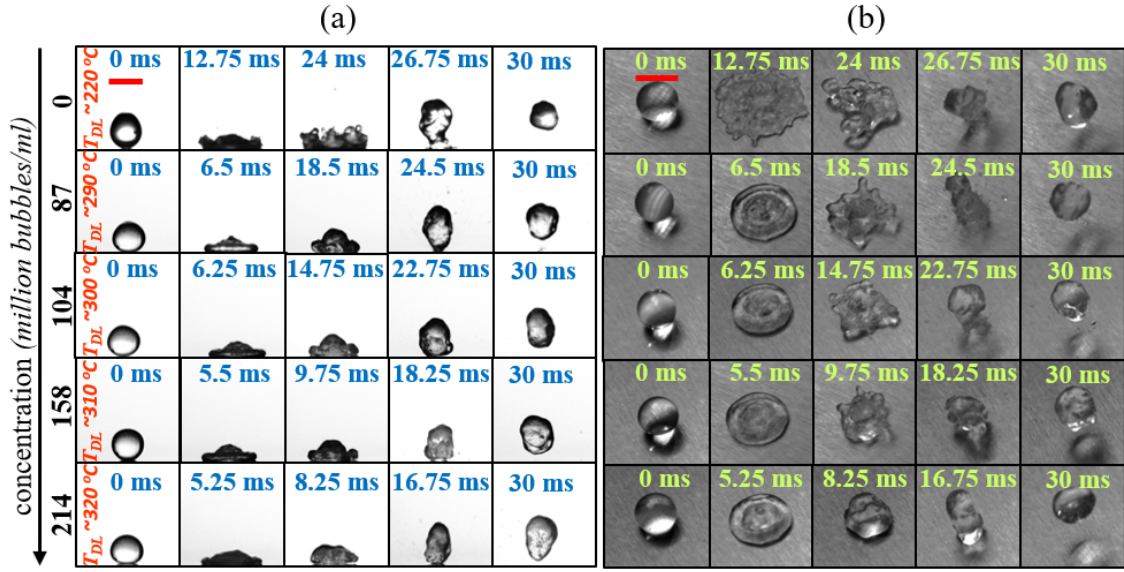


Figure 7.6: Influence of nanobubble concentration on T_{DL} : Temporal evolution (a) side-view and (b) top views of impacting droplets with a low impact velocity of $U=0.5$ m/s at their respective T_{DL} s. The scale bar represents 2.64 mm and is the same for all cases. The first row with 0 million bubbles/ml shows water droplets and nanobubble dispersion concentration increases from top to bottom (the arrow at the extreme left shows concentration values).

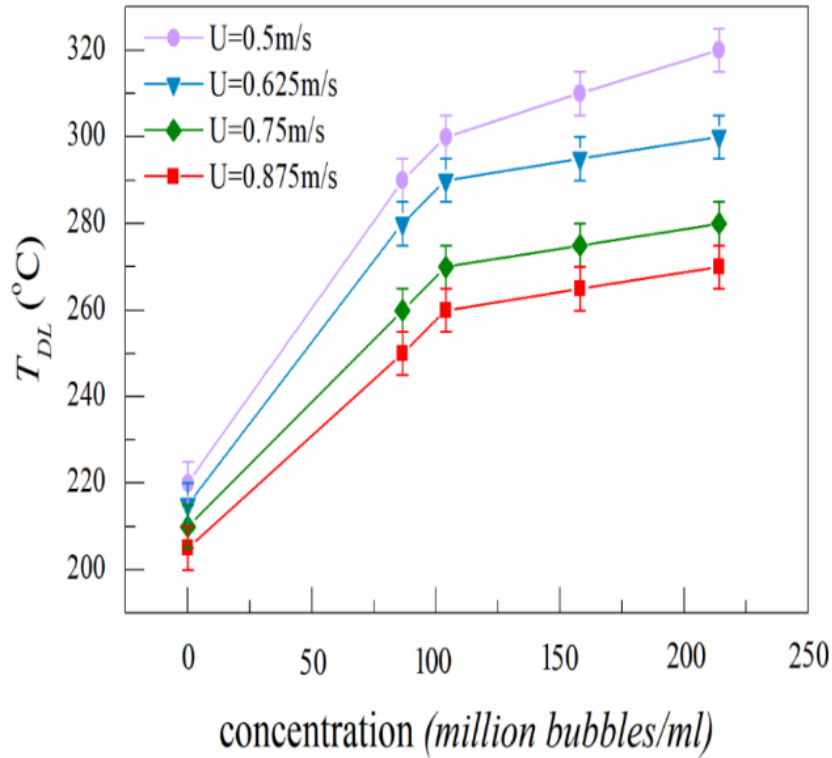


Figure 7.7: Effect of droplet impact velocity on dynamic Leidenfrost temperature (T_{DL}) for different nanobubbles concentrations. The error bars represent variation of $\pm 5^\circ\text{C}$.

For the same We , the T_{DL} increases with the increase in NB concentration. With the change in NB concentration, there is change in material properties like density, viscosity,

surface tension and drop equilibrium size. Consequently, we need another non dimensional number i.e. Ohnesorge number (Oh), which represents the ratio of viscous force to both inertial and surface tension force. To elucidate the role of viscous effects, we have probed the dependence of T_{DL} on the Ohnesorge number in the figure. 7.8.(b). It must be noted that Oh is lowest for the highest concentration NB fluid ($Oh \sim 0.00186$) and highest for DI water ($Oh \sim 0.0021$). For a fixed NB fluid, the T_{DL} decreases with increasing velocity. This observation is in agreement with figure 7.7. For a fixed impact velocity, T_{DL} decreased with an increase of Oh and follows the scaling relationship $T_{DL} \sim Oh^{-0.45}$.

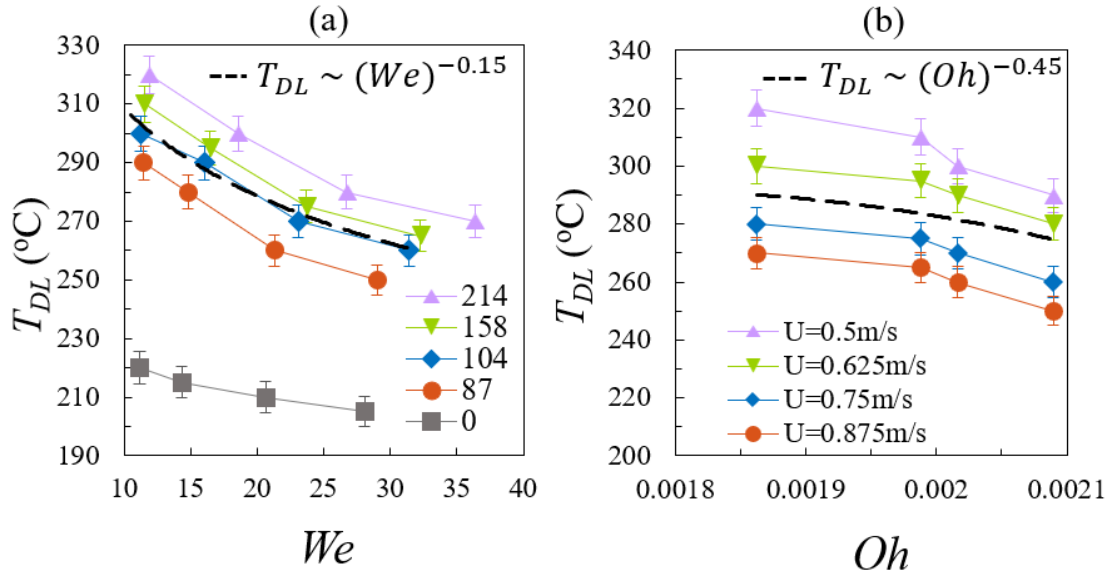


Figure 7.8: Relationship of T_{DL} with (a) We (In above Fig:7.8.a; the legend values represent million bubbles/ml, for instance legend value 214 represents the fluid with the dissolved oxygen nanobubbles concentration of 214 million bubbles/ml) and (b) Oh for different nanobubble concentrations. The dashed lines represent the scaling relationships obtained from the data. The lowest Oh value is of NB fluid 214 million bubbles/ml whereas the highest Oh value is of water.

Analogous to our previous study of Leidenfrost phenomena with surfactant droplets [9], we have attempted to elucidate the effect of all responsible forces of the NB fluid droplets, we introduced a scaling relationship by combining both nondimensional numbers We and Oh through least squares regression. We illustrated the scaling relationship with experimental data points (T_{DL}) against the calculated (fitted value of scaling relation) (T_{DL}) in the figure. 7.9. The experimental results of T_{DL} are fitted as following pattern: $T_{DL} = (aOh^{-b} + c)We^{-d} + e$. Through least squares regression, the empirical correlation of T_{DL} as a function of We and Oh (within $\pm 10\%$ confidence interval, refer cyan color shaded region in Fig.7.9.) is attained as follows: $T_{DL} = (16.5Oh^{-0.45} + 160)We^{-0.15} + 18$. Although the percentage of the confidence interval is significant, we believe that this empirical correlation will provide an approximated reference value for future researchers in this field especially for engineering research and developmental activities in the domain.

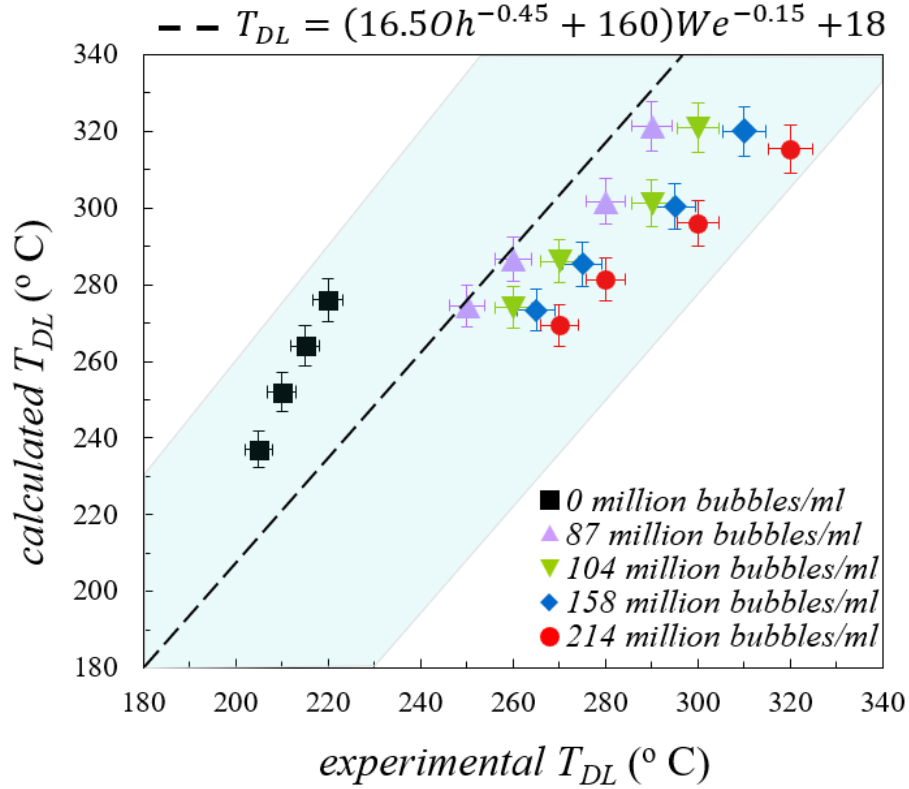


Figure 7.9: The scaling correlation between the experimental and calculated T_{DL} of various nanobubbles concentrations.

7.3.5 Residence time of the droplets at T_{DL}

The nondimensional residence time (t_r^*) of the droplets during the Leidenfrost state of different test fluids i.e., at T_{DL} are illustrated in figure 7.7. We defined the nondimensional residence time ($t_r^* = t_r / t_i$) as the ratio of residence time (t_r) to the impact time ($t_i = D_o / U_o$), where D_o and U_o represent pre-impact droplet diameter and impact velocity respectively. The residence time (t_r) is calculated from the moment of droplet impact to the onset of lift-off. Figure 7.10. (a) illustrates the temporal snapshots of the nondimensional residence time of different concentrations of NB fluid droplets at almost same We during their corresponding dynamic Leidenfrost stage. From figure 7.10b, it has been observed that for a nearly same We , the nondimensional residence time (t_r^*) reduces with increase in NB concentration. From Fig. 7.8.a, it is observed that the T_{DL} decreases with increase of NB concentration for same We . Since higher substrate temperature indicates faster heat transfer rate, it is expected that the t_r^* reduces with increasing NB concentration. We scaled the nondimensional residence time (t_r^*) from the experimental data points with respect to We as $t_r^* \sim We^{0.75}$. For a given NB fluid, with increase of We , the T_{DL} is lowered. Consequently, at lower T_{DL} , lower heat transfer rate results in higher residence time with increasing We .

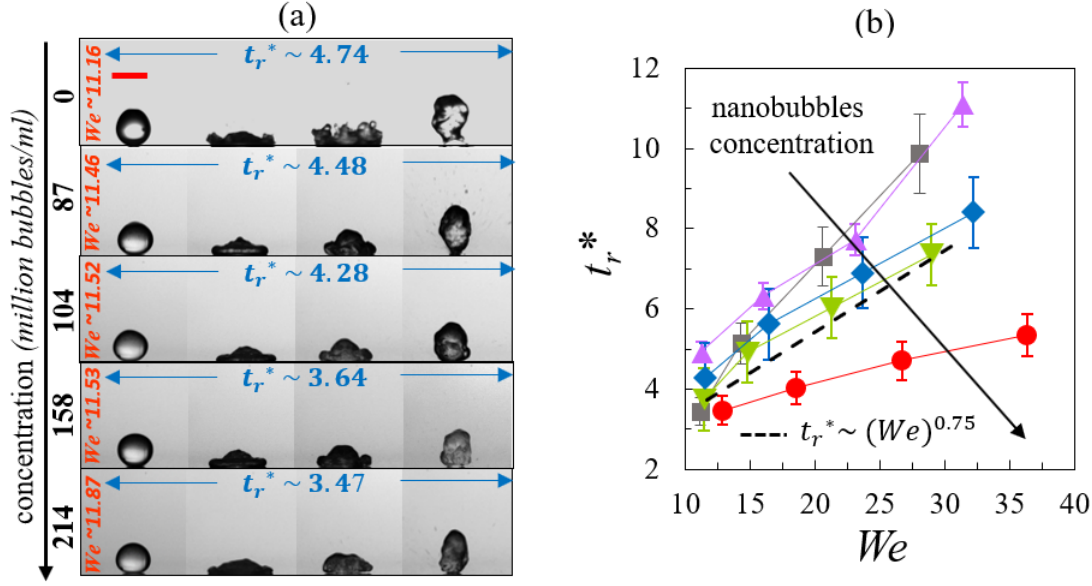


Figure 7.10: The non dimensional residence time of different concentrations of nano bubbles dissolved water droplets (a) side view snapshots for varied bubble concentrations at an almost same We (b) over different Weber (We) numbers respectively. (b) The symbols (\square), (\triangle), (∇), (\diamond) and (\circ) represent different bubble concentrations of 0 (water), 87, 104, 158 and 214 million bubbles/ml respectively. The downward arrow is indicating increasing NB concentration.

7.3.6 Bubble coalescence during the Leidenfrost regime ($T_s \sim T_{DL}$)

In this section, we have highlighted the bubble coalescence process during dynamic Leidenfrost stage (i.e., at T_{DL}). Fig. 7.11. illustrates the coalescence of nano-bubbles into macrobubble within the droplet during Leidenfrost stage (at T_{DL}). At the moment of impact, the dissolved nanobubbles are not traceable by high-speed photography (Fig. 7.11. 1st column) as it is not possible to resolve the nanoscale dimensions using the conventional optical lens. Column-wise visual inspection reveals that nanobubbles start to coalesce from the onset of the retraction stage (Fig. 7.11. 3rd column, 2nd row onwards) as millimeter size bubbles. Multiple bubbles of the order of \sim mm starts to emerge from 4th column onwards. It must be noted that the DI water droplets (Fig. 7.11. first row) does not show any such emergence of macro-bubbles as it is nearly devoid of dissolved gases. The life duration of these macro-bubbles is more than \sim 100 ms. Emergence of macrobubbles were also observed in drops with dissolved gas components at $T_l=300^\circ\text{C}$ [219]. However, water droplets containing additives like polymers or surfactants [75], [173] with negligible dissolved gas exhibited no such macrobubbles to best of our knowledge. The emergence of such bubbles and associated rotation of the droplets in the levitated state are also shown in the supplementary videos. Such rotation of droplets during Leidenfrost induced hovering stage are previously observed in the case of water [220] and polymer droplets [73].

To emphasize the transformation of nanobubbles into macrobubble through microbubbles coalescence within the droplet during dynamic Leidenfrost stage, multiple

rebounding stages of the liquid droplet (stages I, III and V in Fig. 7.11. signify 1st, 3rd and 5th rebound) during both retraction and levitation stages, with their corresponding time frames have been illustrated in Figure.7.11. The stages have been sequentially distinguished as nanobubbles activation, micro-bubbles formation, micro-bubbles coalescence and macro-bubble formation. From figure.7.11, it was noted that the rate of microbubbles coalescence enhances with an increase of NB concentration due to the great variation in their respective T_{DL} s. It has also been observed that the fluid droplet with lower nanobubble concentration attains macrobubble formation relatively in a shorter time than higher nanobubble concentration.

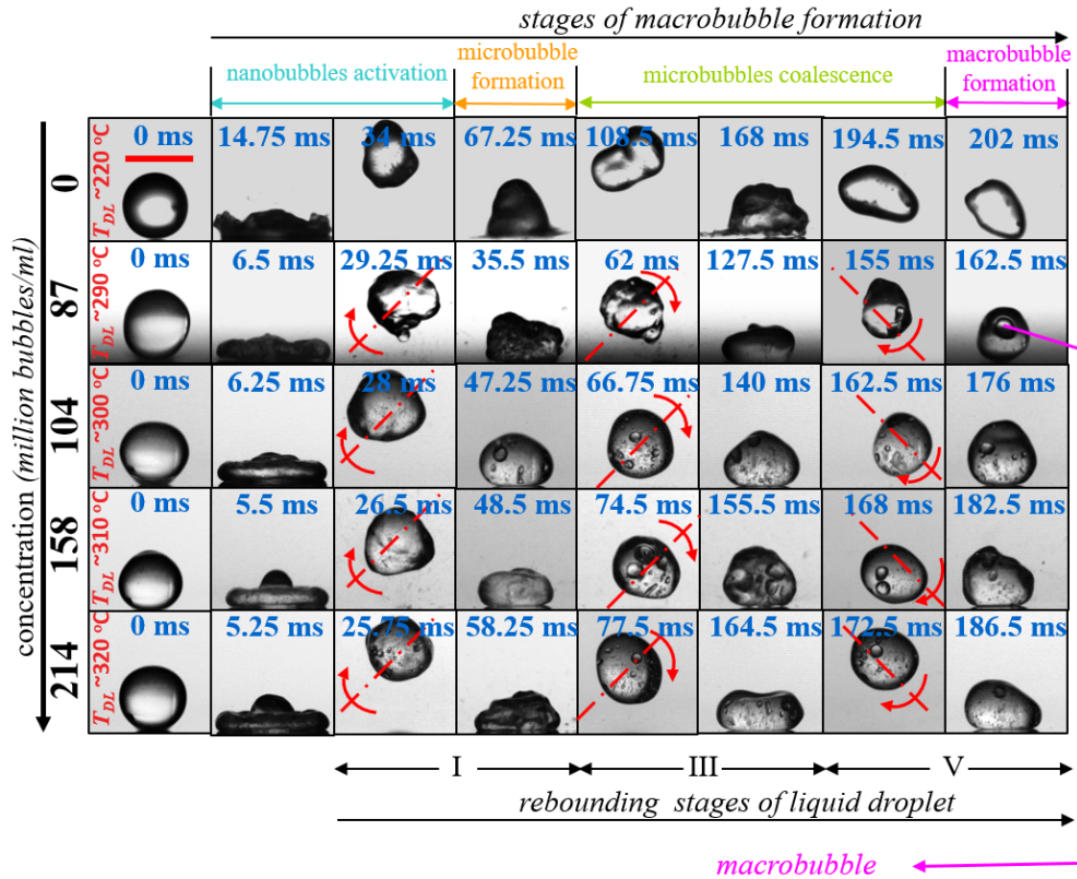


Figure 7.11: Transformation of nanobubbles into macrobubble through microbubbles coalescence inside liquid droplet during dynamic Leidenfrost stage (i.e., at T_{DL}) at a fixed impact velocity $U=0.5\text{m/s}$. The scale bar represents 2.64 mm and is the same for all figures. The first row (0 million bubbles/ml) represents deionized water droplets and nanobubbles concentration increases from top to bottom rows.

7.3.7 Droplet rebound dynamics at T_{DL}

The bouncing dynamics of the droplets of different NB concentrations during the Leidenfrost state is illustrated in figure 7.12. The bouncing dynamics is characterized by the non dimensional rebound height (h_{max}/R) as the ratio of the maximum rebound height of the droplet to its pre-impact radius. It is readily evident that the nondimensional rebound height (h_{max}/R) for a fixed impact velocity decreases with an increase in NB

concentration. In case of DI water droplets, the bouncing height increases with impact velocity. On the contrary, for the droplets of NB fluids, the nondimensional rebound height decreases with increased impact velocity.

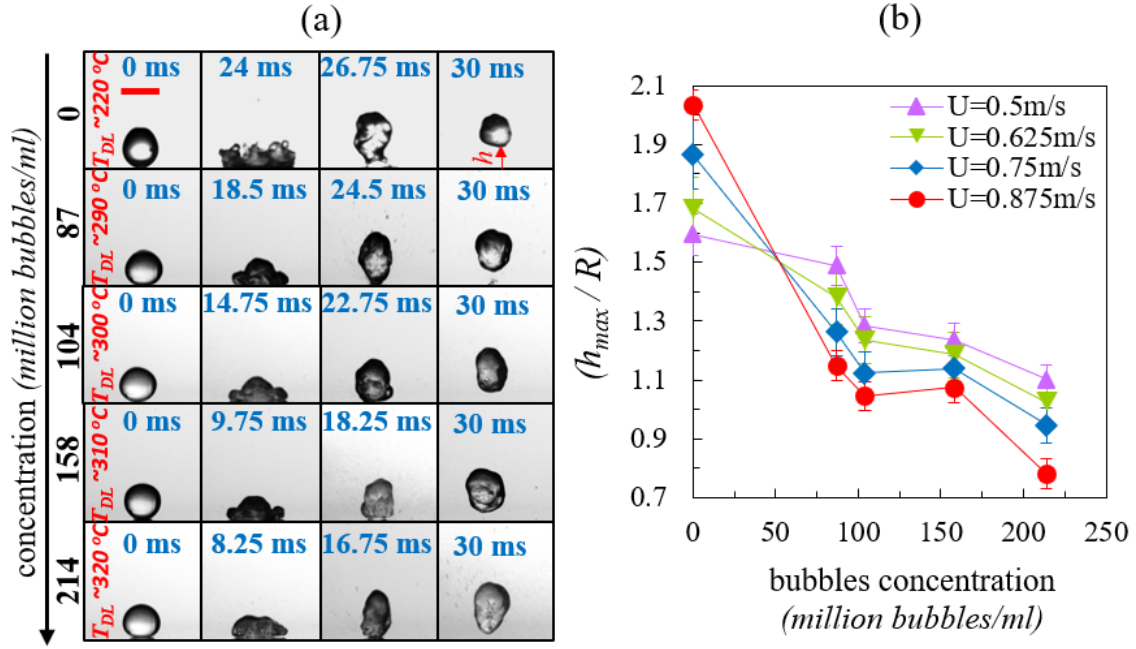


Figure 7.12: The maximum nondimensional rebound height (h_{max}/R) of different concentrations of nanobubbles dispersed droplets during dynamic Leidenfrost stage (a) side view snapshots for varied bubble concentrations at an impact velocity $U=0.5$ m/s (b) maximum nondimensional rebound height (h_{max}/R) respectively.

7.3.8 Effect of impact momentum in post Leidenfrost regime ($T_s \sim 400^\circ\text{C}$) $> T_{DL}$

Next, we presented the dependence of impact velocity (impact momentum) on various rebound behaviours during the impact of NB droplets at a fixed superheated substrate temperature (i.e., $(T_s \sim 400^\circ\text{C}) > T_{DL}$) in Fig. 7.13. The representative NB fluid has concentration of 87 million bubbles/ml. At low impact velocity ($U=0.5$ m/s) droplet rebounds and stays intact without any indication of splash. This behaviour was termed as rebounding Leidenfrost state. At slightly higher impact velocities (i.e., $U=0.625$ and 0.75 m/s) drop rebound was observed along with spray like ejection of secondary droplets. This behaviour was termed as spraying Leidenfrost state. On further increase of impact velocity ($U=0.875$ m/s), droplets undergo fragmentation into smaller droplets during the retraction process. This state was termed as fragmenting Leidenfrost stage. The regime maps of these behaviour as function of We and substrate temperature were discussed in the next section (see Fig. 7.14.).

7.3.9 Boiling regime map

Finally, Fig. 7.14a and b represents the phase diagram of different boiling regimes

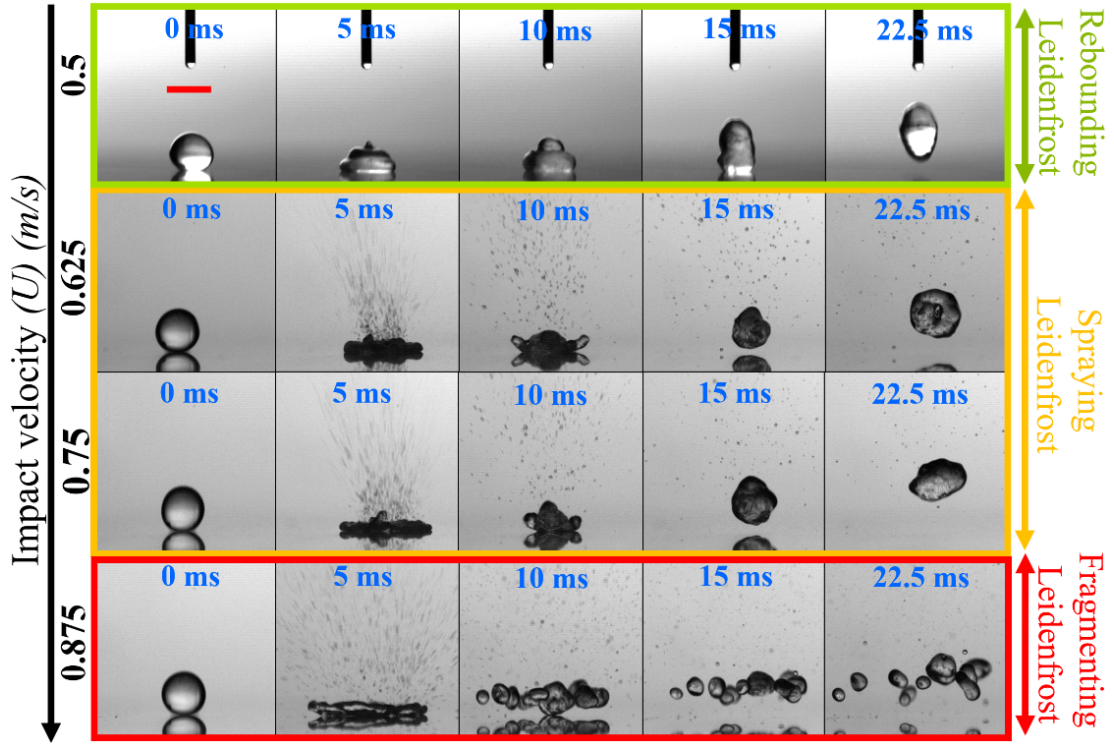


Figure 7.13: Impact velocity dependence on different Leidenfrost states of nanobubbles dispersed fluid droplets with a particular concentration (87 million bubbles/ml) at a fixed elevated substrate temperature ($T_s \sim 400^\circ\text{C}$).

of DI water and NB fluid droplets respectively as a function of We and substrate temperature. The highest concentration of NB i.e., 214 million bubbles/ml was chosen as the representative fluid. The various boiling regimes are distinguished as CCR mode (I), transition boiling (II), rebounding Leidenfrost state (III), spraying Leidenfrost state (IV) and fragmentation Leidenfrost state (V). In contrast to DI water droplets, NB fluid drops witnesses the emergence of CCR mode (I) and spraying Leidenfrost state (IV). In addition, the regime (II) of transition boiling is much bigger in case of NB fluids due to higher T_{DL} than DI water drops. The demarcation zone between II and III for both water and NB fluids suggests that T_{DL} is decreasing with We , reminiscent of figure 7.7a.

Similarly, the Leidenfrost (bounce off nature of the impacting parent droplet) state has been distinguished as rebounding Leidenfrost state (III), spraying Leidenfrost state (IV) and fragmentation Leidenfrost state (V) respectively. At this context, it is noteworthy to discuss the contrasting phase regimes of transition boiling (II) and Fragmenting Leidenfrost state (V) in water and NB fluid. Due to the CCR mode in NB fluids, the transition boiling is happening at lower temperature (150°C) only in case of high We (~ 40). Similarly in comparison to water, the fragmentation boiling in case of NB fluids is happening at much higher We . This happens due to the emergence of regime (IV) in NB fluids.

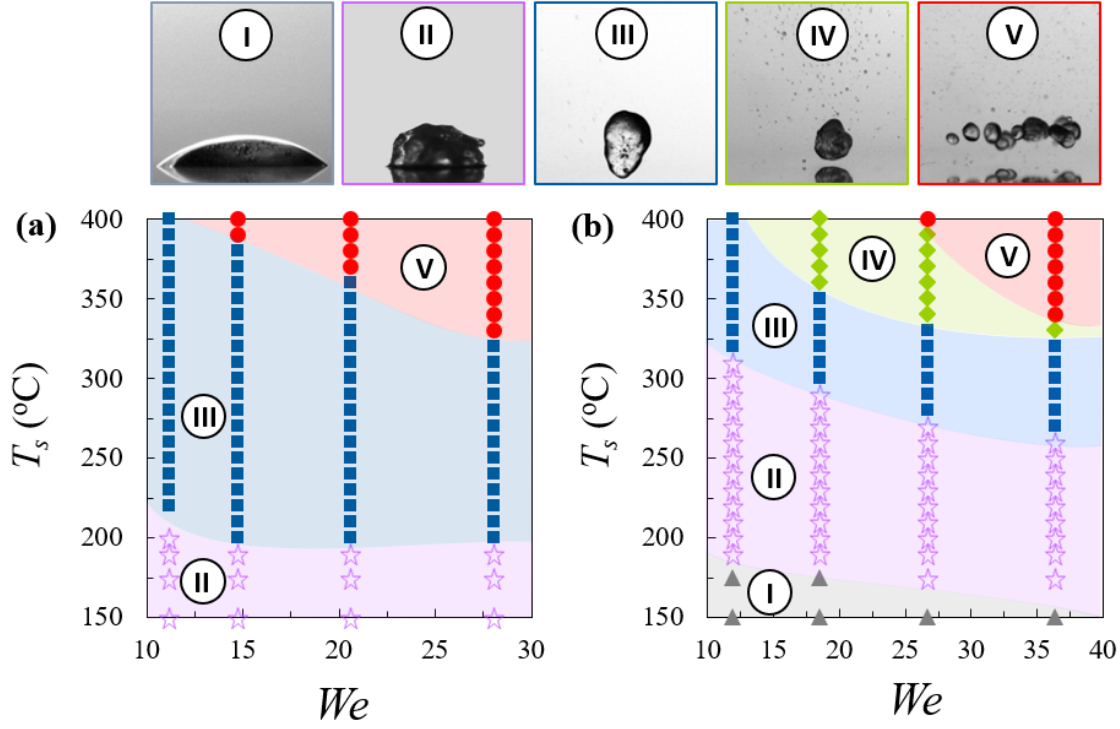


Figure 7.14: Phase map of boiling regimes of impacting droplets with varied Weber (We) numbers of (a) deionized water and (b) NB fluid (concentration of 214 million bubbles/ml) drops. The top row shows representative snapshots of the different boiling behaviors.

7.4 Conclusions

This thesis presents a novel method to enhance the dynamic Leidenfrost phenomenon by using nanobubbles dispersed fluid droplets. We note that the NB droplets show several different phenomenology during boiling in the pre- and post-Leidenfrost regime. It was shown that for a given impact velocity, the T_{DL} increases with increase in NB concentration, and the NB fluids delay the Leidenfrost effect by significant amounts. The empirical correlation of T_{DL} ($T_{DL} \sim We^{-0.15}$ and $We^{-0.45}$) developed with experimental data points in the form of nondimensional numbers such as Weber number (We) and Ohnesorge numbers (Oh). We have shown that rewetting due to the presence of the dispersed NBs and possible formation of microscale gas layer between the solid-liquid interface could be crucial mechanisms for the delayed Leidenfrost state. Finally, we have demarcated the different boiling regimes of impacting nanobubbles dispersed fluid droplets through regime phase maps as a function of Weber number (We) and substrate temperatures (T_s). The emergence of regimes like CCR (constant contact radius) mode and spraying Leidenfrost state was observed in case of NB fluids. We believe that our findings will encourage future researchers and developers to explore the potential use of NB fluids in thermal management of high temperature devices and components.

Chapter 8

Conclusion

8.1 Conclusion

As an overall closure of the dissertation, this section serves as the concluding chapter by summarizing its major findings. Chapter 3 aimed to achieve the first objective by varying the concentrations of polymer (PEG-400) and magnetic nanoparticles (Fe_3O_4) in non-Newtonian ferrofluids to perform droplet impact experiments on superhydrophobic surfaces under different Weber numbers (We) and various horizontal magnetic field strengths. The experimental results showed that non-Newtonian ferrofluid droplets undergo orthogonal spreading and exhibit an increase in non-dimensional maximum spreading (ξ_{max}) with an increase in the concentration of polymer and magnetic particles in the presence of a magnetic field. The experimental magnetohydrodynamics (MHD) of non-Newtonian ferrofluid droplets revealed that the magnetoelastic instability of induced polymer chains under an external magnetic field leads to suppressing the droplet rebound on the superhydrophobic surface. A detailed regime map was developed, and a new magnetic Weissenberg number (Wi_M) was introduced to segregate the rebound and non-rebound stages of the droplet.

Similar to the first objective, the second objective (Chapter-4) deals with the drop impact dynamics of non-Newtonian dielectric droplets on superhydrophobic surfaces and aims to explore the role of electro-elastic effects on anti-superhydrophobicity by arresting droplet rebound under external DC electric field. Stable colloidal solutions of titanium dioxide (TiO_2) dispersed in a polymeric (PEG-400) solution were used as a non-Newtonian dielectric fluid. Experimental electrohydrodynamics (EHD) of non-Newtonian dielectric droplets show the onset of elliptical spreading of the liquid lamella and report that non-dimensional maximum elliptical spreading (ξ_{max}) increases with an increase of dielectric particle concentration at a fixed polymer concentration and We against applied electric field. A new non-dimensional number called electric Eotvos number (Eo_e) has been introduced to understand the clubbed effect of both elastic and electric effects of non-Newtonian dielectric droplets under an external electric field. electroelastic instability of non-Newtonian dielectric droplets revealed that the tendency of anti-superhydrophobicity to suppress the droplet rebound increases with an increasing polymer and dielectric particle concentration against increased (Eo_e).

Chapters 3-4 provide a potential solution to address the scarcity of research on managing non-Newtonian droplets in alternative inkjet printing technologies, including MHD and EHD inkjet printing. The proposed solution aims to minimize ink wastage by suppressing droplet rebound using external magnetic and electric fields.

In addition to investigating the elastohydrodynamics of non-Newtonian droplets on superhydrophobic (SH) surfaces subjected to external magnetic and electric fields, this dissertation also delved into the realm of thermofluidic instabilities arising from Leidenfrost dynamics. This was accomplished by employing complex fluid droplets, such as surfactants, nanocolloids, and nanobubbles dispersed fluids. Chapter-5 was dedicated to exploring the thermohydrodynamics of surfactant droplets impacting heated substrates at different Weber numbers (We), with the addition of anionic (SDS) and cationic (CTAB) surfactants to water. At superheated temperatures, the dynamic surface tension of surfactant monomers destabilized thin vapor layer formation during the droplet retraction stage. This led to the development of instability of thermal Marangoni currents associated with dynamic surface tension, referred to as Taylor-Marangoni stability, which suppressed the dynamic Leidenfrost phenomenon. The study also introduced a scaling analysis to investigate the variation of dynamic Leidenfrost temperature and discussed the role of reducing pre-impact droplet size in terms of Bo . Additionally, novel thermohydrodynamic phenomena, such as trampoline dynamics and central jet ejection of surfactant droplets at extremely superheated states were also reported.

Similar to objective 3 (chapter-5), objective 6 (chapter-6) aimed to investigate the morphed inception of the dynamic Leidenfrost regime during the droplet impact of nanocolloids. The study uses stable colloidal solutions of aluminum oxide (Al_2O_3) nanoparticles as the nanocolloidal fluids. The research focuses on altering the microstructure of the substrate by depositing a residue sheet during the spreading and retraction stages, which ultimately delays the dynamic Leidenfrost point. It also demarcates different stages of boiling through a regime map in detail.

The final objective in chapter 7 introduces a new approach to study drop impact dynamics on a heated substrate by dispersing oxygen nanobubbles in aqueous solutions. The study focuses on the use of NB fluids to delay the onset of dynamic Leidenfrost temperature by increasing the concentration of nanobubbles. Empirical correlations were developed to highlight the change in T_{DL} with varying nanobubble concentrations at different Weber numbers. Additionally, a detailed regime map was created to report various modes of the boiling stage during pre and post-Leidenfrost stages.

The common goal of the last three chapters (chapters 5-7) is to mitigate the Leidenfrost effect during spray cooling processes. This is achieved by introducing novel coolants or altering the substrate's microstructure to enhance heat transfer. The research aims to

improve the efficiency of spray cooling processes by delaying or suppressing the onset of the dynamic Leidenfrost temperature, which can significantly impact the cooling performance of these systems.

8.2 Future scope of the work

Based on the research conducted in the preceding chapters, some recommendations have been made for future work, including:

1. One potential recommendation for future work is to investigate the impact of both magnetohydrodynamics (MHD) and electrohydrodynamics (EHD) of non-Newtonian ferrofluid droplets and non-Newtonian dielectric droplets on soft substrates, respectively. This study could specifically focus on providing insights into the spreading dynamics, drop rebound control, and splash control of these droplets on soft substrates under the influence of both magnetic and electric fields.
2. Another potential recommendation for future work is to explore the coalescence of non-Newtonian droplets under the influence of external fields, such as magnetic and electric fields. This study could focus on investigating the coalescence dynamics of non-Newtonian droplets under different external fields and analyzing the impact dynamics of various parameters, such as polymer concentration, particle concentration and field strength on coalescence behavior. The research could potentially provide insights into new ways to control coalescence in non-Newtonian droplet systems, which could have important implications for a variety of applications, including microfluidic devices and industrial processes. By investigating the coalescence behavior of non-Newtonian droplets under the influence of external fields, the study could also provide a better understanding of the fundamental physics underlying droplet coalescence in complex fluid systems.
3. Another potential recommendation for future work is to extend the investigation of Leidenfrost dynamics to complex fluid droplets onto heated liquids. This study could focus on understanding the micron vapor layer interfacial instabilities that arise when complex fluid droplets are subjected to heating. By studying the Leidenfrost dynamics of complex fluids, the research could provide insights into how the rheological properties of the fluids affect the vapor layer stability and the resulting heat transfer characteristics. The study could also investigate how external factors, such as surface roughness and substrate properties, impact the Leidenfrost dynamics of complex fluid droplets.

References

- [1] Hans-Jürgen Butt, Ilia V. Roisman, Martin Brinkmann, Periklis Papadopoulos, Doris Vollmer, and Ciro Semperebon. Characterization of super liquid-repellent surfaces. *Current Opinion in Colloid Interface Science*, 19(4):343–354, 2014. doi: <https://doi.org/10.1016/j.cocis.2014.04.009>. URL <https://www.sciencedirect.com/science/article/pii/S1359029414000478>.
- [2] Jaroslaw Drelich. Guidelines to measurements of reproducible contact angles using a sessile-drop technique. *Surface Innovations*, 1(4):248–254, 2013. doi: 10.1680/si.13.00010. URL <https://doi.org/10.1680/si.13.00010>.
- [3] Tommi Huhtamäki, Xuelin Tian, Juuso T. Korhonen, and Robin H. A. Ras. Surface-wetting characterization using contact-angle measurements. *Nature Protocols*, 13(7):1521–1538, Jul 2018. doi: 10.1038/s41596-018-0003-z. URL <https://doi.org/10.1038/s41596-018-0003-z>.
- [4] Juuso T. Korhonen, Tommi Huhtamäki, Olli Ikkala, and Robin H. A. Ras. Reliable measurement of the receding contact angle. *Langmuir*, 29(12):3858–3863, 2013. doi: 10.1021/la400009m. URL <https://doi.org/10.1021/la400009m>. PMID: 23451825.
- [5] Ines M. Hauner, Antoine Deblais, James K. Beattie, Hamid Kellay, and Daniel Bonn. The dynamic surface tension of water. *The Journal of Physical Chemistry Letters*, 8(7):1599–1603, 2017. doi: 10.1021/acs.jpclett.7b00267. URL <https://doi.org/10.1021/acs.jpclett.7b00267>. PMID: 28301160.
- [6] Ines M Hauner, Antoine Deblais, James K Beattie, Hamid Kellay, and Daniel Bonn. The dynamic surface tension of water. *J Phys Chem Lett*, 8(7):1599–1603, March 2017.
- [7] R. Miller, E.V. Aksenenko, and V.B. Fainerman. Dynamic interfacial tension of surfactant solutions. *Advances in Colloid and Interface Science*, 247:115–129, 2017. ISSN 0001-8686. doi: <https://doi.org/10.1016/j.cis.2016.12.007>. URL <https://www.sciencedirect.com/science/article/pii/S0001868616303062>. Dominique Langevin Festschrift: Four Decades Opening Gates in Colloid and Interface Science.
- [8] Mohsin J. Qazi, Simon J. Schlegel, Ellen H.G. Backus, Mischa Bonn, Daniel Bonn, and Noushine Shahidzadeh. Dynamic surface tension of surfactants in the presence of high salt concentrations. *Langmuir*, 36(27):7956–7964, 2020. doi: 10.1021/acs.langmuir.0c01211. URL <https://doi.org/10.1021/acs.langmuir.0c01211>. PMID: 32545966.

- [9] Gudlavalleti VVS Vara Prasad, Purbarun Dhar, and Devranjan Samanta. Postponement of dynamic leidenfrost phenomenon during droplet impact of surfactant solutions. *International Journal of Heat and Mass Transfer*, 189: 122675, 2022. ISSN 0017-9310. doi: <https://doi.org/10.1016/j.ijheatmasstransfer.2022.122675>. URL <https://www.sciencedirect.com/science/article/pii/S0017931022001570>.
- [10] Rupresha Deb, Bhaskarjyoti Sarma, and Amaresh Dalal. Magnetic-field mediated active propulsion of ferrofluid droplets on a wire. *Langmuir*, 39(23):8244–8254, 2023. doi: 10.1021/acs.langmuir.3c00717. URL <https://doi.org/10.1021/acs.langmuir.3c00717>. PMID: 37264796.
- [11] Gudlavalleti V V S Vara Prasad, Purbarun Dhar, and Devranjan Samanta. Magneto-elastic effect in non-newtonian ferrofluid droplets impacting superhydrophobic surfaces. *Langmuir*, 37(32):9673–9682, 2021. doi: 10.1021/acs.langmuir.1c00885. URL <https://doi.org/10.1021/acs.langmuir.1c00885>. PMID: 34350767.
- [12] Qian-Ping Li, Yi Ouyang, Xiao-Dong Niu, Youhua Jiang, Ming-Fu Wen, Ze-Qin Li, Mu-Feng Chen, De-Cai Li, and Hiroshi Yamaguchi. Maximum spreading of impacting ferrofluid droplets under the effect of nonuniform magnetic field. *Langmuir*, 38(8):2601–2607, 2022. doi: 10.1021/acs.langmuir.1c03272. URL <https://doi.org/10.1021/acs.langmuir.1c03272>. PMID: 35179906.
- [13] A. Ray, V.B. Varma, P.J. Jayaneel, N.M. Sudharsan, Z.P. Wang, and R.V. Ramanujan. On demand manipulation of ferrofluid droplets by magnetic fields. *Sensors and Actuators B: Chemical*, 242:760–768, 2017. ISSN 0925-4005. doi: <https://doi.org/10.1016/j.snb.2016.11.115>. URL <https://www.sciencedirect.com/science/article/pii/S092540051631913X>.
- [14] Nilamani Sahoo, Purbarun Dhar, and Devranjan Samanta. Vertical magnetic field aided droplet-impact- magnetohydrodynamics of ferrofluids. *Colloids and Surfaces A: Physicochemical and Engineering Aspects*, 633:127872, 2022. ISSN 0927-7757. doi: <https://doi.org/10.1016/j.colsurfa.2021.127872>. URL <https://www.sciencedirect.com/science/article/pii/S0927775721017416>.
- [15] BA Toms. On the early experiments on drag reduction by polymers. *The Physics of Fluids*, 20(10):S3–S5, 1977.
- [16] A. Chetoui, M. Ghemid, M. R. Khelladi, and A. Zouaoui. First synthesis of monodispersed microparticles of copper oxide films by pulsed spray pyrolysis (psp): structural, optical, and morphological investigations. *Applied Physics A*, 126(1): 61, Jan 2020. ISSN 1432-0630. doi: 10.1007/s00339-019-3240-2. URL <https://doi.org/10.1007/s00339-019-3240-2>.

- [17] A.L. Yarin. Drop impact dynamics: Splashing, spreading, receding, bouncing.... *Annual Review of Fluid Mechanics*, 38(1):159–192, 2006. doi: 10.1146/annurev.fluid.38.050304.092144. URL <https://doi.org/10.1146/annurev.fluid.38.050304.092144>.
- [18] H. Almohammadi and A. Amirfazli. Asymmetric spreading of a drop upon impact onto a surface. *Langmuir*, 33(23):5957–5964, 2017. doi: 10.1021/acs.langmuir.7b00704. URL <https://doi.org/10.1021/acs.langmuir.7b00704>.
- [19] Claas Willem Visser, Ralph Pohl, Chao Sun, Gert-Willem Römer, Bert Huis in ‘t Veld, and Detlef Lohse. Toward 3d printing of pure metals by laser-induced forward transfer. *Advanced Materials*, 27(27):4087–4092, 2015.
- [20] Jungho Kim. Spray cooling heat transfer: The state of the art. *International Journal of Heat and Fluid Flow*, 28(4):753–767, 2007. doi: <https://doi.org/10.1016/j.ijheatfluidflow.2006.09.003>. URL <https://www.sciencedirect.com/science/article/pii/S0142727X06001639>.
- [21] Milan Visaria and Issam Mudawar. Application of two-phase spray cooling for thermal management of electronic devices. In *2008 11th Intersociety Conference on Thermal and Thermomechanical Phenomena in Electronic Systems*, pages 275–283, 2008. doi: 10.1109/ITHERM.2008.4544280.
- [22] Martin A. M. Gijs, Frédéric Lacharme, and Ulrike Lehmann. Microfluidic applications of magnetic particles for biological analysis and catalysis. *Chemical Reviews*, 110(3):1518–1563, 2010. doi: 10.1021/cr9001929. URL <https://doi.org/10.1021/cr9001929>.
- [23] Frieder Mugele and Jean-Christophe Baret. Electrowetting: from basics to applications. *Journal of Physics: Condensed Matter*, 17(28):R705, 2005. doi: 10.1088/0953-8984/17/28/R01. URL <https://dx.doi.org/10.1088/0953-8984/17/28/R01>.
- [24] Matin Torabinia, Ali Farzbod, and Hyejin Moon. Electromechanical model to predict the movability of liquids in an electrowetting-on-dielectric microfluidic device. *Journal of Applied Physics*, 123(15):154902, 2018. doi: 10.1063/1.5014045. URL <https://doi.org/10.1063/1.5014045>.
- [25] Božidar Lišić. Heat transfer control during quenching. *Mater. Manuf. Process.*, 24(7-8):879–886, May 2009.
- [26] J. D. Bernardin and I. Mudawar. The Leidenfrost Point: Experimental Study and Assessment of Existing Models. *Journal of Heat Transfer*, 121(4):894–903, 1999. doi: 10.1115/1.2826080. URL <https://doi.org/10.1115/1.2826080>.
- [27] Gustav Graeber, Kartik Regulagadda, Pascal Hodel, Christian Küttel, Dominic Landolf, Thomas M. Schutzius, and Dimos Poulikakos. Leidenfrost droplet

- trampolining. *Nature Communications*, 12(1):1727, 2021. doi: 10.1038/s41467-021-21981-z. URL <https://doi.org/10.1038/s41467-021-21981-z>.
- [28] Anne-Laure Biance, Christophe Clanet, and David Quéré. First steps in the spreading of a liquid droplet. *Phys. Rev. E*, 69:016301, Jan 2004. doi: 10.1103/PhysRevE.69.016301. URL <https://link.aps.org/doi/10.1103/PhysRevE.69.016301>.
- [29] Ilia V. Roisman, Romain Rioboo, and Cameron Tropea. Normal impact of a liquid drop on a dry surface: model for spreading and receding. *Proceedings of the Royal Society of London. Series A: Mathematical, Physical and Engineering Sciences*, 458(2022):1411–1430, 2002. doi: 10.1098/rspa.2001.0923. URL <https://royalsocietypublishing.org/doi/abs/10.1098/rspa.2001.0923>.
- [30] Yongan Gu and Dongqing Li. Liquid drop spreading on solid surfaces at low impact speeds. *Colloids and Surfaces A: Physicochemical and Engineering Aspects*, 163(2):239–245, 2000. ISSN 0927-7757. doi: [https://doi.org/10.1016/S0927-7757\(99\)00295-2](https://doi.org/10.1016/S0927-7757(99)00295-2). URL <https://www.sciencedirect.com/science/article/pii/S0927775799002952>.
- [31] D. M. Anderson and S. H. Davis. The spreading of volatile liquid droplets on heated surfaces. *Physics of Fluids*, 7(2):248–265, 1995. doi: 10.1063/1.868623. URL <https://doi.org/10.1063/1.868623>.
- [32] Gangtao Liang, Yang Chen, Liuzhu Chen, and Shengqiang Shen. Maximum spreading for liquid drop impacting on solid surface. *Industrial & Engineering Chemistry Research*, 58(23):10053–10063, 2019. doi: 10.1021/acs.iecr.9b02014. URL <https://doi.org/10.1021/acs.iecr.9b02014>.
- [33] Gangtao Liang and Issam Mudawar. Review of drop impact on heated walls. *International Journal of Heat and Mass Transfer*, 106:103–126, 2017. ISSN 0017-9310. doi: <https://doi.org/10.1016/j.ijheatmasstransfer.2016.10.031>. URL <https://www.sciencedirect.com/science/article/pii/S0017931016324097>.
- [34] Tuan Tran, Hendrik J. J. Staat, Andrea Prosperetti, Chao Sun, and Detlef Lohse. Drop impact on superheated surfaces. *Phys. Rev. Lett.*, 108:036101, Jan 2012. doi: 10.1103/PhysRevLett.108.036101. URL <https://link.aps.org/doi/10.1103/PhysRevLett.108.036101>.
- [35] G. Castanet, O. Caballina, and F. Lemoine. Drop spreading at the impact in the leidenfrost boiling. *Physics of Fluids*, 27(6):063302, 2015. doi: 10.1063/1.4922066. URL <https://doi.org/10.1063/1.4922066>.
- [36] Gangtao Liang, Shengqiang Shen, Yali Guo, and Jili Zhang. Boiling from liquid drops impact on a heated wall. *International Journal of Heat and Mass Transfer*, 100:48–57, 2016. ISSN 0017-9310. doi: <https://doi.org/10.1016/j>

- ijheatmasstransfer.2016.04.061. URL <https://www.sciencedirect.com/science/article/pii/S0017931016306548>.
- [37] Maanasa Bhat, R. Sakthikumar, and D. Sivakumar. Fuel drop impact on heated solid surface in film evaporation regime. *Chemical Engineering Science*, 202:95–104, 2019. ISSN 0009-2509. doi: <https://doi.org/10.1016/j.ces.2019.03.017>. URL <https://www.sciencedirect.com/science/article/pii/S0009250919302325>.
- [38] V.G. Labeish. Thermohydrodynamic study of a drop impact against a heated surface. *Experimental Thermal and Fluid Science*, 8(3):181–194, 1994. ISSN 0894-1777. doi: [https://doi.org/10.1016/0894-1777\(94\)90047-7](https://doi.org/10.1016/0894-1777(94)90047-7). URL <https://www.sciencedirect.com/science/article/pii/0894177794900477>.
- [39] David Quéré. Leidenfrost dynamics. *Annual Review of Fluid Mechanics*, 45(1): 197–215, 2013. doi: [10.1146/annurev-fluid-011212-140709](https://doi.org/10.1146/annurev-fluid-011212-140709). URL <https://doi.org/10.1146/annurev-fluid-011212-140709>.
- [40] Philippe Bourrianne, Cunjing Lv, and David Quéré. The cold leidenfrost regime. *Science Advances*, 5(6):eaaw0304, 2019. doi: [10.1126/sciadv.aaw0304](https://doi.org/10.1126/sciadv.aaw0304). URL <https://www.science.org/doi/abs/10.1126/sciadv.aaw0304>.
- [41] Vance Bergeron, Daniel Bonn, Jean Yves Martin, and Louis Vovelle. Controlling droplet deposition with polymer additives. *Nature*, 405(6788):772–775, Jun 2000. doi: [10.1038/35015525](https://doi.org/10.1038/35015525). URL <https://doi.org/10.1038/35015525>.
- [42] Regan Crooks, Justin Cooper-White, and David V. Boger. The role of dynamic surface tension and elasticity on the dynamics of drop impact. *Chemical Engineering Science*, 56(19):5575–5592, 2001. ISSN 0009-2509. doi: [https://doi.org/10.1016/S0009-2509\(01\)00175-0](https://doi.org/10.1016/S0009-2509(01)00175-0). URL <https://www.sciencedirect.com/science/article/pii/S0009250901001750>. Festschrift in honour of Dr. R.A. Mashelkar.
- [43] A. Rozhkov, B. Prunet-Foch, and M. Vignes-Adler. Impact of drops of polymer solutions on small targets. *Physics of Fluids*, 15(7):2006–2019, 2003. doi: [10.1063/1.1580480](https://doi.org/10.1063/1.1580480). URL <https://doi.org/10.1063/1.1580480>.
- [44] Denis Bartolo, Arezki Boudaoud, Grégoire Narcy, and Daniel Bonn. Dynamics of non-newtonian droplets. *Phys. Rev. Lett.*, 99:174502, Oct 2007. doi: [10.1103/PhysRevLett.99.174502](https://link.aps.org/doi/10.1103/PhysRevLett.99.174502). URL <https://link.aps.org/doi/10.1103/PhysRevLett.99.174502>.
- [45] M. I. Smith and V. Bertola. Effect of polymer additives on the wetting of impacting droplets. *Phys. Rev. Lett.*, 104:154502, Apr 2010. doi: [10.1103/PhysRevLett.104.154502](https://link.aps.org/doi/10.1103/PhysRevLett.104.154502). URL <https://link.aps.org/doi/10.1103/PhysRevLett.104.154502>.
- [46] Bavand Keshavarz, Eric C. Houze, John R. Moore, Michael R. Koerner, and Gareth H. McKinley. Ligament mediated fragmentation of viscoelastic liquids. *Phys.*

- Rev. Lett.*, 117:154502, Oct 2016. doi: 10.1103/PhysRevLett.117.154502. URL <https://link.aps.org/doi/10.1103/PhysRevLett.117.154502>.
- [47] Pradeep P. Bhat, Santosh Appathurai, Michael T. Harris, Matteo Pasquali, Gareth H. McKinley, and Osman A. Basaran. Formation of beads-on-a-string structures during break-up of viscoelastic filaments. *Nature Physics*, 6(8):625–631, Aug 2010. ISSN 1745-2481. doi: 10.1038/nphys1682. URL <https://doi.org/10.1038/nphys1682>.
- [48] Michael Zenou, Amir Sa’ar, and Zvi Kotler. Digital laser printing of aluminum micro-structure on thermally sensitive substrates. *Journal of Physics D: Applied Physics*, 48(20):205303, apr 2015. doi: 10.1088/0022-3727/48/20/205303. URL <https://dx.doi.org/10.1088/0022-3727/48/20/205303>.
- [49] Abrar Ahmed, Brian A. Fleck, and Prashant R. Waghmare. Maximum spreading of a ferrofluid droplet under the effect of magnetic field. *Physics of Fluids*, 30(7):077102, 2018. doi: 10.1063/1.5032113. URL <https://doi.org/10.1063/1.5032113>.
- [50] Juan-Cheng Yang, Tian-Yu Qi, Tian-Yang Han, Jie Zhang, and Ming-Jiu Ni. Elliptical spreading characteristics of a liquid metal droplet impact on a glass surface under a horizontal magnetic field. *Physics of Fluids*, 30(1):012101, 2018. doi: 10.1063/1.5000054. URL <https://doi.org/10.1063/1.5000054>.
- [51] Shai Rahimi and Daniel Weihs. Experimental investigation of magneto-rheological droplet impact on a smooth surface. *Journal of Magnetism and Magnetic Materials*, 321(19):3178–3182, 2009. ISSN 0304-8853. doi: <https://doi.org/10.1016/j.jmmm.2009.05.050>. URL <https://www.sciencedirect.com/science/article/pii/S0304885309005721>.
- [52] Rajeev Dhiman and Sanjeev Chandra. Rupture of thin films formed during droplet impact. *Proceedings of the Royal Society A: Mathematical, Physical and Engineering Sciences*, 466(2116):1229–1245, 2010. doi: 10.1098/rspa.2009.0425. URL <https://royalsocietypublishing.org/doi/abs/10.1098/rspa.2009.0425>.
- [53] Rajeev Dhiman and Sanjeev Chandra. Rupture of radially spreading liquid films. *Physics of Fluids*, 20(9):092104, 2008. doi: 10.1063/1.2978186. URL <https://doi.org/10.1063/1.2978186>.
- [54] Sungchan Yun and Geunbae Lim. Ellipsoidal drop impact on a solid surface for rebound suppression. *Journal of Fluid Mechanics*, 752:266–281, 2014. doi: 10.1017/jfm.2014.332.
- [55] Weiwei Deng and Alessandro Gomez. The role of electric charge in microdroplets impacting on conducting surfaces. *Physics of Fluids*, 22(5):051703, 2010. doi: 10.1063/1.3431739. URL <https://doi.org/10.1063/1.3431739>.

- [56] Sungchan Yun, Jiwoo Hong, and Kwan Hyoung Kang. Suppressing drop rebound by electrically driven shape distortion. *Phys. Rev. E*, 87:033010, Mar 2013. doi: 10.1103/PhysRevE.87.033010. URL <https://link.aps.org/doi/10.1103/PhysRevE.87.033010>.
- [57] Danial Khojasteh, Mohammad Karim Dehghan Manshadi, Seyed Mahmood Mousavi, Freshteh Sotoudeh, Reza Kamali, and Alireza Bordbar. Electrically modulated droplet impingement onto hydrophilic and (super)hydrophobic solid surfaces. *Journal of the Brazilian Society of Mechanical Sciences and Engineering*, 42(4):153, Mar 2020. ISSN 1806-3691. doi: 10.1007/s40430-020-2241-6. URL <https://doi.org/10.1007/s40430-020-2241-6>.
- [58] Sung Uk Ryu and Sang Yong Lee. Maximum spreading of electrically charged droplets impacting on dielectric substrates. *International Journal of Multiphase Flow*, 35(1):1–7, 2009. ISSN 0301-9322. doi: <https://doi.org/10.1016/j.ijmultiphaseflow.2008.09.003>. URL <https://www.sciencedirect.com/science/article/pii/S0301932208001377>.
- [59] Seyed Reza Mahmoudi, Kazimierz Adamiak, and G. S. Peter Castle. Spreading of a dielectric droplet through an interfacial electric pressure. *Proceedings of the Royal Society A: Mathematical, Physical and Engineering Sciences*, 467(2135):3257–3271, 2011. doi: 10.1098/rspa.2011.0220. URL <https://royalsocietypublishing.org/doi/abs/10.1098/rspa.2011.0220>.
- [60] Vitaliy Yurkiv, Alexander L. Yarin, and Farzad Mashayek. Modeling of droplet impact onto polarized and nonpolarized dielectric surfaces. *Langmuir*, 34(34):10169–10180, 2018. doi: 10.1021/acs.langmuir.8b01443. URL <https://doi.org/10.1021/acs.langmuir.8b01443>. PMID: 30063834.
- [61] Cesar Palma and Robert Deegan. Electrowetting on semiconductors. *Applied Physics Letters*, 106(1):014106, 2015. doi: 10.1063/1.4905348. URL <https://doi.org/10.1063/1.4905348>.
- [62] Chen Jiang, Hanbin Ma, David G. Hasko, and Arokia Nathan. Influence of polarization on contact angle saturation during electrowetting. *Applied Physics Letters*, 109(21):211601, 2016. doi: 10.1063/1.4968189. URL <https://doi.org/10.1063/1.4968189>.
- [63] Longquan Chen, Chunli Li, Nico F. A. van der Vegt, Günter K. Auernhammer, and Elmar Bonaccorso. Initial electrospreeding of aqueous electrolyte drops. *Phys. Rev. Lett.*, 110:026103, Jan 2013. doi: 10.1103/PhysRevLett.110.026103. URL <https://link.aps.org/doi/10.1103/PhysRevLett.110.026103>.
- [64] G. Manukyan, J. M. Oh, D. van den Ende, R. G. H. Lammertink, and F. Mugele. Electrical switching of wetting states on superhydrophobic surfaces: A route

- towards reversible cassie-to-wenzel transitions. *Phys. Rev. Lett.*, 106:014501, Jan 2011. doi: 10.1103/PhysRevLett.106.014501. URL <https://link.aps.org/doi/10.1103/PhysRevLett.106.014501>.
- [65] G. McHale, C. V. Brown, and N. Sampara. Voltage-induced spreading and superspreading of liquids. *Nature Communications*, 4(1):1605, Mar 2013. ISSN 2041-1723. doi: 10.1038/ncomms2619. URL <https://doi.org/10.1038/ncomms2619>.
- [66] Quoc Vo and Tuan Tran. Droplet ejection by electrowetting actuation. *Applied Physics Letters*, 118(16):161603, 2021. doi: 10.1063/5.0044500. URL <https://doi.org/10.1063/5.0044500>.
- [67] Kaixuan () Zhang, Jiayi () Zhao, Yang () Liu, and Shuo () Chen. Analytical prediction of electrowetting-induced jumping motion for droplets on textured hydrophobic substrates: Effects of the wetting states. *Physics of Fluids*, 34(3):032001, 2022. doi: 10.1063/5.0082832. URL <https://doi.org/10.1063/5.0082832>.
- [68] Anne-Laure Biance, Christophe Clanet, and David Quéré. Leidenfrost drops. *Physics of Fluids*, 15(6):1632–1637, 2003. doi: 10.1063/1.1572161. URL <https://aip.scitation.org/doi/abs/10.1063/1.1572161>.
- [69] Minori Shirota, Michiel A. J. van Limbeek, Chao Sun, Andrea Prosperetti, and Detlef Lohse. Dynamic leidenfrost effect: Relevant time and length scales. *Phys. Rev. Lett.*, 116:064501, Feb 2016. doi: 10.1103/PhysRevLett.116.064501. URL <https://link.aps.org/doi/10.1103/PhysRevLett.116.064501>.
- [70] Mohammad Khavari, Chao Sun, Detlef Lohse, and Tuan Tran. Fingering patterns during droplet impact on heated surfaces. *Soft Matter*, 11:3298–3303, 2015. doi: 10.1039/C4SM02878C. URL <http://dx.doi.org/10.1039/C4SM02878C>.
- [71] Lucia Rueda Villegas, Sébastien Tanguy, Guillaume Castanet, Ophélie Caballina, and Fabrice Lemoine. Direct numerical simulation of the impact of a droplet onto a hot surface above the leidenfrost temperature. *International Journal of Heat and Mass Transfer*, 104:1090–1109, 2017. ISSN 0017-9310. doi: <https://doi.org/10.1016/j.ijheatmasstransfer.2016.08.105>. URL <https://www.sciencedirect.com/science/article/pii/S0017931016303015>.
- [72] Long Qiao, Zhong Zeng, Haiqiong Xie, Hao Liu, and Liangqi Zhang. Modeling leidenfrost drops over heated liquid substrates. *International Journal of Heat and Mass Transfer*, 128:1296–1306, 2019. ISSN 0017-9310. doi: <https://doi.org/10.1016/j.ijheatmasstransfer.2018.09.082>. URL <https://www.sciencedirect.com/science/article/pii/S0017931018322683>.

- [73] Purbarun Dhar, Soumya Ranjan Mishra, Ajay Gairola, and Devranjan Samanta. Delayed leidenfrost phenomenon during impact of elastic fluid droplets. *Proceedings of the Royal Society A: Mathematical, Physical and Engineering Sciences*, 476(2243):20200556, 2020. doi: 10.1098/rspa.2020.0556. URL <https://royalsocietypublishing.org/doi/abs/10.1098/rspa.2020.0556>.
- [74] Y. M. Qiao and S. Chandra. Experiments on adding a surfactant to water drops boiling on a hot surface. *Proceedings of the Royal Society of London. Series A: Mathematical, Physical and Engineering Sciences*, 453(1959):673–689, 1997. doi: 10.1098/rspa.1997.0038. URL <https://royalsocietypublishing.org/doi/abs/10.1098/rspa.1997.0038>.
- [75] Hua Chen, Wen long Cheng, Yu hang Peng, and Li jia Jiang. Dynamic leidenfrost temperature increase of impacting droplets containing high-alcohol surfactant. *International Journal of Heat and Mass Transfer*, 118:1160–1168, 2018. ISSN 0017-9310. doi: <https://doi.org/10.1016/j.ijheatmasstransfer.2017.11.100>. URL <https://www.sciencedirect.com/science/article/pii/S0017931017334142>.
- [76] M. Prat, P. Schmitz, and D. Poulikakos. On the Effect of Surface Roughness on the Vapor Flow Under Leidenfrost-Levitated Droplets. *Journal of Fluids Engineering*, 117(3):519–525, 09 1995. ISSN 0098-2202. doi: 10.1115/1.2817293. URL <https://doi.org/10.1115/1.2817293>.
- [77] JOHN D BERNARDIN, CLINTON J STEBBINS, and ISSAM MUDAWAR. Effects of surface roughness on water droplet impact history and heat transfer regimes. *International Journal of Heat and Mass Transfer*, 40(1):73–88, 1996. ISSN 0017-9310. doi: [https://doi.org/10.1016/S0017-9310\(96\)00067-1](https://doi.org/10.1016/S0017-9310(96)00067-1). URL <https://www.sciencedirect.com/science/article/pii/S0017931096000671>.
- [78] Hyungdae Kim, Bao Truong, Jacopo Buongiorno, and Lin-Wen Hu. On the effect of surface roughness height, wettability, and nanoporosity on leidenfrost phenomena. *Applied Physics Letters*, 98(8):083121, 2011. doi: 10.1063/1.3560060. URL <https://doi.org/10.1063/1.3560060>.
- [79] C.T. Avedisian and J. Koplik. Leidenfrost boiling of methanol droplets on hot porous/ceramic surfaces. *International Journal of Heat and Mass Transfer*, 30(2):379–393, 1987. ISSN 0017-9310. doi: [https://doi.org/10.1016/0017-9310\(87\)90126-8](https://doi.org/10.1016/0017-9310(87)90126-8). URL <https://www.sciencedirect.com/science/article/pii/0017931087901268>.
- [80] Meng Shi, Ratul Das, Sankara Arunachalam, and Himanshu Mishra. Suppression of leidenfrost effect on superhydrophobic surfaces. *Physics of Fluids*, 33(12):122104, 2021. doi: 10.1063/5.0064040. URL <https://doi.org/10.1063/5.0064040>.

- [81] Ryo Matsumoto and Koji Hasegawa. Self-propelled leidenfrost droplets on a heated glycerol pool. *Scientific Reports*, 11(1):3954, Feb 2021. ISSN 2045-2322. doi: 10.1038/s41598-021-83517-1. URL <https://doi.org/10.1038/s41598-021-83517-1>.
- [82] Vishal Talari, Prakhar Behar, Yi Lu, Evan Haryadi, and Dong Liu. Leidenfrost drops on micro/nanostructured surfaces. *Frontiers in Energy*, 12(1):22–42, Mar 2018. ISSN 2095-1698. doi: 10.1007/s11708-018-0541-7. URL <https://doi.org/10.1007/s11708-018-0541-7>.
- [83] Hao () Wang, Jinliang () Xu, Xiaojing () Ma, and Jian () Xie. Evaporation of leidenfrost droplet on thin soluble liquid bath with thermal non-equilibrium effect. *Physics of Fluids*, 34(9):093320, 2022. doi: 10.1063/5.0108939. URL <https://doi.org/10.1063/5.0108939>.
- [84] S Sudo, N Wakamatsu, T Ikohagi, H Nishiyama, M Ohaba, and K Katagiri. Magnetic field effects in the impact of a magnetic fluid drop. *Journal of Magnetism and Magnetic Materials*, 201(1):285–289, 1999. ISSN 0304-8853. doi: [https://doi.org/10.1016/S0304-8853\(99\)00029-3](https://doi.org/10.1016/S0304-8853(99)00029-3). URL [https://doi.org/10.1016/S0304-8853\(99\)00029-3](https://doi.org/10.1016/S0304-8853(99)00029-3).
- [85] Jiandong Zhou and Dengwei Jing. Effects of vertical magnetic field on impact dynamics of ferrofluid droplet onto a rigid substrate. *Phys. Rev. Fluids*, 4:083602, Aug 2019. doi: 10.1103/PhysRevFluids.4.083602. URL <https://link.aps.org/doi/10.1103/PhysRevFluids.4.083602>.
- [86] Nilamani Sahoo, Gargi Khurana, Devranjan Samanta, and Purbarun Dhar. Collisional ferrohydrodynamics of magnetic fluid droplets on superhydrophobic surfaces. *Physics of Fluids*, 33(1):012012, 2021. doi: 10.1063/5.0032610. URL <https://doi.org/10.1063/5.0032610>.
- [87] Ted Mao, David C. S. Kuhn, and Honghi Tran. Spread and rebound of liquid droplets upon impact on flat surfaces. *AIChE Journal*, 43(9):2169–2179. doi: <https://doi.org/10.1002/aic.690430903>. URL <https://aiche.onlinelibrary.wiley.com/doi/abs/10.1002/aic.690430903>.
- [88] Purbarun Dhar, Soumya Ranjan Mishra, and Devranjan Samanta. Onset of rebound suppression in non-newtonian droplets post-impact on superhydrophobic surfaces. *Phys. Rev. Fluids*, 4:103303, Oct 2019. doi: 10.1103/PhysRevFluids.4.103303. URL <https://link.aps.org/doi/10.1103/PhysRevFluids.4.103303>.
- [89] Duyang Zang, Xiaolu Wang, Xingguo Geng, Yongjian Zhang, and Yongmei Chen. Impact dynamics of droplets with silica nanoparticles and polymer additives. *Soft Matter*, 9:394–400, 2013. doi: 10.1039/C2SM26759D. URL <http://dx.doi.org/10.1039/C2SM26759D>.

- [90] Sungchan Yun and Geunbae Lim. Ellipsoidal drop impact on a solid surface for rebound suppression. *Journal of Fluid Mechanics*, 752:266–281, 2014. ISSN 0022-1120. doi: 10.1017/jfm.2014.332. URL <https://doi.org/10.1017/jfm.2014.332>.
- [91] C. Antonini, F. Villa, I. Bernagozzi, A. Amirfazli, and M. Marengo. Drop rebound after impact: The role of the receding contact angle. *Langmuir*, 29(52):16045–16050, 2013. doi: 10.1021/la4012372. URL <https://doi.org/10.1021/la4012372>. PMID: 24028086.
- [92] Min Y. Pack, Angela Yang, Antonio Perazzo, Boyang Qin, and Howard A. Stone. Role of extensional rheology on droplet bouncing. *Phys. Rev. Fluids*, 4:123603, Dec 2019. doi: 10.1103/PhysRevFluids.4.123603. URL <https://link.aps.org/doi/10.1103/PhysRevFluids.4.123603>.
- [93] Vivek Jaiswal, Raghvendra Kumar Dwivedi, A. R. Harikrishnan, and Purbarun Dhar. Magnetohydrodynamics- and magnetosolutal-transport-mediated evaporation dynamics in paramagnetic pendant droplets under field stimulus. *Phys. Rev. E*, 98: 013109, Jul 2018. doi: 10.1103/PhysRevE.98.013109. URL <https://link.aps.org/doi/10.1103/PhysRevE.98.013109>.
- [94] Ajay Katiyar, Purbarun Dhar, Tandra Nandi, and Sarit K. Das. Magnetic field induced augmented thermal conduction phenomenon in magneto-nanocolloids. *Journal of Magnetism and Magnetic Materials*, 419:588–599, 2016. ISSN 0304-8853. doi: <https://doi.org/10.1016/j.jmmm.2016.06.065>. URL <https://www.sciencedirect.com/science/article/pii/S0304885316312082>.
- [95] Nilamani Sahoo, Gargi Khurana, A.R. Harikrishnan, Devranjan Samanta, and Purbarun Dhar. Post impact droplet hydrodynamics on inclined planes of variant wettabilities. *European Journal of Mechanics - B/Fluids*, 79:27–37, 2020. ISSN 0997-7546. doi: <https://doi.org/10.1016/j.euromechflu.2019.08.013>. URL <https://www.sciencedirect.com/science/article/pii/S0997754619303115>.
- [96] Guangyao Cui and Ian Jacobi. Magnetic control of ferrofluid droplet adhesion in shear flow and on inclined surfaces. *Langmuir*, 36(36):10885–10891, 2020. doi: 10.1021/acs.langmuir.0c02369. URL <https://doi.org/10.1021/acs.langmuir.0c02369>.
- [97] Carlo Rigoni, Stefano Bertoldo, Matteo Pierno, Delphine Talbot, Ali Abou-Hassan, and Giampaolo Mistura. Division of ferrofluid drops induced by a magnetic field. *Langmuir*, 34(33):9762–9767, 2018. doi: 10.1021/acs.langmuir.8b02399. URL <https://doi.org/10.1021/acs.langmuir.8b02399>.
- [98] Ajay Katiyar, Purbarun Dhar, Sarit K. Das, and Tandra Nandi. Near-field magnetostatics and néel–brownian interactions mediated magneto-rheological

- characteristics of highly stable nano-ferrocolloids. *Soft Matter*, 11:1614–1627, 2015. doi: 10.1039/C4SM02458C. URL <http://dx.doi.org/10.1039/C4SM02458C>.
- [99] Hyungmo Kim, Chan Lee, Moo Hwan Kim, and Joonwon Kim. Drop impact characteristics and structure effects of hydrophobic surfaces with micro- and/or nanoscaled structures. *Langmuir*, 28(30):11250–11257, 2012. doi: 10.1021/la302215n. URL <https://doi.org/10.1021/la302215n>.
- [100] Chunfang Guo, Danyang Zhao, Yanjun Sun, Minjie Wang, and Yahua Liu. Droplet impact on anisotropic superhydrophobic surfaces. *Langmuir*, 34(11):3533–3540, 2018. doi: 10.1021/acs.langmuir.7b03752. URL <https://doi.org/10.1021/acs.langmuir.7b03752>.
- [101] Ziliang Zhao, Xiangling Ji, Rumiana Dimova, Reinhard Lipowsky, and Yonggang Liu. Viscoelasticity of poly(ethylene glycol) solutions on supported lipid bilayers via quartz crystal microbalance with dissipation. *Macromolecules*, 48(6):1824–1831, 2015. doi: 10.1021/acs.macromol.5b00095. URL <https://doi.org/10.1021/acs.macromol.5b00095>.
- [102] Xueda Shi, Stephen Kenney, Ganesh Chapagain, and Gordon F. Christopher. Mechanisms of onset for moderate mach number instabilities of viscoelastic flows around confined cylinders. *Rheologica Acta*, 54(9):805–815, Oct 2015. ISSN 1435-1528. doi: 10.1007/s00397-015-0875-6. URL <https://doi.org/10.1007/s00397-015-0875-6>.
- [103] V. Tirtaatmadja, G. H. McKinley, and J. J. Cooper-White. Drop formation and breakup of low viscosity elastic fluids: Effects of molecular weight and concentration. *Physics of Fluids*, 18(4):043101, 2006. doi: 10.1063/1.2190469. URL <https://doi.org/10.1063/1.2190469>.
- [104] Viktor Grishaev, Carlo Saverio Iorio, Frank Dubois, and A. Amirfazli. Complex drop impact morphology. *Langmuir*, 31(36):9833–9844, 2015. doi: 10.1021/acs.langmuir.5b02162. URL <https://doi.org/10.1021/acs.langmuir.5b02162>.
- [105] Cameron;Marengo Marco; Rioboo, Romain;Tropea. Outcomes from a drop impact on solid surfaces. *Atomization and Sprays*, 11, 2001. doi: 10.1615/AtomizSpr.v11.i2.40. URL [10.1615/AtomizSpr.v11.i2.40](https://doi.org/10.1615/AtomizSpr.v11.i2.40).
- [106] Devranjan Samanta, Yves Dubief, Markus Holzner, Christof Schäfer, Alexander N. Morozov, Christian Wagner, and Björn Hof. Elasto-inertial turbulence. *Proceedings of the National Academy of Sciences*, 110(26):10557–10562, 2013. doi: 10.1073/pnas.1219666110. URL <https://www.pnas.org/doi/abs/10.1073/pnas.1219666110>.
- [107] R. G. Larson, Eric S. G. Shaqfeh, and S. J. Muller. A purely elastic instability in taylor–couette flow. *Journal of Fluid Mechanics*, 218:573–600, 1990. ISSN

- 0022-1120. doi: 10.1017/S0022112090001124. URL <https://doi.org/10.1017/S0022112090001124>.
- [108] E S G Shaqfeh. Purely elastic instabilities in viscometric flows. *Annual Review of Fluid Mechanics*, 28(1):129–185, 1996. doi: 10.1146/annurev.fl.28.010196.001021. URL <https://doi.org/10.1146/annurev.fl.28.010196.001021>.
- [109] Christopher M. White and M Godfrey Mungal. Mechanics and prediction of turbulent drag reduction with polymer additives. *Annual Review of Fluid Mechanics*, 40(1):235–256, 2008. doi: 10.1146/annurev.fluid.40.111406.102156. URL <https://doi.org/10.1146/annurev.fluid.40.111406.102156>.
- [110] IH Karampelas, S Vader, Z Vader, V Sukhotskiy, A Verma, G Garg, M Tong, and E Furlani. Drop-on-demand 3d metal printing. *Informatics, Electronics and Microsystems*, 4:153–155, 2017.
- [111] Hong Wu, Yunlong Chang, Lin Lu, and Jin Bai. Review on magnetically controlled arc welding process. *The International Journal of Advanced Manufacturing Technology*, 91(9):4263–4273, 2017. doi: 10.1007/s00170-017-0068-9. URL <https://doi.org/10.1007/s00170-017-0068-9>.
- [112] A.M. Gañán-Calvo, J. Dávila, and A. Barrero. Current and droplet size in the electrospraying of liquids. scaling laws. *Journal of Aerosol Science*, 28(2):249–275, 1997. doi: [https://doi.org/10.1016/S0021-8502\(96\)00433-8](https://doi.org/10.1016/S0021-8502(96)00433-8). URL <https://www.sciencedirect.com/science/article/pii/S0021850296004338>.
- [113] Michel Cloupeau and Bernard Prunet-Foch. Electrohydrodynamic spraying functioning modes: a critical review. *Journal of Aerosol Science*, 25(6):1021–1036, 1994. doi: [https://doi.org/10.1016/0021-8502\(94\)90199-6](https://doi.org/10.1016/0021-8502(94)90199-6). URL <https://www.sciencedirect.com/science/article/pii/0021850294901996>.
- [114] S Mishra, K L Barton, A G Alleyne, P M Ferreira, and J A Rogers. High-speed and drop-on-demand printing with a pulsed electrohydrodynamic jet. *Journal of Micromechanics and Microengineering*, 20(9):095026, 2010. doi: 10.1088/0960-1317/20/9/095026. URL <https://dx.doi.org/10.1088/0960-1317/20/9/095026>.
- [115] Wyatt C. Nelson and Chang-Jin ‘CJ’ Kim. Droplet actuation by electrowetting-on-dielectric (ewod): A review. *Journal of Adhesion Science and Technology*, 26(12-17):1747–1771, 2012. doi: 10.1163/156856111X599562. URL <https://www.tandfonline.com/doi/abs/10.1163/156856111X599562>.
- [116] Brayden W. Wagoner, Petia M. Vlahovska, Michael T. Harris, and Osman A. Basaran. Electrohydrodynamics of lenticular drops and equatorial streaming. *Journal of Fluid Mechanics*, 925:A36, 2021. doi: 10.1017/jfm.2021.651. URL <https://doi.org/10.1017/jfm.2021.651>.

- [117] Seyed Esmaeil Mousavi, Abouzar Moshfegh, Hamid Hassanzadeh Afrouzi, Ashkan Javadzadegan, and Davood Toghraie. Simulation of droplet detachment from hydrophobic and hydrophilic solid surfaces under the electric field using lattice boltzmann method (lbm). *Journal of Molecular Liquids*, 313:113528, 2020. ISSN 0167-7322. doi: <https://doi.org/10.1016/j.molliq.2020.113528>. URL <https://www.sciencedirect.com/science/article/pii/S0167732219353048>.
- [118] M. G. Pollack, A. D. Shenderov, and R. B. Fair. Electrowetting-based actuation of droplets for integrated microfluidics. *Lab Chip*, 2:96–101, 2002. doi: 10.1039/B110474H. URL <http://dx.doi.org/10.1039/B110474H>.
- [119] Jun Zeng and Tom Korsmeyer. Principles of droplet electrohydrodynamics for lab-on-a-chip. *Lab Chip*, 4:265–277, 2004. doi: 10.1039/B403082F. URL <http://dx.doi.org/10.1039/B403082F>.
- [120] Jang-Ung Park, Matt Hardy, Seong Jun Kang, Kira Barton, Kurt Adair, Deep kishore Mukhopadhyay, Chang Young Lee, Michael S. Strano, Andrew G. Alleyne, John G. Georgiadis, Placid M. Ferreira, and John A. Rogers. High-resolution electrohydrodynamic jet printing. *Nature Materials*, 6(10):782–789, 2007. doi: 10.1038/nmat1974. URL <https://doi.org/10.1038/nmat1974>.
- [121] Santanu Kumar Das, Amaresh Dalal, and Gaurav Tomar. Electrohydrodynamic-induced interactions between droplets. *Journal of Fluid Mechanics*, 915:A88.
- [122] Nilamani Sahoo, Devranjan Samanta, and Purbarun Dhar. Electrohydrodynamics of dielectric droplet collision on different wettability surfaces. *Physics of Fluids*, 33(11):112005, 2021. doi: 10.1063/5.0065609. URL <https://doi.org/10.1063/5.0065609>.
- [123] Wang Hongchen Sun Mingyang Tian Penghao Wang Yutao Wang Kun Tan, Jie and Dongyue Jiang. Regulating droplet impact on a solid hydrophobic surface through alternating current electrowetting-on-dielectric. *Physics of Fluids*, 33(4):042101, 2021. doi: 10.1063/5.0044823. URL <https://doi.org/10.1063/5.0044823>.
- [124] Qisi Wang, Zhentao Wang, Shiqi Yang, Bin Li, Huibin Xu, Kai Yu, and Junfeng Wang. Experimental study on electrohydrodynamic atomization (ehda) in stable cone-jet with middle viscous and low conductive liquid. *Experimental Thermal and Fluid Science*, 121:110260, 2021. doi: <https://doi.org/10.1016/j.expthermflusci.2020.110260>. URL <https://www.sciencedirect.com/science/article/pii/S0894177720307640>.
- [125] Vance Bergeron. Designing intelligent fluids for controlling spray applications. *Comptes Rendus Physique*, 4(2):211–219, 2003. doi: [https://doi.org/10.1016/S1631-0705\(03\)00043-4](https://doi.org/10.1016/S1631-0705(03)00043-4). URL <https://www.sciencedirect.com/science/article/pii/S1631070503000434>.

- [126] G German and V Bertola. Impact of shear-thinning and yield-stress drops on solid substrates. *Journal of Physics: Condensed Matter*, 21(37):375111, 2009. doi: 10.1088/0953-8984/21/37/375111. URL <https://dx.doi.org/10.1088/0953-8984/21/37/375111>.
- [127] Sang Mo An and Sang Yong Lee. Observation of the spreading and receding behavior of a shear-thinning liquid drop impacting on dry solid surfaces. *Experimental Thermal and Fluid Science*, 37:37–45, 2012. doi: <https://doi.org/10.1016/j.expthermflusci.2011.09.018>. URL <https://www.sciencedirect.com/science/article/pii/S0894177711002007>.
- [128] Kerim Yapici, Nese K. Cakmak, Naciye Ilhan, and Yusuf Uludag. Rheological characterization of polyethylene glycol based tio2 nanofluids. *Korea-Australia Rheology Journal*, 26(4):355–363, Nov 2014. doi: 10.1007/s13367-014-0041-1. URL <https://doi.org/10.1007/s13367-014-0041-1>.
- [129] Wenjea J. Tseng and Kuang-Chih Lin. Rheology and colloidal structure of aqueous tio2 nanoparticle suspensions. *Materials Science and Engineering: A*, 355(1): 186–192, 2003. doi: [https://doi.org/10.1016/S0921-5093\(03\)00063-7](https://doi.org/10.1016/S0921-5093(03)00063-7). URL <https://www.sciencedirect.com/science/article/pii/S0921509303000637>.
- [130] Omar Anis Harzallah and Dominique Dupuis. Rheological properties of suspensions of tio2 particles in polymer solutions. 1. shear viscosity. *Rheologica Acta*, 42(1): 10–19, 2003. doi: 10.1007/s00397-002-0250-2. URL <https://doi.org/10.1007/s00397-002-0250-2>.
- [131] Haisheng Chen, Yulong Ding, Yurong He, and Chunqing Tan. Rheological behaviour of ethylene glycol based titania nanofluids. *Chemical Physics Letters*, 444(4):333–337, 2007. ISSN 0009-2614. doi: <https://doi.org/10.1016/j.cplett.2007.07.046>. URL <https://www.sciencedirect.com/science/article/pii/S0009261407009785>.
- [132] Purbarun Dhar, Vimal Saini, Ankur Chattopadhyay, and Devranjan Samanta. Electro-viscoelasticity of agarose based electrorheological fluids. *Physics of Fluids*, 33(1):013101, 2021. doi: 10.1063/5.0037105. URL <https://doi.org/10.1063/5.0037105>.
- [133] Shu-Rong Yan, Davood Toghraie, Lokman Aziz Abdulkareem, As'ad Alizadeh, Pouya Barnoon, and Masoud Afrand. The rheological behavior of mwcnts-zno/water-ethylene glycol hybrid non-newtonian nanofluid by using of an experimental investigation. *Journal of Materials Research and Technology*, 9(4):8401–8406, 2020. ISSN 2238-7854. doi: <https://doi.org/10.1016/j.jmrt.2020.05.018>. URL <https://www.sciencedirect.com/science/article/pii/S2238785420312849>.

- [134] Wanping Zhang, Zihao Gao, Haiyang Zhu, and Qianjie Zhang. Mixed micellization of cationic/anionic amino acid surfactants: Synergistic effect of sodium lauroyl glutamate and alkyl tri-methyl ammonium chloride. *Journal of Dispersion Science and Technology*, 43(14):2227–2239, 2022. doi: 10.1080/01932691.2021.1929289. URL <https://doi.org/10.1080/01932691.2021.1929289>.
- [135] Hisaschi T. Tee, Romina Zipp, Kaloian Koynov, Wolfgang Tremel, and Frederik R. Wurm. Poly(methyl ethylene phosphate) hydrogels: Degradable and cell-repellent alternatives to peg-hydrogels. *European Polymer Journal*, 141:110075, 2020. doi: <https://doi.org/10.1016/j.eurpolymj.2020.110075>. URL <https://www.sciencedirect.com/science/article/pii/S0014305720317894>.
- [136] Simon J. Haward, Thomas J. Ober, Mónica S.N. Oliveira, Manuel A. Alves, and Gareth H. McKinley. Extensional rheology and elastic instabilities of a wormlike micellar solution in a microfluidic cross-slot device. *Soft Matter*, 8:536–555, 2012. doi: 10.1039/C1SM06494K. URL <http://dx.doi.org/10.1039/C1SM06494K>.
- [137] Simon J. Haward, Naoyuki Kitajima, Kazumi Toda-Peters, Tsutomu Takahashi, and Amy Q. Shen. Flow of wormlike micellar solutions around microfluidic cylinders with high aspect ratio and low blockage ratio. *Soft Matter*, 15:1927–1941, 2019. doi: 10.1039/C8SM02099J. URL <http://dx.doi.org/10.1039/C8SM02099J>.
- [138] Yuchuan Cheng, Zihui Zhao, Hui Wang, Letian Hua, Aihua Sun, Jun Wang, Zhixiang Li, Jianjun Guo, and Gaojie Xu. Strong electrorheological performance of smart fluids based on tio2 particles at relatively low electric field. *Frontiers in Materials*, 8, 2021. doi: 10.3389/fmats.2021.764455. URL <https://www.frontiersin.org/articles/10.3389/fmats.2021.764455>.
- [139] X. P. Zhao, Q. Zhao, and X. M. Gao. Optical activity of electrorheological fluids under external electric field. *Journal of Applied Physics*, 93(7):4309–4314, 2003. doi: 10.1063/1.1559435. URL <https://doi.org/10.1063/1.1559435>.
- [140] Anežka Lengálová, Vladimír Pavlínek, Petr Sáha, Otakar Quadrat, Takeshi Kitano, and Jaroslav Stejskal. Influence of particle concentration on the electrorheological efficiency of polyaniline suspensions. *European Polymer Journal*, 39(4):641–645, 2003. doi: [https://doi.org/10.1016/S0014-3057\(02\)00281-1](https://doi.org/10.1016/S0014-3057(02)00281-1). URL <https://www.sciencedirect.com/science/article/pii/S0014305702002811>.
- [141] Minhee Lee, Young Soo Chang, and Ho-Young Kim. Drop impact on microwetting patterned surfaces. *Physics of Fluids*, 22(7):072101, 2010. doi: 10.1063/1.3460353. URL <https://doi.org/10.1063/1.3460353>.
- [142] Joo Hyun Moon, Dae Yun Kim, and Seong Hyuk Lee. Spreading and receding characteristics of a non-newtonian droplet impinging on a heated surface. *Experimental Thermal and Fluid Science*, 57:94–101, 2014. doi: <https://doi.org/>

- 10.1016/j.expthermflusci.2014.04.003. URL <https://www.sciencedirect.com/science/article/pii/S0894177714000910>.
- [143] Ivan U. Vakarelski, Joseph D. Berry, Derek Y. C. Chan, and Sigurdur T. Thoroddsen. Leidenfrost vapor layers reduce drag without the crisis in high viscosity liquids. *Phys. Rev. Lett.*, 117:114503, Sep 2016. doi: 10.1103/PhysRevLett.117.114503. URL <https://link.aps.org/doi/10.1103/PhysRevLett.117.114503>.
- [144] H. Linke, B. J. Alemán, L. D. Melling, M. J. Taormina, M. J. Francis, C. C. Dow-Hygelund, V. Narayanan, R. P. Taylor, and A. Stout. Self-propelled leidenfrost droplets. *Phys. Rev. Lett.*, 96:154502, 2006. doi: 10.1103/PhysRevLett.96.154502. URL <https://link.aps.org/doi/10.1103/PhysRevLett.96.154502>.
- [145] Guillaume Lagubeau, Marie Le Merrer, Christophe Clanet, and David Quéré. Leidenfrost on a ratchet. *Nature Physics*, 7(5):395–398, 2011. doi: 10.1038/nphys1925. URL <https://doi.org/10.1038/nphys1925>.
- [146] Guillaume Dupeux, Marie Le Merrer, Christophe Clanet, and David Quéré. Trapping leidenfrost drops with crenelations. *Phys. Rev. Lett.*, 107:114503, Sep 2011. doi: 10.1103/PhysRevLett.107.114503. URL <https://link.aps.org/doi/10.1103/PhysRevLett.107.114503>.
- [147] Ambre Bouillant, Timothée Mousterde, Philippe Bourrianne, Antoine Lagarde, Christophe Clanet, and David Quéré. Leidenfrost wheels. *Nature Physics*, 14(12):1188–1192, 2018. doi: 10.1038/s41567-018-0275-9. URL <https://doi.org/10.1038/s41567-018-0275-9>.
- [148] V. Bertola and K. Sefiane. Controlling secondary atomization during drop impact on hot surfaces by polymer additives. *Physics of Fluids*, 17(10):108104, 2005. doi: 10.1063/1.2112667. URL <https://aip.scitation.org/doi/abs/10.1063/1.2112667>.
- [149] V. Bertola. An experimental study of bouncing leidenfrost drops: Comparison between newtonian and viscoelastic liquids. *International Journal of Heat and Mass Transfer*, 52(7):1786–1793, 2009. doi: <https://doi.org/10.1016/j.ijheatmasstransfer.2008.09.028>. URL <https://www.sciencedirect.com/science/article/pii/S0017931008005875>.
- [150] Pengfei Liu, Ranjith Kandasamy, Jin Yao Ho, Huicheng Feng, and Teck Neng Wong. Comparative study on the enhancement of spray cooling heat transfer using conventional and bio-surfactants. *Applied Thermal Engineering*, 194:117047, 2021. ISSN 1359-4311. doi: <https://doi.org/10.1016/j.applthermaleng.2021.117047>. URL <https://www.sciencedirect.com/science/article/pii/S1359431121004919>.
- [151] Peipei Zhang, Baoxu Peng, Xiaoxiao Yang, Jingming Wang, and Lei Jiang.

- Regulating droplet dynamic wetting behaviors using surfactant additives on high-temperature surfaces. *Advanced Materials Interfaces*, 7(14):2000501, 2020.
- [152] Sijia Lyu, Varghese Mathai, Yujie Wang, Benjamin Sobac, Pierre Colinet, Detlef Lohse, and Chao Sun. Final fate of a leidenfrost droplet: Explosion or takeoff. *Science Advances*, 5(5):eaav8081, 2019. doi: 10.1126/sciadv.aav8081. URL <https://www.science.org/doi/abs/10.1126/sciadv.aav8081>.
- [153] Tadashi Kajiya, Wataru Kobayashi, Tohru Okuzono, and Masao Doi. Controlling the drying and film formation processes of polymer solution droplets with addition of small amount of surfactants. *The Journal of Physical Chemistry B*, 113(47):15460–15466, 2009. doi: 10.1021/jp9077757. URL <https://doi.org/10.1021/jp9077757>.
- [154] Hanne Hoffman, Rick Sijs, Thijs de Goede, and Daniel Bonn. Controlling droplet deposition with surfactants. *Phys. Rev. Fluids*, 6:033601, 2021. doi: 10.1103/PhysRevFluids.6.033601. URL <https://link.aps.org/doi/10.1103/PhysRevFluids.6.033601>.
- [155] Mounir Aytouna, Denis Bartolo, Gerard Wegdam, Daniel Bonn, and Salima Rafai. Impact dynamics of surfactant laden drops: dynamic surface tension effects. *Experiments in Fluids*, 48(1):49–57, 2010. doi: 10.1007/s00348-009-0703-9. URL <https://doi.org/10.1007/s00348-009-0703-9>.
- [156] Xiaoguang Zhang and Osman A. Basaran. Dynamic surface tension effects in impact of a drop with a solid surface. *Journal of Colloid and Interface Science*, 187(1):166–178, 1997. doi: <https://doi.org/10.1006/jcis.1996.4668>. URL <https://www.sciencedirect.com/science/article/pii/S0021979796946688>.
- [157] V. Bertola. An impact regime map for water drops impacting on heated surfaces. *International Journal of Heat and Mass Transfer*, 85:430–437, 2015. ISSN 0017-9310. doi: <https://doi.org/10.1016/j.ijheatmasstransfer.2015.01.084>. URL <https://www.sciencedirect.com/science/article/pii/S0017931015000927>.
- [158] Junseok Park and Dong Eok Kim. Dynamics of liquid drops levitating on superheated surfaces. *International Journal of Thermal Sciences*, 152:106321, 2020. ISSN 1290-0729. doi: <https://doi.org/10.1016/j.ijthermalsci.2020.106321>. URL <https://www.sciencedirect.com/science/article/pii/S1290072919318150>.
- [159] Gilad Chaniel, Mark Frenkel, Victor Multanen, and Edward Bormashenko. Paradoxical coffee-stain effect driven by the marangoni flow observed on oil-infused surfaces. *Colloids and Surfaces A: Physicochemical and Engineering Aspects*, 522:355–360, 2017. doi: <https://doi.org/10.1016/j.colsurfa.2017.03.009>. URL <https://www.sciencedirect.com/science/article/pii/S0927775717302431>.

- [160] R.T. van Gaalen, C. Diddens, H.M.A. Wijshoff, and J.G.M. Kuerten. Marangoni circulation in evaporating droplets in the presence of soluble surfactants. *Journal of Colloid and Interface Science*, 584:622–633, 2021. doi: <https://doi.org/10.1016/j.jcis.2020.10.057>. URL <https://www.sciencedirect.com/science/article/pii/S0021979720313977>.
- [161] Dongdong Liu and Tuan Tran. Size-dependent spontaneous oscillations of leidenfrost droplets. *Journal of Fluid Mechanics*, 902:A21.
- [162] Abhishek Kaushal, Vivek Jaiswal, Vishwajeet Mehandia, and Purbarun Dhar. Solutothermal-hydrodynamics influenced evaporation kinetics of saline sessile droplets. *European Journal of Mechanics - B/Fluids*, 83:130–140, 2020. doi: <https://doi.org/10.1016/j.euromechflu.2020.04.014>. URL <https://www.sciencedirect.com/science/article/pii/S0997754620300248>.
- [163] Abhishek Kaushal, Vishwajeet Mehandia, and Purbarun Dhar. Ferrohydrodynamics governed evaporation phenomenology of sessile droplets. *Physics of Fluids*, 33(2):022006, 2021. doi: 10.1063/5.0040712. URL <https://doi.org/10.1063/5.0040712>.
- [164] Gayatri Paul, Indranil Manna, and Prasanta Kumar Das. Formation, growth, and eruption cycle of vapor domes beneath a liquid puddle during leidenfrost phenomena. *Applied Physics Letters*, 103(8):084101, 2013. doi: 10.1063/1.4819095. URL <https://doi.org/10.1063/1.4819095>.
- [165] Franck Celestini, Thomas Frisch, and Yves Pomeau. Take off of small leidenfrost droplets. *Phys. Rev. Lett.*, 109:034501, 2012. doi: 10.1103/PhysRevLett.109.034501. URL <https://link.aps.org/doi/10.1103/PhysRevLett.109.034501>.
- [166] Aditya Jha, Pierre Chantelot, Christophe Clanet, and David Quéré. Viscous bouncing. *Soft Matter*, 16:7270–7273, 2020. doi: 10.1039/D0SM00955E. URL <http://dx.doi.org/10.1039/D0SM00955E>.
- [167] Anayet Ullah Siddique, Marcus Trimble, Feng Zhao, Mark M. Weislogel, and Hua Tan. Jet ejection following drop impact on micropillared hydrophilic substrates. *Phys. Rev. Fluids*, 5:063606, 2020. doi: 10.1103/PhysRevFluids.5.063606. URL <https://link.aps.org/doi/10.1103/PhysRevFluids.5.063606>.
- [168] Colin Pounder. Johann gottlob leidenfrost. 06 2008.
- [169] G. Grant, J. Brenton, and D. Drysdale. Fire suppression by water sprays. *Progress in Energy and Combustion Science*, 26(2):79–130, 2000. doi: [https://doi.org/10.1016/S0360-1285\(99\)00012-X](https://doi.org/10.1016/S0360-1285(99)00012-X). URL <https://www.sciencedirect.com/science/article/pii/S036012859900012X>.
- [170] Suresh V. Garimella, Amy S. Fleischer, Jayathi Y. Murthy, Ali Keshavarzi, Ravi Prasher, Chandrakant Patel, Sushil H. Bhavnani, R. Venkatasubramanian,

- Ravi Mahajan, Y. Joshi, Bahgat Sammakia, Bruce A. Myers, Len Chorosinski, Martine Baelmans, Prabhu Sathyamurthy, and Peter E. Raad. Thermal challenges in next-generation electronic systems. *IEEE Transactions on Components and Packaging Technologies*, 31(4):801–815, 2008. doi: 10.1109/TCAPT.2008.2001197.
- [171] H van Dam. Physics of nuclear reactor safety. *Rep. Prog. Phys.*, 55(11):2025–2077, November 1992.
- [172] Gail Duursma, Khellil Sefiane, and Aiden Kennedy. Experimental studies of nanofluid droplets in spray cooling. *Heat Transfer Engineering*, 30(13):1108–1120, 2009. doi: 10.1080/01457630902922467. URL <https://doi.org/10.1080/01457630902922467>.
- [173] Gayatri Paul, Prasanta Kumar Das, and Indranil Manna. Nanoparticle deposition from nanofluid droplets during leidenfrost phenomenon and consequent rise in transition temperature. *International Journal of Heat and Mass Transfer*, 148:119110, 2020. doi: <https://doi.org/10.1016/j.ijheatmasstransfer.2019.119110>. URL <https://www.sciencedirect.com/science/article/pii/S0017931019337974>.
- [174] Gudlavalleti V V S Vara Prasad, Harsh Sharma, Neelkanth Nirmalkar, Purbarun Dhar, and Devranjan Samanta. Augmenting the leidenfrost temperature of droplets via nanobubble dispersion. *Langmuir*, 38(51):15925–15936, 2022. doi: 10.1021/acs.langmuir.2c01891. URL <https://doi.org/10.1021/acs.langmuir.2c01891>.
- [175] Franck Celestini and Geoffroy Kirstetter. Effect of an electric field on a leidenfrost droplet. *Soft Matter*, 8:5992–5995, 2012. doi: 10.1039/C2SM25656H. URL <http://dx.doi.org/10.1039/C2SM25656H>.
- [176] D. D. Hall and I. Mudawar. Predicting the Impact of Quenching on Mechanical Properties of Complex-Shaped Aluminum Alloy Parts. *Journal of Heat Transfer*, 117(2):479–488, 1995. doi: 10.1115/1.2822547. URL <https://doi.org/10.1115/1.2822547>.
- [177] Hyungdae Kim, Gregory DeWitt, Thomas McKrell, Jacopo Buongiorno, and Lin wen Hu. On the quenching of steel and zircaloy spheres in water-based nanofluids with alumina, silica and diamond nanoparticles. *International Journal of Multiphase Flow*, 35(5):427–438, 2009. doi: <https://doi.org/10.1016/j.ijmultiphaseflow.2009.02.004>. URL <https://www.sciencedirect.com/science/article/pii/S0301932209000226>.
- [178] R. C. Prasad, J. E. S. Venart, and N. Mani. *Thermal Conductivity of Methane and Ethane*, pages 81–91. 1985. doi: 10.1007/978-1-4684-4916-7_9. URL https://doi.org/10.1007/978-1-4684-4916-7_9.
- [179] Sang M. Kwark, Ratan Kumar, Gilberto Moreno, Jaisuk Yoo, and Seung M. You. Pool boiling characteristics of low concentration nanofluids. *International Journal*

- of Heat and Mass Transfer*, 53(5):972–981, 2010. doi: <https://doi.org/10.1016/j.ijheatmasstransfer.2009.11.018>. URL <https://www.sciencedirect.com/science/article/pii/S0017931009006188>.
- [180] Daniel P. Rini, Ruey-Hung Chen, and Louis C. Chow. Bubble Behavior and Nucleate Boiling Heat Transfer in Saturated FC-72 Spray Cooling . *Journal of Heat Transfer*, 124(1):63–72, 2001. doi: 10.1115/1.1418365. URL <https://doi.org/10.1115/1.1418365>.
- [181] Ruey-Hung Chen, Louis C. Chow, and Jose E. Navedo. Optimal spray characteristics in water spray cooling. *International Journal of Heat and Mass Transfer*, 47(23):5095–5099, 2004. doi: <https://doi.org/10.1016/j.ijheatmasstransfer.2004.05.033>. URL <https://www.sciencedirect.com/science/article/pii/S0017931004002364>.
- [182] Ruey-Hung Chen, Louis C Chow, and Jose E Navedo. Effects of spray characteristics on critical heat flux in subcooled water spray cooling. *International Journal of Heat and Mass Transfer*, 45(19):4033–4043, 2002. doi: [https://doi.org/10.1016/S0017-9310\(02\)00113-8](https://doi.org/10.1016/S0017-9310(02)00113-8). URL <https://www.sciencedirect.com/science/article/pii/S0017931002001138>.
- [183] Ivo Iavicoli, Luca Fontana, and Gunnar Nordberg. The effects of nanoparticles on the renal system. *Critical Reviews in Toxicology*, 46(6):490–560, 2016. doi: 10.1080/10408444.2016.1181047. URL <https://doi.org/10.1080/10408444.2016.1181047>.
- [184] Hyuk-min Kwon, James C. Bird, and Kripa K. Varanasi. Increasing leidenfrost point using micro-nano hierarchical surface structures. *Applied Physics Letters*, 103(20):201601, 2013. doi: 10.1063/1.4828673. URL <https://doi.org/10.1063/1.4828673>.
- [185] John D. Bernardin and Issam Mudawar. A Leidenfrost Point Model for Impinging Droplets and Sprays . *Journal of Heat Transfer*, 126(2):272–278, 2004. doi: 10.1115/1.1652045. URL <https://doi.org/10.1115/1.1652045>.
- [186] John D. Bernardin and Issam Mudawar. A Cavity Activation and Bubble Growth Model of the Leidenfrost Point . *Journal of Heat Transfer*, 124(5):864–874, 2002. doi: 10.1115/1.1470487. URL <https://doi.org/10.1115/1.1470487>.
- [187] Nilanjana Basu, Gopinath R. Warrier, and Vijay K. Dhir. Onset of Nucleate Boiling and Active Nucleation Site Density During Subcooled Flow Boiling . *Journal of Heat Transfer*, 124(4):717–728, 2002. doi: 10.1115/1.1471522. URL <https://doi.org/10.1115/1.1471522>.
- [188] Colin Pounder. De aquae communis nonnullis qualitatibus tractatus j.g. leidenfrost 1756, 05 2015.

- [189] M. Pasandideh-Fard, S.D. Aziz, S. Chandra, and J. Mostaghimi. Cooling effectiveness of a water drop impinging on a hot surface. *International Journal of Heat and Fluid Flow*, 22(2):201–210, 2001. doi: [https://doi.org/10.1016/S0142-727X\(00\)00086-2](https://doi.org/10.1016/S0142-727X(00)00086-2). URL <https://www.sciencedirect.com/science/article/pii/S0142727X00000862>.
- [190] Daniel Tam, Volkmar von ARNIM, G H McKINLEY, and A E Hosoi. Marangoni convection in droplets on superhydrophobic surfaces. *J. Fluid Mech.*, 624:101–123, April 2009. doi: 10.1017/S0022112008005053. URL <https://www.cambridge.org/core/journals/journal-of-fluid-mechanics/article/marangoni-convection-in-droplets-on-superhydrophobic-surfaces/489509747D5D62B2703E74815872955D>.
- [191] Ambre Bouillant, Caroline Cohen, Christophe Clanet, and David Quéré. Self-excitation of leidenfrost drops and consequences on their stability. *Proceedings of the National Academy of Sciences*, 118(26):e2021691118, 2021. doi: 10.1073/pnas.2021691118. URL <https://www.pnas.org/doi/abs/10.1073/pnas.2021691118>.
- [192] Thomas Jollans and Michel Orrit. Explosive, oscillatory, and leidenfrost boiling at the nanoscale. *Phys. Rev. E*, 99:063110, Jun 2019. doi: 10.1103/PhysRevE.99.063110. URL <https://link.aps.org/doi/10.1103/PhysRevE.99.063110>.
- [193] Corey Kruse, Troy Anderson, Chris Wilson, Craig Zuhlke, Dennis Alexander, George Gogos, and Sidy Ndao. Extraordinary shifts of the leidenfrost temperature from multiscale micro/nanostructured surfaces. *Langmuir*, 29(31):9798–9806, 2013. doi: 10.1021/la401936w. URL <https://doi.org/10.1021/la401936w>.
- [194] Mengnan Jiang, Yang Wang, Fayu Liu, Hanheng Du, Yuchao Li, Huanhuan Zhang, Suet To, Steven Wang, Chin Pan, Jihong Yu, David Quéré, and Zuankai Wang. Inhibiting the leidenfrost effect above 1,000 °c for sustained thermal cooling. *Nature*, 601(7894):568–572, Jan 2022. doi: 10.1038/s41586-021-04307-3. URL <https://doi.org/10.1038/s41586-021-04307-3>.
- [195] N. Nirmalkar, A. W. Pacek, and M. Barigou. On the existence and stability of bulk nanobubbles. *Langmuir*, 34(37):10964–10973, 2018. doi: 10.1021/acs.langmuir.8b01163. URL <https://doi.org/10.1021/acs.langmuir.8b01163>.
- [196] N. Nirmalkar, A. W. Pacek, and M. Barigou. Interpreting the interfacial and colloidal stability of bulk nanobubbles. *Soft Matter*, 14:9643–9656, 2018. doi: 10.1039/C8SM01949E. URL <http://dx.doi.org/10.1039/C8SM01949E>.
- [197] N. Nirmalkar, A. W. Pacek, and M. Barigou. Bulk nanobubbles from acoustically cavitated aqueous organic solvent mixtures. *Langmuir*, 35(6):2188–2195, 2019. doi: 10.1021/acs.langmuir.8b03113. URL <https://doi.org/10.1021/acs.langmuir.8b03113>.

- [198] Joost H. Weijss, James R. T. Seddon, and Detlef Lohse. Diffusive shielding stabilizes bulk nanobubble clusters. *ChemPhysChem*, 13(8):2197–2204, 2012.
- [199] Beng Hau Tan, Hongjie An, and Claus-Dieter Ohl. How bulk nanobubbles might survive. *Phys. Rev. Lett.*, 124:134503, 2020. doi: 10.1103/PhysRevLett.124.134503. URL <https://link.aps.org/doi/10.1103/PhysRevLett.124.134503>.
- [200] P. S. Epstein and M. S. Plesset. On the stability of gas bubbles in liquid-gas solutions. *The Journal of Chemical Physics*, 18(11):1505–1509, 1950. doi: 10.1063/1.1747520. URL <https://doi.org/10.1063/1.1747520>.
- [201] Karthik S. Babu and Jayendra K. Amamcharla. Generation methods, stability, detection techniques, and applications of bulk nanobubbles in agro-food industries: a review and future perspective. *Critical Reviews in Food Science and Nutrition*, 0(0):1–20, 2022. doi: 10.1080/10408398.2022.2067119. URL <https://doi.org/10.1080/10408398.2022.2067119>.
- [202] Muidh Alheshibri, Jing Qian, Marie Jehannin, and Vincent S. J. Craig. A history of nanobubbles. *Langmuir*, 32(43):11086–11100, 2016. doi: 10.1021/acs.langmuir.6b02489. URL <https://doi.org/10.1021/acs.langmuir.6b02489>.
- [203] Ashutosh Agarwal, Wun Jern Ng, and Yu Liu. Principle and applications of microbubble and nanobubble technology for water treatment. *Chemosphere*, 84(9):1175–1180, 2011. ISSN 0045-6535. doi: <https://doi.org/10.1016/j.chemosphere.2011.05.054>. URL <https://www.sciencedirect.com/science/article/pii/S0045653511006242>.
- [204] Xiaozhou Fan, Luofu Wang, Yanli Guo, Zhui Tu, Lang Li, Haipeng Tong, Yang Xu, Rui Li, and Kejing Fang. Ultrasonic nanobubbles carrying anti-psma nanobody: Construction and application in prostate cancer-targeted imaging. *PLOS ONE*, 10(6):1–13, 2015. doi: 10.1371/journal.pone.0127419. URL <https://doi.org/10.1371/journal.pone.0127419>.
- [205] Santosh K. Misra, Goutam Ghoshal, Manas R. Gartia, Zhe Wu, Arun K. De, Mao Ye, Corinne R. Bromfield, Emery M. Williams, Kuldeep Singh, Krishnarao V. Tangella, Laurie Rund, Klaus Schulten, Lawrence B. Schook, Partha S. Ray, Everette C. Burdette, and Dipanjan Pan. Trimodal therapy: Combining hyperthermia with repurposed bexarotene and ultrasound for treating liver cancer. *ACS Nano*, 9(11):10695–10718, 2015. doi: 10.1021/acsnano.5b05974. URL <https://doi.org/10.1021/acsnano.5b05974>.
- [206] Akiomi Ushida, Tomiichi Hasegawa, Toshiyuki Nakajima, Hiroshige Uchiyama, and Takatsune Narumi. Drag reduction effect of nanobubble mixture flows through micro-orifices and capillaries. *Experimental Thermal and Fluid Science*, 39:54–59, 2012. doi: <https://doi.org/10.1016/j.expthermflusci.2012.01.008>. URL <https://www.sciencedirect.com/science/article/pii/S089417771200009X>.

- [207] Kosuke Ebina, Kenrin Shi, Makoto Hirao, Jun Hashimoto, Yoshitaka Kawato, Shoichi Kaneshiro, Tokimitsu Morimoto, Kota Koizumi, and Hideki Yoshikawa. Oxygen and air nanobubble water solution promote the growth of plants, fishes, and mice. *PLOS ONE*, 8(6):1–7, 2013. doi: 10.1371/journal.pone.0065339. URL <https://doi.org/10.1371/journal.pone.0065339>.
- [208] Shu Liu, Seiichi Oshita, Yoshio Makino, Qunhui Wang, Yoshinori Kawagoe, and Tsutomu Uchida. Oxidative capacity of nanobubbles and its effect on seed germination. *ACS Sustainable Chemistry & Engineering*, 4(3):1347–1353, 2016. doi: 10.1021/acssuschemeng.5b01368. URL <https://doi.org/10.1021/acssuschemeng.5b01368>.
- [209] Ma Leticia Jose C. Basilan, <https://orcid.org/0000-0003-3105-2252>, Maycee Padilla, and <https://orchid.org/0000-0001-5025-12872>, maleticiajose.basilan@deped.gov.ph, maycee.padilla@deped.gov.ph, Department of Education- SDO Batangas Province, Batangas, Philippines. Assessment of teaching english language skills: journal =.
- [210] Harsh Sharma and Neelkanth Nirmalkar. Enhanced gas-liquid mass transfer coefficient by bulk nanobubbles in water. *Materials Today: Proceedings*, 57: 1838–1841, 2022. doi: <https://doi.org/10.1016/j.matpr.2022.01.029>. URL <https://www.sciencedirect.com/science/article/pii/S2214785322000554>.
- [211] Kalyani Agarwal, Mohit Trivedi, and Neelkanth Nirmalkar. Does salting-out effect nucleate nanobubbles in water: Spontaneous nucleation? *Ultrasonics Sonochemistry*, 82:105860, 2022. doi: <https://doi.org/10.1016/j.ultsonch.2021.105860>. URL <https://www.sciencedirect.com/science/article/pii/S1350417721004028>.
- [212] R.T. van Gaalen, H.M.A. Wijshoff, J.G.M. Kuerten, and C. Diddens. Competition between thermal and surfactant-induced marangoni flow in evaporating sessile droplets. *Journal of Colloid and Interface Science*, 622:892–903, 2022. ISSN 0021-9797. doi: <https://doi.org/10.1016/j.jcis.2022.04.146>. URL <https://www.sciencedirect.com/science/article/pii/S0021979722007214>.
- [213] Christopher Vega-Sánchez, Sam Peppou-Chapman, Liwen Zhu, and Chiara Neto. Nanobubbles explain the large slip observed on lubricant-infused surfaces. *Nat. Commun.*, 13(1):351, January 2022. doi: 10.1038/s41467-022-28016-1. URL <https://doi.org/10.1038/s41467-022-28016-1>.
- [214] Abhishek Kaushal, Vivek Jaiswal, Vishwajeet Mehandia, and Purbarun Dhar. Competing thermal and solutal advection decelerates droplet evaporation on heated surfaces. *European Journal of Mechanics - B/Fluids*, 91:129–140, 2022. doi: <https://doi.org/10.1016/j.euromechflu.2021.10.003>. URL <https://www.sciencedirect.com/science/article/pii/S0997754621001679>.

- [215] Dong In Yu, Ho Jae Kwak, Seung Woo Doh, Ho Seon Ahn, Hyun Sun Park, Moriyama Kiyofumi, and Moo Hwan Kim. Dynamics of contact line depinning during droplet evaporation based on thermodynamics. *Langmuir*, 31(6):1950–1957, 2015. doi: 10.1021/la504971y. URL <https://doi.org/10.1021/la504971y>.
- [216] Divya Panchanathan, Philippe Bourrianne, Philippe Nicollier, Abhijatmedhi Chottratanapituk, Kripa K. Varanasi, and Gareth H. McKinley. Levitation of fizzy drops. *Science Advances*, 7(28):eabf0888, 2021. doi: 10.1126/sciadv.abf0888. URL <https://www.science.org/doi/abs/10.1126/sciadv.abf0888>.
- [217] H Müller-steinhausen, N Epstein, and A.P Watkinson. Effect of dissolved gases on subcooled flow boiling heat transfer. *Chemical Engineering and Processing: Process Intensification*, 23(2):115–124, 1988. ISSN 0255-2701. doi: [https://doi.org/10.1016/0255-2701\(88\)80005-9](https://doi.org/10.1016/0255-2701(88)80005-9). URL <https://www.sciencedirect.com/science/article/pii/0255270188800059>.
- [218] Mohammad Khavari and Tuan Tran. Universality of oscillating boiling in leidenfrost transition. *Phys. Rev. E*, 96:043102, Oct 2017. doi: 10.1103/PhysRevE.96.043102. URL <https://link.aps.org/doi/10.1103/PhysRevE.96.043102>.
- [219] Qiang Cui, Sanjeev Chandra, and Susan McCahan. The Effect of Dissolving Gases or Solids in Water Droplets Boiling on a Hot Surface . *Journal of Heat Transfer*, 123(4):719–728, 2001. doi: 10.1115/1.1376394. URL <https://doi.org/10.1115/1.1376394>.
- [220] Simeng Chen and Volfango Bertola. Jumps, somersaults, and symmetry breaking in leidenfrost drops. *Phys. Rev. E*, 94:021102, 2016. doi: 10.1103/PhysRevE.94.021102. URL <https://link.aps.org/doi/10.1103/PhysRevE.94.021102>.

List of Publications

Journals Published

1. Gudlavalleti V V S Vara Prasad, Purbarun Dhar and Devranjan Samanta,, "Magneto-Elastic Effect in Non-Newtonian Ferrofluid Droplets Impacting Superhydrophobic Surfaces," *Langmuir*, vol. 37, no. 32, pp. 9673–9682, Aug. 2021. Accessed: Aug. 5, 2021. [Online]. Available: <https://doi.org/10.1021/acs.langmuir.1c00885> [Langmuir]
2. Gudlavalleti V V S Vara Prasad, Purbarun Dhar and Devranjan Samanta, "Triggering of electro-elastic anti-superhydrophobicity during non-Newtonian droplets collision," *Proceedings of the Royal Society A*, vol. 479, p. 20220612, Jul. 2023. Accessed: Jul. 26, 2023. [Online]. Available: <https://royalsocietypublishing.org/doi/abs/10.1098/rspa.2022.0612> [Proceedings of the Royal Society A]
3. Gudlavalleti V V S Vara Prasad, Purbarun Dhar and Devranjan Samanta, "Postponement of dynamic Leidenfrost phenomenon during droplet impact of surfactant solutions," *International Journal of Heat and Mass Transfer*, vol. 189, p. 122675, Jun. 2022. Accessed: Jun. 15, 2022. [Online]. Available: <https://doi.org/10.1016/j.ijheatmasstransfer.2022.122675> [International Journal of Heat and Mass Transfer]
4. Gudlavalleti V V S Vara Prasad, Mohit Yadav, Purbarun Dhar and Devranjan Samanta, "Morphed inception of dynamic Leidenfrost regime in colloidal dispersion droplets" *Physics of Fluids*, vol. 35, p. 012107, Jan. 2023. Accessed: Jan. 5, 2023. [Online]. Available: <https://doi.org/10.1063/5.0131609> [Physics of Fluids]
5. Gudlavalleti V V S Vara Prasad, Harsh Sharma, Neelkanth Nirmalkar, Purbarun Dhar and Devranjan Samanta, "Augmenting the Leidenfrost temperature of droplets via nanobubble dispersion" *Langmuir*, vol. 38, no. 51, pp. 15925–15936, Dec. 2022. Accessed: Dec. 12, 2022. [Online]. Available: <https://doi.org/10.1021/acs.langmuir.2c01891> [Langmuir]
6. Gudlavalleti V V S Vara Prasad, Manjeet Meena, Chandra Shekhar, Manigandan Sabapathy, Purbarun Dhar and Devranjan Samanta, "Shift of dynamic Leidenfrost point using microemulsions" [manuscript under preparation]
7. Gudlavalleti V V S Vara Prasad, Harshvardhan, Purbarun Dhar and Devranjan Samanta, "Suppression of Leidenfrost phenomenon in alcohol-water binary mixture droplets" [manuscript under preparation]

8. Gudlavalleti V V S Vara Prasad, Purbarun Dhar, Devranjan Samanta and Parmod Kumar, "Numerical investigation of droplet impact hydrodynamics on superhydrophobic wedges" [manuscript under preparation]

Gudlavalleti V V S Vara Prasad

Doctoral Researcher

Fluid Mechanics Research Lab (FMRL)
Department of Mechanical Engineering
Indian Institute of Technology Ropar
Rupnagar-140001, Punjab, India.

Email: varaprasadgudlavalleti@gmail.com

Web: <https://sites.google.com/view/varaprasad1993>



[Google Scholar](#) [Research Gate](#) [LinkedIn](#)

An enthusiastic dedicated researcher with 2 years of teaching experience. Impressive work ethic and commitment to create a challenging learning environment while tackling novel research problems. Submitted Doctoral dissertation by publishing 5 reputed journals as a 1st author.

Education

| | | |
|---------------------|-----------------------------------------------------------------|-------------|
| Ph.D.(Mechanical) | Indian Institute of Technology Ropar, India | 2018 – 2023 |
| M.Tech.(Thermal) | Jawaharlal Nehru Technological University Kakinada, India | 2015 – 2017 |
| B.Tech.(Mechanical) | Rajiv Gandhi University of Knowledge Technologies Nuzvid, India | 2010 – 2014 |

Experience

| | | |
|---------------------|------------------------------------------------|-------------|
| Teaching Assistant | Indian Institute of Technology Ropar, India | 2018 – 2023 |
| Assistant Professor | QIS College of Engineering & Technology, India | 2017 – 2018 |
| Assistant Professor | Gudlavalleru Engineering College, India | 2014 – 2015 |

Research Interests

Areas of Research:

Droplets, CFD, OpenFOAM, Boiling , Multiphase Flows, Multiphase Heat Transfer, Wettability , Interfacial science, Microfluidics, Complex Fluids, Rheology, Viscoelasticity, Evaporation, Condensation, Electromagnetism, Freezing, Refrigeration & Air conditioning .

Keywords:

Droplets, Wettability, Superhydrophobicity, Boiling, Leidenfrost effect, colloids, polymers, surfactants, nano fluids, bubbles, ferrofluids, dielectrics, Viscoelastic, emulsion, non-Newtonian fluids, electromagnetism.

Skills

Experimental: Highspeed photography, Contact angle meter, Rheometer, Hot plate, Electromagnet.

Numerical: Open FOAM (CFD), Multiphase Flows, Paraview (post-processing)

Coding: C, C++ (Basics), MATLAB(Basics)

Softwares: ImageJ(Image processing), Solid works (part assembly) , RheoCompass , Origin, MS Office.

Doctoral Research

Dissertation Title: Elasto-hydrodynamic and thermo fluidic instabilities in complex fluid droplets

Thesis Advisors: [Dr. Devranjan Samanta](#) and [Dr. Purbarun Dhar](#)

My Ph.D. Dissertation, titled "Elasto-hydrodynamic and Thermo-fluidic Instabilities in Complex Fluid Droplets," delves into two primary issues facing inkjet printing technology: elasto-hydrodynamics and spray cooling technology: thermo-fluidics. My research work was highly interdisciplinary, covering different research areas including Droplet Dynamics, Wettability, Interfacial phenomena, Complex fluids, Multiphase Heat Transfer, Electromagnetism, and Electro-Magneto Rheology. In my dissertation, On the one hand, I investigated the role of elasto-hydrodynamic instabilities such as magneto-elastic instability and electro-elastic instability during droplet impact of non-Newtonian ferrofluids and non-Newtonian dielectric droplets, respectively. On the other hand, I examined the role of thermo-fluidic instabilities at the dynamic Leidenfrost stage, such as Taylor-Marangoni instabilities, the role of vapor embryo on interfacial rewetting behavior, and the effect of residue deposition on surface morphology during droplet impact of surfactant droplets, nanobubbles loaded droplets, and nanocolloidal droplets respectively.

Publications

1. **Gudlavalleti V V S Vara Prasad**, Purbarun Dhar and Devranjan Samanta, "Magneto-Elastic Effect in Non-Newtonian Ferrofluid Droplets Impacting Superhydrophobic Surfaces", **2021** [[Langmuir](#)]
2. **Gudlavalleti V V S Vara Prasad**, Purbarun Dhar and Devranjan Samanta, "Postponement of dynamic Leidenfrost phenomenon during droplet impact of surfactant solutions", **2022** [[International Journal of Heat and Mass Transfer](#)]
3. **Gudlavalleti V V S Vara Prasad**, Harsh Sharma, Neelkanth Nirmalkar, Purbarun Dhar and Devranjan Samanta, "Augmenting the Leidenfrost temperature of droplets via nanobubble dispersion", **2022** [[Langmuir](#)]
4. **Gudlavalleti V V S Vara Prasad**, Mohit Yadav, Purbarun Dhar and Devranjan Samanta, "Morphed inception of dynamic Leidenfrost regime in colloidal dispersion droplets", **2023** [[Physics of Fluids](#)]
5. **Gudlavalleti V V S Vara Prasad**, Purbarun Dhar and Devranjan Samanta, "Triggering of electro-elastic anti-superhydrophobicity during non-Newtonian droplets collision", **2023** [[Proceedings of the Royal Society A](#)]
6. **Gudlavalleti V V S Vara Prasad**, Manjeet Meena, Chandra Shekhar, Manigandan Sabapathy, Purbarun Dhar and Devranjan Samanta, "Shift of dynamic Leidenfrost point using microemulsions", **2023** [manuscript under preparation]
7. **Gudlavalleti V V S Vara Prasad**, Harshvardhan, Purbarun Dhar and Devranjan Samanta, "Suppression of Leidenfrost phenomenon in alcohol-water binary mixture droplets", **2023** [manuscript under preparation]
8. **Gudlavalleti V V S Vara Prasad**, Purbarun Dhar, Devranjan Samanta and Parmod Kumar, "Numerical investigation of droplet impact hydrodynamics on superhydrophobic wedges", **2023** [manuscript under preparation]

References

1. **Dr. Devranjan Samanta** (my doctoral advisor)
Assistant Professor,
Department of Mechanical Engineering,
Fluid Mechanics Lab,
Indian Institute of Technology Ropar,
Rupnagar-140001, Punjab, India.

Email: devranjan.samanta@iitrpr.ac.in

2. **Dr. Purbarun Dhar** (my doctoral advisor)
Assistant Professor,
Department of Mechanical Engineering,
Hydrodynamics and Thermal Multiphysics Lab,
Indian Institute of Technology Kharagpur
West Bengal - 721302, India.

Email: purbarun@mech.iitkgp.ac.in

3. **Dr. Parmod Kumar** (collaborator)
Assistant Professor,
School of Mechanical and Materials Engineering,
Indian Institute of Technology Mandi,
Himachal Pradesh - 175075, India.

Email: parmod@iitmandi.ac.in